UNIVERSITE BRETAGNE LOIRE

UNIVERSITÉ DE NANTES

Thèse de Doctorat

Aubin THIBAULT DE CHANVALON

Mémoire présenté en vue de l'obtention du
grade de Docteur de l'Université de Nantes
sous le sceau de l'Université Bretagne Loire

École doctorale : VENAM

Discipline : Science de la Terre
Spécialité : Biogéosciences
Unités de recherche : CNRS UMR 6112 LPG-BIAF / Ifremer-LBCM

Soutenue le 25 Mars 2016
Thèse N° : 78175

Transformation de la phase solide à travers l'estuaire de la Loire en relation avec son environnement chimique et biologique.

JURY

Rapporteurs :	Filip J. R. MEYSMAN, Senior Scientist, NIOZ, Yerseke, Pays-Bas Cécile GROSBOIS, Professeur, Université François Rabelais, Tours
Examinateurs :	Joan M. BERNHARD, Senior Scientist, Woods Hole Oceanographic Institution, Etats-Unis Bruno DEFLANDRE, Maître de Conférences, Université de Bordeaux Patrick LAUNEAU, Professeur, Université de Nantes
Invités :	Nils RISGAARD-PETERSEN, Senior Scientist, Université d'Aarhus, Danemark Christine DUPUY, Professeur, Université de la Rochelle Ricardo RISO, Professeur, Université de Brest
Directeur de Thèse :	Emmanuelle GESLIN, Maître de Conférences HDR, Université d'Angers
Co-directeur de Thèse :	Joël KNOERY, Chercheur, Ifremer Edouard METZGER, Maître de Conférences, Université d'Angers

Avant-propos

Ce travail a été réalisé dans le laboratoire LPG-BIAF (UMR CNRS 6112) à l'Université d'Angers et dans le laboratoire de biochimie des contaminants métalliques de l'Ifremer de Nantes. Il a été financé par le projet « Réseau de Suivi et de Surveillance de l'Estuaire de la Loire » (RS2E) de l'Observatoire des Sciences de l'Univers Nantes Atlantique (OSUNA). Par ce contexte, ce travail ainsi bénéficié d'échanges facilités entre différents laboratoires de la région des Pays de la Loire. Des campagnes de terrains ont été réalisées conjointement avec le laboratoire MMS (Nantes et Angers) le Laboratoire Subatech de l'école des Mines de Nantes. Plusieurs développements méthodologiques (en cours) ont aussi été amorcés avec Subatech, l'Ifsttar de Nantes et le LPGN de l'Université de Nantes. Des bourses de mobilité ont permis de financer 2 séjours à l'étranger. D'abord, dans le cadre d'une summerschool organisée par l'ICBM "Biogeochemistry of tidal flats and beaches of the southern North Sea coast (Wadden Sea)" du 10 au 24 aout 2013 à Spiekeroog, Wilhelmshaven et Oldenburg (Allemagne). Puis dans le cadre d'une invitation au NIOZ financé sur l'ERC Grant 306933 de Filip Meysman du 1er au 14 février 2015 à Yerseke (Pays-Bas).

Remerciements

La lecture de ce manuscrit n'est pas encore commencée, et peut être vous arrêterez vous à la fin de cette page, qu'il faut vous prévenir : ce par quoi vous commencez est ce par quoi je termine. Aimable circonstance qui me permet de vider mon sac plein dans le vôtre, encore vide. Ce soir, à 20h30, j'ai terminé ma thèse et j'ai 27 ans. Un gâteau d'anniversaire m'attend à la maison, une femme aussi. Léa, toi qui en premier m'as permis de mener à bien ce projet en me soutenant par tes attentions quotidiennes, ta ferveur de débattre, ton oreille affutée et ta patience pour les nombreux retards accumulées pendant ces trois années. L'année passée jour pour jour, elle attendait déjà que je revienne des Pays-Bas alors que Louise, notre fille, n'avait pas 2 mois. Pour la détente que tu m'apportes notamment quand tu n'arrives pas à dormir et que tu as besoin d'être bercée ; pour la distance, le recul que tu m'imposes de prendre vis-à-vis de mes besognes de thésard, merci petite puce pour cette aide insoupçonnée. Parmi les autres soutiens imprévus - mais en beaucoup plus rationnels, il m'apparait important de citer Filip Meysman, rencontré au hasard d'un congrès et qui, pour ma dernière année, m'a débloqué de l'imbroglio des codages numériques dans lequel je m'avançais tête baissée. Hasard relatif, après réflexion, puisque fortement provoqué par la grande qualité diplomatique d'Edouard. Ce wookiee amical, encadrant et mentor, qui a d'ailleurs provoqué de nombreuses autres choses au cours de mes travaux de thèse et a surtout été d'un indéfectible soutien, ne m'a abandonné qu'une fois, dans la vase, le jour de mes 25 ans, pour aller assister (et aider) à la naissance de sa fille. Heureusement, qu'Aurélia –sorte de d'Artagnan de mon encadrement était là pour le relayer. Car deux autres encadrants - Emmanuelle et Joël - doivent aussi être mis à l'honneur, ne serait-ce que pour la constance de leur soutien malgré la divergence de l'intérêt scientifique dont l'évidence ne fit que croitre au cours de ce travail. Merci profondément de m'avoir laissé choisir comment construire ce sujet de thèse (et de m'avoir aidé à l'organiser). C'est, me semble-t-il, une chance dont bien peu de doctorants ont pu profiter avec autant de plaisir. Merci à Frans pour m'avoir énormément aidé à publier mon premier article et à Eric Viollier pour m'avoir donné le goût de la diagenèse précoce (!). Merci aux membres de jury de prendre de le temps de juger mon travail et aux membres du CST – Christine Dupuy et Ricardo Riso – dont les critiques l'ont précieusement jalonné lors de réunions de travail parfois épiques. Merci aussi à tous les stagiaires, techniciens, ingénieurs, chercheurs qui m'ont aidé à récolter l'impressionnante base de données de ce projet et dont la liste à la Prévert donnerait quelque chose comme : Carole, Eric, Olivier, Sylvette, Sandrine, Vona, Meryem, Antony, Romain, Fiona, Tiphaine, Isabelle, Jean-François, Livia, Ismaïl, Pierre, Florian, Sophie, Clément, Grégoire, Eve, Catherine, Bastien, Pia, Briz, Hélène… mais elle n'est probablement pas exhaustive (la nuit s'avance). En tout cas, un merci va particulièrement à Christophe, Emmanuelle et Dominique pour m'avoir appris pendant de nombreuses journées à utiliser avec rigueur et efficacité l'outil fondamental des géochimistes : l'ICPMS ; et à Patrick et Manuel pour m'avoir appris et aidés à utiliser l'outil dans lequel réside une bonne part de l'originalité de ce travail : la caméra hyperspectrale. Merci enfin aux doctorants que j'ai pu côtoyer, qui m'ont appris le dur métier de thésard et que j'observe actuellement osciller dans les remous de l'après thèse : Aurore, Jennifer, Dewi, Clémence, Florian et Julie. Bon courage aux suivants : Jassin, Charlotte, Laurie, Matthieu et Briz !

Table des matières

Avant-propos ..... **iii**
Remerciements ..... **v**
Table des matières ..... **vii**

Introduction **1**

1 Fonctionnement de l'estuaire de la Loire 3
1.1 Les apports du Bassin versant 3
1.2 Fonctionnement hydraulique de l'estuaire. 6
1.3 Fonctionnement hydro-sédimentaire 10
1.4 La biologie des vasières intertidales 12

2 Géochimie du fer et des éléments associés à travers l'estuaire 15
2.1 Cycle du fer 16
2.2 La diagenèse précoce 23

3 Organisation de l'étude 27

Partie 1 :
Importance de l'hétérogénéité à faible échelle dans la vasière des Brillantes **31**

1 Distribution en 2 dimensions des foraminifères benthiques vivants dans le compartiment anoxiques du sédiment d'une vasière estuarienne (Estuaire de la Loire) 33

2 Imagerie simultanée de nitrite et nitrate à l'échelle submillimétrique à travers l'interface eau-sédiment 51

3 Cartographie bidimensionnelle de la remobilisation du fer dans des sédiments marins à une échelle submillimétrique 65

Partie 2 :
Quantification de la transformation du fer réactif et des éléments associés lors du transfert des particules à travers l'estuaire de la Loire 89

1 Recyclage sédimentaire du manganèse, du fer et du phosphore dans une vasière estuarienne, Loire, France 91

2 Nouvelles connaissances apportées par l'échantillonnage en deux dimensions sur les relations entre fer et phosphore sédimentaires 107

3 Fer, manganèse et terres rares comme proxies des transformations des particules à travers l'estuaire de la Loire 123

Synthèse et Perspectives 139

1 Fonctionnement de la vasière 140
1.1 Fonctionnement géochimique de la vasière : 140
1.2 Fonctionnement et importance des microhabitats benthiques 142

2 Importance des estuaires dans le cycle du fer 144

Bibliographie 149
Tables 171
Figures 173
Annexe 181

Introduction

Le cycle géologique des roches se déroule en partie à la surface de la Terre, dans ce qu'il est maintenant convenu d'appeler la « zone critique », à savoir : *la zone hétérogène à la surface de la Terre dans laquelle des interactions complexes entre les roches, le sol, l'eau, l'air et les organismes vivants régulent les habitats naturels et déterminent la disponibilité des ressources nécessaires à la vie* (NRC, 2001). Cette zone critique assure notamment le transfert des particules terrigènes produites par l'érosion des continents vers les bassins sédimentaires. La variabilité temporelle et l'hétérogénéité spatiale des environnements traversés constituent autant de conditions physico-chimiques qui modifient la composition chimique et minéralogique des particules. Ce travail de doctorat cherche à mieux comprendre les transformations réalisées lors du transfert des particules fluviatiles du milieu continental au milieu océanique. Cette zone de mélange entre les eaux douces et les eaux salées définit l'estuaire.

Dans les environnements estuariens, l'évolution de la salinité correspond à une modification des espèces chimiques dissoutes qui modifie les équilibres entre la phase dissoute et la phase solide et entraine des échanges par adsorption/désorption ou précipitation/dissolution. De plus, cette transition saline contraint fortement les possibilités de développement des espèces biologiques et assure ainsi le développement d'un écosystème particulier. Cet écosystème est un maillon essentiel de la transformation des particules, notamment parce qu'il abrite des espèces dites « ingénieurs de l'écosystème » (Jones et al., 1996). Enfin, la dynamique des marées permet aux particules fines (limons et argiles) de sédimenter dans l'estuaire (Dalrymple et al., 1992), et d'y être stockées temporairement dans des conditions chimiques susceptibles d'entrainer leur dissolution (Froelich et al., 1979). L'objectif de cette thèse de doctorat est d'étudier les transformations des particules fines lors de leur transfert à travers l'estuaire de la Loire. Cependant, devant l'étendue des réactions et modifications possibles, il a été choisi de centrer l'effort de recherche sur les transformations subies par le fer et les éléments qui lui sont associés (aluminium, manganèse, terres rares, phosphore et azote). En effet, la compréhension de son cycle géochimique est un enjeu important puisqu'il s'agit d'un nutriment limitant la production primaire dans près de la moitié des océans (Moore et al., 2001, 2013). De plus, les oxydes de fer favorisent le stockage du carbone organique au cours des temps géologiques (Lalonde et al., 2012). A l'échelle de l'estuaire, la forte affinité d'autres métaux et métalloïdes comme l'arsenic, cuivre ou chrome avec les oxydes de fer module leur mobilité (Turner, 2000). Enfin, les oxydes de fer immobilisent par adsorption de grandes quantités de phosphore et pourraient contrôler la disponibilité de ce nutriment dans l'estuaire (Sundby et al., 1992). En nous basant sur l'étude de l'estuaire de la Loire, nous chercherons à répondre aux questions suivantes :

- Quels sont les processus responsables de la modification de la teneur en fer des particules lors de transfert à travers l'estuaire ?
- Quels sont les facteurs régulant ces transformations ?
- Quelle est l'importance de ces transformations dans le fonctionnement géochimique de l'estuaire ?
- Quelle est l'importance de ces transformations dans le fonctionnement écologique de l'estuaire ?

1 Fonctionnement de l'estuaire de la Loire

1.1 Les apports du bassin versant

1.1.1 Les apports dissous

La Loire draine un bassin versant de 117 045 km^2 (Figure 1) qui s'étend à partir du Massif Central, traverse le sud du Bassin Parisien et recouvre l'ouest et le sud du massif armoricain. A Nantes, le débit journalier médian est de 890 $m^3.s^{-1}$ avec un maximum en crue (fréquence décennale sur la période 1967-2015) de 5200 $m^3.s^{-1}$ et un minimum en étiage de 120 $m^3.s^{-1}$ (DREAL Pays-de-Loire, 1994). Un suivi hebdomadaire permet d'illustrer la période d'étiage en été et la période des crues en hiver (Figure 2). Cette variation du débit est le paramètre majeur contraignant les apports à l'estuaire (Manickam et al., 1985; Moatar and Meybeck, 2005). Ainsi, la composition de la Loire en éléments dissous dépend fortement de la saison. Les éléments majeurs (Na^+, K^+, Mg^{2+}, SO_4^{2-} et Cl^-) sont généralement dilués lorsque le débit augmente (Grosbois et al., 2000). Les nutriments (phosphates et nitrates ; Figure 3) sont appauvris en été à cause de leur utilisation par les producteurs primaires (Moatar and Meybeck, 2005). De plus, dans le cas du nitrate, le lessivage des sols plus élevé en hiver et probablement la dénitrification estivale (voir ci-dessous) accentuent cet effet (Moatar and Meybeck, 2005). Comme fréquemment en milieu continental (Jordan et al., 2008), le phosphore est complètement consommé lors des efflorescences estivales de phytoplancton (Meybeck et al., 1988; Gorse et al., 2010) et limite ainsi la production primaire (Minaudo et al., 2015). La concentration en carbone organique dissous (COD) est comprise entre 2,8 et 4,3 mg L^{-1} en étiage et croît jusqu'à 7 $mg.L^{-1}$ en crue ou lors d'efflorescences estivales (Gorse et al., 2010). Il s'agit de concentrations assez faibles, les grands fleuves ayant généralement des concentrations comprises entre 4 et 6 $mg.L^{-1}$ (Ingri et al., 2000). Les variations de concentration en COD en fonction du débit ont précédemment été décrites, par exemple pour des rivières boréales (rivière Kalix, Suède ; moyenne([COD])=3.4 mg L^{-1} ; Ingri et al.,

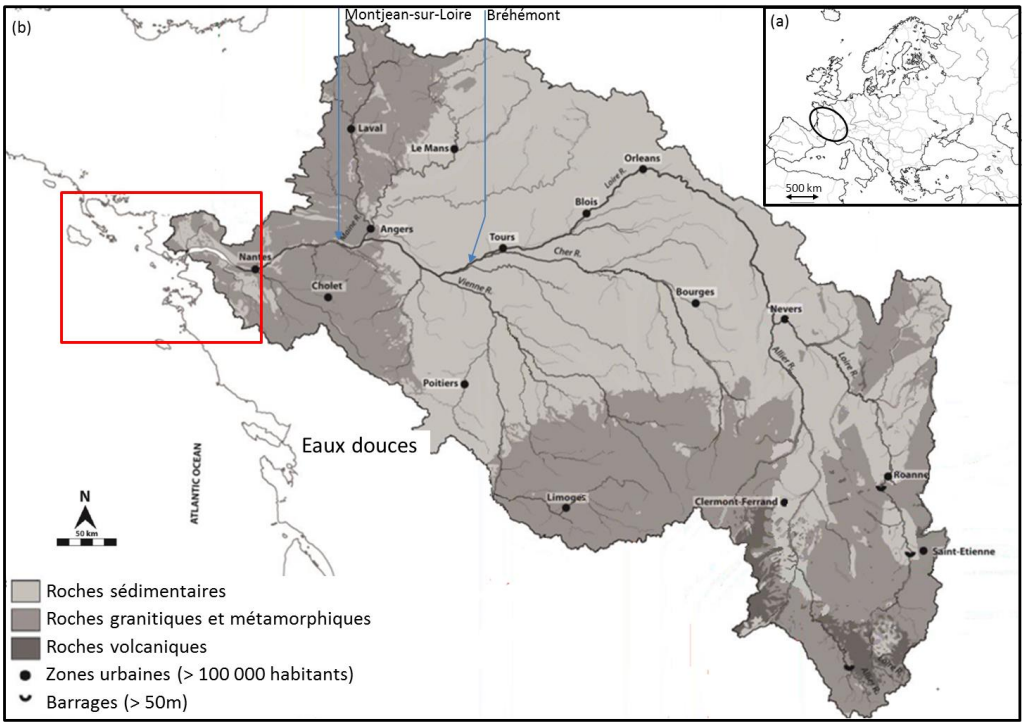

Figure 1 (a) Localisation du bassin versant de la Loire (b) Carte géologique simplifié du bassin versant de la Loire, d'après Dhivert (2014). Le rectangle rouge indique la localisation de la Figure 5.

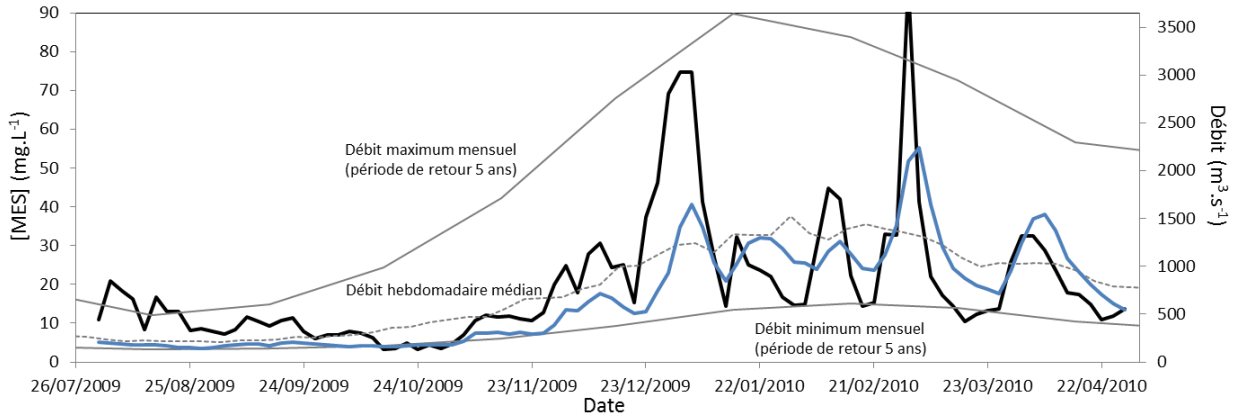

Figure 2 Exemple d'une année hydrologique illustrée par le débit (en bleu) et la concentration en matière en suspension ([MES] ; en noir) à Montjean-sur-Loire (entre Nantes et Angers; Gorse 2010 et DREAL Pays-de-Loire, 2015)

2000) et tropicales (rivière Mengong, Cameroun ;8 < [COD] < 25 mg L^{-1} ; Viers et al., 2000; Gaillardet et al., 2003).

1.1.2 Les apports solides

Les apports solides sont caractérisés par les matières en suspension (MES), traditionnellement définies par le résidu après filtration à travers une maille de 0,2 à 0,7 µm. Le flux d'entrée des particules dans l'estuaire est généralement estimé à partir de la concentration en MES que multiplie le débit, les mesures pouvant être instantanées ou moyennées sur une certaine période. Ainsi, selon les années, le flux de MES entrant dans l'estuaire de la Loire varie entre 0,5 et 2,3.10^6 t.an^{-1} (Figueres et al., 1985; Manickam et al., 1985; Migniot, 1993; Négrel, 1997; Gorse et al., 2010; SOGREAH, 2010). Cette approche néglige la complexité du transport sédimentaire mais permet de mettre en évidence la forte relation entre l'apport en particules estimé par la concentration en MES et le débit Q (Figure 2). Cette relation n'est cependant pas linéaire et est soumise à une importante hystérésis (Wood, 1977) : lors de la décrue, la concentration en MES diminue avec le débit mais en proportion moindre que lors de la crue car les particules facilement mises en mouvements ont déjà été expulsées.

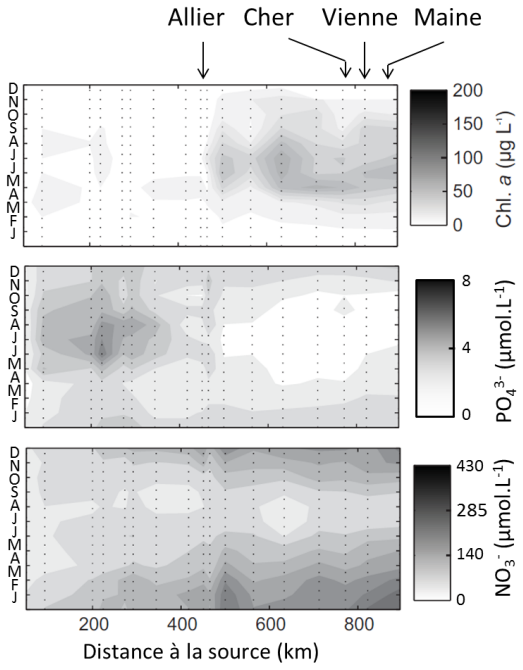

Figure 3 Evolution spatiale et annuelle des médianes mensuelles (calculées sur la période 2002-2012) de concentration de Chlorophylle a, phosphate et nitrate (Minaudo et al., 2015)

La composition chimique des particules arrivant à l'estuaire est très mal renseignée. Cependant, Grosbois et al. (2001) présentent les données d'un suivi quasi-hebdomadaire de prélèvements de MES réalisé pendant 2 ans à Bréhémont (entre Tours et Saumur ; Figure 4). Bien que n'englobant que la moitié amont du bassin versant de la Loire, une telle approche permet de faire ressortir les tendances majeures : une matrice siliceuse de concentration constante au cours de l'année (SiO_2=68±6 % de la masse du sédiment sec) à laquelle se rajoute : soit de la calcite lors des étiages (Manickam et al., 1985; Négrel and Grosbois, 1999; Négrel et al.,

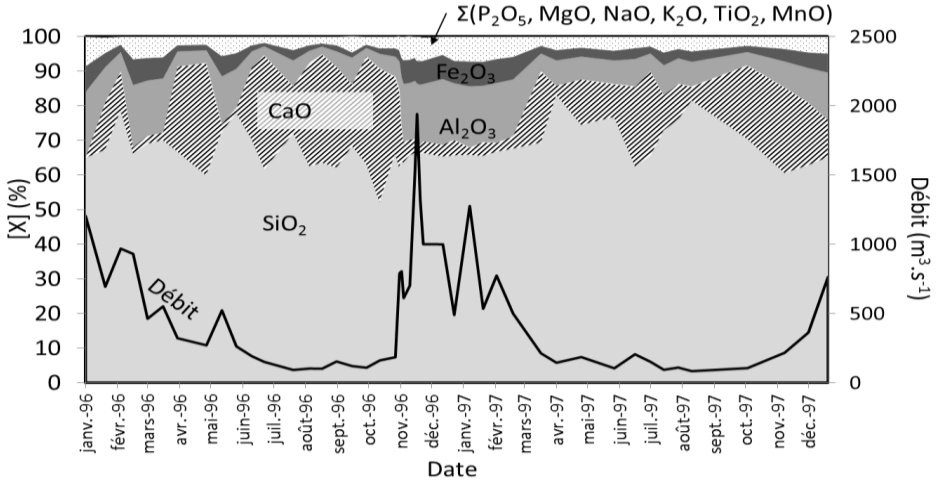

Figure 4 Suivi annuel de la composition des particules en suspension et du débit pour les années 1996-1997 (Grosbois et al., 2001)

2000), soit de l'aluminium et du fer (et Mg, K ou Ti ; r^2>0.88 avec Al_2O_3) lors des périodes de crue (Figure 4).

L'ensemble des échantillons est souvent sursaturé vis-à-vis de la calcite et ne permettent pas sa dissolution (Manickam et al., 1985; Négrel et al., 2000). Les variations de concentration de calcite sont donc liées à une inhibition de la précipitation authigène pendant l'hiver, probablement due à la modification de la calcite déjà cristallisée. En effet, il est plus facile d'obtenir la cristallisation d'un ion par nucléation hétérogène (à la surface d'un cristal préalablement existant) que par nucléation homogène (à partir d'aucune forme cristalline ; Stumm, 1992). Deux scénarii ont été proposés : (1) l'augmentation estivale du pH liée aux conditions eutrophes, libère les sites de nucléation d'un carcan de composés organiques (Manickam et al., 1985; Meybeck et al., 1988), ce qui accélère fortement la vitesse de précipitation de la calcite ou (2) l'augmentation du nombre de diatomées en été représente autant de nouvelles particules qui, bien que siliceuses, offrent une surface de nucléation pour la précipitation de la calcite (Grosbois et al., 2001).

L'augmentation de la proportion de Al et Fe en période de crue est en accord avec des observations spatiales plus globales (Canfield, 1997; Viers et al., 2009) et s'explique par une modification des minéraux secondaire formés. L'augmentation du ruissellement modifie à la fois la minéralogie des argiles produites lors de l'érosion, notamment avec un apport plus important du Massif Central lors des crues (Manickam et al., 1985; Négrel and Grosbois, 1999), et augmente la quantité d'hydroxydes de fer et de manganèse précipités sur les lieux de l'érosion et qui restent stables durant leur transport (Canfield, 1997; Négrel et al., 2000).

Une partie des apports solides (non représentés dans la Figure 4), est composée de particules organiques. Certaines de ces particules sont aussi issues de l'érosion des sols et sont présentes à une concentration relativement constante (~5% des particules totales ; Meybeck et al., 1988; Gorse et al., 2010). Une seconde partie, produite par les algues, est en proportion variable selon les saisons : de près de zéro en hiver elle pouvait représenter plus de 50% en masse des particules en suspension en été (Meybeck et al., 1988 ; la masse de matière organique étant estimée à 2,5 fois la masse du carbone organique). Le degré d'eutrophisation de la Loire (Crouzet, 1983) ayant fortement diminué ces 15 dernières années (Minaudo et al., 2015), probablement grâce à la diminution des rejets de phosphore, les données plus récentes font état d'un maximum de 20% de matière algale en été (Gorse et al., 2010; Minaudo et al., 2015).

1.2 Fonctionnement hydraulique de l'estuaire

1.2.1 Hydrodynamique

Le mélange des eaux douces et salées se fait progressivement à partir du front de salinité, défini par un doublement de la concentration en chlorure (Meybeck et al., 1988). La Figure 5 illustre l'emprise de l'estuaire selon une limite aval définie à la salinité de 30 (86% d'eau de mer et 14% d'eau de rivière). La position de ces fronts de salinité dépend du débit qui la déplace en aval lors des crues, et de la marée qui la fait osciller suivant la dynamique tidale. La marée montante (le flot) entraine l'eau vers l'amont et inverse ainsi le sens du courant. La remontée saline dans la Loire atteint rarement l'amont de Nantes (réseau SYVEL, Groupement d'intérêt Public Loire Estuaire, GIP LE), limite à partir de laquelle nous définirons le début de l'estuaire. A l'étale, le courant s'annule puis reprend une direction descendante déplaçant la zone de mélange vers l'aval. La Figure 6 illustre cette situation : les oscillations de salinité correspondent au rythme des marées. Ces aller-retour augmentent aussi le temps de résidence des eaux dans l'estuaire de la Loire à 2 semaines environ (Ciffroy et al., 2003b). La Figure 6 illustre cette situation : les oscillations de salinité correspondent au rythme des marées. La Figure 6 montre aussi que lorsque le débit augmente (il dépasse 3000 $m^{-3}.s^{-1}$ entre le 15 et le 20 février), la salinité diminue ; ainsi, à fort débit, l'eau au droit de Donges est quasi-constamment douce. De plus, lorsque le coefficient de marée augmente, l'amplitude des oscillations de la salinité augmente en surface (du 12 au 17 mars 2014 ; Figure 6) grâce à un mélange des eaux plus efficace. Une donnée peu intuitive est l'augmentation de la salinité en profondeur entre le 6 et le 10 mars pour des coefficients de marée particulièrement faibles. Ces mesures montrent une stratification des eaux fortement marquée (eaux douces en surface et eaux salées, plus denses, près du fond) lors d'une importante influence fluviale (fort débit et/ou faible coefficient de marée). En effet, le mélange des eaux douces et salées est réalisé par les turbulences

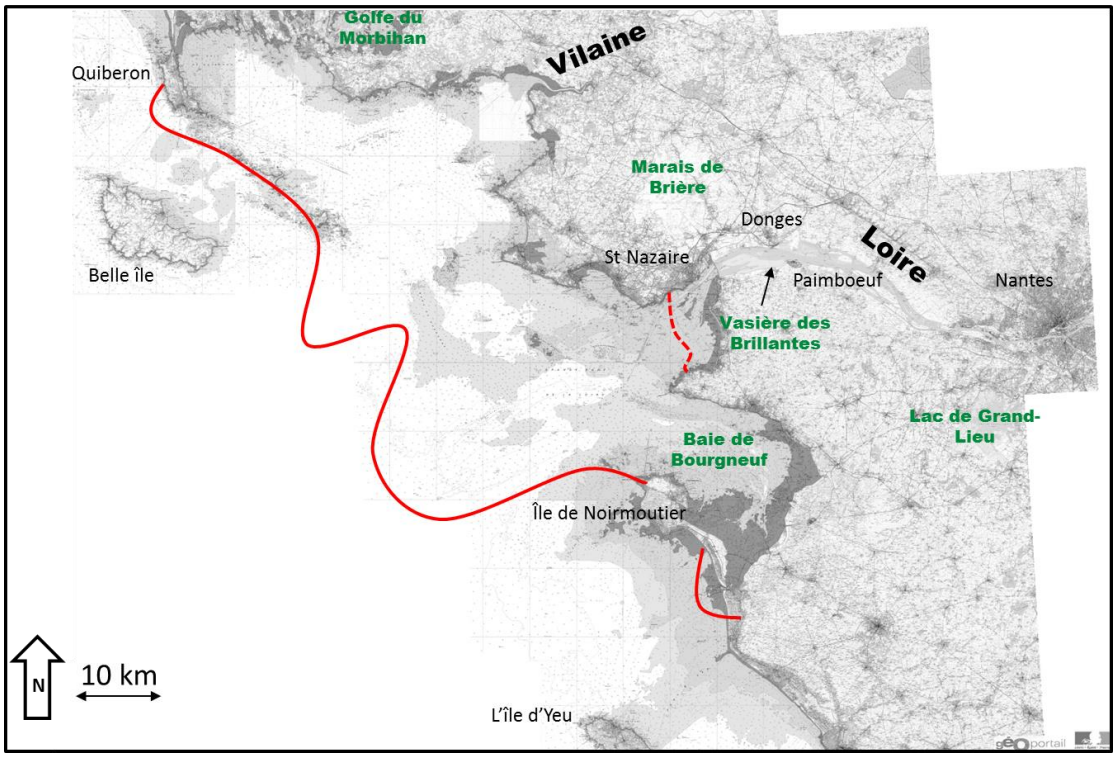

Figure 5 Carte de l'estuaire de la Loire (géoportail, SHOM, IGN). En rouge, isocontours de salinité journalière de surface à S=30 le 20 février 2014 (trait plein) et le 7 août 2015 (pointillés) estimés par le modèle mars3D (d'après previmer.org). Le débit de la Loire à ces date est respectivement de 3000 m^3s^{-1} et de 130 m^3s^{-1} (DREAL Pays de la Loire).

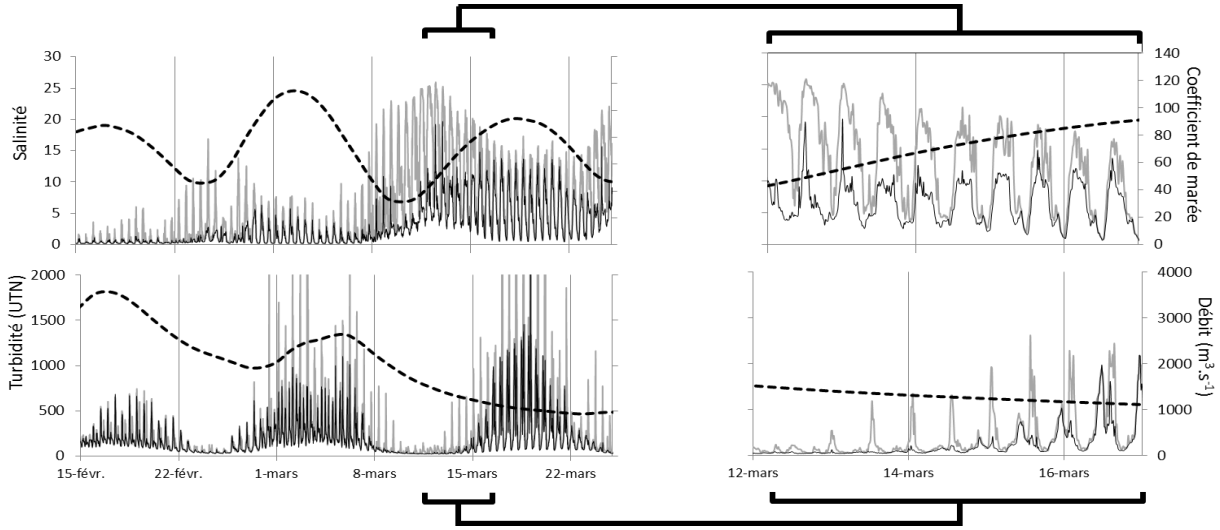

Figure 6 Dynamique temporelle et verticale de l'influence des crues et des marées illustrées à partir : en haut, du coefficient de marée (pointillés) et des estimations de salinité (calculé à partir de la conductivité, en noir pour la « surface » et en gris en « profondeur ») et en bas, du débit (pointillés) et de la turbidité (en noir pour la « surface » et en gris en « profondeur »). Les deux capteurs sont situé à Donges et distants verticalement de 4 m (réseau SYVEL - GIP LE; DREAL Pays de la Loire).

qui sont des structures hydrauliques complexes (typiquement les tourbillons) générées à l'interface de masses d'eau dont la différence des vitesses est importante. Les tourbillonnements ainsi produits sont responsables du mélange à l'échelle de la colonne d'eau. Ainsi, en cas de courants de marée importants, des tourbillons sont produits à l'interface du sédiment du fond de l'estuaire. De même, un fort vent va créer des turbulences à la surface ce qui permet la plupart du temps, un mélange homogène sur toute la profondeur de la colonne d'eau de l'estuaire (Wolanski, 2007). Cependant, si les courants de marée ne sont pas assez importants, les eaux douces ne sont pas suffisamment mélangées par la turbulence ce qui augmente la vitesse moyenne des eaux de surface vers l'aval et produit une stratification des eaux : l'eau douce reste en surface et la gravité maintient l'eau salée (plus dense) en profondeur (Figure 7; Pritchard, 1955; Simmons, 1955; Allen, 1972; Avoine et al., 1981). De part cette stratification, les courants de marée vont surtout influencer la vitesse moyenne en profondeur qui s'inversent alors vers l'amont. Ce processus est caractérisé par la formation d'un « coin salé » au fond de l'estuaire.

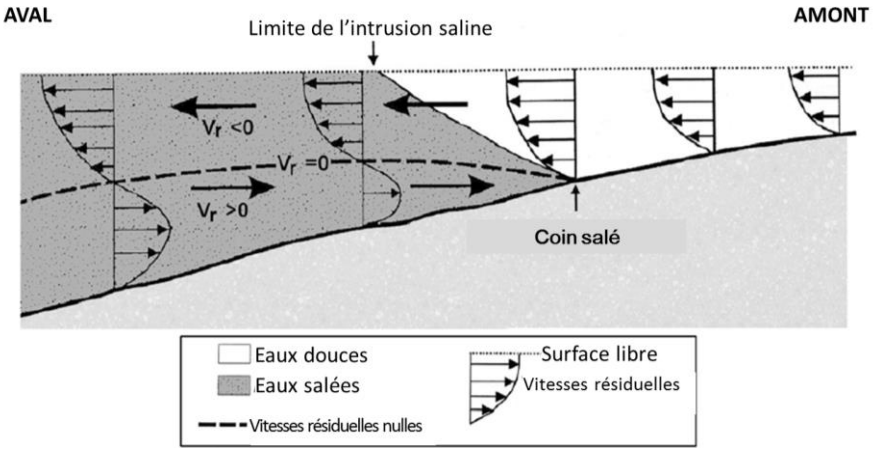

Figure 7 Champs des vitesses moyennées sur un cycle de marée (dites résiduelles) caractéristiques d'un estuaire. D'après Allen et al., 1972 cité par Deloffre 2006

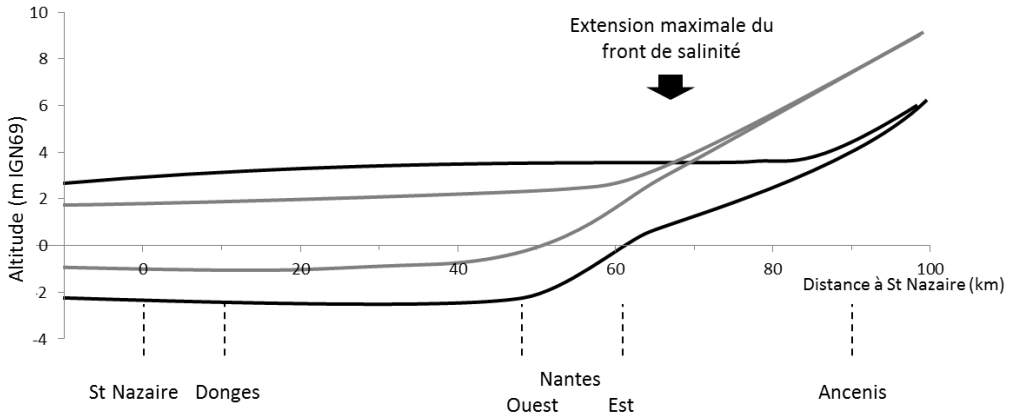

Figure 8 Enveloppe des marées (maximum et minimum de hauteur d'eau) pour: (1) en gris, faible coefficient de marée (47) fort débit (1500 $m^3.s^{-1}$) ; (2) en noir, fort coefficient (90) faible débit (240 $m^3.s^{-1}$). Sources: GPMNSN, DREAL Pays de la Loire, DDT49, DTM44, d'après le GIP Loire Estuaire (Cahier indicateur L1.A1)

La dynamique tidale est aussi visible sur les variations de hauteur d'eau. La Figure 8 représente les maxima et minima de la hauteur d'eau au cours de deux marées contrastées. Ainsi, le marnage augmente et se propage plus loin en amont pour les grands coefficients de marée. Il est important de noter que l'horizontalité du niveau de basse mer entre Nantes et St Nazaire est générée par les aménagements réalisés pour faciliter la navigation. Avant le XX^{ème} siècle, le marnage à Nantes était plus faible d'envrion 3 m lors des coefficients de marée importants (GIP LE, 2002).

1.2.2 Mélange des espèces dissoutes

Au sein de l'estuaire et à l'échelle de la colonne d'eau (quelques mètres de hauteur), le mélange entre les eaux douces et salées est produit par les turbulences qui vont augmenter leur surface de contact. A une échelle plus fine (de l'ordre du millimètre), à travers cette surface de contact, c'est la diffusion qui entraine les ions dissous des zones salées vers les zones moins salées. La salinité est uniquement fonction de la proportion du mélange entre eaux douces et eaux salées (on parle d'élément *conservatif le long du mélange*). Ainsi, la mesure de la salinité permet de s'affranchir de la connaissance de la structure exacte des turbulences pour estimer l'avancement du mélange entre les deux eaux (on dit que la salinité est un traceur du mélange) selon :

$$\chi_r + \chi_o = 1 \qquad (1)$$

$$S = S_r\,\chi_r + S_o\,\chi_o \qquad (2)$$

Avec χ_r et χ_O les portions respectivement d'eau de la rivière et d'eau de l'océan dans l'échantillon de salinité *S*. S_r et S_o sont les valeurs de salinité respectivement dans la rivière et dans l'océan. Si un élément diffuse de la même manière que le sel (conservatif), il se mélangera dans les mêmes proportions :

$$C = C_r\,\chi_r + C_o\,\chi_o \qquad (3)$$

Par combinaison de (2) et (3), il vient :

$$\chi_o = \frac{S - S_r}{S_O - S_r} = \frac{C - C_r}{C_O - C_r} \qquad (4)$$

$$C = S\frac{C_O - C_r}{S_O - S_r} + C_r - S_r\frac{C_O - C_r}{S_O - S_r} \qquad (5)$$

Avec *C*, la concentration de l'élément conservatif, C_r et C_o les concentrations respectivement dans la rivière et dans l'océan. Tous les termes de droite dans l'équation (5) sauf le premier (*S*) sont des constantes, l'équation correspond donc à une droite sur une représentation de *C* en fonction de *S* (Figure 9a). Pour un élément qui ne se comporte pas comme la salinité, on observe une déviation au-dessus ou en-dessous de la droite de mélange selon qu'il s'agisse d'un enrichissement ou d'un appauvrissement (Figure 9a).

Afin de quantifier cet enrichissement (ou appauvrissement) en fonction de la salinité, un modèle mathématique a été proposé par Boyle et al. (1974). En

eau douce, le flux de matière d'un élément de concentration *C* est généré uniquement par déplacement de la matrice (ici l'eau). On parle de flux advectif :

$$A_c = Q_w C \qquad (6)$$

Avec Q_w le débit de la rivière à un instant donné.

Dans l'estuaire, il faut aussi prendre en compte le mélange lié à la diffusion D_c que l'on estime à partir de la salinité. Ce modèle suppose un gradient de salinité immobile dans l'estuaire, il n'est donc valable que pour estimer des flux instantanés indépendamment du flux produit par le déplacement du gradient de salinité. On admet :

$$D_c(S) = -\frac{dC}{dS} Q_w (S - S_r) \qquad (7)$$

Ce qui permet de calculer le flux total de chaque élément (Q_c) en chaque point de salinité :

$$Q_c = D_c + A_c \qquad (8)$$

$$Q_c(S) = Q_w[C - (S - S_r)\frac{dC}{dS}] \qquad (9)$$

Cette formule s'exprime géométriquement : lorsqu'on représente la variation de la concentration d'un élément en fonction de la salinité (Figure 9b), la partie de l'équation (9) entre crochet correspond à la projection de la tangente de *C(S)* en *S* sur l'axe vertical de salinité S_r (pointillés de la Figure 9b). On retrouve bien qu'un élément conservatif est décrit par une droite, mais en plus, cette approche permet d'estimer la position des apports ou des réactions générant les déviations par rapport à la salinité. Cependant cette approche n'est valable que sous l'hypothèse d'un équilibre instantané entre *C* et *S* c'est-à-dire qu'il n'y a qu'une seule valeur possible de concentration à une salinité donnée. On verra plus loin que d'autres facteurs variant indépendamment de la salinité (pH, O_2, [MES], alcalinité, pour les principaux) peuvent modifier la concentration des éléments dissous et s'opposer ainsi à l'hypothèse d'équilibre instantanée entre *C* et *S*.

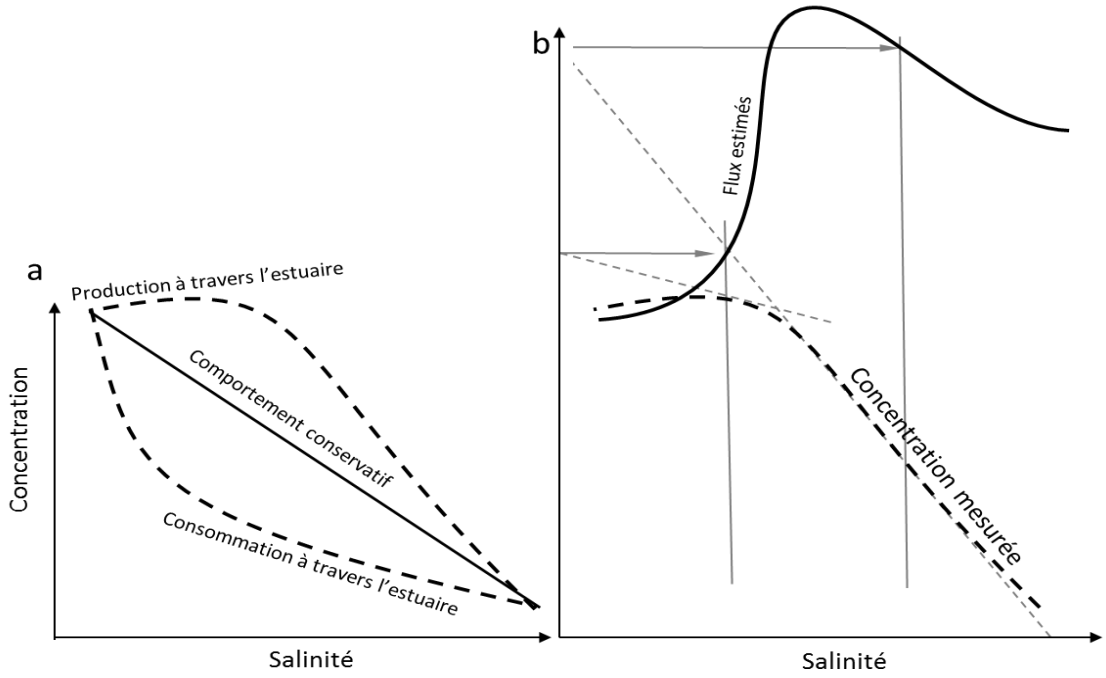

Figure 9 (a) Représentation simplifiée de profils de concentrations le long du gradient de salinité de l'estuaire permettant d'identifier la réactivité d'un élément dissous (b) Exemple d'estimation des flux par la méthode géométrique (voir texte) à partir d'un des profils précédent. Les échelles verticales sont arbitraires.

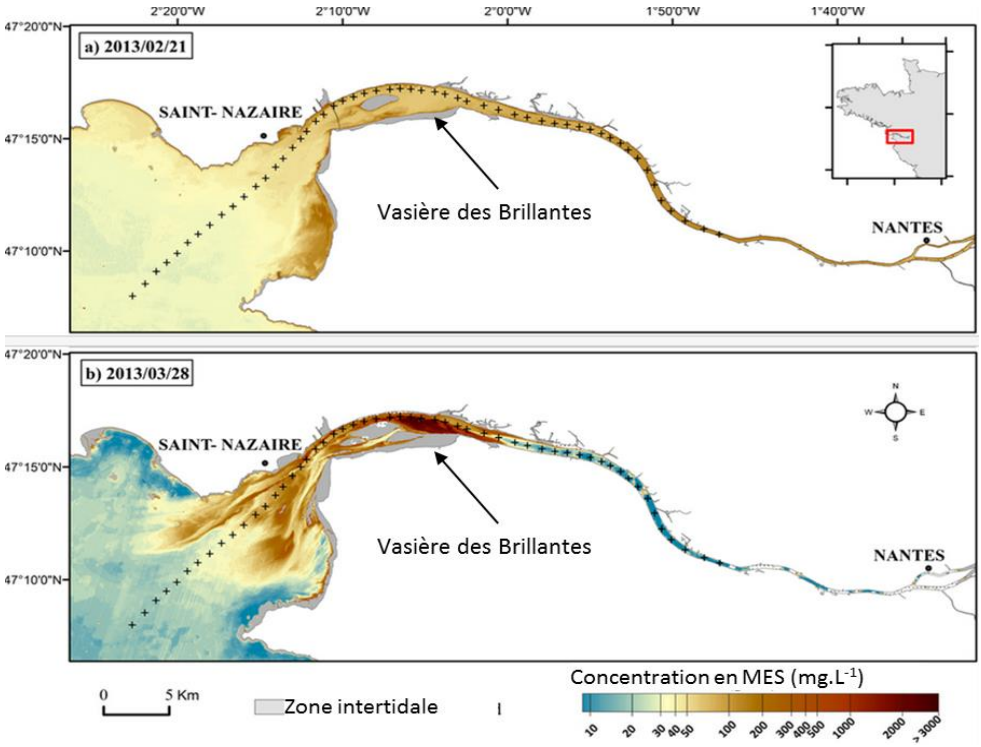

Figure 10 Distribution de la MES estimée à partir d'images satellites (SPOT 4; Gernez et al., 2015) les 21 février 2013 (faible coefficient de marée, fort vent, débit maximum des 15 derniers jours: 3560 $m^3.s^{-1}$) et 28 mars 2013 (fort coefficient de marée, vent faible, débit maximum des 15 derniers jours: 1800 $m^3.s^{-1}$). Les croix indiquent la position du chenal de navigation.

1.3 Fonctionnement hydro-sédimentaire

1.3.1 Conditions de dépôt/remise en suspension

L'oscillation des masses d'eau (Figure 6) et la stratification saline (Figure 7) piègent les particules apportées dans l'estuaire et ne les libèrent vers l'océan que pendant les périodes de fortes crues (Ciffroy et al., 2003b). Ce « filtre estuarien » (Schubel and Kennedy, 1984; Chernetsky, 2012) bloque préférentiellement les particules fines (silt et argiles ; Dalrymple et al., 1992). En effet, une augmentation faible de la salinité modifie la charge électrique de la surface des particules fines qui s'agglomèrent par floculation sous forme de floc ce qui augmente leur taille et donc leur vitesse de chute (Migniot, 1968; Van Leussen, 1988). L'importance de ce processus dépend donc de la position du front salin, de l'évolution de la salinité en aval et de la composition chimique des particules. Par exemple, la quantité de matière organique liée aux particules fines influence fortement leur comportement (Eisma, 1986). De plus, durant l'étale, le courant s'annule ce qui permet une sédimentation des particules plus fines. Lors du dépôt, près du fond, les particules atteignent parfois des concentrations telles que leur vitesse de chute devient nulle. Cette suspension s'appelle la crème de vase et concerne près de 90% de la MES à chaque étale de marée en étiage (Maurice, 1994). Une fois déposée, cette crème de vase se tasse sous son propre poids en quelques heures et s'immobilise : l'eau est expulsée et la porosité diminue, on dit alors que la vase est faiblement consolidée. Le processus de consolidation se poursuit ensuite pendant plusieurs semaines. Ainsi, plus le temps passe après un évènement de dépôt, plus l'énergie nécessaire à la remise en suspension de la vase est importante.

Cependant, une partie des particules piégées est régulièrement remise en suspension, notamment lors des courants de flot et de jusant, ce qui est particulièrement visible lors des marées importantes (qui produisent de forts courants). Ainsi, la turbidité augmente avec le coefficient des marées et la profondeur (Figure 6). A l'échelle d'une marée, les maxima de turbidité sont mesurées lors des plus fort

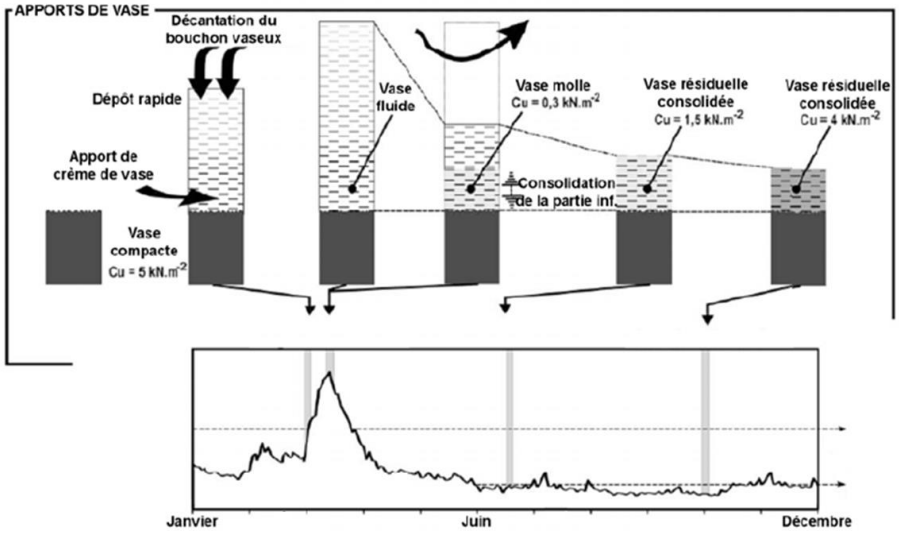

Figure 11 Schéma conceptuel du cycle annuel d'engraissement d'une vasière, réalisé à partir du suivi d'une vasière subtidale de l'estuaire de la Seine (Lesueur et Lesourd, 1999)

courants, au flot et au jusant, lorsque la hauteur d'eau est minimale (à faible salinité ; Figure 6). Lorsqu'elles sont en suspension, ces particules forment ce que l'on appelle le bouchon vaseux. Pour l'estuaire de la Loire, l'asymétrie de l'onde de marée favorise les courants de flot (vers l'amont) par rapport aux courants de jusant et s'oppose ainsi à l'expulsion rapide du bouchon vaseux par la courant du fleuve (Festa and Hansen, 1978). Cependant, en cas de crue, l'asymétrie de l'onde de marée n'est pas assez efficace et les particules sont expulsées.

1.3.2 La sédimentation des vasières intertidales

Les rives de l'estuaire sont souvent à l'abri des principaux courants et recouvertes uniquement lorsque la marée est haute, ce qui coïncide avec le minimum de courant. Elles peuvent ainsi former des zones de dépôt privilégié des particules fines appelées les vasières intertidales. Selon leur altitude, la fréquence de recouvrement varie et définit ainsi des écosystèmes différents. La partie haute (au-dessus de la hauteur moyenne des marées hautes) est souvent végétalisée et nommée *schorre*. Plus bas, parfois séparée par une falaise d'un ou deux mètres, la vase est presque toujours nue et se nomme la *slikke*. Le site d'étude de ce travail de doctorat est situé sur la slikke de la vasière des Brillantes (Figure 5).

L'intensité et la dynamique de dépôt de la vase dépend en premier lieu de la masse de particules en suspension au-dessus de la vasière à marée haute (Deloffre, 2005). La Figure 6 illustre la nécessité d'un fort coefficient de marée pour mettre en suspension un stock particulaire suffisant pour créer un bouchon vaseux important. Bien qu'aucune étude détaillée ne soit disponible dans le cas de la vasière des Brillantes, les mesures en continu de turbidité indiqueraient un bouchon vaseux plus important au droit de la vasière lors des crues peu importantes (1000-2000 $m^3.s^{-1}$; Bertier, 2009 ; Gernez et al., 2015 ; Figure 10).

Deux autres conditions favorisent la sédimentation des particules : la floculation et l'absence de turbulence. Ainsi, la proximité du front de salinité favorise la floculation, ce qui correspond, dans le cas de la vasière des Brillantes, à un débit de l'ordre de 2000 $m^3.s^{-1}$ (Figure 6). Enfin, il faut une turbulence suffisamment faible au-dessus de la vasière pour ne pas gêner le dépôt : il est nécessaire d'avoir peu de vent (Deloffre, 2005). Ces conditions restent à confirmer par des études plus détaillées sur cette vasière car au sein même d'une seule vasière les dépôts peuvent être extrêmement contrastés comme illustrés par Goubert et al. (2008, 2010) pour une vasière de l'estuaire de la Vilaine (à 30 km au Nord de l'estuaire de la Loire). Cependant, les recherches sur l'estuaire de la Seine ont pu montrer une cyclicité annuelle liée au dépôt de crue (Lesueur and Lesourd, 1999; Deloffre et al., 2006 ;

Figure 11), suivi d'une forte période d'érosion avant que la vase ne se consolide et résiste à la remise en suspension.

Trois paramètres autres que la hauteur de sédiment déposé sont importants à prendre en compte lors de la description des dépôts : (1) la hauteur de sédiment remise en suspension puis redéposée au cours de chaque marée (entre 1 et 5 mm ; Deloffre, 2005) ; (2) la morphologie de la surface qui peut fortement varier, typiquement après un coup de vent (Goubert et al., 2010) et (3) la présence de faunes susceptibles de mélanger, agglomérer, protéger ou remettre en suspension le sédiment des vasières.

1.4 La biologie des vasières intertidales

La complexité des transformations subies par les particules dans la couche critique vient en grande partie de l'impact des organismes vivants. Ils peuvent réaliser directement les transformations chimiques (photosynthèse, respiration, biominéralisation) ou contraindre les conditions de réalisation de ces transformations en modifiant leur environnement immédiat (production d'exsudats, *biomixing*, *bioirrigation*). Dans le cas des vasière intertidales, l'oscillation des marées et de la salinité définissent un écosystème propice au développement du microphytobenthos. Cette flore benthique profite des longues durées d'émersion et d'ensoleillement, particulièrement en haut de vasière (Benyoucef, 2014 ; Figure 12) pour assurer une production de matière organique importante. Très facilement consommé, ce microphytobenthos permet à une importante faune benthique de se développer. On distinguera la méiofaune, composée d'organismes hétérotrophes de taille inférieure à 2 mm (ex : ostracodes, copépodes, nématodes, foraminifères), de la macrofaune, composée des organismes hétérotrophes de taille plus importante. Parmi la macrofaune, 49 espèces de vers, crustacés et mollusques ont été inventoriées dans les sédiments de l'estuaire de la Loire (GIP LE, 2011). Par ses mouvements et ses modes de nutrition la faune benthique est responsable de nombreux mélanges appelés bioturbation, concernant à la fois les particules et l'eau qui les entourent.

1.4.1 La bioturbation

Certains organismes benthiques réalisent des activités qui contraignent des processus importants à l'échelle de leur environnement et participent à sa transformation. L'impact de certains de ces organismes benthiques s'étend bien au-delà de leur position et de leurs activités à un moment donné. On les appelle « ingénieurs de l'écosystème » (Jones et al., 1996). Dans les vasières, de nombreux organismes peuvent prétendre à un tel titre. Par exemple, les diatomées forment un biofilm à la surface des vasières limitant la remise en suspension des particules (Decho, 2000). Cependant, l'archétype des activités d'ingénierie des écosystèmes est la réalisation de terriers par la macrofaune benthique. Le creusement de ces terriers fait partie de la bioturbation, plus généralement définie comme l'ensemble des transports de matière perpétué par les animaux et modifiant de manière directe ou indirecte la matrice sédimentaire (« *all transport processes carried out by animals that directly or indirectly affect sediment matrices* » ; (Kristensen et al., 2012)). Ce « labour » animal est particulièrement important dans l'équilibre actuel des écosystèmes continentaux (Darwin, 1881; Turbé et al., 2010) et dans l'histoire de l'évolution (Bottjer et al., 2000; Meysman et al., 2006; Boyle et al., 2014).

L'impact des terriers est souvent décrit par trois processus : (1) la formation du terrier déplace les particules le long des parois. Lorsque les espèces changent régulièrement de terrier (par exemple *Hediste diversicolor* présent sur notre site d'étude), ce processus devient très important et génère un fort mélange entre les particules de surface et celles situées plus en profondeur. (2) L'existence du terrier dont les parois sont parfois consolidées par des exsudats organiques, modifie la porosité du sédiment, sa perméabilité et génère ainsi une forte hétérogénéité modifiant le comportement hydraulique et hydrosédimentaire du substrat (Murray et al., 2002). Il a été montré que l'existence de terriers pouvait déstabiliser le sédiment et favoriser sa remise en suspension (Widdows and Brinsley, 2002). Enfin, (3) l'activité des habitants : certains (organismes détritivores, par exemple le bivalve *Scrobicularia plana*) déplacent le sédiment afin d'y trouver la matière

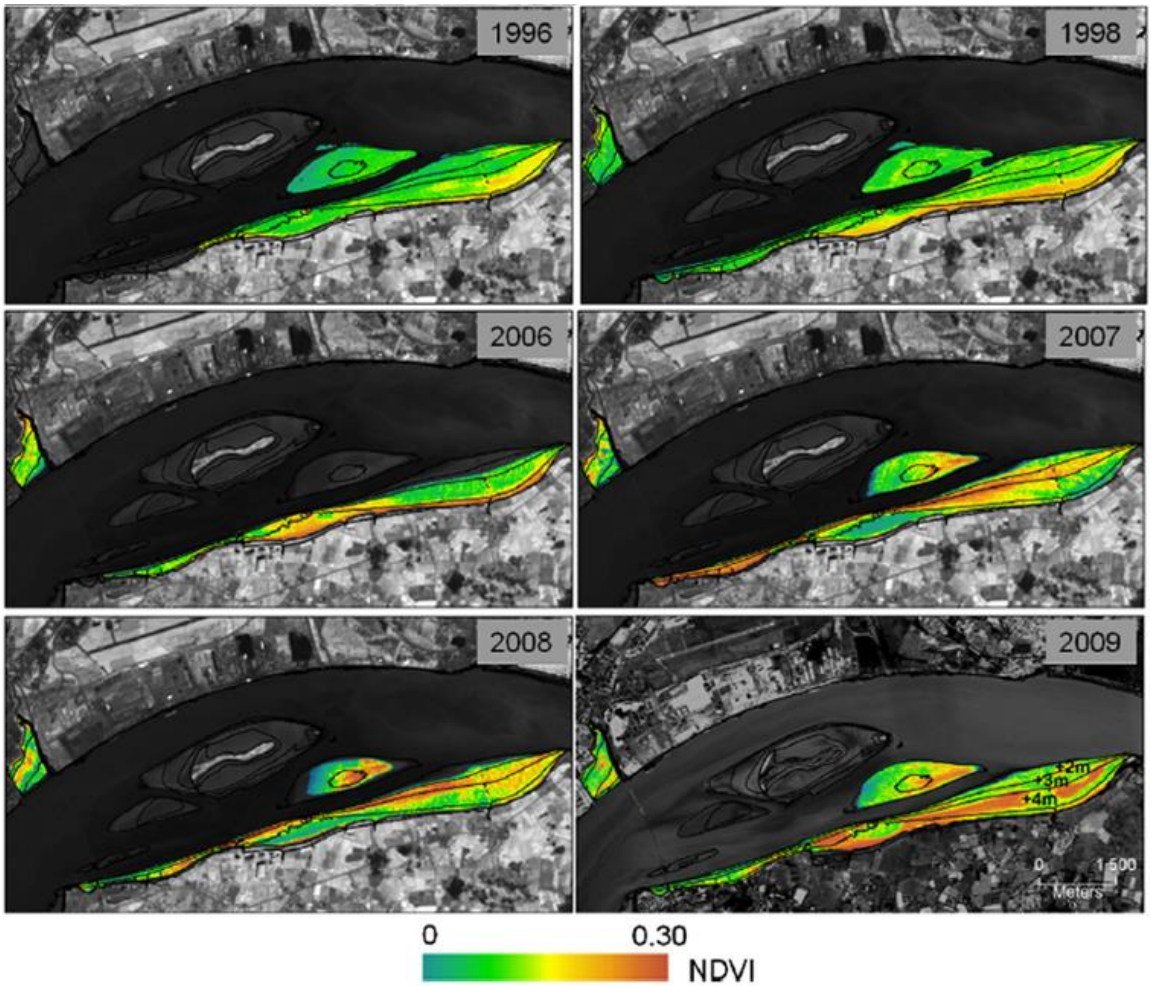

Figure 12 Exemple de répartition estivale du microphytobenthos estival sur la vasière des Brillantes, au cours d'une vingtaine d'année. L'indicateur utilisé est le NDVI (Normalized Difference Vegetation Index) calculé à partir d'une image multispectrale du satellite SPOT (Benyoucef, 2014). Les mesures *in situ* réalisées entre 2013 et 2015, font état d'une concentration en Chl a de l'ordre de 40 à 200 $mg.m^{-2}$ sur les deux premiers millimètres de sédiment (Méléder, pers. com.)

organique qu'ils consomment, d'autres (organismes filtreurs, typiquement *H. diversicolor*) aspirent dans leur terrier l'eau de surface puis la filtrent afin de se nourrir.

La part de la bioturbation réalisant un mouvement des particules est englobée par le terme *biomixing* alors que la part décrivant un mouvement des masses d'eau se nomme *bioirrigation*. L'étude du *biomixing* permet donc de mieux comprendre les processus responsables de l'enfouissement des particules déposées à la surface des vasières, notamment celles riches en fer.

1.4.2 **Le biomixing**

La manière dont sont déplacées les particules varie énormément entre différentes espèces benthiques. Afin d'améliorer la description du transport des particules pour le modéliser et quantifier son impact, une classification a été élaborée (François et al., 1997; Kristensen et al., 2012). Trois principaux critères sont retenus : la distance parcourue par chaque particule lors d'un déplacement, la direction et la localisation du déplacement et enfin le délai d'attente entre deux déplacements (Wheatcroft et al., 1990; Meysman et al., 2008a, 2008b, 2010a). Si aucune direction n'est privilégiée (direction aléatoire) alors les mouvements désordonnés des particules peuvent être décrits de la

même manière que les mouvements des ions en solution (selon un mouvement brownien). En conséquence, si (1) l'échantillonnage décrit le mouvement avec une résolution spatiale correspondant à plusieurs fois la distance réalisée lors d'un déplacement et si (2) l'observation dure suffisamment longtemps pour englober un certain nombre de déplacement, alors le biomixing peut être décrit comme un processus diffusif (Meysman et al., 2010a). Si les protocoles usuels réalisent des observations *suffisamment englobantes* dans l'espace par rapport aux mouvements réalisés sous la contrainte d'un organisme donné, on dit que cet organisme est un biodiffuseur. Ainsi, *H. diversicolor* qui déplace les particules le long de ses terriers sur de courtes distances (<mm) est décrit comme *gallery biodiffusor*.

Cependant, cette dénomination néglige la nécessité d'avoir des observations *suffisamment englobantes* temporellement. C'est-à-dire qu'il faut idéalement réaliser un suivi temporel du mélange ou, en cas d'échantillonnage ponctuel *in situ*, qu'il faut estimer depuis combien de temps les particules étudiées sont soumises au *biomixing*. Si le *biomixing* est permanent cela revient à estimer « le temps de vie » d'une particule dans le milieu étudié. Ainsi, si « le temps de vie » d'une particule est trop court, le *biomixing* ne peut pas être assimilé à de la diffusion car il va induire une forte hétérogénéité. D'après cette théorie, il est donc possible de prévoir l'impact du *biomixing* sur l'hétérogénéité d'un type de particule (Figure 13). Le microphytobenthos des vasières par exemple, se reproduit, grandit en surface du sédiment là où de la lumière est disponible. Une fois enfoui en profondeur, il est consommé par les bactéries en quelques jours, voire quelques semaines (Alldredge and Cohen, 1987). Par comparaison, la fréquence d'évènements de biomixing perpétués par *H. diversicolor* est estimée à quelques semaines (Meysman et al., 2003b). Ainsi si l'on prélève du sédiment anoxique, seuls les terriers les plus récents auront enfoui du microphytobenthos encore intact. Toutes les cellules de microphytobenthos seront concentrées autour de ces quelques terriers, elles auront donc une distribution très hétérogène complètement différente d'un gradient de diffusion. *A contrario*, un foraminifère peut survivre dans les couches profondes, privé d'oxygène, pendant plus d'un an (Langlet et al., 2013; Nardelli et al., 2014) mais se reproduit essentiellement en surface. Ainsi, les foraminifères vivant observés dans le sédiment prélevé auront été apportés au cours de nombreux évènements de biomixing et seront théoriquement répartis de manière plus homogène selon un profil diffusif diminuant de la surface vers la profondeur. Les foraminifères sont donc un témoin important des processus de *biomixing*.

1.4.3 Les foraminifères benthiques

Les foraminifères benthiques sont des organismes unicellulaires eucaryotes apparus au cours du cambrien inférieur (il y a ~500 millions d'années). Ils ont depuis colonisé la plupart des écosystèmes sédimentaires :

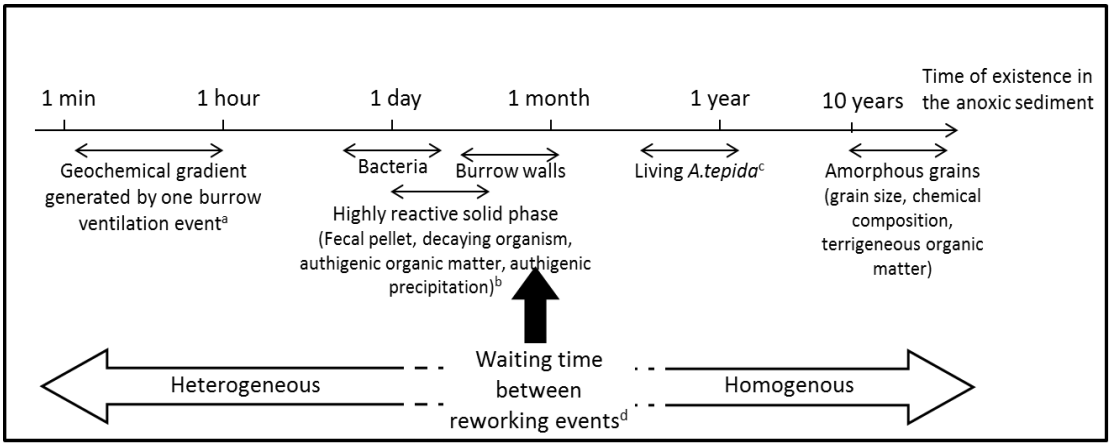

Figure 13 Diagramme de l'impact du biomixing sur l'hétérogénéité, modifié d'après Meysman et al., 2008. [a] d'après Fenchel, (1996); Wenzhofer and Glud (2004), [b] d'après Alldredge and Cohen (1987); Zhu et al. (2006) [c] d'après Heinz and Geslin (2012); Nardelli et al. (2014) [d] d'après Meysman et al. (2003).

océans ouverts, côtiers, les milieux abyssaux (Cushman, 1927; Snider et al., 1984; Enge et al., 2012), les sources hydrothermales (Molina-Cruz and Ayala-López, 1988; Panieri et al., 2005), les lagunes hypersalines (Debenay et al., 1989) et les milieux continentaux d'eau douce (Boltovskoy, 1958; Pawlowski et al., 1999). Ces adaptations à de nombreux environnements ont été réalisées en modifiant l'organisation interne de leur unique cellule dont la grande complexité est actuellement un champ de recherche particulièrement prolifique (*e.g.* Lee et al., 1979; Bernhard et al., 2000; Grzymski et al., 2002; Risgaard-Petersen et al., 2006). Leur cellule se distingue des autres eucaryotes unicellulaires par (1) la capacité de se déformer par des extensions rétractiles extrêmement allongées nommées « pseudopodes » et animées d'un mouvement interne parfois vers l'extérieur, parfois vers la cellule et qui forment un réseau dense tout autour de celle-ci (Figure 14). Ces pseudopodes leur permettent de se déplacer, se nourrir, se protéger, respirer et se reproduire. (2) L'existence d'une paroi extérieure appelée « test » qui peut être organique, agglutinée (composée de matériaux exogènes consolidés par un ciment), carbonatée (calcaire ou aragonite) ou siliceuse. Ce test a la propriété intéressante de pouvoir se conserver dans le sédiment et est un indicateur essentiel pour reconstituer les environnements passés. Et enfin, (3) une reproduction alternant entre un mode sexué et un mode asexué (Loeblich and Tappan, 1992; Sen Gupta, 1999). La taxonomie des foraminifères s'appuie historiquement sur la forme du test, généralement produit par une superposition de loges, chaque loge représentant une étape supplémentaire de la croissance du foraminifère.

Il a été choisi de chercher à expliquer les variations spatiales de densité de foraminifères en s'appuyant sur les notions de transport-réaction habituellement utilisées pour décrire les ions en solution. Ainsi l'organisation spatiale des foraminifères est expliquée en termes de production (=reproduction), diffusion (=*biomixing*), consommation (=mortalité) et advection (=mobilité). En supposant la mobilité nulle en profondeur, et en ayant connaissance de la vitesse de reproduction et de la mortalité des foraminifères, il est possible de calculer l'intensité du *biomixing* à partir de

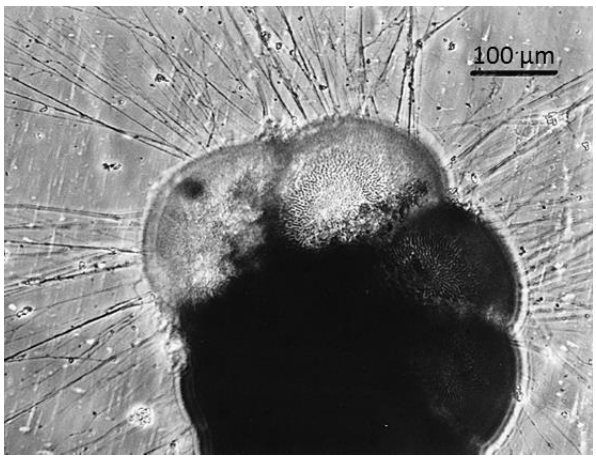

Figure 14 Un foraminifère benthique (*Ammonia tepida*) avec son réseau de pseudopodes (Debenay et al., 1998)

profils verticaux de densité de foraminifère. Inversement, si la mobilité n'est pas nulle, elle est probablement contrôlée par les conditions environnementales et notamment géochimiques du sédiment. De part leur taille, l'étude des gradients de densité des foraminifères est réalisable sur quelques centimètres, ce qui correspond aussi à la longueur caractéristique des gradients géochimiques. Cette adéquation permetterait aux foraminifères, s'ils étaient capables de se déplacer en profondeur, de renseigner l'importance des microhabitats et des signatures géochimiques associées sur l'organisation de l'écologie benthique de la vasière.

2 Géochimie du fer et des éléments associés à travers l'estuaire

2.1 Cycle du fer

2.1.1 Spéciation du fer à travers son transfert continent-océan

Le fer est l'un des éléments les plus abondants dans la croûte terrestre, et aussi le métal de transition le plus demandé par les processus biologiques (Raiswell and Canfield, 2012). Il est présent sous 3 principaux états redox : le Fe(0), Fe(II) et Fe (III), ce dernier étant le seul thermodynamiquement stable en milieu oxygéné (Figure 15a). Les cinétiques d'oxydation de ses formes réduites solides, sont suffisamment lentes pour que Fe(0) et Fe(II) puissent être observés. Par exemple, Fe (II) représente ~50% du fer particulaire provenant de l'érosion de massifs jeunes (arc volcanique de Kuril-Kamtchaka) et moins de 10% pour des massifs âgés fortement érodés (Précambrien, Lam et al., 2012) . Cependant, lorsqu'elles mettent en jeu les formes dissoutes, les cinétiques (à pH>6) sont beaucoup plus rapides. Le temps de demi-vie de Fe (II) varie ainsi de quelques jours à pH=6 à quelques heures à pH=7. La présence de surfaces métalliques ou la polymérisation (prépondérante à pH>7) accélèrent encore le processus (Henry et al., 1992; Stumm, 1992; Rose and David Waite, 2007) et conduit à des temps de demi-vie de Fe(II) de l'ordre de quelques minutes dans un environnement bien oxygéné (Millero et al., 1987; Wang and Van Cappellen, 1996; Martin, 2003).

Sous sa forme la plus oxydée, Fe(III) a très peu d'affinité avec les ligands inorganiques majeurs (H_2O, OH^-, HCO_3^-, CO_3^{2-}) : il est très peu soluble (Millero et al., 1995; Gaillardet et al., 2003). Lors des processus érosifs, Fe(III) se concentre donc dans les minéraux secondaires (argiles et (oxyhydr)oxides de fer essentiellement ; Canfield, 1997). A l'échelle mondiale, la quasi-totalité du transfert de fer des continents vers l'océan se réalise sous l'une de ces deux formes solides (Martin and Meybeck, 1979). Cependant, dans certaines rivières riches en carbone organique dissous (COD), la matière organique complexe le fer et représente la quasi-totalité du transfert (*e.g.* Escoube et al., 2009) avec des concentrations qui peuvent atteindre

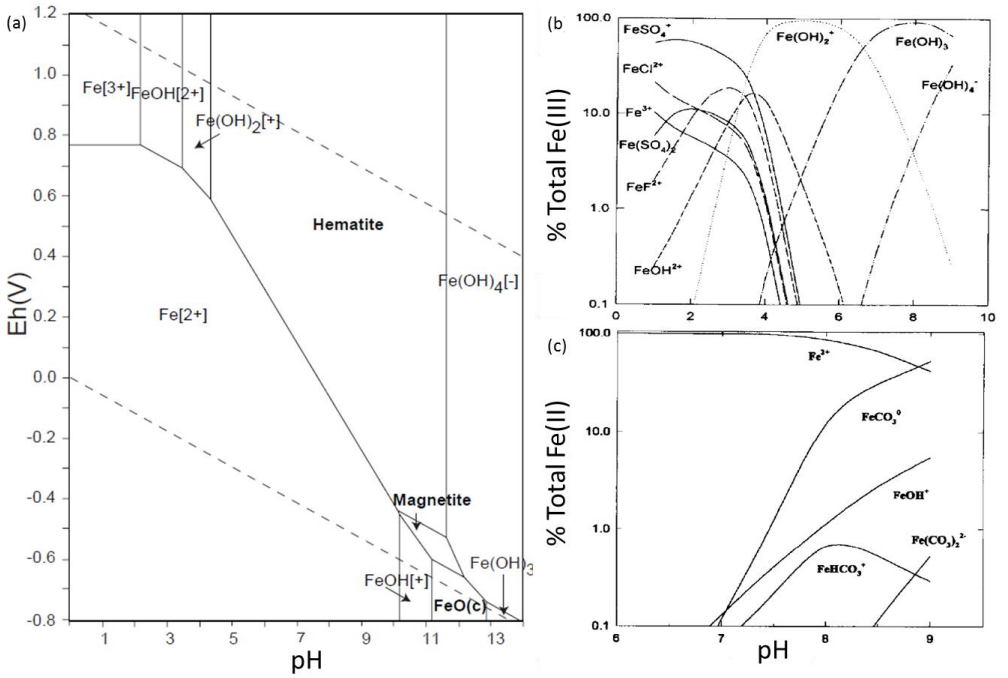

Figure 15 (a) Diagramme Eh-pH pour le système Fe-O-H à 25°C, 10^5 Pa et une concentration de fer dissous de 10^{-10} mol.kg^{-1} d'après la base de donnée LLNL (Lawrence Livermore National Lab.) cité par Takeno (2005). (b,c) Modèle de spéciation de Fe(III) et Fe(II) dissous à S=35, en ne prenant en compte que les complexes inorganiques (Millero et al., 1995).

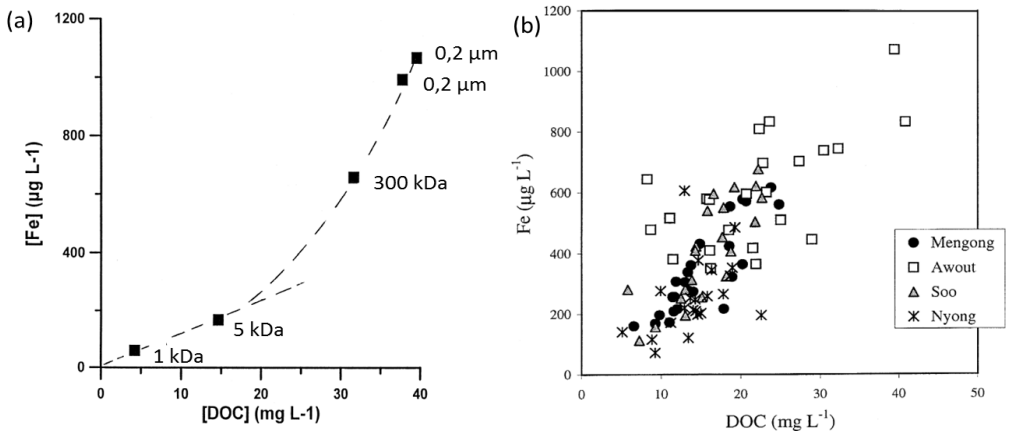

Figure 16 (a) Evolution de la teneur en fer et en carbone organique dissous (COD) lors de filtration successive d'un échantillon venant de la rivière Awout (Cameroun). Cette rivière draine un bassin versant de foret tropicale et présente un pH=4,74 et [DOC]~40mg.L^{-1}; Dupré et al., 1999). Les concentrations des filtrats à 0,2 µm proviennent de deux techniques de filtrations différentes. (b) Concentration de fer en fonction de la concentration en COD (Viers et al., 2000). 1200 µg L^{-1}~ 20 µmol L^{-1}.

~40 µmol L^{-1} en milieu polaire (Pokrovsky and Schott, 2002). La taille de ces complexes organiques est souvent trop faible (<0.22 µm) pour qu'ils soient retenus lors d'une filtration frontale ; certains sont supérieurs à 1nm : on dit qu'il s'agit de colloïdes (Rose and David Waite, 2007). Des techniques de filtrations plus fines (ultrafiltration) et plus délicates à mettre en œuvre (Hoffmann et al., 1981; Dupré et al., 1999) sont nécessaires pour isoler ces complexes (Figure 16a). Il est néanmoins possible de mettre en évidence la complexation du fer à l'aide de sa corrélation avec la concentration en COD (Figure 16b ; Viers et al., 2000; Pokrovsky and Schott, 2002). L'importance de la forme colloïdale dans la spéciation du fer, modifie très largement le comportement du dissous (<0,4µm). Par exemple, elle explique la sursaturation apparente par rapport aux expérimentations en laboratoire (Moore et al., 1979; Boyd and Ellwood, 2010) et la stabilisation pendant plusieurs jours de Fe(II) « dissous » (Kieber et al., 2005; Hopwood et al., 2015). Le comportement des colloïdes organo-ferriques dépend fortement de la composition, extrêmement variée, des composés organiques (Dittmar and Paeng, 2009). On se contentera ici d'identifier trois groupes majeurs (Boyd and Ellwood, 2010; Gledhill and Buck, 2012): les composés organiques provenant (1) de la dégradation des algues, (2) de la dégradation de la litière continentale et (3) exsudés par certains organismes dans l'objectif de complexer le fer (appelés sidérophores).

En milieu océanique, les concentrations de fer mesurées dans le compartiment dissous (<0,4µm) sont beaucoup plus faibles que dans les rivières (<2 nmol.L^{-1}). Le fer ne forme quasiment pas de complexes avec les anions du milieu marin (Figure 15b, c). Ainsi, 99% du fer dissous (<0,4µm) dans l'océan est complexé par des composés organiques colloïdaux ou/et dissous (Gledhill and van den Berg, 1994; Kuma et al., 1996; Gledhill and Buck, 2012). En surface, le fer est utilisé comme nutriment ce qui atténue encore sa concentration (Rueler and Ades, 1987; Boyd and Ellwood, 2010). Le fer est d'ailleurs considéré comme limitant la production primaire dans près de la moitié des océans (Martin and Fitzwater, 1988; Moore et al., 2001, 2013). Sous la zone euphotique, le fer et les molécules organiques associées précipitent lentement, d'abord sous forme de colloïdes organiques puis sous forme de particules qui chutent au fond des océans (Wu and Luther, 1994; Wu et al., 2001; Van der Zee et al., 2003; Bergquist et al., 2007; Hunter and Boyd, 2007; Boyd and Ellwood, 2010; Gledhill and Buck, 2012). On appellera cette évolution progressive du dissous vers le particulaire sous le contrôle de la matière organique « coagulation ». Cette transformation est à différencier de la floculation qui traduit une augmentation de la taille des particules. L'imbrication du fer et de la matière organique se retrouve d'ailleurs à des échelles de temps plus vastes ; puisque environ 25% du carbone stocké dans les sédiments vieux de 1000-1500 ans semble être lié aux oxydes de fer réactifs (Lalonde et al., 2012).

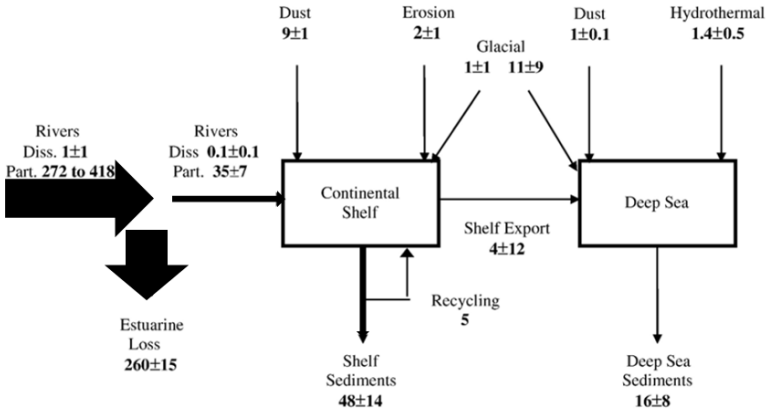

Figure 17 Cycle du fer réactif d'après Raiswell (2006) en $Tg.y^{-1}$ (1 Tg = 10^{12} g). La largeur des flèches est proportionnelle au flux de fer représenté. Haese (2006) propose un flux entre l'estuaire et l'océan côtier sensiblement différent à 163-251 $Tg.y^{-1}$ (*i.e.* une perte en estuaire de 108 à 167 $Tg.y^{-1}$)

2.1.2 Réactivité du fer particulaire (>0,4µm)

Depuis Bemmelen et al. (1877 ; cité par Mehra and Jackson, 1958) de nombreux protocoles d'extraction chimique ont été proposés pour identifier les phases réactives du fer dans les particules. On distinguera trois types d'extraction selon leurs objectifs :

(1) Afin d'estimer les risques de contamination de l'eau en différents métaux fortement liés au fer, la méthode de Tessier et al. (1979) identifie et extrait en plusieurs étapes 5 phases différentes de fer selon leur réactivité (fer adsorbé, lié aux carbonates, sous forme d'oxydes, lié à la matière organique et résiduel (essentiellement liée aux argiles)). Cette méthode est la plus utilisée (~9000 citations d'après Google Scholar), elle a été modifiée puis standardisée par le bureau européen communautaire de référence (Rauret et al., 1999). Victime de son succès, elle est aussi très critiquée (voir les reviews de Filgueiras et al., 2002 et Bacon and Davidson, 2008). En effet, elle prétend extraire de manière sélective de nombreux éléments (Al, As, Cd, Co, Cr, Cu, Mn, Ni, Pb, Sb, Zn ; Larner et al., 2006), et néglige ainsi les spécificités de chacun. Enfin, la réalisation en cascade des extractions chimiques est réputée modifier la spéciation et donc le résultat des étapes situées en aval, ce qui présente autant de biais potentiels.

(2) Afin d'extraire l'ensemble des oxydes de fer réagissant avec les sulfures d'hydrogène dans les dépôts sédimentaires (voir §2.2.2) et ainsi estimer les variations chimiques de la composition des océans à l'échelle de l'histoire de la terre, l'extraction des oxydes proposée par Rauret et al. (1999) à base d'hydroxylamine (NH_2OH) n'est pas assez puissante (Poulton and Canfield, 2005). Pour extraire les oxydes faiblement réactifs aux sulfures (temps de demi vie, $t_{1/2}$~1 an ; Canfield et al., 1992; Poulton et al., 2004) le dithionite de sodium ($Na_2S_2O_4$) est fréquemment utilisé (dans un pH variant de 4,8 à 7,3 selon les études ; Mehra and Jackson, 1958; Canfield, 1989; Haese et al., 1997; Poulton and Raiswell, 2002; Lalonde et al., 2012). Ce protocole permet de définir la somme des oxydes réactifs lorsqu'est négligée la réactivité du fer présent dans les argiles ($t_{1/2}$~100 000 an par rapport aux sulfures; Canfield et al., 1992). En ajoutant le fer dissous et les sulfures de fer (ayant déjà réagi avec les sulfures d'hydrogène) on obtient le fer hautement réactif (Fe_{HR}). Poulton and Raiswell (2002), Haese (2006) et Raiswell (2006) proposent un cycle global et actuel du Fe_{HR} (Figure 17). Bien que les incertitudes soient souvent élevées, un tel travail met en évidence l'importance majeure des processus estuariens pour comprendre le cycle du fer dans la couche critique, et les incertitudes qui subsistent sur son estimation. Cette perte en estuaire est étayée par trois arguments : (i) la diminution de fer réactif (extrait à l'hydroxylamine) mis en évidence dans l'estuaire de Beaulieu (Angleterre ; Figure 18) le long du gradient de salinité alors que le fer non-réactif reste constant (Moore et al., 1979), (ii) la diminution progressive en fer réactif entre les particules en suspension de la rivière du Mississippi

Species	Rivers	Cont. Margin	Deep Sea
Fe_{HR}/FeT	0.43±0.03	0.28±0.06	0.25±0.10
Fe_{PR}/FeT	0.25±0.01	0.23±0.07	0.26±0.15
Fe_U/FeT	0.31±0.02	0.50±0.06	0.49±0.15

Table 1 Spéciation moyenne du fer solide dans les matière en suspension des rivière (n = 34), en océan côtier (profondeur < 1000 m; n = 46) et en océan profond (profondeur > 1000 m; n = 56) ; Poulton and Raiswell 2002.

(Fe_{HR}/Fe_T=0.52), les particules du delta (Fe_{HR}/Fe_T=0.47) et le sédiment du delta (Fe_{HR}/Fe_T=0.43 ; Trefry and Presley, 1982) et (iii) le bilan à l'échelle mondiale des rapports Fe_{HR}/Fe_T et Fe_U/Fe_T entre le sédiment des rivières plus riche en Fe_{HR} et celui des océans plus riche en Fe_U (Poulton and Raiswell, 2002 ; Table 1). Avec : Fe_T le fer total, extrait avec un mélange d'acide HF-$HClO_4$-HNO_3, Fe_H le fer extrait avec HCl chauffé, Fe_{PR} (pauvrement réactif) défini par différence ($Fe_{PR}=Fe_H-Fe_{HR}$) ainsi que Fe_U, le fer *un-reactive* ($Fe_U=Fe_T-Fe_H$). Cependant dans les trois cas, aucun processus n'a été identifié précisément.

(3) Afin d'extraire le fer accessible par les bactéries, des protocoles d'extraction moins agressifs ont été proposés. Cependant, la biodisponibilité du fer dépend des communautés bactériennes présentes et des conditions physico-chimiques du milieu. En milieu oxygéné, la réduction du Fe(III) en Fe(II) permet sa dissolution. Cette propriété est utilisée par les bactéries à la surface des océans pour assimiler le fer, alors nutriment limitant (Maldonado and Price, 2001; Rijkenberg et al., 2008). Les mécanismes exacts de cette dissolution sont actuellement abondamment étudiés et combineraient l'effet des sidérophores émis par les bactéries et de la photoréduction (Finden et al., 1984; Waite and Morel, 1984; Johnson et al., 1994, 1997; Barbeau et al., 2001; Barbeau, 2006). Un tel mécanisme pourrait expliquer la forte diminution de fer particulaire en surface sur la Figure 19b.

En milieu anoxique, dans la colonne sédimentaire, certaines bactéries sont capables d'obtenir de l'énergie en couplant la réduction du fer avec l'oxydation de la matière organique (chemoorganohétérotrophie ; réaction 4, Table 2) et probablement avec l'oxydation de certains composés soufrés (chemolithohétérotrophie ; Tebo and Obraztsova, 1998;

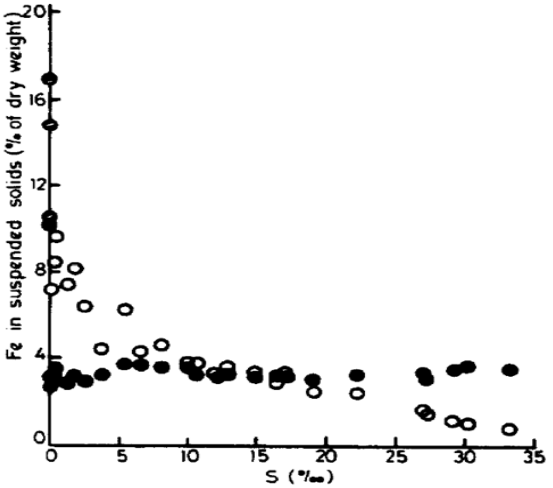

Figure 18 Spéciation du fer solide dans les particules en suspension de l'estuaire de Beaulieu, le fer extrait à l'hydroxylamine est en blanc, le fer total (extrait avec HF-$HClO_4$-HNO_3) est en noir, Moore et al., 1979.

Holmes et al., 2004 ; réaction 20, Table 2). L'identification, la classification de ces bactéries et des mécanismes mis en œuvre pour récupérer cette énergie sont des découvertes récentes qui font l'objet de nombreuses études dont on trouvera des bilans dans Lovley et al. (2004) et Lovley et al. (2011). Une comparaison entre différents extracteurs chimiques et l'une de ces bactéries, *Shewanella putrefaciens*, indique

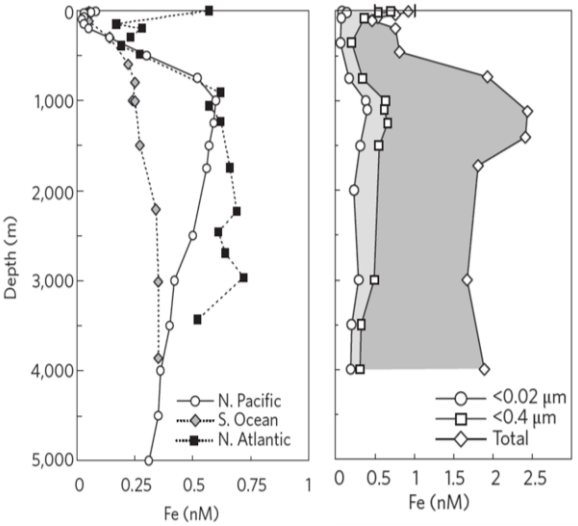

Figure 19 (a) profile des concentration de fer dissous (<0,4 µm) dans différents océans, l'enrichissement en surface dans l'océan Atlantique est probablement lié à un apport de poussière du Sahara (Bergquist et al., 2007; Kirayama et al., 2009), (b) spéciation du fer (Wu et al., 2001; Boyle et al., 2005); cité par Boyd and Ellwood, 2010

	Primary redox reactions (1–7)	dpH	ΔTA
1	$(CH_2O)(NH_3)_{\gamma N}(PO_4)_{\gamma P} + O_2 \Rightarrow \mathbf{CO_2} + \gamma^N\mathbf{NH_3} + \gamma^P\mathbf{H_3PO_4} + H_2O$	-1.32×10^{-3}	$\gamma^N-\gamma^P$
2	$(CH_2O)(NH_3)_{\gamma N}(PO_4)_{\gamma P} + 0.8\mathbf{HNO_3} \Rightarrow \mathbf{CO_2} + \gamma^N\mathbf{NH_3} + \gamma^P\mathbf{H_3PO_4} + 0.4N_2 + 1.4H_2O$	-0.26×10^{-3}	$0.8+\gamma^N-\gamma^P$
3	$(CH_2O)(NH_3)_{\gamma N}(PO_4)_{\gamma P} + (0.8+0.6\gamma^N)\mathbf{HNO_3} \Rightarrow \mathbf{CO_2} + \gamma^P\mathbf{H_3PO_4} + [0.4+0.8\gamma^N]N_2 + [1.4+1.8\gamma^N]H_2O$	-0.33×10^{-3}	$0.8+0.6\gamma^N-\gamma^P$
4	$(CH_2O)(NH_3)_{\gamma N}(PO_4)_{\gamma P} + 2Fe_2O_3 + 8H^+ \Rightarrow \mathbf{CO_2} + \gamma^N\mathbf{NH_3} + \gamma^P\mathbf{H_3PO_4} + 5H_2O + 4Fe^{2+}$	9.2×10^{-3}	$\gamma^N-\gamma^P+8$
5	$(CH_2O)(NH_3)_{\gamma N}(PO_4)_{\gamma P} + 2MnO_2 + 4H^+ \Rightarrow \mathbf{CO_2} + \gamma^N\mathbf{NH_3} + \gamma^P\mathbf{H_3PO_4} + 3H_2O + 2Mn^{2+}$	3.94×10^{-3}	$\gamma^N-\gamma^P+4$
6	$(CH_2O)(NH_3)_{\gamma N}(PO_4)_{\gamma P} + 0.5\mathbf{H_2SO_4} \Rightarrow \mathbf{CO_2} + \gamma^N\mathbf{NH_3} + \gamma^P\mathbf{H_3PO_4} + H_2O + 0.5\mathbf{H_2S}$	-0.64×10^{-3}	$\gamma^N-\gamma^P+1$
7	$(CH_2O)(NH_3)_{\gamma N}(PO_4)_{\gamma P} \Rightarrow 0.5\mathbf{CO_2} + \gamma^N\mathbf{NH_3} + \gamma^P\mathbf{H_3PO_4} + 0.5CH_4$	-0.58×10^{-3}	$\gamma^N-\gamma^P$
	Reoxidation reactions (8–19)	**dpH**	**ΔTA**
8	$\mathbf{NH_3} + 2O_2 \Rightarrow \mathbf{HNO_3} + H_2O$	-2.55×10^{-3}	−2
9	$\mathbf{NH_3} + \mathbf{HNO_2} \Rightarrow N_2 + 2H_2O$	8.20×10^{-5}	0
10	$Mn^{2+} + 0.5O_2 + H_2O \Rightarrow MnO_2 + \mathbf{2H^+}$	-2.63×10^{-3}	−2
11	$Fe^{2+} + 0.5O_2 + H_2O \Rightarrow 0.5Fe_2O_3 + \mathbf{2H^+}$	-2.63×10^{-3}	−2
12	$Fe^{2+} + 0.2\mathbf{HNO_3} \Rightarrow Fe(OOH) + N_2 + \mathbf{2H^+}$	-2.37×10^{-3}	−2.2
13	$Fe^{2+} + 0.5MnO_2 + 0.5H_2O \Rightarrow 0.5Fe_2O_3 + 0.5Mn^{2+} + \mathbf{H^+}$	-1.32×10^{-3}	−1
14	$\mathbf{H_2S} + 2O_2 \Rightarrow \mathbf{H_2SO_4}$	-1.35×10^{-3}	−2
15	$CH_4 + 2O_2 \Rightarrow \mathbf{CO_2} + 2H_2O$	-1.48×10^{-3}	0
16	$CH_4 + \mathbf{H_2SO_4} \Rightarrow \mathbf{H_2S} + \mathbf{CO_2} + 2H_2O$	-0.13×10^{-3}	2
17	$FeS + 2.25O_2 + H_2O \Rightarrow 0.5Fe_2O_3 + \mathbf{H_2SO_4}$	-2.63×10^{-3}	−2
18	$FeS + 4MnO_2 + \mathbf{10H^+} \Rightarrow 4Mn^{2+} + \mathbf{H_2SO_4} + Fe^{2+} + 4H_2O$	10.52×10^{-3}	8
19	$FeS + 2Fe(OH)_3 + \mathbf{6H^+} \Rightarrow 3Fe^{2+} + S^0$	7.89×10^{-3}	6
	Precipitation, other secondary reactions (20–27)	**dpH**	**ΔTA**
20	$FeOOH + 1.5\mathbf{H_2S} \Rightarrow FeS + 2H_2O + 0.5S^0$	1.92×10^{-3}	0
21	$Fe^{2+} + \mathbf{H_2S} \Rightarrow FeS + \mathbf{2H^+}$	-1.35×10^{-3}	−2
22	$FeS + \mathbf{H_2S} \Rightarrow FeS_2 + H_2$	1.28×10^{-3}	0
23	$Mn^{2+} + \mathbf{CO_3^{2-}} \Rightarrow MnCO_3$	-1.15×10^{-3}	−2
24	$Fe^{2+} + \mathbf{CO_3^{2-}} \Rightarrow FeCO_3$	$-1.15\ 10^{-3}$	−2
25	$Ca^{2+} + \mathbf{H_2SO_4} + 2H_2O \Rightarrow CaSO_4.2H_2O + \mathbf{2H^+}$	0.0	0
26	$\mathbf{H_2S} + 2Fe(OH)_3 + 4H^+ \Rightarrow 2Fe^{2+} + S^0 + 6H_2O$	6.54×10^{-3}	4
27	$\mathbf{H_2S} + MnO_2 + \mathbf{2H^+} \Rightarrow Mn^{2+} + S^0 + 2H_2O$	3.91×10^{-3}	2
	Adsorption, air–sea exchange (28–31)	**dpH**	**ΔTA**
28	$\mathbf{H^+} \Rightarrow H^+_{\equiv}$	1.32×10^{-3}	1
29	$\mathbf{CO_2} \Rightarrow CO_2(air)$	1.48×10^{-3}	0
30	$NH_3 \Rightarrow NH_3(air)$	-1.23×10^{-3}	−1
31	$\mathbf{NH_4^+} \Rightarrow NH_4^+{\equiv}$	0.08×10^{-3}	0
	Primary production, calcification,calcite dissolution (32–35)	**dpH**	**ΔTA**
32	$\mathbf{CO_2} + \gamma^N\mathbf{NH_3} + \gamma^P\mathbf{H_3PO_4} + H_2O \Rightarrow (CH_2O)(NH_3)_{\gamma N}(PO_4)_{\gamma P} + O_2$	1.32×10^{-3}	$-\gamma^N+\gamma^P$
33	$\mathbf{CO_2} + \gamma^N\mathbf{HNO_3} + \gamma^P\mathbf{H_3PO_4} + (1+\gamma^N)H_2O \Rightarrow (CH_2O)(NH_3)_{\gamma N}(PO_4)_{\gamma P} + (1+2\gamma^N)O_2$	1.70×10^{-3}	$\gamma^N+\gamma^P$
34	$\mathbf{CO_3^{2-}} + Ca^{2+} \Rightarrow CaCO_3$	-1.15×10^{-3}	−2
35	$CaCO_3 \Rightarrow \mathbf{CO_3^{2-}} + Ca^{2+}$	1.15×10^{-3}	2

Table 2 Réactions biochimiques et physiques principales se déroulant dans les 20 premiers centimètres de la colonne sédimentaire. Ces équations sont issues des travaux de Froelich et al. (1979) et Lovley (1991) et ont été modifiées par Mucci et al. (2000) et Soetaert et al. (2007) ; elles supposent une oxydation complète de la matière organique (production de CO_2), elles ne prennent pas en compte la nitrification de l'ammoniac produit (représenté ici par l'acide associé, majoritaire en milieu océanique, l'ammonium), supposent une dissolution totale du CO_2 (pas de formation de bulles par exemple) et représentent la somme des espèce de carbone inorganique dissous par HCO_3^- (dont l'équilibre instantané avec $CO_{2(d)}$, CO_3^{2-} et H_2CO_3 est fonction de la salinité, de la température et du pH). Les variations de pH (dpH) sont calculées pour les conditions suivantes: pH=8,2, T=25°C, S=35, p= 1atm, γ^N = 0,156 et γ^P = 0,0094 (stœchiométrie de Redfield). ΔTA indique la variation d'alcalinité total. Soetaert et al., 2007.

que l'extraction du fer par la méthode de Ferdelman (1988) et Kostka and Luther III (1994) obtient les résultats les plus proches de l'activité réductrice de *Shewanella putrefaciens* (Hyacinthe et al., 2006). Cette extraction chimique est réalisée à partir d'ascorbate en milieu neutre (pH=7.5) et surestime seulement de 50%

l'efficacité réductrice de *S. putrefaciens.* Ce protocole est très sélectif des phases les plus réactives à l'égard des sulfures (Raiswell et al., 2010) et le fer extrait évolue proportionnellement à l'activité réductrice de *S. putrefaciens* lorsque les oxydes disponibles varient. Nous utilisons ce dernier protocole dans cette thèse.

2.1.3 Réactivité du fer dans les particules en suspension des estuaires

Nous avons précédemment décrit les grandes étapes du cycle du fer dans la zone critique, tel qu'il est actuellement connu. L'importance des estuaires a été soulignée (Figure 17). Il s'agit maintenant de décrire les principaux mécanismes modifiant la composition en fer des particules à travers les estuaires afin d'identifier les processus susceptibles d'expliquer la perte extrêmement importante de Fe_{HR} mise en évidence par Poulton and Raiswell (2002).

La désorption des métaux liés aux particules augmente généralement avec la salinité car de nouveaux anions (surtout SO_4^{2-} et Cl^-) complexent les métaux et augmentent ainsi leur solubilité. Simultanément, les ligands organiques d'origine continentale sont remplacés par des ligands organiques d'origine océanique. Enfin, l'apparition de cations compétiteurs des métaux sur les sites d'adsorption réduit les sites d'adsorption disponibles pour ces derniers (Stumm, 1992; Turner, 1996; Turner and Millward, 2002). Ce comportement a été illustré à partir du cuivre et du cadmium dans l'estuaire de la Loire (Gonzalez et al., 2001; Waeles et al., 2004, 2009). Cependant, les processus d'adsorption dépendent de nombreux facteurs et des paramétrages multiples sont systématiquement réalisés pour obtenir une description fine des équilibres dans un environnement aussi dynamique que les estuaires. La dynamique du bouchon vaseux est particulièrement complexe à prendre en compte ; les processus d'adsorption sont fortement dépendant des métaux étudiés et d'autre sources/puits de métaux dissous perturbent les signaux étudiés (Thouvenin et al., 2007; Delhez and Wolk, 2013).

Le caractère faiblement prédictif des modèles obtenus rend ainsi difficile la démonstration de l'importance de l'adsorption de surface par rapport à d'autres processus. Par exemple, des particules échantillonnées à Montjean-sur-Loire (en amont de l'estuaire de la Loire) et marquées isotopiquement par adsorption, ont révélé qu'après mélange avec de l'eau de la Loire de différentes salinités, seul le cadmium (et dans une moindre mesure Zn et Cs) se comporte en accord avec les théories d'adsorption, contrairement à Co, Mn, Ag et Fe (Ciffroy et al., 2003a). Ce processus sera donc négligé dans le cadre de notre étude.

Le fer ayant une forte affinité avec les ligands organiques, sa spéciation évolue selon leurs propriétés. Or, une part importante de la matière organique coagule avec l'augmentation de la salinité : les cations présents dans l'eau de mer (1) neutralisent par adsorption les charges négatives des groupements organiques et (2) diminuent l'influence de la répulsion électrostatique en augmentant la force ionique de la solution (Black and Riddick, 1960; Stumm et al., 1962; Liang and Morgan, 1990).

L'importance de ce processus dans les estuaires a été démontrée par Sholkovitz (1976) en mélangeant de l'eau (filtrée) de rivière avec de l'eau (filtrée) de l'océan. Après une demi-heure, le mélange n'évolue plus et le résidu après filtration du mélange est analysé (Figure 20) ; plus la salinité augmente, plus la coagulation est importante. Par ailleurs, plus la concentration de fer dissous (<0,4 µm) dans la rivière est importante, plus la concentration de ligands organiques est élevée et plus la coagulation est importante. Cependant, ce processus semble effectif uniquement à forte concentration de fer dissous (Figure 21a) dans des rivières riches en colloïdes organiques (de l'ordre d'1 $mg.L^{-1}$ d'acide humique). La réalisation d'ultrafiltration à différentes salinités (Figuères et al., 1978 ; Figure 21b) et l'analyse isotopique du fer (Escoube et al., 2009) ont permis de confirmer cette relation. Cependant, la coagulation est susceptible d'augmenter le ratio Fe_{HR}/Fe_T mesuré dans les particules, et non de le diminuer (les colloïdes organo-ferriques sont par définition, riches en Fe_{HR}). Le scénario proposé par Poulton and Raiswell (2002) est que cette coagulation est suivie d'une floculation générant un dépôt préférentiel de particules avec un ratio Fe_{HR}/Fe_T élevé. La confirmation de cette proposition nécessite donc l'identification de zones de

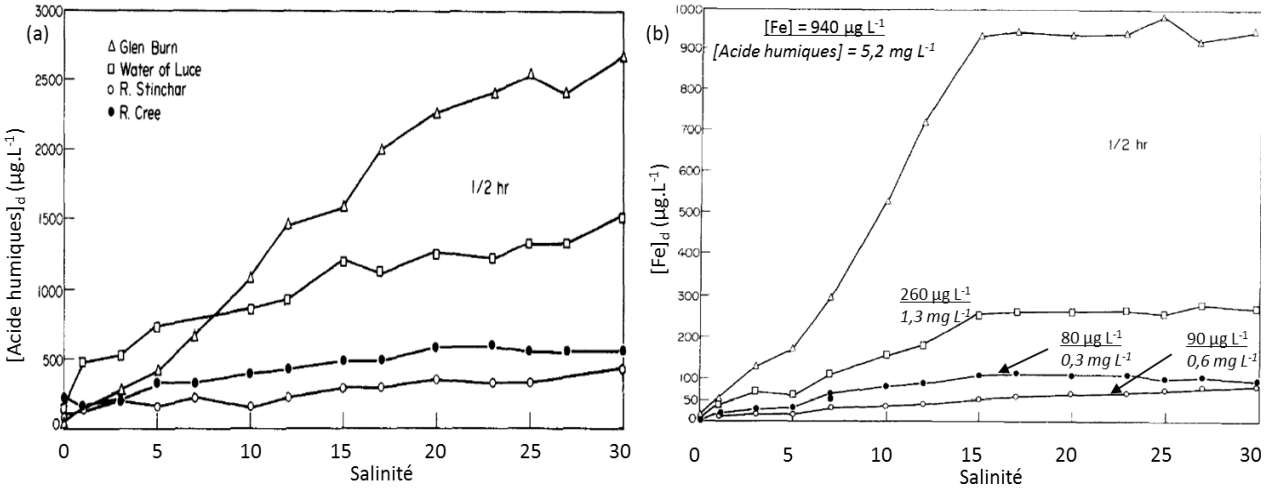

Figure 20 Démonstration de l'importance de la coagulation en estuaire (Sholkovitz 1976). (a) concentration en matière humique (classe de matière organique) ayant coagulée après 30 minutes de mélange entre de l'eau de 4 rivières d'Écosse et de l'eau de mer filtrée (la portion de chacune est indiquée par la salinité), (b) idem pour le fer, les concentrations sont exprimées en µg.L (d'eau de rivière) $^{-1}$. Les concentrations en *acide humique* et en fer en amont des estuaires sont indiquées. Les concentrations de fer mesurées en amont de l'estuaire de la Loire sont généralement comprises entre 10 et 30 µg.L^{-1} (Brach-Papa, pers. com.).

dépôt en milieu estuarien, riches en Fe_{HR}, ce qui n'a pas été mis en évidence jusqu'à maintenant (Poulton and Raiswell, 2002). Dans le cas de l'estuaire de la Loire, la concentration du fer dissous en amont semble trop faible (10 à 30 µg.L^{-1} ; Brach-Papa, pers. com.) pour soutenir ce processus de manière importante. Enfin, à l'échelle du globe, l'apport dans les estuaires de Fe_{HR} sous forme particulaire est largement supérieur à l'apport dissous (Raiswell, 2006 ; Figure 17) aussi un mécanisme de coagulation-floculation-dépôt des colloïdes organo-ferriques serait marginal pour expliquer la forte perte de Fe_{HR} estimée dans les estuaires. Une troisième possibilité de transformation du fer dans les estuaires est la dissolution réductrice réalisée dans les dépôts lors des transformations de la diagenèse précoce.

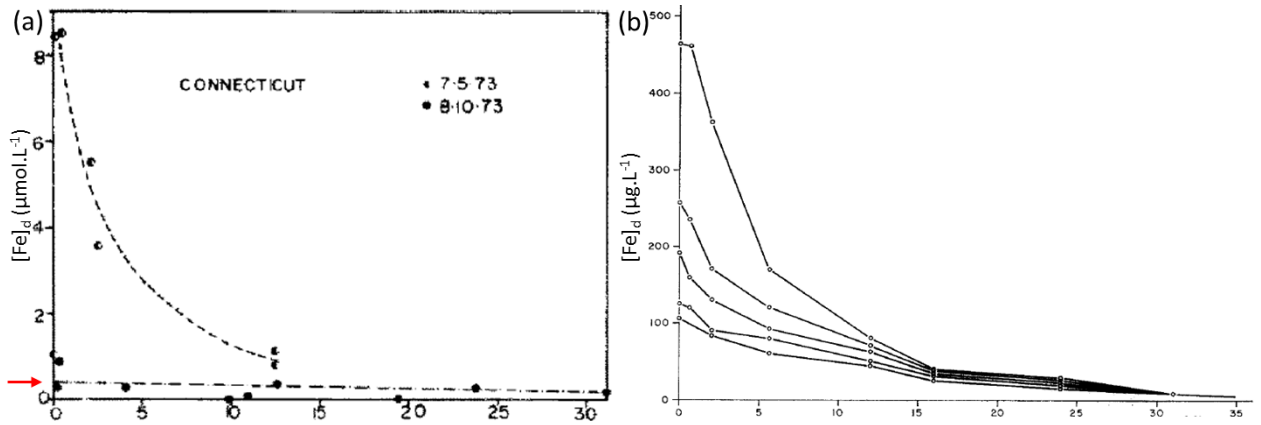

Figure 21 Exemple de profiles de fer dissous selon la salinité. (a) Estuaire du Connecticut (E-U) à deux périodes différentes après filtration à 0,7 µm, le caractère non conservatif n'est visible qu'en cas de très forte concentration (1 µmol.L^{-1} ~ 56 µg.L^{-1}; Boyle 1977), la flèche rouge correspond aux concentrations mesurées en amont de l'estuaire de la Loire (Brach-Papa pers. com.) (b) Estuaire du Congo (Zaïre), chaque trait correspond à une concentration après filtration à respectivement (de haut en bas) 1,2; 0,45 ; 0,22 ; 0,05 et 0,025 µm (Figuères et al., 1978).

2.2 La diagenèse précoce

2.2.1 Géochimie des dépôts récents : état transitoire et bouchon vaseux

La faible perméabilité des dépôts de particules fines, au fond et sur les berges de l'estuaire limite fortement les échanges d'ions entre la colonne sédimentaire et la colonne d'eau, qui se réalisent uniquement via les terriers et par diffusion moléculaire. Ainsi, si l'on suppose un état initial où le sédiment est complètement oxygéné (lorsqu'il vient de se déposer par exemple), la matière organique déposée avec le sédiment nourrit une faune bactérienne qui respire et consomme l'oxygène (réaction 1, Table 2) jusqu'à atteindre sa disparition complète au bout d'un certain temps (de l'ordre d'une dizaine d'heures ; Aller, 2004), sauf proche de la surface où son approvisionnement régulier en O_2 est assuré par un échange diffusif avec la colonne d'eau (supposée riche en oxygène). La concentration en oxygène atteint alors un état stationnaire régit par l'équilibre entre la diffusion à travers l'interface eau-sédiment et sa consommation par les bactéries. Cet état est généralement décrit par une diminution linéaire de la concentration en oxygène dans la colonne d'eau à l'approche du sédiment (zone appelée couche de diffusion, typiquement d'une épaisseur de 1 mm ; Santschi et al., 1991) suivie d'une forte diminution après l'interface, jusqu'à disparition complète après quelques millimètres ou centimètres.

Une fois l'oxygène absent, les bactéries utilisent d'autres oxydants (accepteurs d'électrons) disponibles pour respirer la matière organique, en utilisant d'abord (et jusqu'à quasi-épuisement) le plus rentable énergétiquement (réaction 2-7, Table 2) avant de passer à l'oxydant suivant. Les oxydants sont successivement consommés suivant l'ordre O_2>NO_3^- >Mn(IV)>Fe(III)>SO_4^{2-} (Figure 22) ; ces réactions de consommation de la matière organique sont appelées réactions primaires de la diagenèse précoce. Les éléments réduits issus des réactions primaires vont alors diffuser dans la colonne sédimentaire et réagir les uns avec les autres, on appelle ces réactions les réactions secondaires (par exemple les réactions 8-27, Table 2). Un certain nombre de ces réactions secondaires régénèrent la forme oxydée des couples

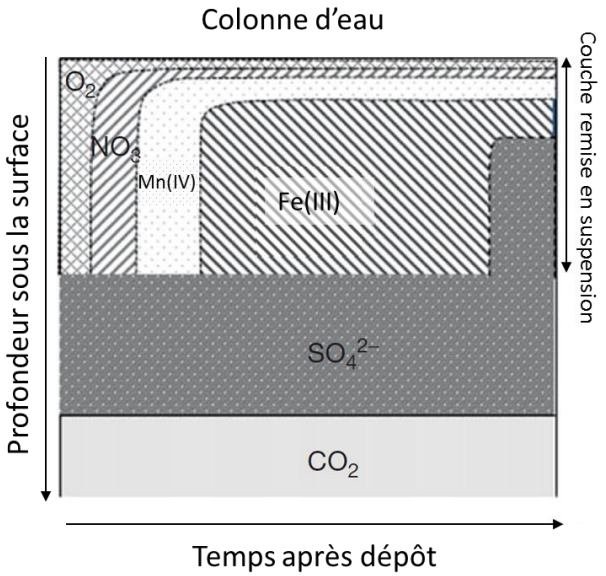

Figure 22 Profondeur de consommation des principaux oxydants dans la colonne sédimentaire après évènement de remise en suspension. Le temps nécessaire pour atteindre l'état stationnaire des réactions du fer est estimé plus long car les oxydes de fer (solide) représentent un stock plus important que les autres oxydants. Aller (2004)

redox, qui rediffuse (ou est transportée par biomixing en cas de phase solide) jusqu'à une zone où elle correspond de nouveau à l'oxydant le plus énergétique. Ce mécanisme de réapprovisionnement/recyclage permet après un certain temps d'atteindre un état stationnaire entre réduction par réactions primaires et réoxydation par réactions secondaires (Figure 22).

Le temps nécessaire à la mise en place de cet état stationnaire dans un dépôt dépend des concentrations d'oxydant disponible initialement, des cinétiques d'oxydation et de réduction et de la fréquence de remise en suspension de ce dépôt, s'il n'est pas permanent. Ainsi, dans le cas de sédiment remis en suspension à chaque marée (toutes les 6 heures), les bactéries vont quasi-uniquement consommer de l'oxygène alors que dans le cas d'une remise en suspension uniquement pendant les marées de vives eaux (tous les 10-15 jours), les bactéries vont réduire l'oxygène et les nitrates disponibles en moins d'une journée (Aller, 2004; Abril et al., 2010) puis commencer à réduire les oxydes de manganèses disponibles. Ces deux fréquences correspondent à la dynamique sédimentaire du bouchon vaseux. Ainsi, les oxydes de fer ne sont réduits théoriquement dans le

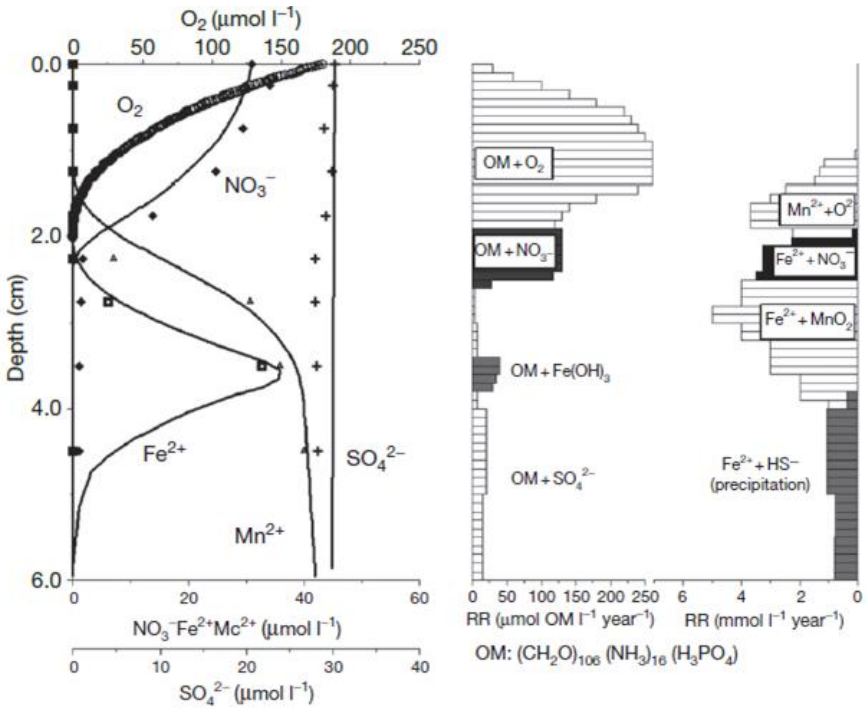

Figure 23 (a) Modélisations de profiles typiquement observés dans la colonne sédimentaire. (b) vitesse des réactions primaires et secondaires en fonction de la profondeur. Pfeifer (2002)

bouchon vaseux que dans le cas où les particules le composant sont très pauvres en oxyde de manganèse réactif (*i.e.* de l'ordre de moins de 10 µmol.g^{-1}). Cependant, dans les vasières intertidales où la dynamique sédimentaire de dépôt/resuspension est contrôlée par les évènements de crue et de vent important, les dépôts peuvent être stabilisés pendant plusieurs mois d'affilés ce qui permet probablement aux oxydes de fer réactif d'être dissous par la respiration anaérobie des bactéries.

Lors de la remise en suspension d'une partie du sédiment plusieurs processus ont lieu simultanément. (1) Le mélange de l'eau interstitielle avec la colonne d'eau dilue et libère les éléments qui ont pu être enrichis dans l'eau interstitielle durant la diagenèse, comme le carbone inorganique dissous (Abril et al., 2004), le carbone organique dissous ou l'ammonium (Maurice, 1994). (2) Les réactions chimiques résultant du mélange d'une eau oxygénée et d'une eau anoxique oxydent les espèces réduites dissoutes (comme ΣS^{2-}, Fe^{2+} et Mn^{2+}) et solides (comme FeS) ce qui consomme une grande quantité d'oxygène et explique probablement les fortes diminutions d'O_2 observées par Thouvenin et al. (1994) et parfois sa disparition complète (Abril et al., 2004). (3) Enfin le mélange des particules avec la colonne d'eau modifie les équilibres d'adsorption et désorbe probablement des éléments qui étaient enrichis dans les particules nouvellement remises en suspension.

2.2.2 Géochimie des dépôts permanents : état stationnaire

En cas de dépôt suffisamment long, l'état stationnaire décrit une succession de couches (appelées fronts redox) caractérisées par la consommation d'un unique oxydant. L'oxydant le plus rentable (O_2) définit la couche en contact avec la surface. En dessous, les couches sont définies par des oxydants de moins en moins rentables (Figure 22). Ces réactions modifient fortement les concentrations en ions dans l'eau interstitielle, comme le pH et l'alcalinité (Table 2). Les oxydes de fer solides sont ainsi dissous par les bactéries à quelques centimètres de profondeur (Figure 23a), généralement sous la zone de réduction des oxydes de Mn et au-dessus de la zone de réduction de SO_4^{2-}. Cependant il est possible de voir ces fronts redox s'inverser partiellement (Postma and Jakobsen, 1996), par exemple si les oxydes de fer sont fortement

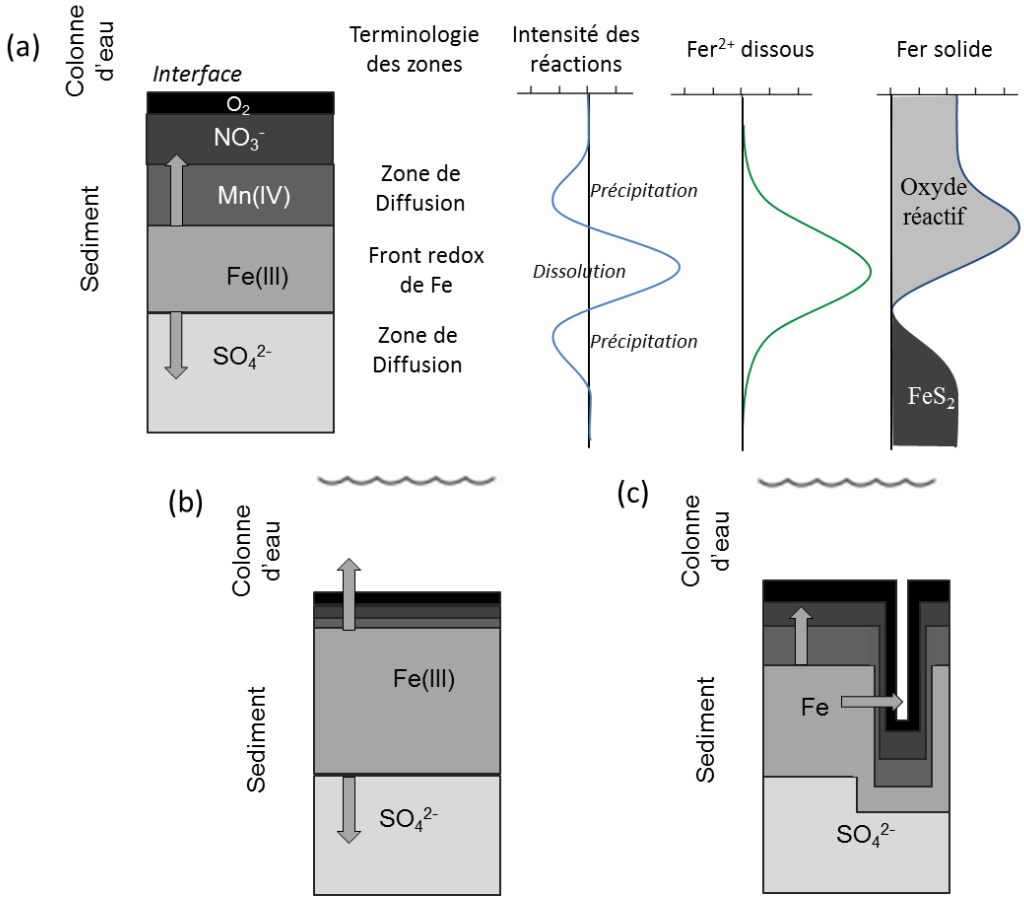

Figure 24 Processus diagénétiques idéalisés affectant la composition en fer des particules (a) dans la condition de référence (état stationnaire, pas de perte par diffusion dans la colonne d'eau, symétrie des processus de précipitation sous forme oxidée et réduite), (b) dans une condition d'intensification de la consommation du carbone organique, (c) en cas de biodiffusion. Modifié d'après Aller (1982)

cristallisés et ainsi moins rentables énergétiquement. De plus, certaines réactions secondaires (réactions 19,20 et 26, Table 2) réalisent aussi la dissolution réductrice et abiotique des oxydes de fer, sans qu'il soit toujours facile de séparer les différents processus en se basant uniquement sur les concentrations dissoutes. Par exemple, l'estimation de Pfeifer et al. (2002 ; Figure 23) néglige certaines réactions primaires (oxydation de la matière organique par les oxydes de manganèse) et l'ensemble des réactions secondaires susceptibles de réduire de manière abiotique les oxydes de fer.

Sans réaliser de simplifications aussi importantes, on sait que le front redox du fer (où se produit la dissolution des oxydes représentés par Fe(III)) est nécessairement entouré de deux zones de précipitation (Figure 24a): (1) au-dessus, une précipitation par oxydation (due essentiellement aux oxydes de manganèse ; réaction 11-13, Table 2), (2) en dessous, une précipitation sous forme réduite (de type FeS, essentiellement due aux produits de la sulfato-réduction, réactions 20-24, Table 2). La Figure 24a représente par facilité ces deux zones de précipitation de manière symétrique. Or ceci dépend des cinétiques réactionnelles relatives à chacune des réactions. Une telle symétrie produit des zones de diffusion du fer dissous réduit (Fe^{2+}) d'épaisseur égale au-dessus et en dessous du front redox du fer qui se superposent aux fronts redox de Mn(IV) et de SO_4^{2-} (représentées par les flèches grises ; Figure 24a). Cette dynamique produit sur le solide un enrichissement en oxyde dans la 1^{ere} zone de diffusion, une forte diminution dans le front redox et une augmentation de Fe solide réduit

(représenté ici par FeS_2). L'enrichissement en oxyde dépend théoriquement de l'asymétrie des processus de précipitation : plus la précipitation en FeS_2 est importante par rapport à la précipitation en oxyde de Mn, moins l'enrichissement est important. Enfin, la concentration finale en FeS_2 est égale à la concentration initiale en oxyde réactif (tel qu'indiqué sur la Figure 24a) uniquement si aucune perte vers la colonne d'eau ne s'est effectuée.

En effet, une partie du fer dissous produit dans la colonne sédimentaire peut être transférée vers la colonne d'eau et ceci dans deux conditions principales : (1) par déplacement des fronts redox vers la surface ce qui permet à la zone de diffusion d'atteindre l'interface (Figure 24b). Ce scénario pourrait se produire lors de dépôts extrêmement riches en matière organique facilement consommable par les bactéries (dite labile), lors de dépôt riche en oxydes de fer ou de diminution de la concentration en oxygène dans la colonne d'eau. Et (2), par l'existence de terriers dont le renouvellement fréquent de l'eau assure un transfert advectif du sédiment vers la colonne d'eau (*bioirrigation*, Figure 24c). Une fois dans la colonne d'eau le fer dissous précipite probablement sous forme d'oxydes colloïdaux dont une partie est transférée plus en aval. Ainsi une partie du fer est définitivement séparée des particules déposées. L'un des objectifs principaux de cette thèse est d'estimer si la remise en suspension de ces particules appauvries suffit à expliquer la diminution de la teneur de Fe_{HR}.

2.2.3 Impact de la diagenèse précoce sur la disponibilité des nutriments

La respiration anaérobique réalisée dans les dépôts sédimentaires modifie aussi la distribution des principaux nutriments : le phosphate (PO_4^{3-}) et le nitrate (NO_3^-). En premier lieu, la dégradation de la matière organique dans le sédiment libère les nutriments (sous forme réduite) qui diffusent et sont relâchés dans la colonne d'eau, on parle de recyclage des nutriments. Cependant, les nitrates sont aussi consommés en tant qu'oxydant lorsque l'oxygène vient à manquer. Le sédiment « pompe » alors des nitrates venant de la colonne d'eau, c'est la dénitrification. Enfin, les phosphates ont une très forte affinité pour la phase solide inorganique, notamment par adsorption sur les oxydes de fer (Rehm, 1985; Sundby et al., 1992; Slomp et al., 1996; Anschutz et al., 1998). Le phosphate peut donc être libéré vers la colonne d'eau lors de la dissolution réductrice des oxydes de fer ou au contraire être adsorbé par des oxydes sous-saturés lors des épisodes de remise en suspension. De manière contrastée, un sédiment peut donc être une source ou un puits vis-à-vis de chacun de ces nutriments. La compréhension de ces mécanismes est primordiale car ils modulent la disponibilité des nutriments ce qui souvent contrôle l'intensité de la production primaire dans la colonne d'eau.

En effet, en milieu océanique, NO_3^- et PO_4^{3-} sont majoritairement produits par le recyclage de la matière organique et leur concentration traduit l'équilibre entre la vitesse de dégradation de la matière organique et la vitesse de métabolisation des nutriments lors de la production primaire. Cet équilibre a été identifié par la constance du ratio $NO_3^-/PO_4^{3-}=16$ à la surface océanique qui correspond au rapport N/P moyen dans les algues (Redfield, 1934). Cependant, la raison de la constance de cet équilibre, c'est-à-dire qu'il y ait simultanément exactement assez de NO_3^- et de PO_4^{3-} sur presque toute la surface du globe est liée à la capacité de certains producteurs primaires (notamment les cyanobactéries) à fixer le N_2 atmosphérique ce qui leur permet de profiter du surplus de PO_4^{3-} inutilisable par les autres organismes. *In fine* cette fixation enrichie le milieu océanique en NO_3^- jusqu'à l'équilibre $NO_3^-/PO_4^{3-}=14.1$ (Tyrrell and Law, 1997; Tyrrell, 1999). Cet équilibre est légèrement inférieur à celui proposé par Redfield, mais il s'appuie sur un plus grand nombre de données. L'écart entre le rapport dans la colonne d'eau ($NO_3^-/PO_4^{3-}=14.1$) et le rapport dans la matière organique (N/P=16) indique un stress pour les producteurs primaires, produit par le manque de nitrate et qui permet aux cyanobactéries d'obtenir un avantage compétitif grâce à leur capacité fixatrice de N_2. Ce modèle indique donc que le nutriment limitant dans les océans sur le long terme est le phosphate. Cependant, sur de plus courtes périodes et notamment dans l'océan côtier, le rapport NO_3^-/PO_4^{3-} n'est pas tamponnée par la fixation de N_2 et une variation de NO_3^- induit rapidement une variation d'intensité de la production primaire (Ryther and Dunstan, 1971).

Dans la Loire, et (dans une moindre mesure) dans l'estuaire, l'équilibre « production primaire-recyclage » n'est pas atteint et la littérature disponible rapporte systématiquement des rapports NO_3^-/PO_4^{3-} supérieurs à 50 (Meybeck et al., 1988; Gorse et al., 2010; Minaudo et al., 2015). Ce ratio élevé et les résultats du suivi sur le long terme réalisé par Minaudo et al. (2015 ; Figure 3) indiquent que le phosphore limite la production primaire en cas d'efflorescences algales. Lorsqu'il n'y a pas d'efflorescence, la concentration en nutriments n'est pas un facteur limitant et la production primaire est probablement contrôlée par le broutage, la turbulence ou l'ensoleillement. Cependant, la valeur de NO_3^-/PO_4^{3-} élevée indique qu'une fois à l'océan et l'équilibre « production primaire-recyclage » atteint, le phosphore sera limitant dans le panache du fleuve. Il est donc important d'identifier les modifications de ce ratio NO_3^-/PO_4^{3-} dans la colonne d'eau produites par la transformation des particules dans les zones de dépôt.

3 Organisation de l'étude

L'étude bibliographique montre qu'une importante perte de fer réactif présent sur les particules en suspension (Fe_{HR}) devrait accompagner leur transfert à travers un estuaire tel que celui de la Loire. Les processus responsables de telles transformations sont encore incertains, mais la dissolution réductrice des oxydes de fer se déroulant dans la colonne sédimentaire lors des périodes de dépôts semble être le processus le plus probable. Cependant, selon les conditions, cette dissolution « sédimentaire » peut (1) enrichir le sédiment de surface en oxyde de fer (1^{ere} couche diffusive, Figure 24a) et l'appauvrir plus en profondeur (Figure 24a) ou (2) appauvrir les particules par diffusion du fer dissous vers la colonne d'eau avant leur resuspension. Ce second scénario nécessite des conditions particulières : une remontée des fronts redox (Figure 24b) ou une importante *bioirrigation* (Figure 24c). Il n'est actuellement pas possible d'indiquer clairement lequel de ces scénarii est prépondérant. Nous nous intéresserons donc à décrire en détail chacune de ces hypothèses afin d'indiquer si les processus diagénétiques peuvent expliquer la diminution de Fe_{HR} observée dans les particules en suspension.

La 1ère partie, « Importance de l'hétérogénéité à faible échelle dans la vasière des Brillantes », illustre la complexité de l'étude de la zone critique à cause des effets de la macrofaune benthique sur le fonctionnement des vasières. Chacun des chapitres correspond au développement d'une méthode analytique permettant de mieux comprendre l'impact de cette hétérogénéité. Le chapitre 1.1 décrit l'influence du *biomixing* dans les 10 premiers centimètres de sédiment à travers ses conséquences sur la distribution verticale et latérale des foraminifères benthiques en utilisant une méthode d'échantillonnage du sédiment en 2 dimensions et à résolution centimétrique. De plus, la description à haute résolution (200 µm x 200 µm) de Fe_d et phosphore réactif dissous (DRP) dans l'eau interstitielle, permet de décrire l'impact des transformations liées au fer sur l'écologie des foraminifères. Les chapitres 1.2 et 1.3 se concentrent sur la *bioirrigation* réalisée par le mélange des eaux de surface et des eaux interstitielles le long des terriers.

Les deux principaux nutriments (nitrate et phosphate) et le fer dissous sont étudiés en 2 dimensions et à haute résolution grâce à des méthodes de type 2D-DET-CH *i.e.* échantillonnage par gel DET (*Diffusive Equilibrium in Thin film*) en 2 dimensions puis analyse par Colorimétrie Hyperspectrale. La mise en place d'une méthode d'analyse pour les nitrates et les nitrites est l'objet du chapitre 1.2. Dans le chapitre 1.3, le développement d'une méthode de calcul numérique, la procédure « *Savitsky-Golay Filter*» (SGF), permet d'estimer les flux et la production en 2 dimensions et à haute résolution du fer et du phosphate dissous. Cette méthode, couplée à l'identification par photographie des terriers permet de proposer une quantification directe de l'importance de la *bioirrigation* dans l'appauvrissement en fer réactif des particules lors de leur dépôt.

La seconde partie vise à quantifier les transformations des particules lors des périodes de dépôt dans l'estuaire de la Loire à partir des méthodes développées précédemment et de l'analyse chimique des particules. Le chapitre 2.1 propose la description d'un cycle géochimique des vasières intertidales en estuaire. Il détaille notamment l'importance des dépôts de crue, responsables de l'introduction de particules riches en oxydes de fer et en oxydes de manganèse dans la vasière ce qui produit un état transitoire diagénétique pendant plusieurs mois. Lors de certaines campagnes de terrain, ce suivi a été complété par l'étude en deux dimensions des transformations des oxydes de fer et des phosphates (Chapitre 2.2). Ce chapitre s'appuie notamment sur la comparaison des extractions partielles du solide en 2D à l'échelle centimétrique avec les estimations de production réalisées grâce à la procédure SGF appliquée à des données 2D-DET-CH. Enfin, le Chapitre 2.3 identifie les traces de ces transformations benthiques sur les particules prélevées dans la colonne d'eau de l'estuaire pendant différentes conditions hydrologiques. Il compare alors la dynamique du fer aux réactions visibles sur le manganèse et sur les terres rares. Ce dernier chapitre permet de faire le lien entre les processus décrits dans les zones anoxiques des dépôts avec les particules en suspension dans la colonne d'eau et transportées plus en aval, jusque sur le plateau continental.

Ce travail de thèse a été valorisé par 2 communications orales et 4 posters lors du *46th International Liege Colloquium*, du *13th International Estuarine Biogeochemistry Symposium*, Bordeaux, June 2015 et de la *25th Goldschmidt*, Prague, 2015. Il a aussi permis la rédaction de publications (à comité de lecture, rang A) : deux articles acceptés (le Chapitre 1.1 dans *Biogeosciences* et le Chapitre 1.3 dans *Marine Chemistry*), trois articles soumis (Chapitre 1.2 dans *Environmental Science and Technology*, et les Chapitre 2.1 et 2.3 dans *Journal of Sea Research*) et un article en préparation (Chapitres 2.2).

Partie 1 :

Importance de l'hétérogénéité à faible échelle dans la vasière des Brillantes

Partie 1 :

1 Distribution en 2 dimensions des foraminifères benthiques vivants dans le compartiment anoxiques du sédiment d'une vasière estuarienne (Estuaire de la Loire)

A. Thibault de Chanvalon[1,2], E. Metzger[1], A. Mouret[1], F. Cesbron[1], J. Knoery[2], E. Rozuel[2], P. Launeau[1], M. P. Nardelli[1], F. J. Jorissen[1], E. Geslin[1]

[1]{Université d'Angers, Université de Nantes, LPG-BIAF, UMR CNRS 6112, 49045 Angers Cedex, France}

[2]{Ifremer, LBCM, Rue de l'Ile d'Yeu, 44300 Nantes, France}

Article publié dans Biogeosciences 12, 6219–6234.
doi : 10.5194/bg-12-6219-2015

Edited by: L.Levin

ABSTRACT

We present a new rapid and accurate protocol to simultaneously sample living benthic foraminifera in two dimensions in a centimetre scale vertical grid and dissolved iron and phosphorus in two dimensions at high resolution (200µm). Such an approach appears crucial for the study of foraminiferal ecology in highly dynamic and heterogeneous sedimentary systems, where dissolved iron shows a strong variability at a centimetre scale. On the studied intertidal mudflat of the Loire estuary, foraminiferal faunas are dominated by *Ammonia tepida*, which accounts for 92% of the living (CTG-labeled) assemblage. The vertical distribution shows a maximum density in the oxygenated 0-0.4 cm surface layer. A sharp decrease is observed in the next two centimetres, followed by a second well defined maximum in the suboxic sediment layer (3 - 8 cm depth). The presented method yields new information concerning the 2D distribution of living *A. tepida* in suboxic layers. First, the identification of recent burrows by visual observation of the sediment cross-section, and the burrowing activity as deduced from the dissolved iron spatial distribution show no direct relation with the distribution of *A. tepida* at a centimetre scale. This lack of relation appears contradictory to previous studies (Aller and Aller, 1986; Berkeley et al., 2007). Next, the heterogeneity of *A. tepida* in the 3-8 cm depth layer has been quantified by the Moran's Index to identify the scale of parameters controlling the *A. tepida* distribution. The results reveal horizontal patches with a characteristic length of 1 to 2 cm. These patches correspond to areas enriched in dissolved iron likely generated by anaerobic degradation of labile organic matter. These results suggest that the routine application of our new sampling strategy could yield important new insights about foraminiferal life strategies, improving our understanding of the role of these organisms in coastal marine ecosystems.

RESUME

Nous proposons un nouveau protocole rapide et efficace pour échantillonner simultanément et en deux dimensions : les foraminifères benthiques vivants selon une grille verticale centimétrique et les phosphates et le fer dissous à haute résolution (200 µm). Une telle approche semble cruciale dans le cadre d'études sur l'écologie des foraminifères en milieux fortement dynamiques et hétérogènes, dans lesquelles le fer dissous présente une forte variabilité à l'échelle centimétrique. Dans la vasière de l'estuaire de la Loire étudiée, les faunes de foraminifères sont dominées par *Ammonia tepida*, qui représente 92% de l'assemblage vivant (identifiée au CTG). La distribution verticale montre un maximum de densité dans la couche oxygéné de surface (0-0,4 cm). Une diminution rapide est observée sur les deux centimètres suivants. Un second maximum est très bien défini dans les couches suboxiques (3-8 cm de profondeur). La méthode développée ici apporte de nouvelles informations sur la distribution en 2D des *A. tepida* vivant en suboxie. En premier lieu, l'identification des terriers récents par observation de la plaque de sédiment échantillonnée et par identification des zones appauvries en fer dissous, ne correspond pas directement à la distribution d'*A.tepida*. Cette absence de relation semble contradictoire avec les études précédentes (Aller and Aller, 1986; Berkeley et al., 2007). En second lieu, l'hétérogénéité d'*A.tepida* dans la couche entre 3 et 8 cm de profondeur est quantifiée par l'index de Moran afin d'identifier la longueur caractéristique des paramètres contrôlant sa distribution. Les résultats montrent une organisation sous forme de patchs horizontaux dont la longueur caractéristique est comprise entre 1 et 2 cm. Ces patchs se superposent à des zones enrichies en fer dissous probablement produits par la dégradation anaérobique de matière organique labile. Ces résultats suggèrent qu'une application systématique de ce nouveau protocole d'échantillonnage pourrait apporter de nouvelles informations sur les stratégies de développement mises en place par les foraminifères et ainsi améliorer la compréhension de l'importance de ces organismes dans les écosystèmes marins côtiers.

1 Two-dimensional distribution of living benthic foraminifera in anoxic sediment layers of an estuarine mudflat (Loire Estuary, France)

1.1 Introduction

Intertidal estuarine mudflats are transitional areas between land and sea. This intermediate position explains the important horizontal, vertical (in the sediment column) and temporal heterogeneities in physical and chemical sediment properties. It also causes heterogeneous ecological niches with scales ranging from micro- to hectometres. When studying such heterogeneous environments, the observational scale has to be chosen as a function of the scale of the studied ecological niche variability (Wu et al., 2000; Morse et al., 2003; Martiny et al., 2006; Wu and Li, 2006). This is a fundamental prerequisite to further identify potential parameters controlling the heterogeneity of the niches.

Ecological studies of benthic foraminifera attempt to describe the main factors controlling foraminiferal communities, and their variability on different spatial and temporal scales (Buzas et al., 2015). The best described pattern concerns the spatial variability of their vertical distribution in open marine environments, on a hundred-kilometre scale. The conceptual model proposed by Jorissen et al. (1995) considers a regional variability of the spatial organization of foraminiferal taxa in the sediment column, where they occur in a succession of so-called microhabitats. The stratified succession of inhabited sediment layers is supposed to be a response to oxygen and organic matter availability, which changes vertically in the uppermost sediment, but also geographically, when going from oligotrophic (*e.g.* deep water, offshore) to eutrophic (*e.g.* shallow water, nearshore) conditions. In estuarine areas, on smaller scales, other major controls are invoked (e.g. emersion time, grain size, salinity), but they are less well documented. At a kilometre scale, the salinity, salinity variations and more generally the frequency of chemical exchanges with the ocean are often invoked as controls of foraminiferal assemblages (Debenay and Guillou, 2002; Debenay et al., 2006). Within the estuary, especially in cross-shore transects, emersion time seems to be a major controlling factor of species distribution at a decametre scale (Berkeley et al., 2007). But other parameters, such as grain size, pH or organic carbon lability could also have a significant impact. Estuarine foraminiferal faunas seem to show substantial patchiness at metre scale at the sediment surface (Buzas, 1970; Hohenegger et al., 1989; Buzas et al., 2002, 2015). At a decimetre scale, the rare studies performed on intertidal mudflats highlight that grain size and topography could be important controls (Lynts, 1966; Morvan et al., 2006).

Finally, according to our knowledge, only three publications have analyzed the spatial surface organization at a centimetre scale, using an adequate sampling grid (Buzas, 1968 in Rehoboth Bay, Delaware; Olsson and Eriksson, 1974, on the Swedish coast; and de Nooijer, 2007 in the Wadden Sea). These three studies show that foraminiferal densities present a patchy distribution. Buzas (1968) hypothesized that this could be due to individual reproduction, leading to very localized and intermittent density maxima, so called "pulsating patches" (Buzas et al., 2015). Another field approach, at a centimetre scale, is to sample around inhabited burrows, using a non-regular sampling scale, by defining position, size and shape of each sample according to the burrow geometry. In this way Aller and Aller (1986) and Thomsen and Altenbach (1993) studied the foraminiferal distribution around macrofaunal burrows at subtidal stations and observed a threefold enrichment of foraminiferal density in the burrow walls. With a similar sampling strategy, Koller et al. (2006) showed a three hundred-fold enrichment of foraminiferal densities in the burrow walls of an intertidal station. These studies highlight the importance of macrofaunal activity at the centimetre scale as a potential control of foraminiferal spatial organization. They suggest the presence of oxic microenvironments around the burrows generated by bio-irrigation, attractive because of organic matter enrichment (Aller and Aller, 1986). Foraminifera could

specifically colonize these environments favourable for aerobic respiration and therefore be found at depths below average oxygen penetration.

However, another possible explanation for the presence of rich foraminiferal faunas in deeper anoxic layers could be the ability of some species to switch to alternative (*e.g.* anaerobic) metabolisms (Leutenegger and Hansen, 1979; Bernhard and Alve, 1996; Risgaard-Petersen et al., 2006; Heinz and Geslin, 2012). These two possible mechanisms lead to contrasted conclusions concerning ecological strategies. For example, a high density of living foraminifera along burrow walls compared to anoxic surrounding sediments may be explained by a positive response of the foraminiferal community to the availability of oxygen and labile organic matter (Aller and Aller, 1986; Loubere et al., 2011) or as the involuntary consequence of passive downward transport due to macrofaunal bioturbation followed by the development of a short term survival strategy based on a metabolism modification (Douglas, 1981; Alve and Bernhard, 1995; Moodley et al., 1998). *In situ* distribution can answer this question by determining whether subsurface high density is only concomitant with burrows or whether living *Ammonia tepida* are able to modify their metabolism in order to survive in suboxic environments (without both oxygen and sulphide) independently of burrows. Unfortunately, the sampling strategies used in the above mentioned references did not allow establishing the importance of burrows compared to other environmental physico-chemical parameters because the increased density observed in burrow walls was not compared to a "background heterogeneity" at the same scale. This precaution is necessary, especially when the increase of foraminiferal density is not at least of one order of magnitude. Consequently, a large uncertainty remains about the ubiquity and the nature of macrofauna-independent mechanisms that could cause foraminiferal heterogeneity.

The recent development of pore water sampling techniques with high resolution in two dimensions offers the advantage of providing simultaneously geochemical information on vertical and horizontal sub-millimetre scales (Stockdale et al., 2009; Santner et al., 2015). Several studies have evidenced important spatial variability of dissolved iron release into pore water (Jézéquel et al., 2007; Robertson et al., 2008; Zhu and Aller, 2012; Cesbron et al., 2014). This can be due to iron oxide consumption caused by local labile organic matter patches that favour anaerobic respiration (by dissimilatory bacteria; Lovley, 1991) or by enhancement of sulphide transport from the deeper layers through burrows and subsequent abiotic dissolution (Berner, 1970). Conversely, macrofaunal water renewal is also likely to bring oxic water into the burrows which consumes reduced dissolved iron and replenishes the stock of iron oxide. Direct burial of iron oxide by macrofauna may also contribute to the replenishment (Burdige, 2011). The overall role of macrofaunal activity on the sedimentary iron cycle is still unclear (Chapter 1.3; Robertson et al., 2009). Phosphorus is also likely to have a heterogeneous geochemical pattern. Very marked centimetre scale patches were reported (Cesbron et al., 2014), apparently due to nutrient recycling from organic matter. However, iron oxide dissolution can also release adsorbed phosphorus according to a ratio up to P/Fe ~0.2 (based on ascorbate extractions; Anschutz et al., 1998) which can be compared to the theoretical anaerobic respiration ratio of P/Fe ~0.002 (Froelich et al., 1979). Using geochemical fingerprints, the combination of sub-millimetre resolution analyses of dissolved iron and phosphorus is thus likely to (1) confirm the burrow activity (iron oxidation) and (2) identify potential hotspots of organic matter consumption (phosphorus production independent to iron).

In the present paper, we present a new two dimensional sampling technique allowing first the investigation of the relation between benthic foraminifera and dissolved iron, and next, the analysis of the heterogeneity of foraminiferal distribution and then, the identification of the scale of potential controls such as active burrows or labile organic matter patches.

1.2 Material and methods

1.2.1 Site description

The Loire estuary (NW coast of France) is hyper-synchronous: it shows an increasing tidal range upstream (Le Floch, 1961) reaching a maximum spring tidal range of about 7m at 40 km from the mouth. At Donges (in the high tidal range area, right shore) the daily surface salinity range is about 20. Seasonally, surface salinity fluctuates from 0 during floods to 30 during low-water periods (network SYVEL, GIP Loire Estuaire). On the opposite shore, the largest mudflat of the estuary ("Les Brillantes", ~1350 ha) extends downstream from the city of Paimboeuf. During high tide, hydrodynamics (tide, wind induced waves, flow) constrains the sediment deposition/resuspension cycle whereas during low tide, biological factors (bioturbation, biofilm stabilization, benthic primary production; Round, 1964; Vader, 1964; Paterson, 1989) become more important and generate sediment burial and chemical transformations. Microphytobenthic biofilms vary annually between Chl a = 20 mg m^{-2} in January and Chl a = 60 mg m^{-2} in July (Benyoucef et al., 2014). Our sampling site (47°16'56.00"N 2° 3'47.00"W) is located on the slikke of "Les Brillantes" mudflat, below the Mean High Water Neap Tide level (MHWNT), about 20 m offshore from an one metre high cliff. Sediment is mainly composed of silt (92%) with some clay (6%) and sand (2%) (Benyoucef, 2014).

We sampled in May 2013, two weeks after a major flood (discharge volume at Paimboeuf >2500 $m^3.s^{-1}$, hydro.eaufrance.fr). During sampling, the river discharge was 835 m^3 s^{-1} on average. Air temperature was 12.7°C, the weather was cloudy and salinity in the surface waters of the main channel ranged from 0.6 to 20 (data from SYVEL network). Sediment samples were collected at the beginning of low tide. Porosity decreased from 0.917 to 0.825 in the first 5 cm (Chapter 2.1). The calcite saturation state, calculated from alkalinity, sodium and calcium concentrations and pH (Millero, 1979, 1995; Mucci, 1983; Boudreau, 1996; Mucci et al., 2000; Hofmann et al., 2010) was above 1.0 until 9 cm depth (data not shown). The macrofauna was mainly composed of *Hediste diversicolor* (Annelida: Polychaeta, 630 ind m^{-2}) and *Scrobicularia plana* (Mollusca: Bivalvia, 70 ind m^{-2}) (I. Métais, personal communication).

1.2.2 1D sampling and processing

Four cylindrical cores (diameter 8.2 cm) were sampled using Plexiglas tubes. The first two cores were dedicated to foraminiferal analysis and were sliced immediately after sampling; every two millimetres from 0 to 2 cm and every half centimetre between 2 and 5 cm (one replicate has two deeper samples). Surface microtopography induces high uncertainty in the volume of the upper slice. Within one hour after retrieval, in order to distinguish living foraminifera, sediments were incubated with the staining molecule CellTracker Green™ in a final concentration of 1 µmol.L^{-1} in 50 mL of estuarine water for 10-19 hours (Bernhard et al., 2006). CellTracker Green is a non-fluorescent molecule, which is hydrolyzed by nonspecific esterases, producing a fluorescent compound. After incubation, samples were fixed in 3.8% Borax-buffered formalin and stored until analysis. In the laboratory, samples were sieved over 315, 150, 125 and 63 µm meshes, and the 150-315 µm fraction was examined using an epifluorescence stereomicroscope (i.e., 485-nm excitation, 520-nm emission; Olympus ZX12 with a fluorescent light source Olympus URFLT or Nikon SMZ 1500 with a PRIOR Lumen 200). All foraminifera that fluoresced consistently and brightly were wet picked, air dried, identified and counted.

The two other cores were used to constrain geochemistry. The first core was dedicated to microelectrode profiling and solid phase geochemistry. The solid phase was characterized by total organic carbon and reactive iron, manganese and phosphorus, extracted by an ascorbate reagent (buffered at pH 8) during 24 hours (Kostka and Luther, 1995; Anschutz et al., 1998, 2005; Hyacinthe et al., 2001; Hyacinthe and Van Cappellen, 2004). See more details in Annexe 1. Oxygen was analyzed with Clark's type electrodes (50µm tip diameter, Unisense©, Denmark) within the first 5 mm at a 100 µm vertical resolution. In the second core, Diffusive Equilibrium in Thin film in one dimension probes (DET 1D, adapted from Davison and Zhang, 1994; Krom et al., 1994) were incubated during one night for dissolved sodium, iron, manganese and

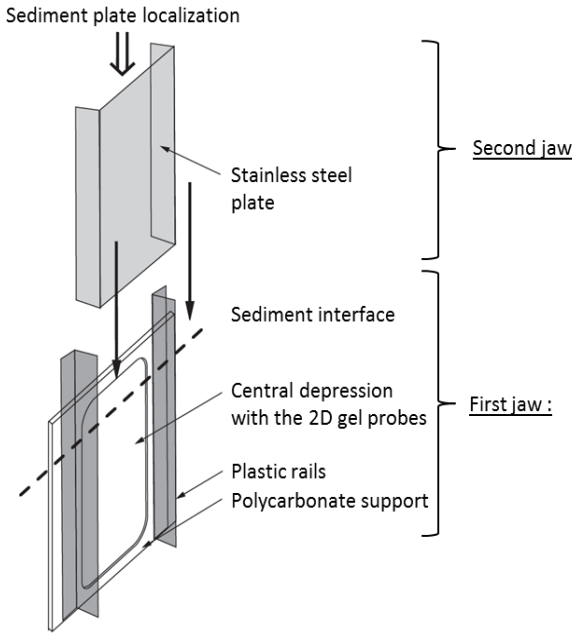

Figure 25 Schematic view of the "jaw device" for simultaneous sampling of sediment and pore water.

phosphorus. Gel samples were eluted in HNO_3 0.01 M and analyzed by ICP-AES. Salinity was estimated from sodium concentration. See more details in Annexe 2.

1.2.3 **2D sampling and processing**

For the two-dimensional sampling, we used a "jaw device", composed of two main parts (jaws; Figure 25). The first jaw is a DET gel probe, which samples the dissolved chemical species from the pore water at high resolution, whereas the second jaw samples a 2 cm-thick slice of the adjacent sediment, from which we sub-sampled 1 cm^3 aliquots for foraminiferal analysis. The first jaw is a 250 mm x 200 mm x 2 mm polycarbonate plate with a central depression of 1 mm that holds a 2D gel probe. The probe is made of two layers: 1) a 180 mm x 97 mm x 0.92 mm polyacrylamide thin-film prepared and rinsed with Milli-Q water (Krom et al., 1994) which reaches equilibrium in a few hours once incubated (called "2D DET gel") and 2) a PVDF porous (0.2 µm) membrane to protect the gel, prevent falling out of the depression and to control diffusion. The 2D DET gel was prepared and mounted less than one week before sampling, was conserved in a wet clean plastic bag and then, deaerated by N_2 bubbling for about 6h before deployment. The sampler was deployed into the sediment at low tide. On both lateral sides of the central depression (Figure 25), plastic rails (2 cm high) were fixed in order to guide the second jaw to slide along the plate. The second jaw is a stainless steel plate (1.5 mm thick) bent on both sides. After equilibration (5h) of the 2D gel, the second jaw was inserted along the guides of the first jaw and the whole device was gently pulled out of the sediment. Once on shore, the 2D gel was separated from the sediment, covered with a plastic-coated aluminium plate and stored in an icebox with dry ice pellets (Cesbron et al., 2014), until final storage in a freezer (-18°C).

The sediment plate was manually cut (with stainless steel trowels) within 30 minutes in 1 cm^3 cubes over a surface of 8 cm x 8 cm. The resulting sampling map is presented in Figure 26 together with the 1D sampling scheme of foraminifera. Next, these sediment cubes were labelled with CTG to recognize living foraminifera (as for the core slices, see 1.2.2). Considering an error of 1 mm for each cut, the volume uncertainty was ~14%, except for surface samples where the microtopography of the sediment surface considerably increases volume uncertainty.

The 2D DET probe was analyzed in order to obtain the concentrations of dissolved iron and dissolved reactive phosphate (DRP ; Cesbron et al., 2014). Quickly, after thawing at ambient temperature, the sample gel was recovered by a reactive gel equilibrated in specific colorimetric reagents. Twenty five minutes after contact, a photograph (reflectance analysis) of superposed gels was taken with a hyperspectral camera (HySpex VNIR 1600) and analyzed (see 6.3 for more details). The resolution (surface area of pixels) was 211 µm x 216 µm. The estimated incertitude is 10% for iron and 11% for DRP. See more details in Annexe 3. To compare the geochemical species distribution (at submillimetre resolution) and foraminiferal density (at centimetre resolution), a handmade R code was written allowing the downscaling of chemical resolution from 0.2 mm to 1 cm.

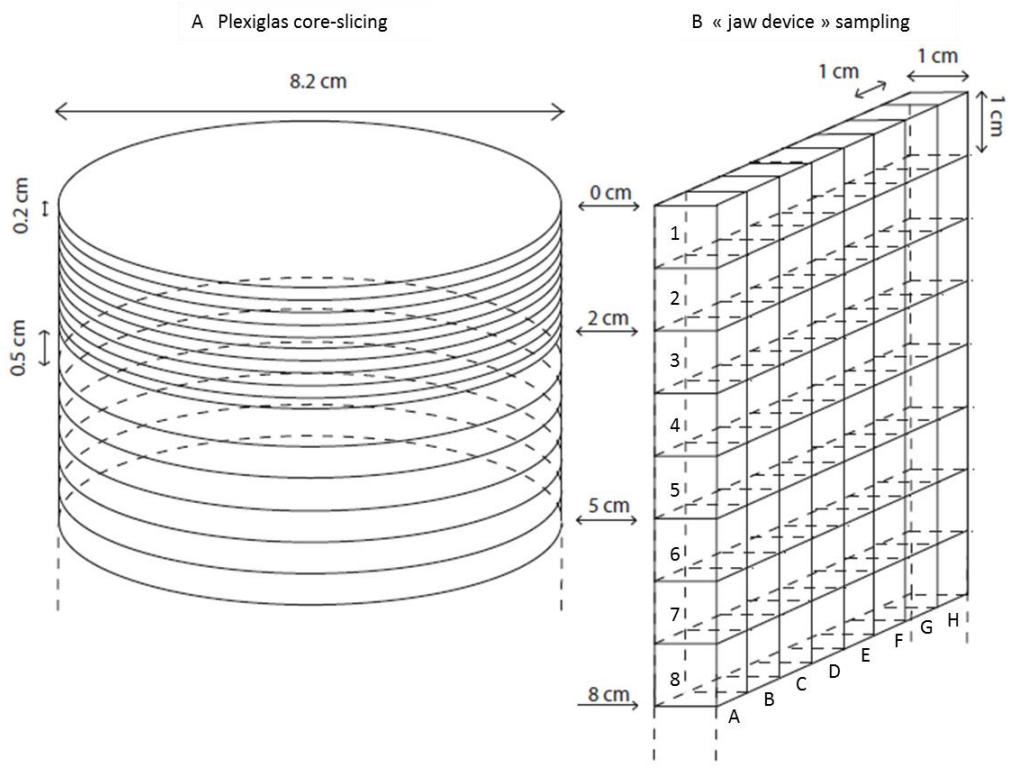

Figure 26 Sediment sampling methodology for living foraminiferal analyses. (a) Usual 1D hand coring and layer slicing. (b) Sediment sampling with the second jaw of the "jaw device" (Fig. 25) and representation of the sediment cubic slicing.

1.2.4 **Statistical analyses**

Patchiness effect or autocorrelation, interpreted as the fact that the density of one square depends on its neighbours, was explored using spatial correlograms built using Moran's Index (I), computed with R package "spdep" following equation (10) (Fortin and Dale, 2005; Bivand et al., 2008; Legendre and Fortin, 2010; Borcard et al., 2011). This index was applied to benthic meiofauna by Blanchard (1990) and Eckman and Thistle (1988) and to foraminifera by Hohenegger et al. (1993). This index calculates the similarity of pair values for one neighbourhood, a neighbourhood being defined by a weight ($w_{i,j}$) function of the distance (d) between pairs.

$$I(d) = \frac{\sum_{i,j}^{n} w_{i,j}(d)(x_i-\bar{x})(x_j-\bar{x})}{\sqrt{\sum_{i}^{n}(x_i-\bar{x})^2}} \times \frac{n}{\sum_{i,j}^{n} w_{i,j}(d)} \qquad (10)$$

Here, the cubes used for Moran's Index have neighbourhoods defined as cubes in direct contact (4 neighbours per sample with a weight of 1, others have 0, also known as "rook connectivity"; Fortin and Dale, 2005). With this configuration, Moran's Index is -1 for a contrasted organization (perfect negative correlation between neighbours) and +1 in case of grouped organization (perfect positive correlation between neighbours). A value close to zero ($I_0=(n-1)^{-1}$) corresponds to no organization or random distribution. The correlogram plots Moran's Index versus the order of the neighbours (o.n.). A decrease of the Moran's Index from positive to negative values characterizes a patchy distribution. The characteristic length of the patchiness is defined as the order of neighbours when $I_{o.n.}=0$ (Legendre and Fortin, 1989). Two dimensional non-random organization has been tested with the alternative hypothesis: $I_{o.n.}>I_0$. The second test examines if there is a preferential direction in the organization (isotropy). Again, the alternative hypothesis $I_{o.n.}>I_0$ for Moran's Index is used, restricting the distance to the tested dimension (vertical or horizontal). Thus, in our case, each sample was compared only with its lateral or vertical neighbours (i.e., 2 neighbours per test).

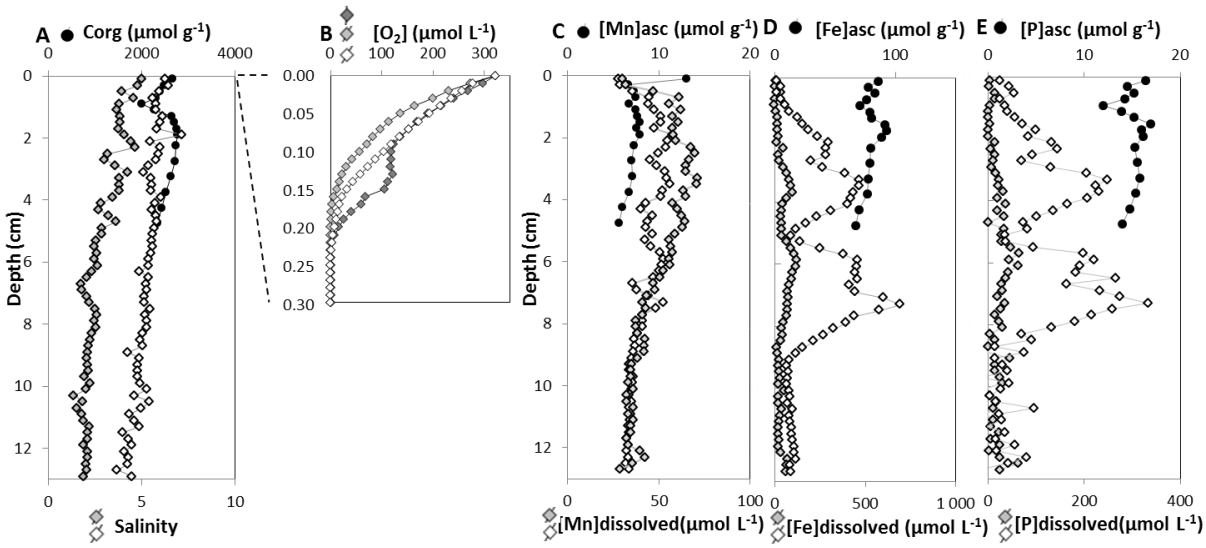

Figure 27 1D geochemical features. (a) Vertical profile of total solid organic carbon (filled circles, uncertainty smaller than symbol size) and profiles of salinity (white and grey diamonds). (b) Typical profiles of dissolved oxygen; the profile with dark-grey diamonds is considered bioturbated. (c, d, e) Vertical profiles of manganese (c), iron (d) and phosphorus (e) in dissolved (white and grey diamonds for DET replicates) and reactive solid phase (ascorbate-leached) from the core (black circles).

1.3 Results

1.3.1 1D geochemical features

Figure 27 shows both solid and dissolved chemical species obtained from the dedicated cores. Total organic carbon (C_{org}, black circles, Figure 27a) decreased from 2700 µmol (g dry sed)$^{-1}$ to 1900 µmol (g dry sed)$^{-1}$ in the first centimetre, then increased sharply until 1.5 cm depth, and finally decreased progressively from 2700 µmol g(dry sed)$^{-1}$ to 2400 µmol g(dry sed)$^{-1}$ at 5 cm depth. Salinity (Figure 27a) ranges from 7.5 to 1.7 with an offset of ~2 between replicates and a decrease of ~3 in the 13 first centimetres. Figure 27b shows the vertical distribution of dissolved oxygen. The three profiles shown (out of 18) are considered representative of the lateral variability in the sediment. Most of the oxygen concentration profiles show the exponential trend typical for undisturbed marine sediments (2 profiles in Figure 27b, with light grey and white diamonds; Revsbech et al., 1980; Berg et al., 1998). However, one third of the O_2 profiles diverged from the exponential model, showing an interruption of the decreasing trend, or even a local increase, at depth (e.g. the profile with dark grey diamonds represented in Figure 27B). The Oxygen Penetration Depth (OPD) remained relatively constant around 2.0 mm (sd=0.2 mm, n=18) despite this heterogeneity.

Figure 27c, d and e show the distribution of manganese, iron and phosphorus, respectively, both in the dissolved phase (grey and open diamonds) and in the easily reducible solid phases (black circles, extracted by ascorbate leaching (Anschutz et al., 2005; Hyacinthe et al., 2006). Extracted manganese (mainly (hydr)oxide, black circles in Figure 27c) showed a strong enrichment of the easily reducible solid phase (until 13 µmol g(dry sed)$^{-1}$) in the first two millimetres, where an important upward diminution was visible in both replicates of the dissolved phase (grey and open diamonds in Figure 27c). Below, the solid phase showed a slightly decrease from 7.9 to 5.6 µmol g(dry sed)$^{-1}$ until 5 cm depth. The dissolved manganese concentration decreased between 4 and 9 cm depth in both replicates (from 70 to 30 µmol L^{-1}). In the solid phase, iron, phosphorus and manganese are strongly correlated when the surface sample is not considered (r^2=0.70 and 0.55 between iron and manganese, and iron and phosphorus, respectively). Profiles of

dissolved iron and phosphorus are also strongly correlated (r^2=0.90, slope=1.87 and r^2=0.47, slope=1.31 for replicates A and B). Iron and phosphorus were remobilized, and therefore appeared in the dissolved phase, between 1 and 9 cm. Both replicates of dissolved iron showed the same four well-described maxima (at least six samples for each maximum) at 2.3, 3.3, 5.9 and 7.3 cm depth but with different concentrations. In replicate A (open diamonds) these maxima have five times higher iron concentrations (up to 700 µmol L^{-1}) than in replicate B.

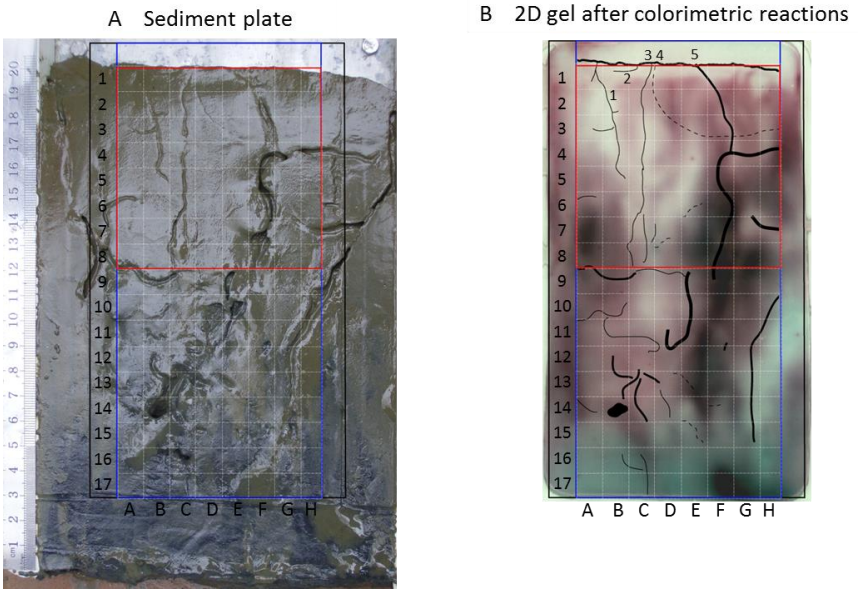

Figure 28 (a) Picture of the sediment plate before cube slicing for foraminiferal analysis (sediment–water interface at the top). (b) Picture of the analysed gel after colorimetric reactions: dissolved iron shown in dark pink and dissolved phosphorus in turquoise (burrows superimposed). The black rectangle corresponds to the gel limit, the blue rectangle to the limit of available data set of dissolved iron and phosphorus and the red rectangle to the limit of the available data set of foraminiferal distribution.

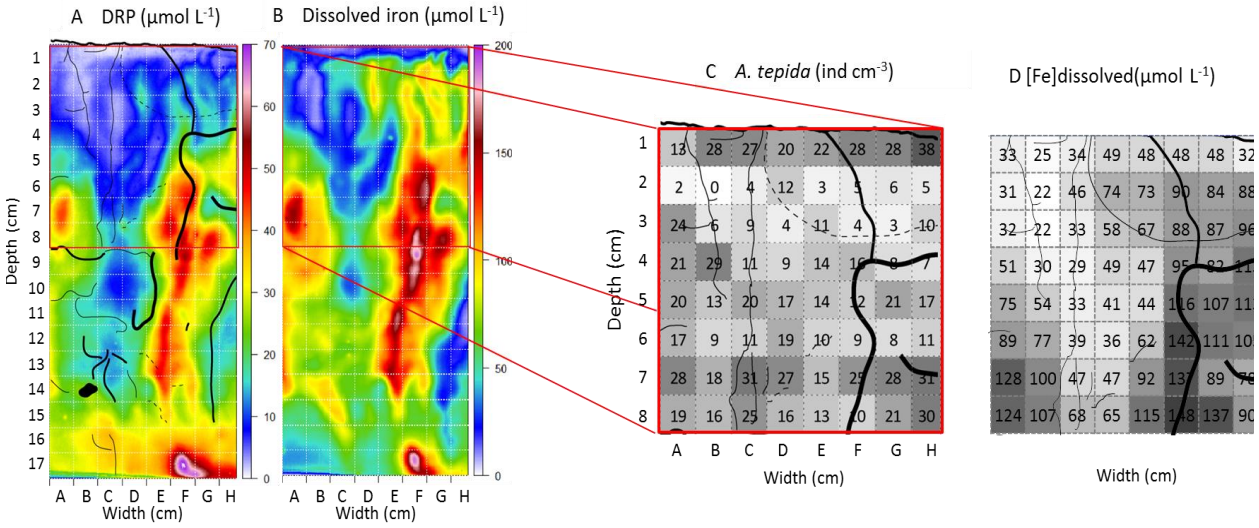

Figure 29 (a, b) Two-dimensional concentrations after numerical analysis of dissolved reactive phosphorus (DRP) and dissolved iron. The distribution of burrows is shown on the DRP plot. Red lines represent the boundary of foraminiferal analysis. (c-d) 2-D distribution of *A. tepida* densities and dissolved iron from the sediment plate with burrow distribution.

1.3.2 Visual features on the sediment plate

Figure 28a shows the sediment slice obtained from the "jaw device" facing the 2D DET gel. In order to facilitate the description, the figures were subdivided in centimetre squares labelled with letters for the horizontal position and numbers for the vertical position. The black rectangle corresponds to the 2D DET gel position, the blue rectangle to the gel signal exploited and the red rectangle to the 2D foraminiferal sampling. Burrows parallel to the cutting plane are visible over their entire length. When perpendicular to the cutting plane, they appear as a dark hole (B14 in Figure 28a). Figure 28b summarizes burrow distributions superimposed on a picture of the gel after equilibration with the colorimetric reagents (pink coloration corresponds to iron and blue to DRP). Five burrows were visibly connected to the sediment surface; their traces mostly extended vertically down to 10 cm depth where their track is lost. Between 10 and 15 cm depth, visible burrow density decreased. Below 15 cm depth, burrows were rarely observed and the sediment was dark (Figure 28a). During slicing of the sediment plate, living polychaetes (*Hediste diversicolor*) were observed in some burrows.

1.3.3 2D DET gel

Figure 29 shows the 2-dimensional datasets, with the distribution of dissolved phosphorus (Figure 29a) and iron (Figure 29b) obtained from the 2D DET gel. For comparison, burrow distribution is shown in Figure 29a. Dissolved iron and phosphorus both appeared a few millimetres below the sediment-water interface. They are positively correlated for the whole plate (r^2= 0.59, slope=2.7). Despite their patchy distribution, both species can be observed along the entire length of the gel probe (i.e. 17 cm depth). A main feature was the occurrence of two prominent vertical structures enriched in dissolved iron and phosphorus (A-B/6-9 and F-G/5-14). The highest concentrations, of about 170 and 50 µmol L^{-1} for iron and phosphorus, respectively, were found within the structure at the right (squares F/8-9). In the structure at the left (A/6-8), iron and phosphorus maxima were around 120 and 25 µmol L^{-1}, respectively.

Most burrows seem to impact the iron concentration. For example, burrows 1, 3 and 5 clearly correspond (in the 4 first centimetres) to a drastic decrease or even disappearance of dissolved iron, whereas other burrows seem to correspond to a dissolved iron enrichment (F-G/5-9). However, some centimetre size patches (e.g. A-B/6-9, H-G/8-9 and F-G/17) seem to be unrelated to burrow structures. Below 15 cm depth, the sediment was dark and dissolved iron generally decreased whereas DRP increased.

1.3.4 Living foraminiferal distribution

Figure 29c shows the distribution of CTG-labelled *A. tepida* determined for 1 cm^3 samples in the sediment facing the 2D DET gel. The analysis of living foraminifera in the 64 cubes (8 cm width * 8 cm depth) takes roughly the same time as the analysis of one core of 8.2 cm of diameter (until 5 cm depth). *Ammonia tepida* was by far the dominant species, accounting for 92% of the total assemblage. The second most frequent species, *Haynesina germanica*, represented 5% but its low density (mostly 0, 1 or 2 individuals per cubic centimetre) was not sufficient to support a reliable discussion. For this reason the data for this species are omitted from the present paper. *A. tepida* density ranged from 0 to 38 ind cm^{-3} with important lateral and vertical variability. The relative standard deviation (rsd) calculated for each row is, on average, 45%, whereas for each column the rsd is 60%, suggesting a slightly more pronounced vertical organization. This is confirmed by the stratification of the richest samples (≥27 ind cm^{-3}) which were found in the topmost cm and below 6 cm depth, whereas the poorest samples (≤ 5 ind cm^{-3}) were found between 1 and 3 cm depth. Each row from the 2D distribution can be represented by a whisker plot (Figure 30). The results confirm a three-step pattern with high densities at the surface (13 to 38 ind. cm^{-3}), lower density between 1 and 3 cm depth (0 to 12 ind cm^{-3} and one outlier at 24 ind cm^{-3}) and increasing values below 3 cm (7 to 31 ind cm^{-3}).

This vertical pattern is also visible in the two studied sediment cores: high densities of *A. tepida* (26 ± 0 ind cm^{-3}) are observed in the first 2 mm (Figure 30), a rapid decrease to minimal densities in the 1.0 - 1.2 cm layer (3 ± 0 ind cm^{-3}), followed by a progressive, somewhat irregular increase until 9 ± 0 ind cm^{-3} below 2 cm depth

to 8cm depth. Despite the different vertical sampling resolution, the densities observed in the cores are in agreement with the average densities observed in the sediment slice cubic samples.

1.4 Discussion

1.4.1 A methodological improvement to characterize heterogeneity

Here, we present for the first time a methodology allowing the simultaneous study of the vertical and horizontal heterogeneity of dissolved chemical species and living foraminifera (determined by CTG labelling) in the 8 first centimetres of the sediment. Figure 30 compares the vertical density distribution of *A. tepida* between the cores (triangles) and the jaw device (whisker plots), sampled a few decimetres apart. Despite the different vertical sampling resolution, the densities observed in the cores (sampling surface of 53 cm^2) are in agreement with the average densities observed in the sediment slice samples (sampled with the "jaw device", sampling surface of 8 cm^2). This similarity suggests a limited horizontal heterogeneity of *A. tepida* at a decimetre scale, although it is impossible to draw firm conclusions on the basis of only three samples (the two cores and the jaw device).

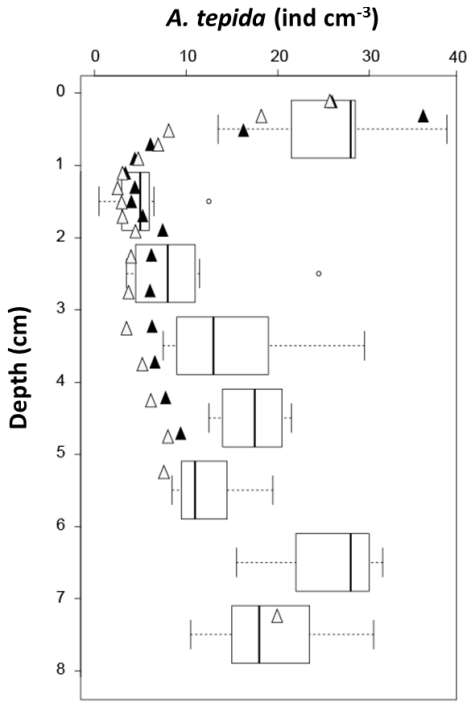

Figure 30 Vertical comparison of *A. tepida* densities from the two cores (filled and open triangles) and the "jaw device" sampling (each box plot represents the distribution of one layer; bars are first and third quartiles for the boxes length and whiskers are below 1.5 interquartiles; open circles are outliers).

The jaw device (boxplot whiskers, Figure 30) reveals a heterogeneous horizontal distribution at the centimetre scale. The centimetre scale heterogeneity is quantified by calculating the Moran's Index that estimates the characteristic length of foraminiferal niches. Figure 31 shows the Moran's Index correlograms applied between 3 and 8 cm depth (suboxic sediment) where high densities of living foraminifera were observed without evident spatial organization. Moran's Index (Figure 31A) reveals a patchy spatial organization of *A. tepida* at a centimetre scale (I_1=0.24, p-value=0.013). For farther neighbours the Moran's Index values drop to zero, describing a random organization. Concerning vertical and horizontal heterogeneities, Moran's index values for direct neighbours are 0.02 and 0.47, with p-values of 0.38 and 0.001, respectively. For second order neighbours, values do not significantly differ from 0 in either direction (data not shown). This means that *A. tepida* specimens tend to be grouped in horizontal spots with a characteristic length of 1-2 cm.

Figure 31b shows the Moran's Index correlogram for iron at 1cm scale resolution (phosphorus is similar and not shown). It shows strong patchiness (I_1=0.7) for direct neighbours in either direction, with a characteristic length of 3-4 cm. The fact that the characteristic lengths of *A. tepida* (Figure 31a) and dissolved iron (Figure 31b) patches are longer than 1 cm suggests that the impact of different sampling thicknesses (0.2 mm for dissolved iron against 1 cm for foraminifera) would not result in major bias. Moreover, this characteristic length is important as it likely corresponds to the characteristic length of the controlling mechanisms (Clark, 1985; Wu and Li, 2006). In fact, the difference in Moran's Index between chemical species and the *A. tepida* density distribution suggests that not exactly the same mechanisms control these parameters. This is an unexpected result, since most conceptual models explain benthic foraminiferal

distribution in the sediment as a direct response to geochemical gradients, especially oxygen and sulphide (Jorissen et al., 1998; Van der Zwaan et al., 1999; Fontanier et al., 2002; Langezaal et al., 2006; Langlet et al., 2013), that intimately control iron remobilization.

1.4.2 Factors generating chemical heterogeneity

The heterogeneity of geochemical patterns is mainly explained by the availability of oxidants mineralizing organic carbon. In the generally applied conceptual model of Froelich et al., (1979), organic matter remineralization is characterized by a succession of horizontal layers where specific oxidants are used. Figure 27 confirms this theoretical vertical stratification: oxygen is rapidly consumed by respiration (about 2 mm depth, Figure 27b); next, reduced dissolved manganese appears (Figure 27c). Dissolved iron appears still deeper, with a first maximum at 2 cm depth. The slopes of the concentration profiles are steeper and the reactive solid phase (Figure 27d and Figure 27c) is more concentrated for iron than for manganese, suggesting a higher reactivity. However, the strictly vertical succession of redox layers is no longer respected in the deeper suboxic layers, as suggested by the presence of multiple maxima of iron (Figure 27d) and by the high lateral heterogeneity observed in Figure 29a and Figure 29b. This high lateral heterogeneity cannot be explained by vertical diffusion of oxygen across sediment-water interface. It appears therefore that a strictly vertical stratification of redox zones, defining a similar foraminiferal microhabitat succession, is not a reasonable assumption, in our study area.

i. Macrofaunal impact on heterogeneity

Macrofauna are assumed to be the most important cause of chemical heterogeneity at a scale of 0.01cm (roughly the foraminiferal scale) to 100 cm (station scale), because of its ability to reorganize the sediment (Meysman et al., 2006; Kristensen et al., 2012). In this way, macrofauna determine whether other factors can impact the heterogeneity of dissolved iron and/or *A. tepida*. Macrofauna modifies: i) the sediment texture/composition (burrow walls or fecal pellets); ii) the redox conditions, by ventilation of their burrows with oxygenated water (bioirrigation) and iii) particle arrangement, by crawling or burrowing (biomixing; Meysman et al., 2006). The efficiency of biomixing to homogenize the sediment mainly depends on two aspects (see Wheatcroft et al., 1990; Meysman et al., 2010a for a more detailed discussion):

(1) The biomixing species assemblage. At the "Les Brillantes" mudflat, the main macrofaunal species are *Hediste diversicolor* (630 ind m^{-2}) and *Scrobicularia plana* (70 ind m^{-2}, I. Métais, pers. comm.). *H. diversicolor* is a gallery-diffusor (particle mixing due to burrowing activity) whereas *S. plana* is an epifaunal biodiffusor (particles are mixed in a random way over short distances along the surface; *e.g.*, François et al., 2002; Kristensen et al., 2012). These two species generate homogeneity or heterogeneity according to the second criterion. See below.

(2) The relation between the average time of existence of the studied objects (here foraminifera and dissolved iron) in the bioturbated area and the average time between two bioturbation events. Frequent bioturbation events generate efficient mixing (homogeneity) whereas rare bioturbation events generate heterogeneity. The average time between two bioturbation events is estimated to days to months by tracer modelling (Wheatcroft et al., 1990; Meysman et al., 2003a, 2008a) while the longevity of foraminifera in suboxic environments is estimated to roughly one year (Langlet et al., 2013; Nardelli et al., 2014). The mean residence time of iron in the dissolved phase is estimated between 2 and 3 days (Chapter 1.3). Therefore, biomixing should generate a homogeneous distribution of foraminiferal density distribution, contrasting with a heterogeneous distribution of dissolved iron (and DRP). The different timespans also suggest that most of the living foraminifera were already present in the suboxic sediment before the visible (most recent) burrows were created. Conversely, the heterogeneity of the dissolved chemical species should be directly related to biomixing and to other factors that have not been homogenised by biomixing *i. e.* with a short time of existence in suboxic environments.

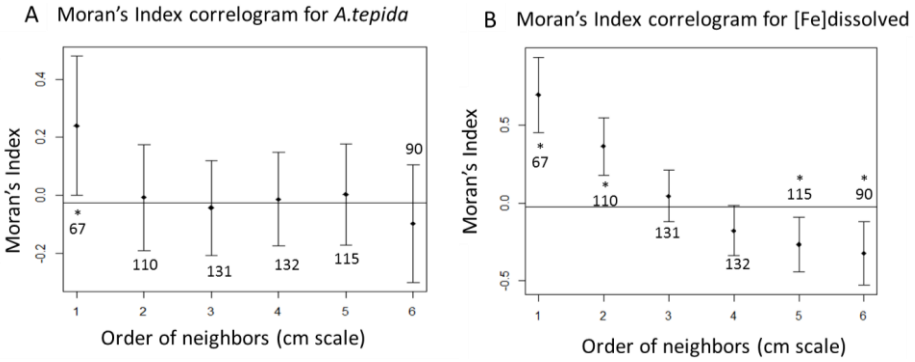

Figure 31 Moran's index correlograms for 3 to 8 cm depth. (a) Moran's index correlogram for *A. tepida* with a 1 cm resolution. (b) Moran's index correlogram for [Fe]dissolved with a 1 cm resolution. An asterisk indicates significant differences from zero; error bars are twice the standard deviation. The numbers are the number of pairs for each order of neighbours.

ii. Geochemical impact of biogenic factors

The factors likely to generate chemical heterogeneity are : (1) Bioirrigation, that mainly causes an increase of oxidant availability (Aller and Aller, 1986; Aller, 2004; Arndt et al., 2013), and (2) Biogenic particles (*e.g.* decaying macrofauna, fecal pellets), that cause an increase of labile carbon availability. Dissolved iron shows two opposite types of behaviour (Aller, 1982): (1) iron precipitates as a hydroxide when the oxidative state of the pore water surrounding active burrows increases (Meyers et al., 1987; Zorn et al., 2006; Meysman et al., 2010b). This is confirmed by visible burrows in Figure 29 in which both dissolved iron and DRP are depleted (Figure 28, numbers 1, 3, 5 (above 6cm depth) and burrows in B-C-D13, E9-11,G-H10-15 and A-B9). These structures are mainly vertical and have a length often exceeding 3 cm, in agreement with the Moran's Index correlogram. Conversely, within the long burrow F-G/5-9, dissolved iron is enriched, indicating that this burrow is abandoned and no oxygen renewal occurs. This feature was also observed for some burrows by Zhu and Aller (2012) and Cesbron et al. (2014). (2) Dissolved iron is produced by anaerobic respiration where biogenic particles increase labile carbon availability, and thereby decrease the oxidative state of surrounding pore waters (Robertson et al., 2009; Stockdale et al., 2010). The geometry and isolation from visible burrows of patches A/7-8, G-H/8-9 and F-G17 in Figure 29a and Figure 29b suggest that they could represent centimetre-wide labile organic matter patches. We hypothesize that these patches correspond to intense remineralization of biogenic particles that dissolve iron oxides.

1.4.3 Mechanisms controlling the *A. tepida* distribution

Figure 29c and Figure 30 clearly describe a three-step pattern in the distribution of *A. tepida*, with high densities at the surface, low densities between 1 and 3 cm depth and a somewhat surprising increase below (in suboxic sediments). A similar pattern was reported, but not discussed, for other intertidal environments (Alve and Murray, 2001; Bouchet et al., 2009). In our study, the consistency of the 8 vertical columns from the plate sampling confirms the robustness of this pattern and the two dimensional approach reveals an organization of *A.tepida* in 1-2 cm patches in the suboxic sediment. The next subchapters discuss possible mechanisms that could explain these features, especially in the suboxic environment where active burrows (supporting biomixing and bioirrigation) and biogenic particles have been identified as factors likely to generate such heterogeneity.

i. Foraminiferal metabolism

Generally, aerobic metabolism is considered as the dominant mechanism in oxic conditions since it is energetically most efficient. In fact, Figure 29c and Figure 30 clearly describe maximal densities of *A. tepida* at the sediment surface (0-2 mm depth) and low densities below (6-18 mm depth). This strong gradient of *A. tepida* density highlights the presence of a continuously oxygenated microhabitat enriched in organic matter (see TOC and O_2 profiles, Figure 27a and Figure 27b) close to the sediment-water interface, favourable for *A. tepida*. Energetic considerations and

some observations that report a strong seasonal variability in the oxic zone (Moodley, 1990; Barmawidjaja et al., 1992), led to assume that foraminifera reproduce preferentially in the oxic layer (de Stigter et al., 1999; Berkeley et al., 2007). Together, these factors explain the maximum density in the surface layer.

Since the work of Richter (1961), numerous publications have reported living benthic foraminifera in suboxic sediment layers (Jorissen et al., 1992; Moodley and Hess, 1992; Bernhard and Sen Gupta, 1999). For intertidal environments, studies have reported living (Rose Bengal stain) foraminifera in subsurface environments since the 1960's (*e. g*. Buzas, 1965, Steineck and Bergstein, 1979). Several *in situ* (Goldstein et al., 1995; Bouchet et al., 2009) and laboratory studies (Moodley and Hess, 1992; Moodley et al., 1998; Pucci et al., 2009; Nardelli et al., 2014; Nomaki et al., 2014) with *A. tepida* also reported survival, activity and even calcification in suboxic conditions. Anaerobic metabolism would be a logical mechanism to explain the presence of large amounts of living foraminifera in suboxic layers. Complete or partial (with endo and/or ectobionts; Bernhard and Alve, 1996) denitrification co-occurring with nitrate storage has been demonstrated for some foraminiferal taxa (Risgaard-Petersen et al., 2006). Nomaki et al. (2014) have suggested denitrification by endobionts for *A. tepida*. However, denitrification has not been measured in *A. tepida*, and only very low intracellular nitrate concentrations were found (Piña-Ochoa et al., 2010; Geslin et al., 2014). It appears therefore unlikely that the abundance of living *A.tepida* in deeper suboxic layers can be explained by active colonization.

ii. Burying and burrow microenvironment

It is clear that biomixing is a likely mechanism to explain the introduction of foraminifera in deeper sediment layers, by passive transport (Alve and Bernhard, 1995; Goldstein et al., 1995; Moodley et al., 1998; Saffert and Thomas, 1998; Jorissen, 1999; Alve and Murray, 2001). However, the spatial distribution resulting from this passive transport has never been well described, or modelled. According to the theory of biomixing, we suggest that the vertical distribution of *A. tepida* can be approached by a diffusion model, which should lead to an exponential downward decrease, with the slope as a function of the mortality rate. Possibly, *A. tepida* is able to survive in suboxic environments using an intermittent aerobic metabolism, using the oxygen that can be punctually available due to bioirrigation (Fenchel, 1996; Wang et al., 2001; Wenzhofer and Glud, 2004; Pischedda et al., 2012). Their activity should progressively decrease once oxygen is depleted; Phipps (2012) suggested that they could finally be immobilized before dying in case of a prolonged absence of oxygen supply. We think that repeated introductions by macrofaunal bioturbation, followed by reduced metabolic activity, leading to immobilisation, is the most likely mechanism to explain the high abundances of living *A. tepida* in suboxic sediments.

Figure 28a and Figure 29b show no relation between visible burrows and living *A. tepida*. This result is in agreement with the different time-scales of the foraminiferal lifespan and the burrows, and with the idea that biomixing homogenizes the *A. tepida* density. It suggests also that the oxygenation obviously generated by formation of new burrows is consumed too fast to allow all infaunal *A. tepida* to migrate to these active burrows. Thus, recent burrow walls are apparently not colonized by specimens of *A. tepida* already present in the suboxic sediment. Our observations contrast with earlier studies, showing increased foraminiferal densities (up to 300 times higher than in the surrounding sediment, rose Bengal staining) in burrow walls. For example, data from burrows of *Amphicteis* sp. at 4800m depth (Aller and Aller, 1986), of *Echiurus echiurus* at 42m depth (Thomsen and Altenbach, 1993) and of *Pestarella tyrrhena* in intertidal sandflats (Koller et al., 2006) all presented high foraminiferal densities. The observed differences could be due to the fact that burrows of various macrofaunal taxa may represent very different environmental conditions and eventually due to a difference in sampling scale, since Thomsen and Altenbach (1993) and Koller et al. (2006) applied an irregular millimetre sampling around burrows. Summarizing, macrofaunal activity would explain transport to and survival in suboxic layers. However, it does not explain the density minimum at 1-3 cm depth.

iii. Sensitivity to geochemical gradients

We think that the most probable explanation for the 1-3 cm density minimum of *A. tepida* is an active upward migration of the specimens, back to the sediment surface, before they are completely immobilized by a lack of oxygen and a strongly lowered metabolism. Numerous studies have already reported that vertical migration of foraminifera allows them to move to more hospitable environments (Jorissen, 1988; Van der Zwaan and Jorissen, 1991; Alve and Bernhard, 1995; Moodley et al., 1998; Gross, 2000; Langezaal et al., 2003; Geslin et al., 2004; Ernst et al., 2005). In an experiment in which populations of *Haynesina germanica* were uniformly mixed in a 6 cm sediment column, Ernst et al. (2006) saw a clear migration back to the surface for the foraminifera living between 1 and 3 cm depth, and suggested that foraminifera living at greater depth were unable to do so. Similarly, Hess et al. (2013) showed that benthic foraminifera are able to migrate through suboxic sediment to reach oxic sediments over a maximal distance of a few centimetres. Active migration towards directly detected oxygen or organic matter over distances beyond 1 cm seems improbable, since this distance is much higher than the typical pseudopodial length (about 1 cm, see Travis and Bowser, 1991). However, as described above, the presence of oxygen could be indirectly detected by other geochemical gradients (*e.g.* NO_3^-, Mn^{2+} or Fe^{2+}, dissolved organic carbon, pCO_2). However, when gradients generated by the oxygen front are imperceptible for *A. tepida*, because they are living too deep in the sediment, or when such gradients are hidden by other sources of geochemical gradients (as organic-rich patches), this upward migration could no longer occur. This could explain why below 3 cm depth, *A. tepida* remains in the deeper sediment layer after being transported there accidentally.

However, the organization of the foraminifera in 1-2 cm wide horizontal patches identified by Moran's Index suggests that *A. tepida* detects not only vertical geochemical gradients, but probably also lateral gradients around degrading biogenic particles. The characteristic length of patches corresponding to biogenic particles identified by dissolved iron maxima

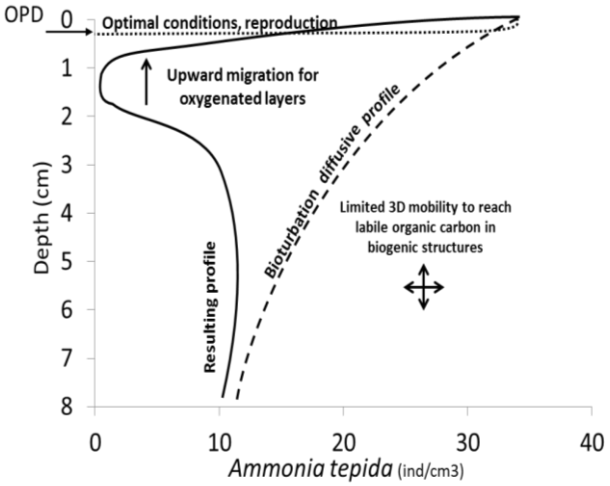

Figure 32 Putative mechanisms explaining the *A. tepida* density profile (OPD: oxygen penetration depth).

(A/7-8, G-H/8-9 and F-G17 in Figure 29b, see §1.4.2ii) is in agreement with the characteristic length of foraminiferal density maxima. For instance, in the 8 first centimetres, the two identified biogenic particle patches (A/7-8, G-H/8-9 in Figure 29b) both correspond to a higher density of *A. tepida* (28-19 and 21-30 ind cm^{-3} respectively; Figure 29c). In agreement with these results and despite a lowered metabolism, we hypothesize that foraminifera could move towards patches of labile organic matter even in deeper suboxic layers. Nevertheless, a better identification of labile carbon patches, replicate sampling with the here-developed strategy and experimental studies with artificial geochemical gradients are necessary to confirm our hypotheses about the behaviour of *A. tepida* in suboxic environments.

Summarizing, we suggest that the distribution of *A. tepida* can be interpreted as the result of not less than five interacting mechanisms (Figure 32). 1) high foraminiferal densities at the surface are the result of the presence of abundant labile organic matter and reproduction in the oxygenated layer (§1.4.3.i), 2) downward transport by macrofaunal biomixing introduces living *A. tepida* in deeper sediment layers (§1.4.3.ii), 3) in the 3 first centimetres foraminifera are capable to migrate back to the oxygenated, organic-rich surface layers once they detect redox gradients, whereas in deeper sediment layers, *A. tepida* are no longer capable to find their way back to the superficial oxygenated layer (§1.4.3.iii), 4) after a prolonged

presence in suboxic conditions, *A. tepida* lower their metabolism and become inactive, 5) foraminifera can be temporarily re-mobilized during intermittent bioirrigation events, and can eventually migrate towards organic-rich microenvironments in their vicinity (§1.4.3.iii). A better identification of labile carbon patches, for example based on alkalinity (Bennett et al., 2015), pCO_2 (Zhu et al., 2006; Zhu and Aller, 2010) or dissolved organic carbon would permit to go further about the role of microenvironments for *A. tepida* distribution.

1.5 Conclusion

We present a new, simple and robust sampling protocol, to obtain the 2D distribution of benthic foraminifera combined with the 2D distribution of geochemical species, here dissolved iron and phosphorus. This technique allows visual observation of burrow features. Geochemical features allowed us to recognise active burrows (with minimal dissolved concentrations), and to determine that areas of dissolved iron and phosphorus enrichment do not always represent abandoned burrows. Our observations on an estuarine mudflat showed an important density of *A. tepida* in suboxic environments with a characteristic length of patches of 1 to 2 cm. Surprisingly, no direct relation was found between active burrows and the *A. tepida* distribution. However, an enrichment of *A.tepida* was observed in some areas where dissimilatory iron reduction was intense, suggesting that even in suboxic environments, there is a relation between the spatial distribution of *A. tepida* and labile organic matter remineralisation. Our results show that the new sampling strategy proposed here can yield important new insights in the functioning of suboxic environments in estuarine mudflats.

Acknowledgements

This study is part of the RS2E – OSUNA project funded by the Région Pays de la Loire. Special thanks are due to Didier Jézéquel from IPGP who designed the « jaw device". Thanks to Clement Chauvin, Cyrille Guindir, Hélène Koroshidi and Eve Chauveau for their support in the field and laboratory. We thank the three editorial reviewers whose comments inspired us to improve our manuscript.

Partie 1 :

2 Imagerie simultanée de nitrite et nitrate à l'échelle millimétrique à travers l'interface eau-sédiment

---

E. Metzger[1], A. Thibault de Chanvalon[1,2], F. Cesbron[1, 3], A. Barbe[1], P. Launeau[1], D. Jézéquel[5], A. Mouret[1]

[1] Université d'Angers, LPG-BIAF, UMR CNRS 6112, 49045 Angers Cedex, France
[2] Ifremer, LBCM, Rue de l'Ile d'Yeu, 44300 Nantes, France
[3] University of West Florida, CEDB, 11000 University Parkway, Pensacola, FL 32514 USA
[4] Université de Nantes, LPG-N, UMR CNRS 6112, 44322 Nantes, France
[5] Institut de Physique du Globe de Paris, Sorbonne Paris Cité, Univ. Paris Diderot, UMR 7154 CNRS, 75005 Paris, France

Article soumis dans Environmental Science and Technology

Edited by: Xiang-dong Li

ABSTRACT

The present study describes new procedures to obtain at sub-millimeter resolution the spatial distribution of nitrite and nitrate in pore waters, combining diffusive equilibrium in thin films (DET), colorimetry and hyperspectral imagery. Nitrite distribution can be easily achieved by adapting the well-known colorimetric method from Griess (1879) and using a common flatbed scanner with a limit of detection about 1.7 µmol L^{-1}. Nitrate distribution can be obtained after reduction into nitrite by a vanadium chloride reagent. However, the concentration of vanadium chloride used in this protocol brings coloration with a wide spectral signature that creates interference that can only be removed by imaging treatment from an entire visible spectrum for each pixel (spectral analysis). This can be achieved only by hyperspectral imaging. The protocol retained in the present study allows obtaining a nitrite/nitrate image with micromolar limit of detection. The methods were applied in sediments from the Loire Estuary after different treatments and allowed to precisely describe two-dimensional millimeter features. The present technique adds to the combination of gel-colorimetry and hyperspectral imagery a very promising new application of wide interest for environmental issues in the context of early diagenesis and benthic fluxes.

RESUME

Cette étude décrit de nouveaux protocoles permettant d'obtenir à une résolution submillimétrique la distribution spatiale des nitrites et des nitrates dans l'eau interstitielle. Ces protocoles s'appuient sur un échantillonnage par DET (Diffusive Equilibrium in Thin film) et une analyse par colorimétrie et imagerie hyperspectrale. La distribution des nitrites peut être facilement obtenue par la méthode de Griess (1879) en utilisant un scanner commercial ; la limite de détection est alors de 1,7 µmol.kg^{-1}. La distribution en nitrate peut être obtenue après réduction en nitrite à l'aide d'un réactif de chlorure de vanadium. Cependant, la concentration de chlorure de vanadium utilisée dans ce protocole produit une coloration avec un large spectre d'absorbance ce qui créé une interférence ne pouvant être levée qu'à l'aide d'un traitement d'image basé sur l'analyse de la totalité du spectre visible pour chaque pixel (analyse spectrale). Ce qui ne peut être réalisé qu'à l'aide de l'imagerie hyperspectrale. Le protocole présenté dans cette étude permet d'obtenir deux images : une de la distribution en nitrate et une de la distribution en nitrite avec des limites de détection micromolaires. Les protocoles ont été appliqués sur du sédiment de l'estuaire de la Loire après différents traitements et ont permis de mettre en évidence des environnements millimétriques enrichis en nitrate en deux dimensions. Ce protocole correspond à une nouvelle application des techniques de colorimétrie sur gel et de caméra hyperspectrale permettant d'appréhender de nombreuses problématiques environnementales notamment liées à la diagenèse précoce et à l'estimation des flux benthiques.

2 Simultaneous nitrite/nitrate imagery at submillimeter scale through the water-sediment interface

2.1 Introduction

Combination of diffusive equilibrium in thin film gel techniques (DET; Davison et al., 1991) and spectrophotometry allows theoretically to reach speciation of nutrients, completing the set of tools existing for porewater chemistry at millimeter and sub-millimeter resolution. However, the main limitation of the combination of colorimetry and gel techniques is the limit of detection (LOD) induced by very small samples (below 100 µL) and subsequent dilution that is required to get sufficient volume for analytical purposes (Koschorreck et al., 2003; Monbet et al., 2008; Metzger et al., 2013). Only miniaturization and sensibility increase of analytical devices permit to overcome this limitation (*e.g.* nanodrop coupled with microplates). This is why most studies combine DET gel sampling with total elementary analyses such as ICP-MS or GF-AAS (Stockdale et al., 2009). Few studies have combined DET sampling with ion chromatography to determine sulfate and nitrate concentrations (Shuttleworth et al., 1999; Mortimer et al., 2002; Krause et al., 2013). In these works, the gel of the DET probe was cut into strips corresponding to a resolution of 2 to 20 mm. This generated at lot of samples to process and represents a time-consuming method, to finally obtain a 1D profile with a rather low resolution. Another alternative to remove such limitation was to generate an image of the distribution of dissolved compounds within the gel by direct contact of the DET gel with a reagent, either contained in another reactive gel (Jézéquel et al., 2007; Robertson et al., 2008) or in a solution (Pagès et al., 2011). Although simple and fast this approach has an important limitation in the case of slow color development: (1) a rapid and uncontrolled back-diffusion of chemicals into the reagent gel or solution, before coloring reaction, combined with lateral diffusion within the probe gel, that forbids any modeling for recalculation of 2D features using kinetics-transport modeling (Jézéquel et al., 2007; Robertson et al., 2008). Such limitation is less important for fast-kinetic reactions such as for iron and alkalinity, which develop coloration in a short time (<1 min.); (2) a need for a rapid processing that generates important handling, forbids postponing analysis and limits the number of probes to be processed. Recent studies (Cesbron et al., 2014; Thibault de Chanvalon et al., 2015a) showed the possibility to freeze gel probes allowing further analysis and almost no limit to the number of probe deployment. However, the major input of these studies was the use of a hyperspectral camera allowing a better sensitivity and a higher spectral resolution (few nanometers instead of few hundred from a RGB image). A spectrum for each pixel allows different post acquisition treatments allowing separation of different contributors to the image at a pixel scale. Cesbron et al. (2014) proposed a method to simultaneously analyze dissolved iron and reactive phosphorous. This is an excellent alternative to probes built with different layers of gel (Pagès et al., 2011) each one being dedicated to one chemistry that need handling skills and do not guarantee a perfect match of the different images (*i.e.* distortion of the gel, gap between images).

As mentioned above, nitrate profiles obtained with gel techniques are limited by LOD of ion chromatography and elution of gel into a solution that significantly dilutes chemicals. For this reason, nitrite is rarely detected and only nitrate quantification can be done. The development of a nitrate probe as a microelectrode by a Danish group in early 2000 (Larsen et al., 2000; Revsbech and Glud, 2009) brought an alternative to perform high-resolution profiling within the sediment at high-resolution (100 µm). Despite an attempt of commercialization by Unisense, only researchers from the original group were able to perform such profiles. Achieving high-resolution profiles of nitrite and nitrate resolution, as shown by several authors, is of major importance to quantify benthic diffusive fluxes and to investigate new reactional pathways for nitrogen transformations within the sediment that is affected by bioturbation. However, at the scale of a microenvironment (burrow wall, root apex, etc…), only multi-species high-resolution

profiles and/or 2D distribution can achieve correlations between chemical species despite high spatial heterogeneity. The recent publication of a method of nitrate reduction using a solution of vanadium chloride (García-Robledo et al., 2014; Schnetger and Lehners, 2014) allow us to examine the possibility to propose a colorimetric protocol for simultaneous nitrite and nitrate determination combining gel sampling, colorimetry and a 2 dimensional image acquisition. Firstly, the present study aims to transpose the famous Griess reaction (Griess, 1879) to gel technique in order to obtain a nitrite image of pore water in a sedimentary setting at a sub-millimeter resolution. Secondly, we examine the possibility to revisit the procedure using vanadium chloride as a nitrate reducer in order to achieve a nitrite/nitrate 2D probe that could successfully be deployed within the sediment.

2.2 Experimental Chapter

2.2.1 Principle of the method

A polyacrylamide gel probe is prepared (polymerized, rinsed and degassed) and deployed within the sediment until diffusional equilibrium with pore water solutes (including NO_2^- and NO_3^-) is reached.

A first reagent gel is prepared, containing the Griess reagent (Griess, 1879; Bratton et al., 1939): the coloring reagent gel, allowing specifically the nitrite determination. A second reagent gel is prepared using vanadium chloride: the reducing reagent gel that reduces nitrate into nitrite, allowing nitrate determination. The probe gel is laid down onto the first coloring reagent gel in order to obtain an image of nitrite distribution as variations of pink coloration over the gel assemblage.

An imagery device allows the digitalization of the colored image (flatbed scanner for nitrite imagery alone, or hyperspectral camera for both nitrite and nitrate determinations).

In order to obtain the nitrate distribution over the gel, the reducing reagent gel is added to the two-layer assemblage after the first digitalization for nitrite. A second digitalization is operated on the three-layer assemblage and the subtraction of signals between both images is performed for each pixel in order to obtain the nitrate contribution over the gel probe.

2.2.2 2D gel probe preparation and deployment

The probe is a polyacrylamide hydrogel mounted on a polycarbonate plate (250 mm high, 150 mm wide and 3 mm thick). The plate has a central depression of 1 mm depth (180 × 97 mm, length × width) that holds the hydrogel keeping the probe tight (Cesbron et al., 2014) The gel is maintained and protected from sediment by a PVDF hydrophilic membrane (0.2 µm, Durapore®) taped on the plate using a PVC adhesive tape (Annexe 4). The gel is a polyacrylamide DET gel prepared according to Jézéquel *et al*. (2007) adapted from Zhang and Davison (1999). In brief, a mixture of acrylamide (30%, Roth), bisacrylamide (2%, Roth), TEMED (Roth) as a catalyzer and ammonium persulfate (APS; 1%, Sigma-Aldrich) as a polymerization initiator, is cast between two plates separated by a spacer. Polymerization occurred after *ca*. 15 min. at room temperature. The gel is rinsed and stored in deionized water (Millipore Milli-Q® system) until use. Before hydration, thickness of the gel is 0.92 mm but reaches about 1mm after 1h hydration. In order to avoid oxygen contamination of anoxic sediment during probe deployment, the probe is deoxygenated by nitrogen bubbling in deionized water (Millipore Milli-Q® system) at least 5 h before deployment. Probes were deployed into sediment for 5 hours allowing equilibration (Pagès et al., 2011).

2.2.3 Reagent gels preparation

Reagent gels are 0.46 mm-thick (0.5 mm after hydration), polyacrylamide hydrogels with the same composition as probe gels (Zhang and Davison, 1999). After polymerization, reagent gels are equilibrated during at least 30 min with 50 mL of a reagent solution in a plastic bag. The coloring reagent solution contains 0.07% sulfanilamide (Roth), 0.01 % N-1-naphthylethylenediamine dihydrochloride (NEDD) (Roth) and 0.14 % HCl (Roth) in Milli-Q® water (uncolored solution). The reducing reagent gel is equilibrated with 50 mL of a vanadium chloride solution (VCl_3 (Sigma Aldrich) 2.9 % (w/v), HCl 1.8 %

(w/v) from a 30% suprapur acid (Roth)). This gel is colored green by the vanadium salt.

2.2.4 Standards gel preparation

The standard gel is prepared by diffusion of standard solutions into a 1-mm thick gel similar to the probe gel (Cesbron et al., 2014): the gel is placed onto a *Plexiglas*® plate and covered by a second *Plexiglas*® plate with 7 circular wells (2.1 cm i.d.) drilled into it. Each well is equipped with a cylindrical tube representing a 5 mL vial when put onto the gel (the base of each cylinder overhangs slightly from the Plexiglas® plate in order to be pressed onto the gel). The Plexiglas® plates are tightened together with 8 small clamps, ensuring sufficient pressure on the gel to avoid leakage of standard solutions. A volume of 3.5 mL of each standard solution was poured into a well and incubated during 1 h in order to ensure diffusive equilibration. Nitrate and nitrite standard solutions were prepared from $NaNO_3$ and $NaNO_2$ salts respectively (Fluka).

2.2.5 Gel assemblage mounting and colorimetric reaction

After equilibration, the coloring reagent gel is removed from the bag and quickly drained before being laid down onto a white plate. Residual drops are gently wiped and the probe gel is laid onto it. The whole assemblage is covered by a cellulose acetate film that protects against evaporation, then scanned after 15 min, the necessary time for the NEDD to react with nitrite and form the so-called pink Azo dye revealing the 2D nitrite distribution.

To reduce nitrate, the cellulose acetate film is carefully removed from the double layer gel assemblage (*i.e*. probe + nitrite reagent gels) and a nitrate reducing gel is laid on top of it. The three-layer gel assemblage is then covered by a clean cellulose acetate film and incubated for 20 min in a 50°C oven under water-saturated atmosphere. This heating step is crucial for accelerating the kinetics of nitrate reduction. At that point, the produced nitrite has reacted with the Griess reagent and the three-layer gel can be scanned at its turn. The calibration gel is processed like the *in situ* gel probe.

Two calibration gels (one from nitrate solutions and one from nitrite solutions) are necessary for estimating the efficiency of nitrate reduction. In order to save time and guarantee comparable conditions, both nitrite and nitrate calibration gels (two strips) are laid side-by-side onto the same reagent gels to be processed together. We also recommend preparing a solution with both nitrate and nitrite for quality control. Solutions ranged between 1.5 and 40 µmol L^{-1} in either NO_2^- or NO_3^-. Linear range of the color intensity towards concentration can be extended using thinner probe or standard gels (*e.g.* 0.5 instead of 1.0 mm). Hence, thinner gels reduce the optical path, resulting in weaker color intensities. As a consequence, the saturation concentration increases but LOD increases as well.

2.2.6 2D imagery methods

i. Nitrite imagery from commercial flatbed scanner

To obtain only nitrite distribution, a commercial flatbed scanner (Canon Canoscan LiDE 600F) was used. From scanned images, intensity of colored zones of the 2D probe was processed by ImageJ® software. Images were decomposed into primary color intensities (red, green and blue (RGB), at about 100 nm wavelength resolution), each being converted to a gray-scale image (Jézéquel et al., 2007). The green color intensity was found to give the most sensitive response, since the nitrite-reagent compound (Azo dye) is pink.

ii. Hyperspectral data acquisition and treatment for nitrite/nitrate mapping

This procedure does not require any specific equipment but does not allow simultaneous quantification of nitrite and nitrate because of the dark green coloration of the reducing reagent and its spectral signature prevents the pink Azo dye to be read. When simultaneous nitrate and nitrite distributions are sought, both nitrite and nitrite+nitrate images have to be obtained with a hyperspectral camera (here, a HySpex VNIR 1600) that has a sufficient wavelength resolution to separate signals coming from different layers of colored gel. The camera has 160 channels, covering the spectral range from 400 nm to 900 nm, with a spectral resolution of 4.5 nm and a sampling interval of 3.7 nm

allowing the analysis of a continuing spectrum. The acquisition time was 2 minutes. The flat assembly gel probe + reactive complex + transparent film was laid down on a Spectralon® plate and then scanned in front of the camera and under controlled halogen light source. The camera was set up in the laboratory to scan samples with square pixels providing a spatial resolution of about 190×190 µm per pixel (camera about 1m above samples).

According to Cesbron et al. (2014) we assume that reflectance spectra are the result of an intimate mixing of colored reagents within a transparent gel. Therefore it is possible to decompose each pixel into different end-members according to their spectra. The decomposition of each pixel is calculated as a linear combination of the logarithm of the different end-member spectra using ENVI® software (unmixing function). In the present study, 3 end-member spectra are considered: (1) the spectral background which corresponds to a Spectralon® plate + the two- or three-layer 2D gel (for respectively the first and the second scan); (2) a spectral nitrite end-member from the highest nitrite concentration of the calibration gel and (3) the spectrum corresponding to the vanadium(III) green coloration obtained from a nitrite-free part of the calibration gel. This unmixing procedure is applied to the calibration gel for signal linearity checking as concentration increases and to the probe gel for NO_2^- and VCl_3 signals separation.

2.2.7 Validation of the method

i. Validation of nitrite/nitrate separation

To ensure a complete separation of signal from nitrite and from nitrate, nitrate and nitrite calibration standards were performed with two composite standards containing both species. The double standard gel (made of two strips, one for each chemical species) is laid onto the Griess reagent gel. At the first stage of the treatment, only the set of circles corresponding to the nitrite standard gel is supposed to turn pink. Obviously, the nitrite + nitrate composite circle would become as pink as its corresponding nitrite concentration enables it.

Once the assemblage is scanned by the hyperspectral camera, the VCl_3 reducing reagent gel is added and the new assemblage goes into the oven as described above (section 2.2.5). After 20 minutes, a new scanning is performed and reduced nitrate into nitrite appears pink. It is important to note that the VCl_3 reducing reagent gel is dark green and low intensity pink is not visible with naked eyes.

After unmixing calculation (§2.2.6.ii), nitrite reflectance from both images can be achieved (*i.e.* before and after addition of the dark green VCl_3 reducing agent gel). From the second image (with the VCl_3 reducing reagent gel) a nitrite + newly produced nitrite image is obtained. From the literature (Schnetger and Lehners, 2014), it is known that 20 min at 50°C is too short to achieve a complete reduction but a longer incubation time will affect the distribution of nitrate because of lateral diffusion (*i.e.* there is a competition between reduction kinetics and loss of signal by diffusion, see below). The comparison of standard curve slopes between nitrite and nitrate standards allows quantifying the efficiency of nitrate reduction into nitrite for each set of experiments and therefore calculation of nitrate concentration.

Summarizing, the first image is used for direct nitrite standardization while the second is used to quantify nitrate reduction efficiency and therefore to quantify the sum of nitrite and the part of nitrate that was reduced during the experience. The same two-step procedure is applied to the probe gel.

The quantification of nitrite on the probe gel (two-layer gel) is for each pixel:

$$[NO_2^-] = slope_{nitrite} \times R_{nitrite} \quad (11)$$

where $slope_{nitrite}$ is the slope of the nitrite standard curve of the first image (without VCl_3 gel); $R_{nitrite}$ is the reflectance of the assembled probe gel before addition of the VCl_3 gel.

The quantification of nitrate on the probe gel (three-layer gel) will be for each pixel:

$$[NO_3^-] = [(slope_{nitrite}^{VCl3} \times R_{VCl3}) - [NO_2^-]] \times slope_{nitrite}^{VCl3}/slope_{nitrate}^{VCl3} \quad (12)$$

where $slope_{nitrite}^{VCl3}$ is the slope of the nitrite standard curve of the second image (with VCl_3 gel); R_{VCl3} is the reflectance of the assembled probe gel after addition of the VCl_3 gel; $slope_{nitrate}^{VCl3}$ is the slope of the nitrate standard curve; $[NO_2^-]$ is the concentration of nitrite for each pixel after standardization of the assembled probe gel before addition of the VCl_3 gel.

ii. Validation of the method for sediment

A series of laboratory experiments using estuarine sediment was realized in order to test the nitrite/nitrate method on more realistic conditions. Sediment was sampled in the Brillantes mudflat from the River Loire estuary (47°16'56.00"N 2° 3'47.00"W). The sediment is mainly composed of silt (92 %) with some clay (6 %) and sand (2 %) and is colonized in particular by microphytobenthic films (diatoms up to 60 mg m^{-2}; (Benyoucef et al., 2014) and bioturbating macrofauna (mainly *Hediste diversicolor* and *Scrobicularia plana*; I. Metais, pers. comm.)

Laboratory experiment on homogenized sediment: sediment sampling occurred in June 2014. The sediment was sieved with a mesh of 1 mm in order to remove macrofauna. After homogenization, sediment was covered with estuarine water and left for equilibration for 12 days in the laboratory. Overlying water was constantly aerated and the system kept in the dark at room temperature until gel probes deployment. The day before deployment, a burrow was created using a 50 mL Falcon® tube and gently removed to keep the artificial burrow, and the probe was inserted in the axis of this artificial structure. Before retrieval of the probe, the surface water was sampled (about 5 cm above the sediment water interface, SWI) and nitrite was analyzed using the classical colorimetric technique with a spectrophotometer.

Laboratory experiment on a non-homogenized sediment: sediment sampling occurred in June 2015. This time, the sediment was neither sieved nor homogenized in order to maintain possible natural structures that could generate nitrite or nitrate microenvironments such as fecal pellets, dead organisms or burrows.

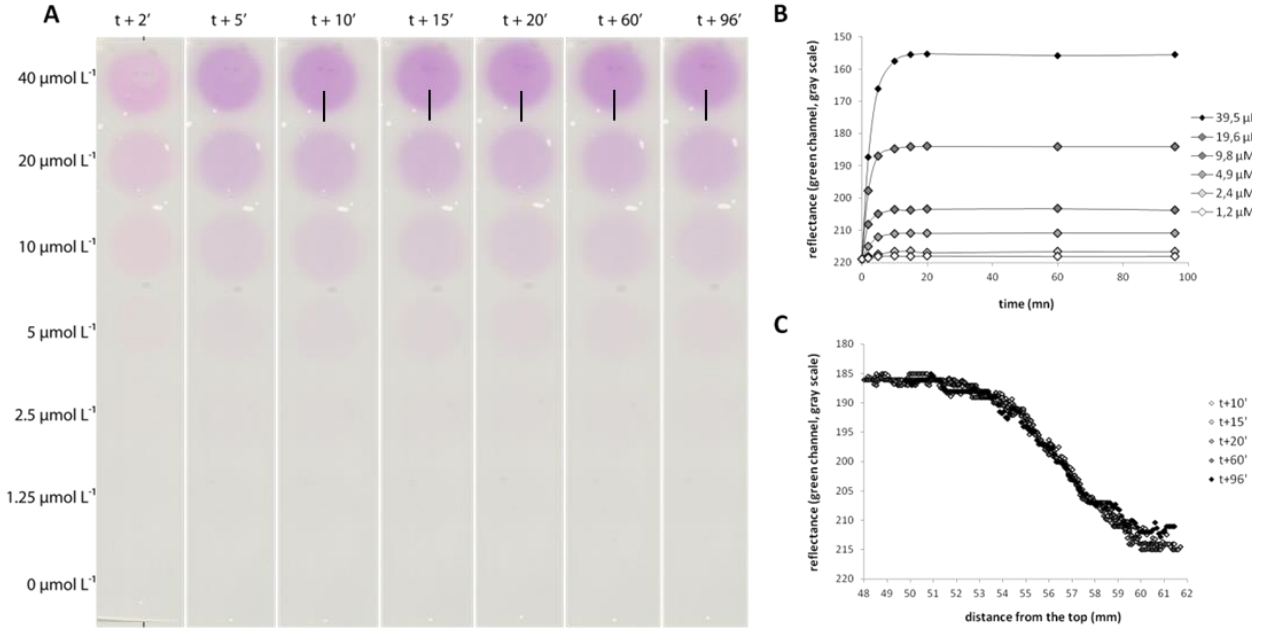

Figure 33 Kinetics of nitrite colorimetric reaction on a gel. A: color evolution of the standard curve over time. B: extracted reflectance (green channel) from images. C: overtime profile evolution across the edge of a well (black line on the images A; 19.5 µmol L-1 NO2-)

2.3 Results & Discussion

2.3.1 Colorimetric measurement of nitrite on a gel

i. Nitrite reaction characteristics

The first test of a protocol for colorimetric nitrite determination using gels consisted in simply starting from the well-known protocol of Griess (1879) modified for seawater by Bendschneider and Robinson (1952) and detailed by Strickland and Parsons (1972) and Grasshof et al. (2009), adapting reagent proportions to gels. The superimposition of one coloring reagent gel with a thickness of 0.5 mm to a probe gel with a thickness of 1 mm corresponds in a dilution with a ratio of 1/1.5 for nitrite from the sample gel and 1/3 for the chemicals from the reagent gel. The gels were prepared as described §2.2. Figure 33 shows the successive images of the calibration gel *versus* time (Figure 33a) and the corresponding reflectance obtained with the commercial flatbed scanner (Figure 33b). The concentration of nitrite standards ranged from 1.25 to 40 µmol L^{-1}. Coloration clearly appears after 2 min. However, below 5 µmol L^{-1} it appears difficult to distinguish nitrite signal with naked eyes and it is necessary to perform a numerical treatment (*e.g.* with ImageJ® densitometry software). Once it is done, the differences between the standards and the background are significant down to a concentration of 1.25 µmol L^{-1}. The time series lasting over 96 min indicates that the colorimetric reaction is complete 10 min after contact between the reagent gel and the calibration gel. This supports the idea that the kinetics of colorimetric reaction is similar to classical spectroscopic measurements and in a gel assemblage (see references above).

Figure 33c shows the evolution of a coloration profile across the edge of the 19.5 µmol L^{-1} nitrite standard-well according to time. The good superimposition of profiles within the time-series indicates that no diffusion seems to take place laterally after contact between the calibration gel and the reagent gel. In particular, there is no visible relaxation of gradient concentration during the colorimetric reaction. However, the asymptotic diffusive profile centered at the limit of the well, that held the standard solution, seems to indicate that during the equilibrium step between the standard solutions and the calibration gel, nitrite is free to diffuse laterally beyond the well limits. Similar observations were made for iron and phosphorous previously (Cesbron et al., 2014). These results indicate that the colored component has a much slower diffusion coefficient than the free nitrite. It also suggests that the time of relaxation of the signal by lateral diffusion of solutes in the gel during handling (i.e. from time of probe retrieving to coloration process), is a crucial parameter that strongly limits the maximal resolution of this method and special care must be taken while interpreting sub-millimeter 2D structures (Harper et al., 1997; Cesbron et al., 2014).

Since the signal does not evolve significantly after 10 minutes, the maximum reflectance intensity can be correlated with standard concentrations to realize a standard curve (coefficient of determination of 0.9972). The standard curve allows calculating a limit of detection (3-fold standard error of the blank) of 1.7 µmol L^{-1} and a limit of quantification (LOQ) about 5 µmol L^{-1} (10-fold standard error of the blank). Accuracy is about 2 µmol L^{-1} within the range from 0 to 40 µmol L^{-1}.

ii. Application on a homogenized sediment

Figure 34 shows the two-dimensional distribution of nitrite obtained after deployment of a gel probe within the sieved sediment that was artificially perturbed. The overall feature of the nitrite distribution seems to follow the shape of the perturbation with concentration up to 15 µmol L^{-1}. The image shows that nitrite concentrations ranged between 10 and 15 µmol L^{-1} in the first centimeter above the SWI. A water sample taken 5 cm above (near the air-water interface), and analyzed classically (with a spectrophotometer), showed a concentration of 5.8 µmol L^{-1} suggesting a nitrite flux from the sediment into the overlying water of the aquarium. As expected, below 2 cm depth (and around the artificial burrow), nitrite is depleted reaching LOD at 5 cm depth, likely by denitrification or anammox processes occurring in the sediment (Burgin and Hamilton, 2007) or abiotically due to lower redox potential.

The first goal of this paper was to transpose the classical nitrite colorimetric determination to a 2D gel in order to describe nitrite distribution at high resolution affected by any sedimentary structure. The results shown here indicate that this goal was achieved.

2.3.2 Simultaneous nitrite and nitrate 2D analysis

i. Optimization of nitrate reduction kinetics

The recent publications (García-Robledo et al., 2014; Schnetger and Lehners, 2014) considering the use of a vanadium chloride solution instead of the widely used granular copperized cadmium column for nitrate reduction to nitrite (Wood et al., 1967) brought new perspectives for the applicability of a colorimetric technique for nitrate in gels. However, there is a major limitation in the transposition of the protocols established by these studies to gel imagery: the slow kinetics of nitrate reduction into nitrite. Hence, a slow colorimetrical reaction would favor relaxation of strong concentration gradients by diffusion of nitrate before immobilization by colorimetrical reaction. To keep the ability of the 2D DET to catch millimeter features in sediment it is necessary to optimize the kinetics of nitrate reduction with VCl_3. Schnetger and Lehners (2014) established that a complete reduction of nitrate into nitrite with VCl_3 takes 10 hours at ambient temperature and 40 min at 45°C using a 0.57 % (w/v) VCl_3 reagent solution. Similar results were found by Garcia-Robledo et al. (2014). In addition, García-Robledo et al. (2014) showed that kinetics is also dependent of the concentration of vanadium and of the acidity of the reducing reagent. At 50°C, they showed that time of nitrate reduction decreases by more than a half when VCl_3 increases from 0.5 to 2 % (w/v). A similar experiment was realized in the present study (see Annexe 5) that showed that for a VCl_3 concentration of 0.017 mol L^{-1} (Schnetger and Lehners, 2014) at 30°C, 100% of nitrate was reduced after 2 h and only 45 min was needed with 0.07 mol L^{-1}. Therefore it is possible to apply this nitrate reduction technique to 2D DET nitrate imagery accepting a relaxation effect during 45 min *i.e.* of about roughly 2 mm (in all directions) which is not ideal for a sub-millimeter resolution image.

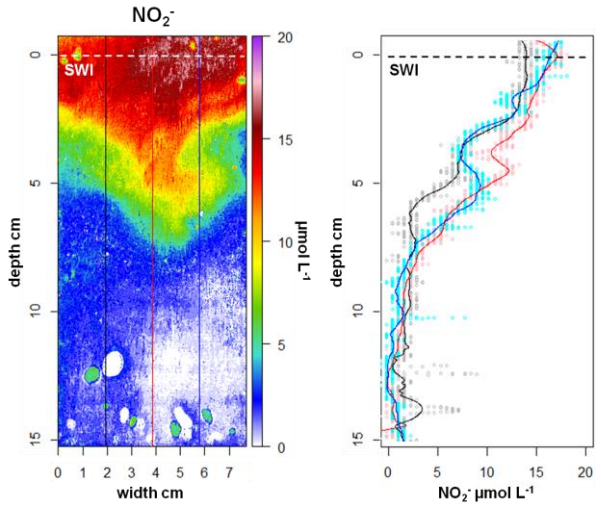

Figure 34 2D nitrite concentration distribution and examples of selected profiles for a sieved and homogenized sediment of the Brillantes mudflat Loire estuary, artificially bioturbated by a 3 cm-diameter tube. Dots are data and lines are smoothed profiles..

ii. Hyperspectral analysis: accuracy and LOD improvements

Use of the vanadium chloride solution (a dark green solution) creates a second problem as the solution absorbs a certain quantity of light with a particular spectral signature and therefore is likely to raise the LOD of the 2D DET nitrate imagery. Preliminary tests performed with commercial flatbed scanner showed that VCl_3 (at 0.07 mol L^{-1}) interferences prevent the detection of nitrate. Further investigation revealed that the hyperspectral camera allows to detect nitrate (despite 0.07 mol L^{-1} of VCl_3) but only above 10 µmol L^{-1}. As shown in the spectra described in the Annexe 6, accuracy of nitrite detection is constrained by the absorption band of the complex coloring reagent + probe + reducing reagent gels between 450 nm and 590 nm. However, the adjunction of a dark green vanadium chloride gel considerably modifies the background. The signal brought by vanadium(III) (between 490 and 660 nm) is spread over the entire visible spectrum including where the nitrite peak develops. To overcome this limitation and keep acceptable reduction kinetics we chose to work with a final concentration of VCl_3 = 0.035 mol L^{-1} in the reducing reagent gel, with a time

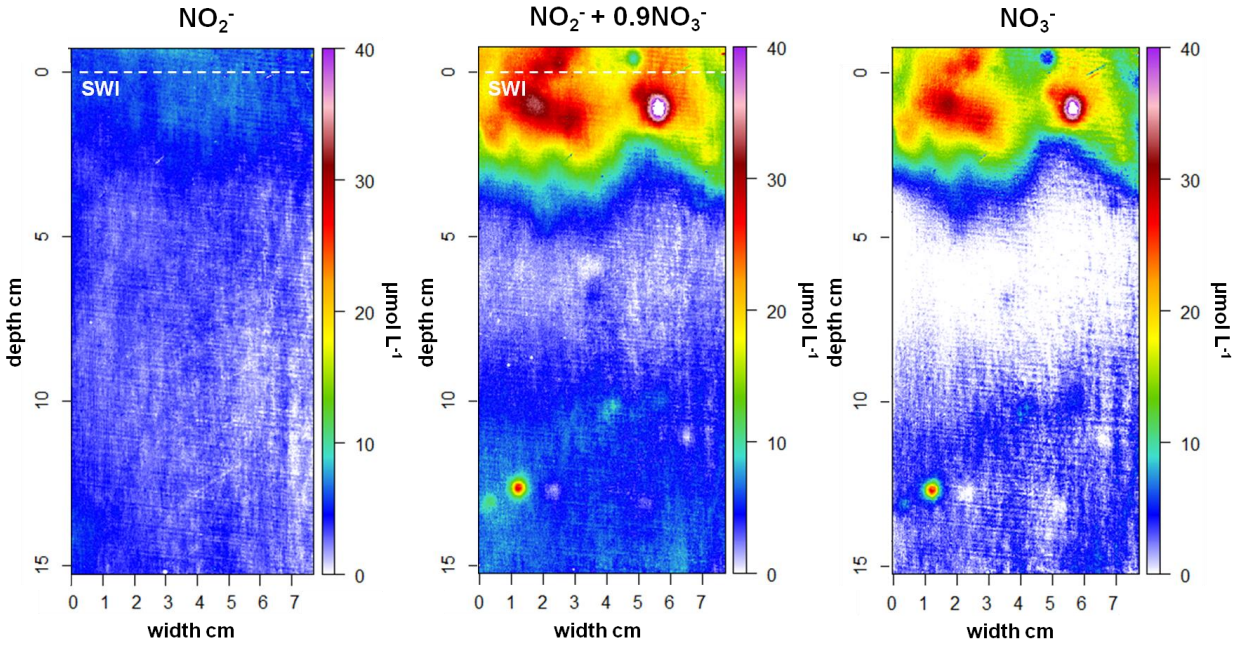

Figure 35 2D nitrite (left), nitrite + reduced nitrate (middle), calculated nitrate (right) for an incubated sediment from the Brillantes mudflat, Loire estuary

span for nitrate reduction of 20 min at the temperature of 50°C.

Standard curves obtained for nitrite and nitrate (Annexe 7) with the optimized protocol for an assemblage of coloring reagent+calibration+reducing reagent gels show good linearity (r^2 = 0.996 and 0.989 for nitrite and nitrate respectively) with a LOD about 1.7 µmol L^{-1} (3-fold standard deviation of the blank reflectance), a 5 µmol L^{-1} LOQ and a 2 µmol L^{-1} accuracy. By analogy with length of cuvettes, thickening the probe gel increases reflectance and therefore would allow LOD increasing if necessary. However, a thicker gel requires an increase of in situ deployment time and results in a decreasing of spatial definition of 2D structures because of lateral diffusion within the gel (Harper et al., 1997).

The comparison of nitrite and nitrate standard curves allows the determination of an averaged nitrate reduction efficiency by comparison of slopes. A 100% nitrate reduction rate would lead to a $slope_{nitrate}/slope_{nitrite}$ equal to 1. Standard curve for nitrate has a slope of 0.0450 (Annexe 7) while the standard curve for nitrite has a slope of 0.0501; the ratio indicates a nitrate reduction efficiency of about 90%. Once, the quantification of nitrate reduction efficiency determined, it is possible to quantify the nitrate concentration within the gel despite the lack of a total reduction of nitrate. Another experiment was realized with slightly different conditions (reduction time of 10 minutes and temperature of 40°C) that gave a nitrate reduction efficiency of about 75%. These results suggest that the interplay between nitrate reduction kinetics and diffusion smoothing of 2D structures has to be considered carefully while biogeochemical interpretations about microniches or other sedimentary structures are hypothesized. This means that a very precise knowledge about diffusion of chemical species within the gel at different temperatures and for each step of the colorimetric protocol has to be acquired for good modeling of signal relaxation and therefore 2D structure reconstruction. A more empiric approach was chosen to evaluate such relaxation in §2.3.1.i for nitrite. Results suggest that, once the pink azo dye is formed, diffusion is greatly slowed down and cannot be observed within the time of the experiment. During the second step of the protocol (nitrate reduction using VCl_3), nitrate can diffuse and signal be relaxed since the Griess reaction did not occur yet. Our results suggest that at a millimeter scale, this would not significantly affect structure shapes but probably affect more chemical gradients across their edges (see next section).

iii. Application on an incubated sediment

Unlike the nitrite testing (§2.3.1), this experiment used sediment taken from the Brillantes mudflat that was neither sieved nor homogenized in order to keep potential sedimentary or biogenic structures. Figure 35 shows the distribution of nitrite obtained from the first scan (*i.e.* first reagent gel over the probe gel) in the left panel and nitrite + reduced nitrate from the second scan in the central panel. Efficiency of nitrate reduction was taken as 90% according to the standardization. The right panel shows the resulting nitrate distribution after nitrite subtraction and efficiency correction. Nitrite remains below 5 µmol L^{-1} over the 15 cm of the gel inserted into the sediment while nitrate shows maximal concentrations over 40 µmol L^{-1} near the SWI. Despite lateral heterogeneity, nitrate seems to decrease below the LOD at 4 cm depth. One can note a spherical patch about 13 cm below the SWI.

Figure 36 and Figure 37 show separately nitrite and nitrate 2D distribution respectively extracted from Figure 35 with appropriate rescaling. Vertical lines over the picture correspond to profile extractions shown in right panels. The three nitrite profiles are very similar suggesting little lateral variability. Near the SWI, nitrite concentration is about 6 µmol L^{-1}. There is a decrease to a minimum of ~2 µmol L^{-1} at 4 cm depth. Below, nitrite concentration remains roughly constant

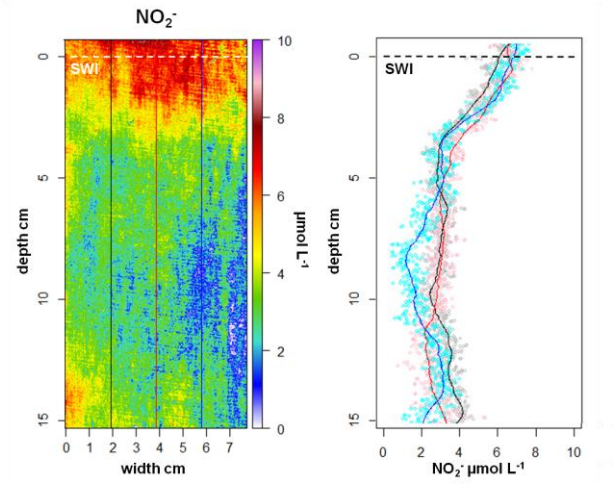

Figure 36 2D nitrite distribution (left) and examples of selected profiles for an incubated sediment of the Brillantes mudflat, Loire estuary. Dots are data and lines smoothed profiles.

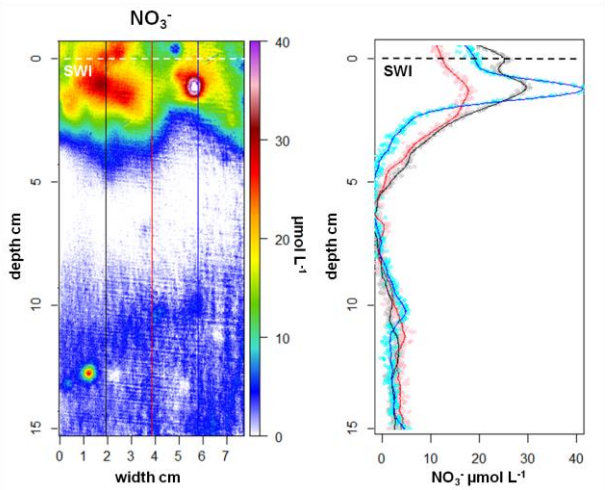

Figure 37 2D nitrate distribution (left) and examples of selected profiles for an incubated sediment of the Brillantes mudflat, Loire estuary. Dots are data and lines smoothed profiles.

between LOD and LOQ (limit of quantification). Nitrate profiles show a more complex pattern (Figure 37). All profiles show a nitrate maximum approximately 1 cm below the SWI indicating nitrification (Sørensen et al., 1979; Burgin and Hamilton, 2007). Then nitrate reaches zero at 5 cm depth. Below 10 cm depth, nitrate seems to be stable at a concentration below LOD. The variability of maximum intensities that ranges between 20 and 40 µmol L^{-1} illustrates the high lateral variability of such sediment at a millimeter scale. Such a variability is visible as well for dissolved iron and phosphorus for *in situ* deployments in the same area (Thibault de Chanvalon et al., 2015) mostly explained by the presence of active burrows of polychaetes.

The lateral variability of nitrate gradients intensity below the SWI highlights the importance of bioturbation for nitrogen cycling (Aller and Aller, 1998; Gilbert et al., 2003; Stief, 2013; Bonaglia et al., 2014) and especially for oxidation of ammonium and nitrate release from sediment into water column. Bioturbation can enhance nitrate consumption producing N_2O and/or N_2 by denitrification or by oxydation of reduced compounds such as FeS or Fe^{2+}, (Hulth et al., 1999) or producing again ammonium by dissimilatory nitrate reduction to ammonium (DNRA). This is of major importance considering the fact that

nutrient availability controls benthic primary production and that microphytobenthic mats play an important role on the food web and on stabilization of the sedimentary substratum (MacIntyre et al., 1996). Important nitrate production would also imply reduction of oxidizers such as manganese and iron oxy(hydroxi)des and therefore enhancement of metal remobilization and recycling (Anschutz et al., 1998; Hulth et al., 1999; Fernandes et al., 2015). Therefore, we offer here the possibility to examine in 2 dimensions, the spatial nitrite and nitrate variability at a sufficient resolution that allows to describe chemical gradients generated by a mm-sized dead organism, a root apex, along a burrow wall. Further, these processes could be quantified with appropriate modeling (Thibault de Chanvalon et al., in press; Zhu et al., 2006). Indeed, a double layer gel can be performed to sample at the same location both nitrite/nitrate and iron/phosphate couples. The image of nitrate distribution shows microenvironments at subsurface, between the oxic zone and the iron remobilization zone, and more surprisingly 13 cm below the interface suggesting that noisy profiles in the literature, that are often obtained from core slicing could not be artifacts but could be a result of the sampling of a microenvironment similar to the one shown here that peaks at about 30 µmol L^{-1}.

Combining colorimetry, gel sampling and hyperspectral imagery, it is possible to assess, at sub-millimeter resolution in 2 dimensions, nitrite and nitrate production/consumption hotspots within a range between 1 and 40 µmol L^{-1} without sampling discretization. However, due to relaxation effects, fidelity of concentration is achieved at a millimeter resolution. This technique is a good alternative to microsensors that allow sub-millimeter profiling but are difficult to perform and time-consuming as several profiles are needed to assess 2D distribution (at a low resolution anyway). The protocol proposed here allowed to describe nitrate release as microniches below the "zero-nitrate" layer and to evidence the lateral variability of nitrate concentration in estuarine muddy sediment. Such technique offers numerous perspectives for laboratory and *in situ* studies dealing with the reactivity of microenvironments such as burrows or decaying macro(meio)fauna locations. Combined to other high-resolution 2D analyses such as Fe/PO_4 gels, this method will provide valuable insights on the mechanisms that control nutrient release and primary production feedback.

Acknowledgement

This study is part of the RS2E – OSUNA project funded by the Région Pays de la Loire. Thanks to Romain Levrard, Livia Defay and Manuel Giraud for their technical help.

Partie 1 :

3 Cartographie bidimensionnelle de la remobilisation du fer dans des sédiments marins à une échelle submillimétrique

---

A. Thibault de Chanvalon[1,2], E. Metzger[1], A. Mouret[1], J. Knoery[2], E. Geslin[1], F.J.R Meysman[3]

[1] Université d'Angers, LPG-BIAF, UMR CNRS 6112, 49045 Angers Cedex, France
[2] Ifremer, LBCM, Rue de l'Ile d'Yeu, 44300 Nantes, France
[3] Department of Ecosystem Studies, The Netherlands Institute of Sea Research (NIOZ), Korringaweg 7, 4401 NT Yerseke, The Netherlands

Article accepté dans Marine Chemistry
doi : 10.1016/j.marchem.2016.04.003

Edited by: G.W.Luther

ABSTRACT

Coastal and shelf sediments are considered as an important source of dissolved iron to the ocean. Here, we present a new numerical approach to estimate geochemical fluxes and production rates in an estuarine sediment at sub-millimetre resolution. This approach is based on application of Savitsky-Golay filter (SGF) procedure to two-dimensional concentration distributions of dissolved iron. We verified the procedure by applying it to artificial data of known production rates, and analysed the resulting uncertainty on production rates and fluxes across the water-sediment interface. This SGF procedure was applied to data from an intertidal mudflat that is strongly impacted by macrofaunal bio-irrigation. Our analysis reveals a strong recycling of iron at millimetre scales with an apparent recycling rate of 3780 ± 1399 µmol m^{-2} d^{-1} and a mean residence time of iron in the dissolved phase of 2.3 days. Visual identification of burrows permitted to calculate separately the diffusive flux across the sediment-water interface (104 ± 20 µmol m^{-2} d^{-1}) and the bio-irrigational flux (410 ± 213 µmol $m^{-2}d^{-1}$). Reactive iron particles will undergo on average 7.4 cycles of dissolution/precipitation before being released to the water column. These results show that estuarine sediments support intensive iron recycling that have probably a large impact on terrigeneous particles before being released into the ocean.

RESUME

Les sédiments côtiers et les plateaux continentaux sont considérés comme une source importante de fer dissous pour les océans. Nous proposons ici une nouvelle méthode de calcul numérique pour estimer les flux géochimiques et les vitesses de productions dans un sédiment estuarien et à une résolution submillimétrique. Cette méthode est basée sur l'application d'un filtre de Savisky-Golay (SGF) à une distribution de concentrations de fer dissous en deux dimensions. La vérification de cette procédure SGF est réalisée à l'aide de distributions théoriques produites à partir de vitesses de production connues. Cette analyse permet aussi de calculer les incertitudes de la procédure sur les vitesses de production et sur les flux à l'interface eau-sédiment. Enfin, la procédure SGF est appliquée sur des données provenant d'une vasière intertidale intensément soumise à la *bioirrigation* produite par la macrofaune. Nous calculons ainsi un recyclage extrêmement important du fer dissous à une échelle submillimétrique quantifié par une vitesse de recyclage apparente (ARR) de 3780 ± 1399 µmol m^{-2} d^{-1} ce qui conduit à l'estimation du temps de résidence moyen du fer en phase dissoute de 2,3 jours. L'identification visuelle des terriers permet de calculer séparément les flux diffusifs à l'interface eau-sédiment (104 ± 20 µmol m^{-2} d^{-1}) et les flux de *bioirrigation* (410 ± 213 µmol $m^{-2}d^{-1}$). Ainsi, le fer réactif lié aux particules réalise en moyenne 7,4 cycles de dissolution/précipitation avant d'être libéré vers la colonne d'eau. Ces résultats illustrent l'important recyclage du fer dans le sédiment estuarien ce qui pourrait modifier considérablement la composition des particules terrigènes lors de leur transfert vers l'océan.

3 Two-dimensional mapping of iron release in marine sediment at submillimeter scale

3.1 Introduction

Dissolved iron acts as a limiting micronutrient controlling oceanic primary production, and in this way, is considered to play an important role in the carbon cycle in the ocean (Martin and Fitzwater, 1988). However, the sources of dissolved iron to the ocean and the mechanisms controlling iron speciation and bioavailability are still weakly constrained, due to the important temporal variability in the iron inputs (Johnson et al., 1999), the spatial heterogeneity of the different sources (Raiswell, 2006; Boyd and Ellwood, 2010; Conway and John, 2014) and the complex speciation and biogeochemical interactions that take place once iron reaches the ocean (Rose and David Waite, 2007; Homoky et al., 2012; Chever et al., 2015).

Coastal and shelf sediments are considered as an important source of dissolved iron to the ocean, with a source strength comparable to riverine inputs and hydrothermal vent emissions (Raiswell and Canfield, 2012; Chever et al., 2015). However the uncertainty on the efflux from near-shore sediments is large, because experimental quantification of the dissolved iron released from sediments is challenging. One important factor that complicates iron flux measurements in coastal and shelf sediments is the presence of benthic fauna. In these sediments, the efflux of a solute out of the sediment is no longer solely driven by diffusion across the sediment-water interface, but results from a large part from bio-irrigation, *i.e.* the enhanced sediment-water exchange due to burrow pumping activities by infauna (Aller, 2001; Meysman et al., 2006). As burrows have complex, three dimensional geometries, this bio-irrigational flux component cannot be quantified with classical methods such as one-dimensional pore water profiling. Flux measurements based on benthic chambers (*e.g.* Sundby et al., 1986; McManus et al., 1997; Noffke et al., 2012) can be biased by iron reactivity after release in the water column and therefore can underestimate the efflux reduced iron due to oxidative precipitation in the chamber (Pakhomova et al., 2007; Severmann et al., 2010). Furthermore, the enclosure of sediments can disturb the natural bio-irrigation activity of fauna, thus influencing the bio-irrigational fluxes of dissolved iron. Finally, sedimentary iron release can also be constrained by the analysis of vertical distributions of iron concentrations and isotopes in the water column. However, interpretation of such isotopic data is often challenging, as it is dependent on numerous and still poorly understood transformations in the water column, which can have a large impact on isotopic signatures (Homoky et al., 2013; Chever et al., 2015).

Coastal and shelf sediments are also characterized by a large internal cycling of iron compounds between reduced and oxidized forms (Raiswell and Canfield, 2012). These redox oscillations are likely to control the speciation of iron (*i.e.* the relative abundance of Fe(II) and Fe(III)) in both pore water and solid phase, and therefore, they can impact the bioavailability of the iron that is released to the coastal ocean. Traditionally the behaviour of freshly precipitated iron oxide is described by Ostwald's rule (Steefel and Van Cappellen, 1990), which implies an increase in cristallinity and an associated decrease in bioavailability as the iron minerals age (Kuma et al., 1992; Yoshida et al., 2006; Bligh and Waite, 2011). However, this unidirectional “aging” may not be representative for coastal sediments, where intensive redox cycling takes place. As a result of the reductive dissolution and subsequent oxidative precipitation, smaller and more reactive (nano)particles are formed (Von Gunten and Schneider, 1991; Taillefert et al., 2000; Magnuson et al., 2001). Redox cycling hence can have an important impact on the composition and reactivity of iron minerals in the sediment. Raiswell (2011) assumes that each redox cycle simply rejuvenates iron oxides and thus increases the bioavailability, whereas Thompson et al. (2006) reports an increase of iron oxide crystallinity after redox cycling due to the preservation of the most crystalline phase during each dissolution cycle. Moreover, new authigenic minerals, such as Fe-P precipitates (Hyacinthe and Van Cappellen, 2004; Egger et al., 2015; Senn et al., 2015), can be formed after reductive

dissolution, and so the redox cycling of iron may also regulate the fluxes, transformation and burial of other elements (*e.g.* phosphorus, trace metals) in the coastal marine environment. Yet, at present, there has been no direct estimation of the recycling intensity (*i.e.* the number of reduction/oxidation cycles an Fe atom experiences before being buried) in coastal sediments. This is because these redox transformations occur at millimetre scale, and are often localized near ventilated burrows of fauna.

In the present study, we propose a new technique to estimate the flux of iron across the sediment-water interface as well as its internal recycling intensity. The technique is based on the numerical analysis of 2D distributions of dissolved iron concentrations in coastal sediments, which are obtained at high resolution (200µm) by the technique of Dissolved Equilibrium in Thin film (DET; Davison et al., 1991), combined with planar colorimetry (2D-DET; (Shuttleworth et al., 1999; Jézéquel et al., 2007; Robertson et al., 2008; Zhu and Aller, 2012).

3.2 Material and methods

3.2.1 Two-dimensional sampling of dissolved Fe

Pore water data were obtained from the intertidal mudflat Les Brillantes in the Loire estuary (France; 47°16'56.00"N; 2° 3'47.00"W). Data collection (02/05/2013) occurred during a period of high river discharge, when fresh water penetrates far downstream into the estuary, and hence, water with a low salinity (range 2-6) inundates the mudflat at high tide. Two-dimensional (2D) distributions of total dissolved iron (Fe_d) were obtained by insertion of a 2D-DET probe into the sediment. The 2D-DET technique quantifies the distribution of a solute in a vertical plane by diffusive equilibration of the pore water with a gel. These Fe_d distributions were complemented by photographs of the sediment section that faced the 2D-DET probes, which then allowed to correlate the pore water data with the presence of burrows and sediment structures. These sediment photographs were obtained by introduction of a so-called "jaw device" into the sediment, which recovers the 2D-DET probe from the sediment, together with the sediment slice that faces the gel probe (Fig. 38a); a detailed description of this

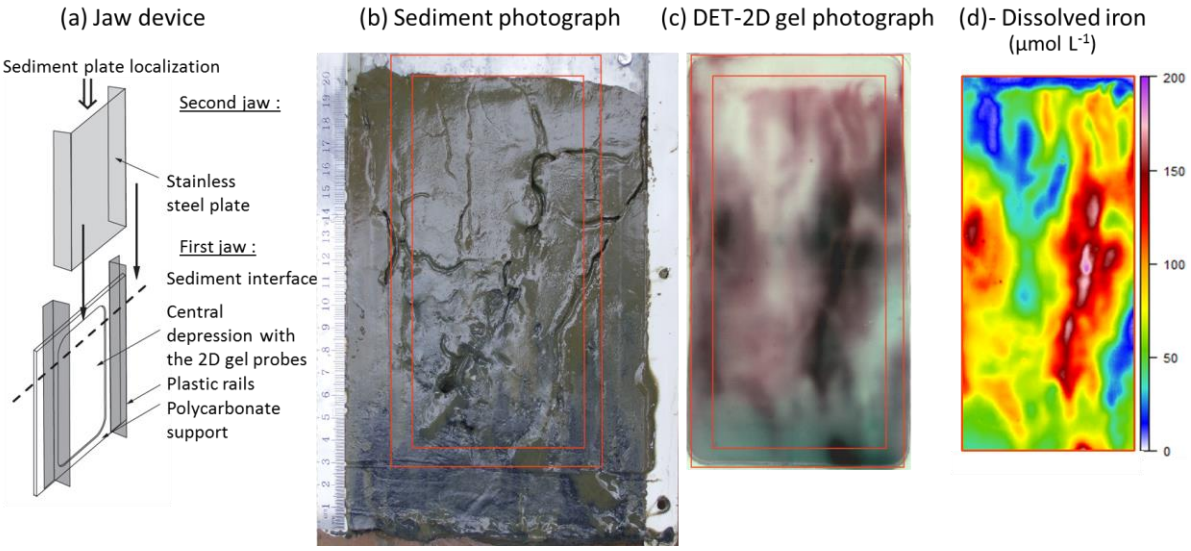

Figure 38 (a) schematic view of the "jaw device" for simultaneous sampling sediment and pore water, (b) photograph of the sediment after retrieval, (c) photograph of the DET-2D gel after colorimetric reactions: dissolved iron appears in dark pink and dissolved phosphorus in turquoise, (d) concentration of dissolved iron in false colour. The analysis of the correspondences between iron and sediment is performed in Fig.45.

instrument is given in Thibault de Chanvalon et al. (2015). Overall, the sampling procedure provides two separate images: (1) a normal bright field image of the face plane of the sampled sediment, which allows the visual identification of burrows and other sediment structures (Fig. 38b), and (2) a false-coloured image generated from the 2D-DET gel probe, which reveals the distribution of dissolved iron in the pore water in two dimensions and at high resolution (Harper et al., 1997; Jézéquel et al., 2007; Cesbron et al., 2014a).

The 2D-DET probe is composed out of a polycarbonate plate with a central depression of 1 mm filled with a polyacrylamide gel (pore size ~2 nm; Zhang and Davison, 1999) that was prepared according to Jézéquel et al. (2007). The plate is subsequently covered by a protective porous PVDF membrane (pore size 0.2 µm) that protects the gel and prevents it from falling out the central depression. The 2D-DET probe was prepared within one week of sampling and was conserved in the dark at 4°C in a moist plastic bag (humidity prevents the gel from drying out). Before deployment, the plastic container bag was deoxygenated by N_2 bubbling for 6 hours. After insertion into the sediment at the beginning of low tide, the 2D-DET probe was deployed for 5 hours during emersion, and recovered before the flood water came in. All deployments occurred during day time. The polycarbonate frame of the 2D-DET probe supports two vertical rails that can guide a stainless steel plate to slide the jaw device into the sediment. This way, at the end of the deployment, the 2D DET probe could be retrieved along with the 2 cm thick sediment layer that was in contact with the gel probe (Fig. 38a).

Upon retrieval, the 2D-DET probe was carefully separated from the sediment, covered with a plastic-coated aluminium plate (to ensure a homogenous freezing process) and stored in a cooling box with dry ice pellets for transport. A picture of the face plane of the sampled sediment was taken with a compact digital camera (Olympus Stylus 7000). Upon arrival in the laboratory, the 2D-DET probe was stored in a freezer (-18°C) until further analysis. This preservation procedure allows storage for up to three months without concentration gradient smoothing due to diffusion within the gel (Cesbron et al., 2014). During analysis, the 2D gel probe was thawed at ambient temperature, and covered by a reactive gel impregnated with specific colorimetric reagents for total dissolved iron (Fe_d). The preparation of the reactive gel was modified from Jézéquel et al. (2007) and Cesbron et al. (2014), and consists of a 0.46 mm thick polyacrylamide gel incubated during 1 hour in a reactive solution (ascorbic acid 30 mM, sulfuric acid 0.558 M, potassium antimony(III) tartrate hydrate 0.40 mM, ammonium molybdate tetrahydrate 18.5 mM and ferrozine 12.2 mM). This reactive solution is sensitive to both dissolved reactive phosphorus (DRP; results not used in this study) and total dissolved iron (Fe_d; Fig. 38c). Iron complexation by the colorimetric reagent is achieved in less than 5 minutes, while DRP coloration takes about 20 minutes (Cesbron et al., 2014). After 25 minutes of contact time, an image of the superposed gels (Fe/P reactive gel + sample gel) was taken with a hyperspectral camera (HySpex VNIR 1600), thus producing a two-dimensional reflectance map. A subsequent spectral analysis of the data allows to discriminate the DRP signal from the Fe_d signal (Cesbron et al., 2014). Eight standard solutions of iron (II) were prepared (from 0 to 200 µM) and exposed to an identical sampling protocol (diffusion in a polyacrylamide gel followed by colorimetric reaction, hyperspectral imaging and spectral analysis). This calibration dataset was used to convert the acquired two-dimensional reflectance map into a Fe_d concentration map (Fig 38d). The resulting uncertainty on the Fe_d concentration has been estimated as < 10% (Thibault de Chanvalon et al., 2015). The spatial resolution of the Fe_d analysis is determined by the pixel size of the hyperspectral camera (200 µm), the ability of the sediment to buffer the pore water concentration (Harper et al., 1997) and the relaxation effect induced by diffusion, once the DET probe boundary is no longer constrained by the sediment (~3 millimetres in 5 minutes; Davison et al., 1994).

Temperature (T) and salinity (S) were measured in the first centimetre of the sediment by insertion of a WTW Series 3110 conductivity meter. For the purpose of this study, depth variations in S and T were not considered. A porosity depth profile was determined on a sediment core (plastic core liner; 3 cm inner diameter) that was retrieved 1 m from the location of

the 2D-DET probe deployment. This sediment core was sliced at 2 mm intervals over the first 2 cm, and using 5 mm intervals up to 5 cm depth. For each depth layer, the porosity was calculated from the mass difference before and after freeze drying, accounting for the salt content of the pore water.

3.2.2 Production rate estimates

Both fluxes and production rates of Fe_d were determined from the recorded 2D distributions based on a two-dimensional reactive transport analysis. From a theoretical point of view, the 2D distribution of a solute in an aquatic sediment can be described by the mass balance equation (Berner, 1980; Boudreau, 1997; Meysman et al., 2005b):

$$\phi \frac{\partial C}{\partial t} = -div\, \boldsymbol{J} + \mathrm{R}(y,z) \qquad (13)$$

In this expression, *C* denotes the concentration, ϕ is the porosity, and *R* represents the production rate, *i.e.*, the net balance of all production and consumption due to biogeochemical reactions. The term $div\ \boldsymbol{J} = \frac{\partial J_y}{\partial y} + \frac{\partial J_z}{\partial z}$ represents the divergence of the flux vector $\boldsymbol{J} = \begin{pmatrix} J_y \\ J_z \end{pmatrix}$. Concentrations, fluxes and rates are dependent on the z-coordinate representing depth into the sediment, and the y-coordinate representing the lateral distance. This flux vector can be specified as (Meysman et al., 2005a):

$$J = -\phi\, D_s\, grad C + \phi\, C\, v \qquad (14)$$

$$\Leftrightarrow \begin{cases} J_y(y,z) = \phi\, C\, v_y - \phi \mathrm{D_s} \dfrac{\partial \mathrm{C}}{\partial \mathrm{y}} \\ J_z(y,z) = \phi\, C\, v_z - \phi \mathrm{D_s} \dfrac{\partial \mathrm{C}}{\partial \mathrm{z}} \end{cases}$$

where D_s is the effective diffusion coefficient of Fe_d in the pore water, and $v = \begin{pmatrix} v_y \\ v_z \end{pmatrix}$ is the advective velocity vector of the pore water. If we assume that (1) advective transport of pore water is negligible (see discussion below) and (2) that the solute distribution is at steady state, we obtain the following expression for the production rate:

$$\mathrm{R}(\mathrm{y},\mathrm{z}) = \mathrm{R_y} + \mathrm{R_z}$$

$$\mathrm{R}(\mathrm{y},\mathrm{z}) = \left[-\phi \mathrm{D_s} \frac{\partial^2 \mathrm{C}}{\partial \mathrm{y}^2} - \left(\phi \frac{\partial \mathrm{D_s}}{\partial \mathrm{y}} + \mathrm{D_s} \frac{\partial \phi}{\partial \mathrm{y}}\right).\frac{\partial \mathrm{C}}{\partial \mathrm{y}}\right] + \left[-\phi \mathrm{D_s} \frac{\partial^2 \mathrm{C}}{\partial \mathrm{z}^2} - \left(\phi \frac{\partial \mathrm{D_s}}{\partial \mathrm{z}} + \mathrm{D_s} \frac{\partial \phi}{\partial \mathrm{z}}\right).\frac{\partial \mathrm{C}}{\partial \mathrm{z}}\right] \qquad (1$$

Equation (3) reveals that it is possible to estimate the total production rate $\mathrm{R}(\mathrm{y},\mathrm{z})$ at each point as the sum of two separate production terms: the first term $\mathrm{R_z}$ is based on the vertical variation of the concentration along the z-axis, and the second term $\mathrm{R_y}$ is solely based on the horizontal variation of the concentration along the y-axis.

The neglect of the advective terms in Eq. (3) requires some consideration. The sediment at the sampling location is a bioturbated, cohesive sediment with a high porosity (> 0.8). Accordingly, the permeability is low, and advective flows in the pore water due to tidal pumping and wave action will not be important (Berner, 1980; Glud et al., 1996; Huettel et al., 2014). Yet, another important type of advection is pore flow inside the burrows. Due to burrow flushing by macrofauna, an advective flow will be created inside the burrow. These burrow flows can be highly variable in time, as the burrow irrigation intensity changes on the order of minutes (Kristensen, 1989; Riisgård and Larsen, 2005; Volkenborn et al., 2010, 2012). The dominant species on Les Brillantes mudflat is the polychaet *Nereis diversicolor*, which shows highly frequent (5-10 minutes) intermittent ventilation (Kristensen, 1981, 2001; Pischedda et al., 2012). As our DET deployments lasted for 5 hours, they will provide a time-averaged picture of this burrow ventilation activity (Harper et al. 1997). Over this time-scale, the mean transport of Fe_d typically implies that dissolved iron diffuses into the burrow across the burrow wall, and is subsequently flushed out by burrow ventilation. By ignoring the advective terms in Eq. (3), the effect of Fe_d removal by burrow flushing will show up as a reactive term R. Therefore, inside actively flushed burrows, the net production rate R will likely

be negative, and should be not be interpreted in terms of geochemical reactions, but in terms of bio-irrigation. So overall, the neglect of advection in our reactive-transport analysis can be justified, provided that the net production term R is correctly interpreted. Outside the burrows, R represents the effect of biogeochemical reactions. Inside the burrows, R predominantly represents the removal of solutes due to burrow ventilation.

The assumption that the solute distribution is at steady state is more difficult to justify *a priori*. There are various processes acting in intertidal mudflats that can drive the pore water into a transient state. These processes also work on different time scales, *e.g.* microphytobenthos activity (diurnal scale), the deposition of a new sediment layer during floods (month scale) or variations in mineralization intensity (seasonal scale). Processes that act on longer time scale than the 2D-DET measurement (5 hours) will not provide large contribution; the pore water iron distribution will attain a quasi-steady state. Still, important transient concentration changes can occur on shorter time scales in bioturbated sediments, due to variations in the intensity of burrow flushing. Ferrous iron concentrations (and other reduced species) may increase when burrow ventilation is stopped, and rapidly decrease, when burrow ventilation restarts. So especially near burrows, we cannot rule out concentration change terms dC/dt, and in our analysis, these terms will be lumped into the production rate R. For this reason, the quantity R should be regarded as an "apparent production rate", which hence may also include transient effects. The assessment of the importance of such concentration change terms dC/dt is beyond the present study, and should be the focus of future work.

Equation (3) reveals what information is needed to calculate the local production rate of dissolved iron: the spatial distribution of the porosity ϕ, the effective diffusion coefficient D_s, and the concentration C, as well as the spatial derivatives of these quantities. Typically, the effective diffusion coefficient D_s is calculated from the relation $D_s=D_{mol}/\theta^2$, where the molecular diffusion coefficient D_{mol} is calculated as an empirical function of temperature and salinity (Boudreau, 1997). Here, we assume that salinity and temperature do not vary in the sediment, and hence, the molecular diffusion coefficient D_{mol} will not be spatially dependent. The molecular diffusion coefficient of Fe_d was calculated from the R package "marelac" (D_{mol} = 5.16 10^{-10} m^2 s^{-1} at T= 12.7 °C and salinity 5.6). The tortuosity θ^2 is typically taken as a function of porosity, as in the modified Weissberg relation, $\theta^2=1-2\ln(\phi)$ (Boudreau, 1996), and so, once the spatial distribution of the porosity is known, the associated tortuosity can be calculated analytically. The porosity in the vertical is usually assumed to be mainly controlled by compaction, while the porosity can vary in the lateral around burrows linings. So both vertical and lateral gradients in porosity and tortuosity can exist. Presently however, such variation of the porosity at sub-millimetre scale cannot be quantified experimentally. Accordingly and to a first approximation, the lateral variation in porosity is neglected here, and only the vertical gradients are accounted for. The porosity is described by an exponential decreasing function of depth $\phi = (\phi_0 - \phi_{inf})\, e^{-\alpha z} + \phi_{inf}$, which was fitted to the measured porosity depth profile and the derivatives $\frac{\partial \phi}{\partial y}$ and $\frac{\partial D_s}{\partial z}$ were subsequently calculated analytically. As a result, the only unknowns that remain in equation (3) are the spatial derivatives of the concentration (*i.e.* $\frac{\partial C}{\partial y}$, $\frac{\partial C}{\partial z}$, $\frac{\partial^2 C}{\partial y^2}$ and $\frac{\partial^2 C}{\partial z^2}$). We will now investigate how these derivatives can be derived from the available dataset.

3.2.3 The Savitzky Golay filter procedure

The Savitzky Golay filter (SGF) procedure (Savitzky and Golay, 1964) is a widely used method for smoothing noisy experimental data and calculating associated derivatives. Briefly, for each point within a data series, the SGF procedure generates a polynomial function that is fitted by the method of least-squares to a central point and its n closest neighbours on either side (*i.e.* on 2n+1 points, the window size). Then the SGF procedure estimates the value (and its derivatives) at the central point by means of evaluating and differentiating the fitted polynomial function. The standard implementation of the SGF filter is described in Gorry (1990) and the algorithm is given in Press et al. (1992). Here, we have implemented the routines in

the open-source programming framework R, which use the function "sgolayfilt" in the extension package "signal" (see Meysman and Burdorf (in prep.) for details).

Two parameters have to be fixed in the SGF procedure: the order (p) of the fitted polynomial and the filter window size (2n+1). The polynomial order is typically set at p = 3, as is done here. The larger the filter window size, the more noise is suppressed, but also the more the data signal is smoothed. Accordingly, an optimal window size suppresses most of the (undesired) experimental noise, while it removes as little signal as possible. The automated (numerical) determination of this optimal window size still forms an active field of research. (Meysman and Burdorf, in prep.) have proposed an automated procedure based on fractal analysis which calculates the fractal dimension D as a function of the window size using the R function "fd.estimate" from the extension package "fractaldim", selecting the "madogram" method to calculate the fractal dimension (Gneiting et al., 2012). As the window size increases, the fractal dimension D decreases, and there is a clear break in the slope of D when it reaches the value of 1. This break point is selected as the optimal window size. More details on this automated procedure to determine the optimal window size are given in (Meysman and Burdorf, in prep.).

Here we implemented the one-dimensional SGF procedure as proposed by (Meysman and Burdorf, in prep.). ; *i.e.* with polynomial order p = 3 and optimal window size selection) to both the rows and columns of the two-dimensional concentration distribution of Fe_d. Application to the columns (z-coordinates) estimates the concentration derivatives in the vertical direction, thus yielding the vertical flux $J_z(y,z)$ and the production rate $R_z(y,z)$ in each point of the concentration matrix. Similarly, application to the rows (y-direction or horizontal) yields the horizontal flux $J_y(y,z)$ and the associated production rate $R_y(y,z)$. As derived above, the total production rate in any given location is then simply obtained as the summation of both production rates, *i.e.* $R(y,z) = R_y(y,z) + R_z(y,z)$. Overall, the end product of our reactive transport analysis is a two-dimensional matrix of production rates, which is then visualized as a false-colour image at the same high resolution as the original concentration dataset.

3.2.4 Model validation procedure

To verify the performance of our SGF procedure, we applied it to a synthetic dataset, which was first created by a forward numerical simulation of the reactive transport model. In a first step, various types of "idealized" or "true" two-dimensional patterns of production rate were defined, *i.e.* $R^{ideal}(y,z)$. The most basic production rate pattern consisted of a localized production spot combined with a uniform first order consumption ($R = -k\,C$) throughout the whole model domain. The localized production was modelled by a symmetrical two-dimensional Gaussian function

$$f(y,z) = R_{max} \exp\left(-\left(\frac{(y-y_0)^2}{2\,\sigma^2} + \frac{(z-z_0)^2}{2\,\sigma^2}\right)\right) \qquad (16)$$

where the coefficient R_{max} is the amplitude, y_0 and z_0 are the coordinates of the centre, and σ is the spreading parameter which is alternatively quantified by the full width at half maximum, *i.e.* FWHM = 2.355 σ. More complex production patterns were constructed by combining multiple of these localized Gaussian production sites (with different amplitudes and spreads) with a uniform first order consumption. The latter generated a distribution that was roughly similar to the natural production rate pattern observed in the field data.

In a second step, the "idealized" 2D production patterns $R^{ideal}(y,z)$ were used as input into a reactive transport model, and the resulting simulations thus generated the "idealized" 2D concentration distribution $C^{ideal}(y,z)$ and the fluxes $J_y^{ideal}(y,z)$ and $J_z^{ideal}(y,z)$. To this aim, the governing 2D mass balance equation (Eq. 13) was numerically solved for steady state using reactive transport model procedure as fully detailed in Soetaert et al. (2010) and Soetaert and Meysman (2012). This numerical solution procedure was implemented in the open-source programming language R.

In a third step, random white noise (*i.e.* with a Gaussian distribution) was added to these idealized

concentration distributions to mimic the random noise generated during experimental data collection. This then provided to obtain suitable "test" concentration distributions C^{test}. The applicable noise level was determined by analysis of the 2D-DET calibration standards. Around 5000 concentration data points from each of the eight 2D-DET calibration Standards were analyzed and plotted. The resulting distribution was fitted by a normal distribution $\mathcal{N}$ (0,var) (Gaussian distribution) with a zero mean. The variance of this normal distribution then determined the applicable noise level. This noise level was quantified by two parameters: the relative standard deviation of the highest concentration standard (rsd_{high} = 1%) and the absolute standard deviation of the lowest concentration standard (sd_{low} = 0.4 µmol L^{-1}). The "test" dataset was subsequently calculated according to:

$$C^{test} = C^{ideal} (1+ C^{err}_{high}) + C^{err}_{low} \qquad (17)$$

where $C^{err}_{low} \sim \mathcal{N}(0,sd_{low})$ and $C^{err}_{high} \sim \mathcal{N}(0,rsd_{high})$

In a fourth and final step, the SGF filter procedure was applied to C_{test}. The synthetic datasets were treated in the exactly same manner as the real datasets. The result is an estimated 2D concentration distribution $C^{estimated}(y,z)$, a vertical and a horizontal flux called $J_z^{estimated}(y,z)$ and $J_y^{estimated}(y,z)$, and an estimated 2D production pattern called $R^{estimated}(y,z)$.

The *reconstruction bias* was calculated as the difference between idealized and reconstructed quantities, *i.e.*:

$$\Delta C(y,z) = C^{ideal}(y,z) - C^{estimated}(y,z) \qquad (18)$$

$$\Delta J_x(y,z) = J_x^{ideal}(y,z) - J_x^{estimated}(y,z) \qquad (19)$$

$$\Delta R(y,z) = R^{ideal}(y,z) - R^{estimated}(y,z) \qquad (20)$$

These reconstruction bias values are calculated at every individual pixel. To summarize the overall accuracy of the model reconstruction, a single Mean Reconstruction Bias (MRB) is introduced

$$MRB\ (\%) = \frac{sd(\Delta C(y,z))}{sd(C^{ideal}(y,z))} * 100 \qquad (21)$$

This indicator requires that we calculate the standard deviation $sd\left(C^{ideal}(y,z)\right)$ of the sampling distribution of the concentrations over the domain, as well as the standard deviation $sd(\Delta C(y,z))$ of the sampling distribution of the concentration reconstruction bias. As a result, the Mean Reconstruction Bias provides a single indicator for a whole 2D domain, summarizing the misfit between the "true" concentration values and the "reconstructed" concentration values. A similar MRB indicator is defined in an analogous way for the 2D reconstruction of fluxes and production rates.

3.3 Results

3.3.1 Model analysis of synthetic datasets

To verify the performance of the reactive transport analysis based on the SGF procedure, it was applied to three synthetic datasets. Each dataset has the same model domain (size = 8.7 cm x 17 cm), but a different production pattern of Fe_d: (1) a single production zone with a broad spreading (FWHM = 2.36 cm, pixel size = 200 µm, R_{max} = 33 µmol L^{-1} d^{-1}, y_0= 4.35 cm z_0= 8.5 cm), (2) a single and highly localized production zone (FWHM = 0.59 cm, pixel size = 200 µm, R_{max} = 286 µmol L^{-1} d^{-1}, y_0= 4.35 cm z_0= 8.5 cm), and (3) a superposition of 25 localized production zones (FWHM range = 0.12 to 5.89 cm, pixel size = 200 µm, R_{max} range = 2.6 to 13 µmol L^{-1} d^{-1}) thus providing a patchy consumption distribution. To enable a suitable comparison, the idealized production rate $R^{ideal}(y,z)$ was scaled in such a way in all three cases, that the resulting 2D concentration distribution showed a maximum concentration of 100 µmol L^{-1}.

Figure 39 shows the results for the concentration, *i.e.* (a) the idealized 2D concentration distribution $C^{ideal}(y,z)$ as generated by the reactive transport model (Fig. 39a) and (b) the 2D distribution of the "estimated" concentration $C^{estimated}(x,y)$ as recovered by the SGF procedure from the purposely noise-compromised data (Fig. 39b). The difference between "idealized" and "estimated" concentration ($\Delta C(y,z)$; Fig. 39c) is vanishingly small for all three synthetic datasets, thus showing that the SGF procedure can accurately reproduce the idealized concentration patterns. The maximum reconstruction bias of 2.5 µmol L^{-1} occurs at

	Concentration	Downward flux	Production rate
dataset n°1	0.58	3.75	12.2
dataset n°2	**2.17**	**7.2**	31.9
dataset n°3	1.6	5.52	**34.8**
Environmental dataset	1.9	-	-

Table 3 Estimation of uncertainties from numerical reconstruction by the Mean Reconstruction Bias (MRB; Eq. 9) for the misfit between the "true" concentration, diffusive flux and production rate values and the "reconstructed" concentration, flux and rate values. Maximum values for diffusive flux and production rate (in bold) defined the uncertainty due to numerical reconstruction (Table 5).

the maximum concentration, *i.e.* at the peak of the localized production zone. When comparing the concentration profiles extracted from the middle section of the model domain, there are no visible differences between the two vertical profiles of C^{ideal} and $C^{estimated}$ (Fig. 39d). The Mean Reconstruction Bias (MRB) ranges from 0.6 to 2.2 % over the three datasets (Table 3, first column).

Figure 40 shows the results of the vertical flux estimation (horizontal fluxes lead to same conclusions and are not shown). Figure 40a shows the original fluxes $J_z^{ideal}(y,z)$, where the blue and red colours represent upward and downward fluxes respectively. As expected for datasets 1 and 2, there are two localized zones of high fluxes on either side of the production maximum, confirming that dissolved iron is

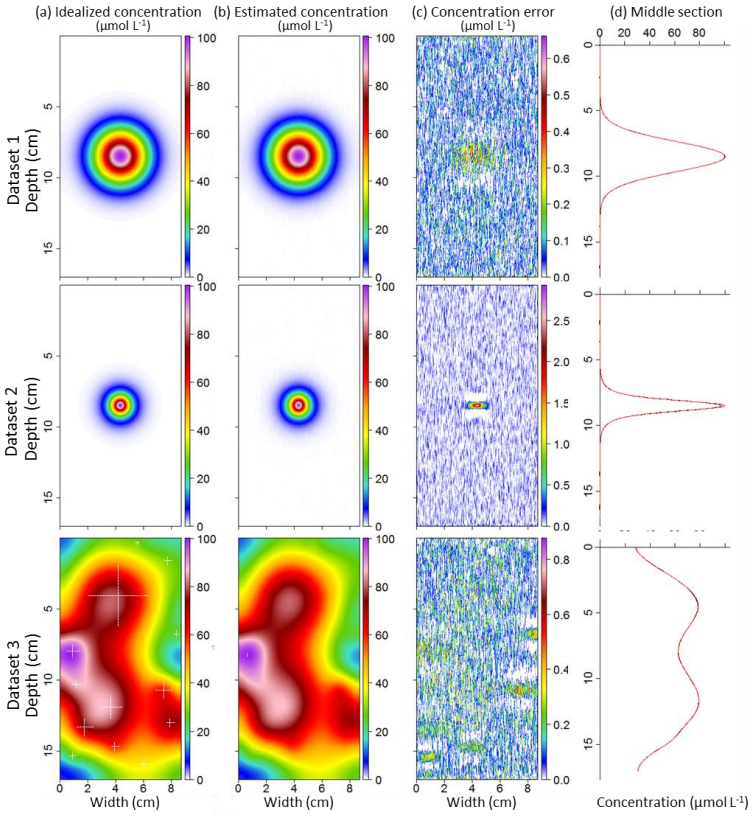

Figure 39 Savitsky-Golay filter (SGF) procedure applied on 2D synthetic datasets (a) idealized concentration distribution $C^{ideal}(x,y)$ (white crosses on dataset 3 indicate the position of most important production patches), (b) "estimated" concentration $C^{estimated}(x,y)$, (c) error on the concentration estimation $\Delta C(x,y)$ and (d) vertical profile extracted from the middle section of C^{ideal} (red) and $C^{estimated}$ (black).

diffusing out the localized production zone in opposite directions. Because fluxes are based on first order derivatives of the "noisy" concentration, these flux distributions are *a priori* more difficult to reconstruct than concentration distributions (the higher the order of the derivatives, the more sensitive to the noise). Figure 40b depicts $J_z^{estimated}(y,z)$ and the reconstruction bias $\Delta J_z(y,z)$ is shown in the Fig. 40c. Vertical profiles (Fig. 40d) show small differences between $J_z^{ideal}(y,z)$ and $J_z^{estimated}(y,z)$. The Mean Reconstruction Bias Indicator ranges from 3.8% to 7.2% (Table 3, second column).

The 2D distribution of the "idealized" production rate $R^{ideal}(y,z)$ is shown in Fig. 41a for the three synthetic datasets. An accurate reconstruction of $R^{estimated}(y,z)$ (Fig. 41b) is more challenging than for fluxes, as it is based on the second-order spatial derivatives of a "noisy" concentration profile. The higher the order of the derivatives, the more susceptible their numerical reconstruction is to noise. The MRB (Table 3, third column) is 12.2% for the broad production patch (dataset n°1) and 31.9% for the narrow production patch (dataset n°2; table 3). These results illustrate the difficulty to simulate narrow localized production zones that generate steep gradients in concentrations. The third dataset presents a higher MRB of 34.8%. Yet overall, the reconstructed production rate pattern (Fig. 41b) closely resembles the original pattern (Fig. 41a). The SGF procedure is able to correctly localize all production patches, even those production zones that are not immediately evident from the concentration dataset. The narrow production zone in synthetic dataset n°3 showed the highest reconstruction error ($\Delta R(y,z)$; Fig. 41c). The vertical transect in Fig. 41d showed a good agreement between $R^{ideal}(y,z)$ and $R^{estimated}(y,z)$, but also revealed noise that is not completely smoothed out by the SGF procedure.

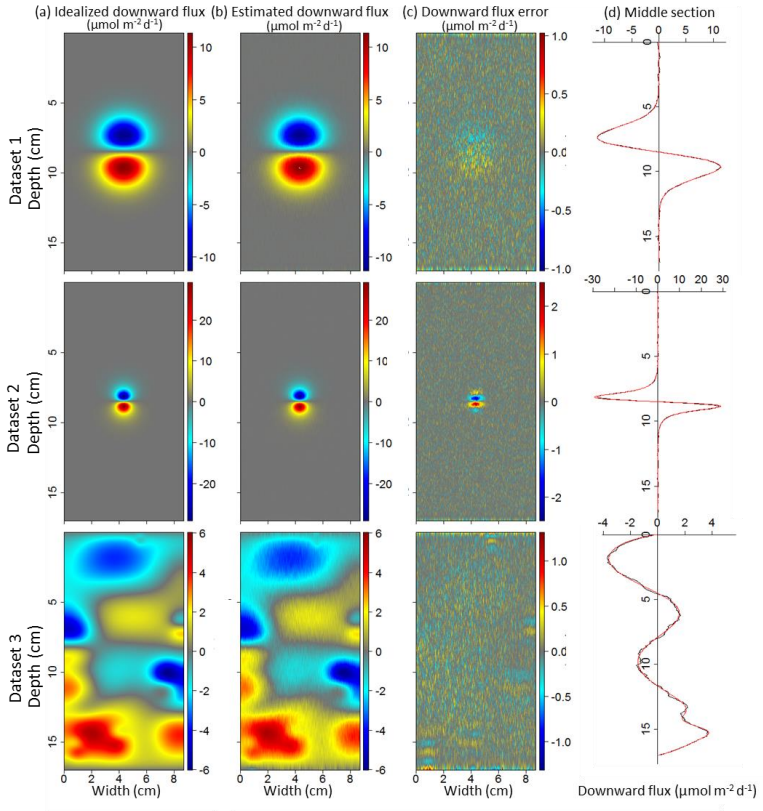

Figure 40 SGF procedure applied on 2D synthetic datasets: (a) idealized flux distribution $J_x^{ideal}(x,y)$, (b) "estimated" flux $J_x^{estimated}(x,y)$. In red: positive downward fluxes. In blue: upward fluxes, (c) error on the downward flux estimation $\Delta J_x(x,y)$ and (d) vertical profile extracted from the middle section of $J_x^{ideal}(x,y)$ (red) and $J_x^{estimated}(x,y)$ (black).

3.3.2 Model analysis of the field dataset

The measured two-dimensional distribution of dissolved iron in the pore water of the Loire estuary mudflat is shown in Fig. 42, alongside the one-dimensional depth profile in porosity. Overall, the sediment is highly porous (mean porosity of 0.86 in the top 5 cm), indicating that fine-grained cohesive mud is accumulating at the field site. However, this porosity depth profile shows a clear subsurface minimum at 0.9 cm depth (Fig. 42a), which is most likely the result of a recent sedimentation event, where a layer of more coarse grained material has been deposited in between two layers of fine-grained sediment. Below this subsurface negative peak, the porosity depth profile gradually declines with depth, as expected from a compacting cohesive sediment. To keep the analysis tractable, we did not attempt to reconstruct the subsurface maximum of porosity, but instead, we captured the overall porosity decrease by fitting an exponential function to the measured porosity depth profile (Fig. 42a; α=0.39, ϕ_0=0.93 and ϕ_{inf}=0.81).

Figure 42b shows the 2D Fe_d distribution that was experimentally retrieved at the field site. This 2D profile was cropped at the left, right borders (by 1 cm) and at the bottom (by 0.8 cm) to remove boundary effects, such as lateral diffusion from the pore water (Harper et al., 1997) or partial desiccation of the gel during experimental handling. The sediment-water interface was estimated from graduations drawn on the DET-2D probe frame during deployment and the overlying water section of the 2D profile was also removed (the final model domain was 7.7 cm x 16.2 cm). Overall, the 2D distribution of Fe_d concentration was highly heterogeneous, with clear zones of iron accumulation interspersed with zones of iron depletion. Apart from the 3 first millimetres near the sediment-water interface, which formed a layer uniformly

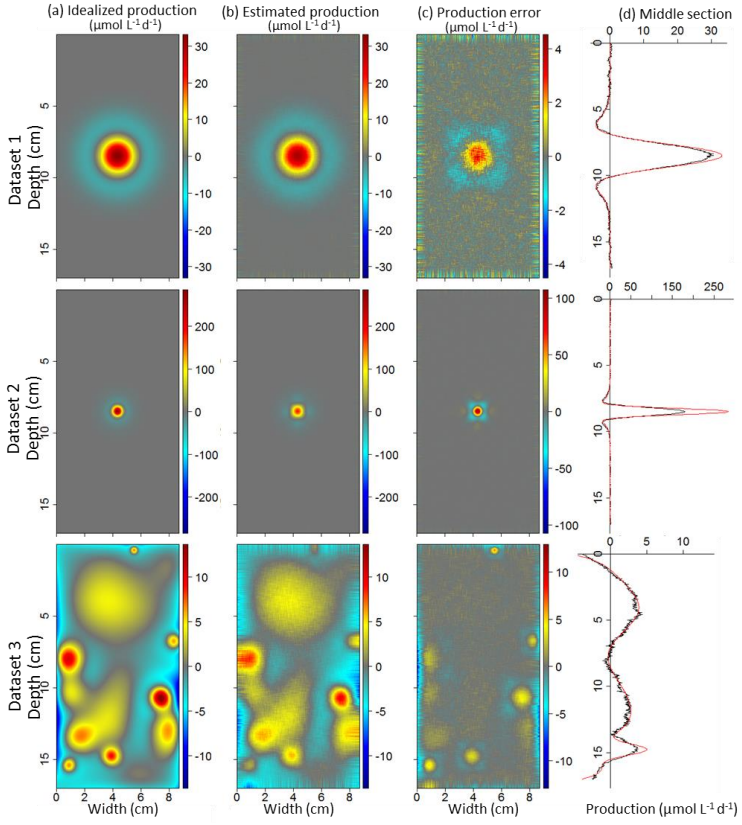

Figure 41 SGF procedure applied on 2D synthetic datasets: (a) idealized reaction rate distribution $R^{ideal}(x,y)$, (b) "estimated" reaction rate $R^{estimated}(x,y)$, (c) error on the reaction rate estimation $\Delta R(x,y)$ and (d) vertical profile extracted from the middle section of $R^{ideal}(x,y)$ (red) and $R^{estimated}(x,y)$ (black).

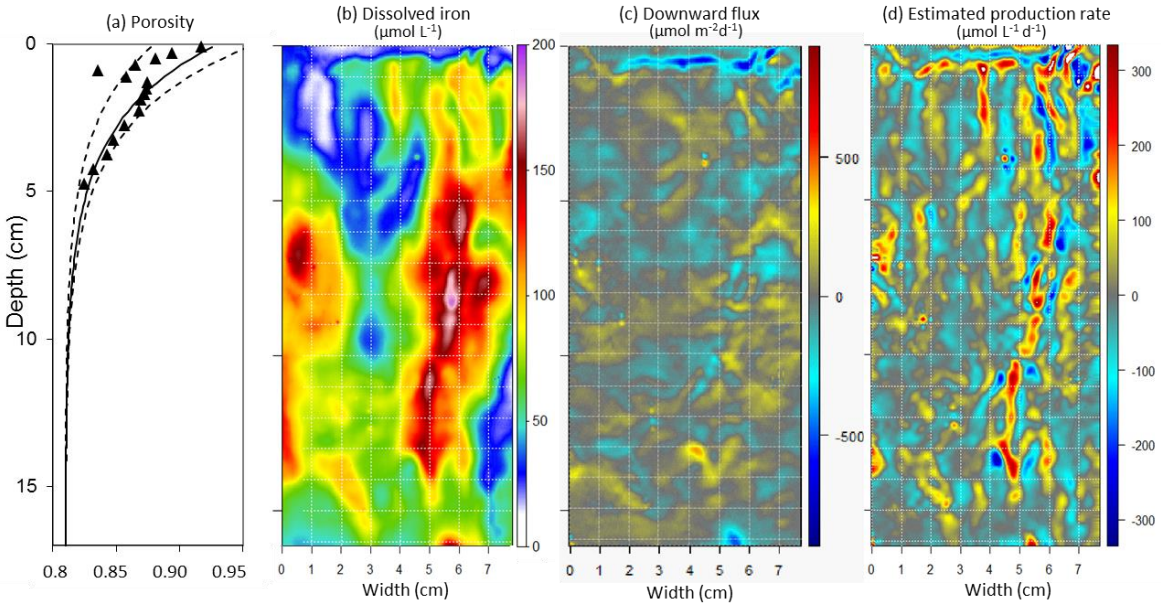

Figure 42 Two dimensional Savitzky-Golay procedure applied on experimental dataset: (a) porosity profile (triangle) and modelled exponential functions of porosity (plain line); the uncertainty on the porosity used to estimate parameter sensitivity is represented by the dotted lines, (b) experimental dataset of dissolved iron concentration in false colour, (c) estimated downward flux from SGF (downward flux in red and upward flux in blue) and (d) estimated reaction rate from SGF.

depleted in iron, no vertical stratification was observable. The dominant features were two vertically elongated "ridges" (width ~2 cm; length ~10 cm) showing high Fe_d concentrations (maximum 150 - 200 µmol L^{-1}) that extended between 5 and 15 cm depth. Alongside, there were narrow, vertically elongated zones of low Fe_d concentrations (0 - 20 µmol L^{-1}), which penetrated as iron-depleted "fingers" into deeper sediment (top left and bottom right of Fig. 42b).

Fig 42c shows the reconstructed 2D flux pattern in the vertical direction (z-axis) as obtained by the SGF procedure. In an idealized 1D-stratified marine sediment, dissolved iron produced by dissimilatory iron reduction typically precipitates near the sediment-water interface upon contact with O_2 and also in the deeper layers upon contact with H_2S. Accordingly, one would expect a bimodal flux distribution, with upward fluxes in the upper layer of the sediment and downward fluxes in deeper sediment horizons. Such a pattern was however not observed. Instead, a very heterogeneous "crest and trough" pattern was recorded, where localized zones with a downward flux (yellow areas) were interspersed with localized zones having an upward flux (blue areas - Fig. 42c). Only near the sediment-water interface, there was a horizontal layer between 0.2 and 0.7 cm depth, where the flux was uniformly directed upwards (a mean upward flux of 193 µmol m^{-2} d^{-1} and maximum flux of 736 µmol m^{-2} d^{-1}). The fluxes in the upper 0.2 cm of the sediment are however lower (mean upward flux of 101 µmol m^{-2} d^{-1}). This transition matches the oxygen penetration depth of 0.2 ± 0.02 cm (n=18; Thibault de Chanvalon et al., 2015), thus suggesting an oxidative removal of dissolved iron near the oxygen penetration depth, which hence reduces the efflux of dissolved iron across the sediment-water interface.

Figure 42d shows the reconstructed production rates, which were also characterized by a heterogeneous spatial distribution. The reconstructed rates span a broad range between consumption and production (99% percentile range = -223 to 274 µmol L^{-1} d^{-1}). Below the top 1 cm, we observed a fragmented pattern, where localized "crests" (small production zones elongated in the vertical direction) were running in parallel to localized "troughs" (narrow consumption zones stretched in the vertical). The production crests matched the Fe_d maxima in the concentration plots, while the production troughs corresponded to the edges

of zones with high Fe_d concentrations. Conversely, along the zones of low Fe_d concentrations, the position of the consumption troughs matched the Fe_d minima, while the production crests corresponded to the edges of the zones with low Fe_d concentrations. Between 0.2 and 0.4 cm depth, Fig. 42d indicates a horizontal layer of iron consumption (minimum -380 µmol L^{-1} d^{-1}; mean -30 µmol L^{-1} d^{-1}), which is followed by a deeper layer of production between 0.6 and 0.9 cm (maximum 586 µmol L^{-1} d^{-1} ; mean 59 µmol L^{-1} d^{-1}). This alternation matches the flux pattern discussed above.

3.3.3 Diffusive flux across the sediment-water interface

As coastal and shelf sediments are important sources of Fe_d to overlying waters, it is crucial to be able to reliably estimate the diffusive flux across the sediment water interface. Typically, this is done by applying Fick's first law to a one-dimensional pore water depth profile, obtained by pore water extraction from vertical slices of sediment. The concentration gradient required in Fick's first law is then determined by linear regression on the data point immediately below the sediment water interface. Here, this pore water extraction procedure was simulated by suitably averaging the 2D concentration distribution (equivalent to 0.5 cm depth slices; Fig. 43a).

The diffusive flux of Fe_d obtained by applying Fick's first law to the resulting 1D profile is 395 µmol m^{-2} d^{-1} (Fig. 43a). This flux value can be compared to the average of the J_z values obtained by the SGF procedure at each pixel point along the sediment-water interface (Figs. 43b and 43c), which provides a flux value of 97 µmol m^{-2} d^{-1} (sd= 99 µmol m^{-2} d^{-1}, n=369). The 2D method calculates the mean flux across a straight horizontal line, and hence, it neglects any surface topography, which may impact the diffusive flux. However, as shown by Røy et al. (2005) for the diffusive flux of oxygen, this topography effect leads to relatively small deviations on the order of ~10%. Instead, the correct vertical positioning of the SWI has a more important impact. The topography of the sediment, and possibly also the sediment sampling and the handling of the 2D-DET gel, generates an uncertainty of at least 1 mm on the vertical positioning of the sediment-water interface (SWI). To assess this

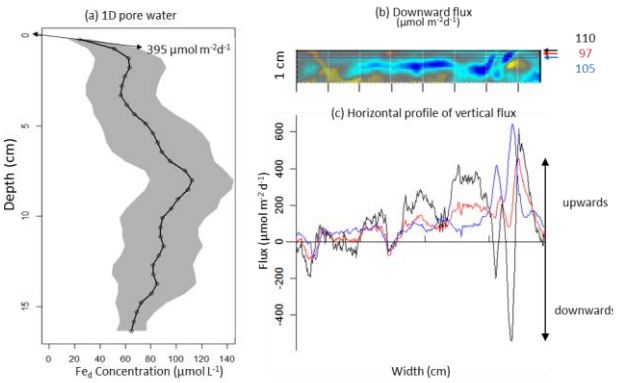

Figure 43 Sediment-water interface estimated flux: (a) 1D iron profile averaged over 0.5 cm thick layers extracted from the 2D iron distribution, grey area represent ±1 standard deviation; the arrow indicates the chemical gradient extracted and the corresponding flux, (b) position of the sediment water interface (SWI) in red, and the uncertainty of ±1 mm on its position (in black and blue); the corresponding averaged dissolved iron upward fluxes estimated from the 2D SGF procedure are indicated in µmol m^{-2} d^{-1} and (c) lateral variability of benthic fluxes according to the SWI position.

uncertainty, we calculated the flux at 1 mm above and below the original interface, which provided a flux of 110 µmol m^{-2} d^{-1} and 105 µmol m^{-2} d^{-1} respectively (Fig. 43b and 43c). These 2D fluxes are hence highly comparable (sd=7 µmol m^{-2} d^{-1}; n=3) despite the large lateral variability in flux values generated by the small scale of our sampling. Overall, the 2D flux obtained (mean of three sections 104 µmol m^{-2} d^{-1}) is 4 times lower than the value obtained by the corresponding 1D analysis (395 µmol m^{-2} d^{-1}). These differences in fluxes are likely due to difference in resolution between the conventional 1D approach (resolution of 5 mm) and the high-resolution 2D approach implemented here (resolution of 0.2 mm). Because the oxygen penetration is shallow (~ 2 mm), intense iron oxidation and precipitation occurs within the upper millimetres, which is beyond the resolution of the conventional 1D approach. Oxidative consumption of Fe_d in the 0.2-0.5cm layer (Fig. 42d) likely decreases the iron release to the overlying water column. This highly localized zone of aerobic iron oxidation is not suitably accounted for by the 1D procedure, thus overestimating the iron efflux from the sediment.

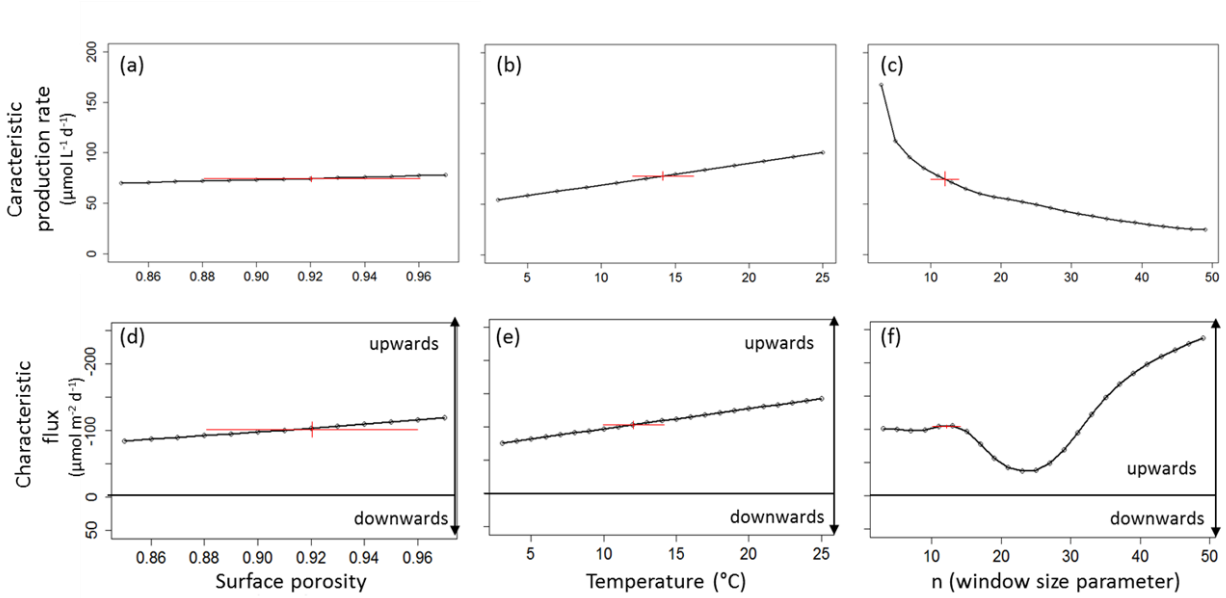

Figure 44 Sensitivity of the model to parameters uncertainty: (a-b-c) standard deviation of the production rate distribution, (d-e-f) Flux across water-sediment interface (black line) with uncertainty due to interface positioning (± 1 mm; grey area); red crosses indicate experimental parameters uncertainties (horizontal branch) and corresponding impact on modelling uncertainty (vertical branch).

3.3.4 Uncertainty assessment

The SGF procedure estimates the fluxes and rates within the pore water, and to this end, it requires a set of input parameters (salinity, temperature, porosity). These parameters are always determined with some experimental uncertainty, and hence, one could ask how sensitive the reconstructed fluxes and rates are to this experimental uncertainty. At the same time, the SGF procedure is also crucially dependent on the choice of the size of the filter window (the smoothing parameter n), which is in the approach here, automatically determined by fractal analysis (see methods). Accordingly, one can also ask how sensitive the reconstructed fluxes and rates are to the numerical selection of the filter window.

To analyse the sensitivity of our reconstruction approach to these input parameters (salinity, temperature, porosity, and filter window), we used the field dataset and varied a single input parameter over a suitable range (each time repeating the SGF procedure and keeping the other input parameters at their baseline value). Salinity variation did not have an important effect (results not shown). This is because the effect of salinity variations on the diffusion coefficient is one hundred times less important than temperature. Figure 44 shows the importance of the variation of surface porosity, temperature and filter window size, on a characteristic production rate (the standard deviation of the estimated production rate distribution) and on a characteristic flux (the mean estimated flux across the sediment-water interface). For each parameter, the SGF procedure is applied for a range of values and the corresponding values of the characteristic production rate and the characteristic flux are calculated.

		Model uncertainty	
	Range of parameter uncertainty	Characteristic flux (µmol m^{-2} d^{-1})	Characteristic production rate (µmol L^{-1} d^{-1})
Temperature	12-16 °C	100,5-112,7 (± 6%)	72,7-81,5 (± 6%
Salinity	2-4	-	-
Surface porosity	0,88-0,96	92,5-116,1 (± 11%)	73,8-79,3 (± 3%
Window size	10-14 n	101,5-106,6 (± 2%)	84,3-70,1 (± 9%
Parameters sensitivity		± 13%	± 11%

Table 4 Estimation of uncertainties from parameters sensitivity. Parameter uncertainties (1st column) are represented by the vertical branch of red crosses from Fig.44. The uncertainties induced on the characteristic flux and on the characteristic production rate correspond to the vertical branch of the Fig.44 and are indicated in the 2nd and 3rd column. The overall uncertainties from parameters sensitivity are calculated by quadratic sum and are reported in the Table 5.

The horizontal red lines in Fig. 44 indicate the experimental uncertainty on the values of surface porosity and temperature, as estimated for the sediment at the field site at the time of sampling (surface porosity range from 0.88 to 0.96; temperature range from 11°C to 15°C). The uncertainty on the filter window size was determined by verifying the uncertainty on the automated detection of the breakpoint in the slope of the fractal dimension D (see methods). The associated uncertainty in the characteristic production rate and characteristic flux are indicated by the vertical red lines in Fig. 44, and are also summarized in Table 4. Overall, the reconstructed production rate is particularly sensitive to the filter window size (Fig.44c) which induces an uncertainty of ± 9% while the reconstructed flux is particularly sensitive to surface porosity variations which induces an uncertainty of ± 11% (Table 4).

Figure 44c shows that an increase of the filter window size (n), decreases the characteristic production rate. This is due to a smoothing of reconstructed concentration data that averages localized production and consumption zones (Fig. 44c). In contrast, Fig. 44f shows a non-linear relation between the characteristic flux and the window size. For larger window sizes (more important smoothing), the characteristic flux first decreases and then increases again. This specific response arises because of the consumption of Fe_d near the oxygen penetration depth, so the Fe_d concentration quickly increases below the oxygen penetration depth (thus increasing the flux for

	Diffusive flux ($\mu mol\ m^{-2}\ d^{-1}$)	Production rate ($\mu mol\ L^{-1}\ d^{-1}$)
Parameters sensitivity	± 13%	± 11%
Numerical reconstruction	± 7%	± 35%
Surface topography	± 10%	-
Surface positionning	± 7%	-
(consumption inside the burrow lumen)	-	*(± 37%)*
SGF uncertainty	± 19%	± 37% *(± 52%)*

Table 5 Overall estimation of the SGF procedure uncertainties. Uncertainty from numerical reconstruction and parameter sensitivity are from Table 3 and Table 4 respectively. Uncertainty for surface topography is from Røy et al. (2005) and uncertainty for surface positioning corresponds to the relative standard deviation of the 3 transects used to calculate the diffusive flux across the SWI. The overall uncertainties are calculated by quadratic sum.

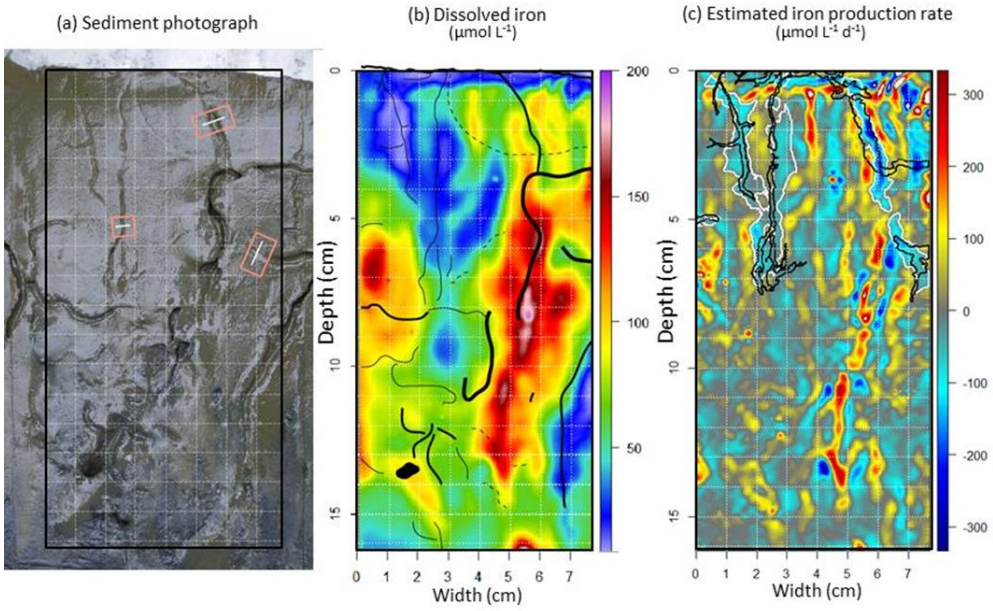

Figure 45 (a) Photograph of the sediment plate with a centimetre grid (white dashed lines); continuous lines within pink rectangles correspond to the 3 examples of cross-sections studied (Fig. 46), (b) dissolved iron concentration in false colour with schematic representation of burrows and (c) Fe_d production rate estimated by SGF, with delimitations of active burrows' surfaces; in black, direct identification by superimposition on the sediment photograph and in white, delimitation according to the interpretation of consumption.

large filter windows). The minimum flux estimated for n=24 is induced by a short plateau on Fe_d at 4mm depth that generates a decrease of the slope (thus of the estimated flux) for intermediate filter windows.

Finally, the quadratic sum of each input parameter uncertainty (temperature, porosity and windows size) generates a "parameters sensitivity uncertainty" of about 11 % for the production rate and 13 % for the flux across the SWI (Table 4). The uncertainty of the whole SGF procedure is calculated by the quadratic sum of (1) the maximal error of numerical reconstruction estimated from the synthetic dataset (§3.3.1; Table 3, bolt values), (2) the "parameters sensitivity uncertainty" (see above; Table 4), (3) the impact of non-linear topography and (4) the error for surface positioning (§3.3.3). Combination by quadratic sum is summarized in the Table 5 and leads to an error of 37% on the characteristic production rate and of 20 % on the characteristic flux. These values are comparable with benthic chamber measurement (*e.g.* Severmann et al., 2010).

3.4 Discussion

3.4.1 Impact of burrow networks on iron cycling

Figure 45 illustrates the close relation between sedimentary features and Fe_d production. Macrofauna renew the water of their burrows with oxygen-rich and Fe_d-poor water obtained from the overlying water column (*e.g.* Meysman et al., 2006). Accordingly, one expects low Fe_d inside actively flushed burrows, as dissolved iron is either transported out of the burrow or aerobically oxidized. This bio-irrigation effect is clearly observable in the top 4 cm of the sediment, where the lumens of macrofauna burrows show a strong depletion in dissolved iron (from 150 µmol L^{-1} in the surrounding area to detection limit in the burrow lumen; Fig 45b; burrows in upper left part). These burrow linings are generally also zones of dissolved iron consumption, surrounded by "linings" of iron production (Fig. 45c). Below 4 cm depth, the relation between burrow systems and the associated Fe_d concentration distribution becomes more complex to interpret. For example, the right hand side of the investigated sediment domain shows a large and well-defined burrow system, of which the deeper parts are associated with elevated iron concentrations (Fig. 45b; red zone at z=5-14 cm, y=4-6.5 cm). From the concentration image alone, one would associate the deeper burrow part with iron production. Similar burrow enrichment is reported by Zhu and Aller (2012) and Cesbron et al. (2014) and is interpreted as abandoned burrows favourable for iron transport. However, when closely scrutinizing the image of the reconstructed production rate (Fig. 45c), one clearly observes a long stretch of consumption penetrating downwards, right where the burrow is, which is flanked by zones of intense production. Overall, the "vertical fingering pattern" with elongated zones of alternating production and consumption zones (Fig. 45c) is striking, and corresponds to a large extent to the presence of vertically oriented burrows. Accordingly, it is clear that iron mobilization takes place in the immediate vicinity of the burrow walls, confirming that burrow construction and ventilation have a considerable impact on sedimentary iron cycling (Aller, 1982; Zhu and Aller, 2012; Cesbron et al., 2014).

To better document the iron cycling near the burrows, Figure 46 displays a detailed zoomed-in image of three separate burrows (pink rectangles in Fig. 8a). The Fe_d concentration profiles and corresponding production rates are shown along transects across the burrow (white line segments in Fig. 45a). Dissolved iron concentrations typically decrease towards the burrow centre, designating iron removal inside the burrow. The production rate transects reveal more detail and allow four separate zones to be distinguished: (1) the burrow lumen displaying strong consumption (2) an inner burrow wall zone with moderate consumption rate, less than inside the burrow, (3) an outer burrow wall zone showing intense production, and (4) the far field away from the burrow that shows either low iron production or consumption.

The removal of Fe_d within the burrow lumen (the grey shaded area in Fig. 46b) is most likely the result of burrow flushing, and the oxidation state of the iron that is exported into the overlying water will largely depend on the oxygen level in the ventilated burrow water. Recently, planar optode studies have demonstrated that burrow flushing can result in plumes of anoxic water

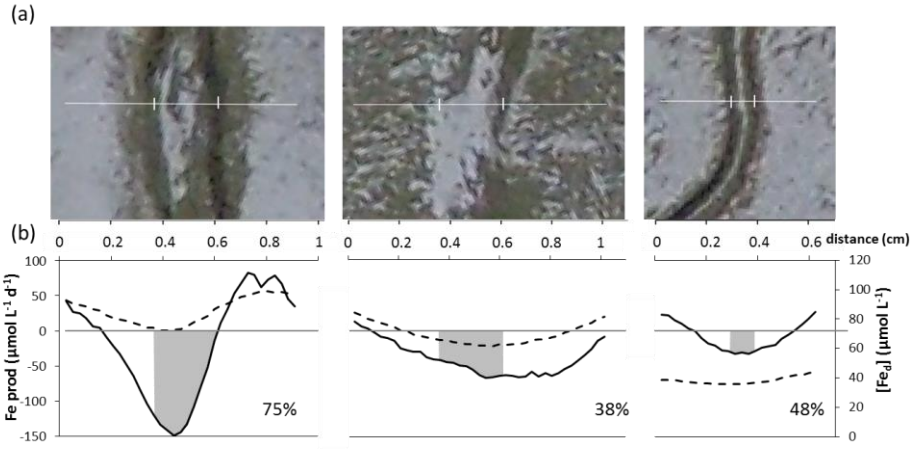

Figure 46 (a) Zoom of the photograph on the three red rectangles from the Fig. 8a: in white, the selected transect across burrow with vertical white bars identifying burrow linings, (b) Fe_d concentration (dotted line) and production rate (black line) along the selected transects with grey areas identifying burrow lumen; percentages of iron consumption inside the burrow bore relatively to the total consumption estimated on the transect are indicated.

that are expelled from the sediment (Volkenborn et al., 2012). If this is the case, ferrous iron will be transported out of the burrow lumen. However, if the burrow water is sufficiently oxygenated, ferrous iron will be oxidized as nanoparticles in suspension (Taillefert et al., 2000; Raiswell et al., 2008), colloïds (Wells and Goldberg, 1994; Huerta-Diaz et al., 2007; Homoky et al., 2011) or form stable dissolved organic-Fe(III) complexes (Liu and Millero, 2002; Gledhill and Buck, 2012). The removal of Fe_d within the first 1-4 mm of the burrow wall (zone 2) is likely the result of oxygen diffusing from the burrow into burrow wall, and reacting with reduced iron (Aller, 1982). This process will produce the accumulation of iron (hydr)oxides within the burrow wall, which are sometimes visible as such orange mineral enrichments that line the burrow. In a transient situation (*e.g.* when the O_2 level in the burrow decreases), these iron (hydr)oxides may again give rise to ferrous iron mobilization, when used for organic matter degradation through dissimilatory iron reduction (Lovley, 1991) or abiotic reduction with hydrogen sulphide (Canfield, 1989; Kostka and Luther, 1995; Theberge and Luther, 1997). This may be one explanation for the observed production in the subsequent outer burrow wall zone. Such reduction of freshly precipitated of Fe(III) may be particularly enhanced once the burrows are abandoned. However, alternative processes for Fe_d formation could be FeS dissolution due to low pH around burrows (Hulth et al., 2002; Rickard, 2006; Zhu et al., 2006). Finally, the iron production/consumption in the far field away from the burrow will be determined by the local availability of geochemical reagents (*e.g.* sulphide, labile organic matter).

3.4.2 Bio-irrigational flux of dissolved iron

In §3.3.3, we estimated the diffusive flux of Fe_d across the sediment-water interface ($\bar{J}_{dif}$ = 104 ± 20 µmol Fe m^{-2} d^{-1}; uncertainty of 19%, see Table 5). However, in coastal sediments subject to bio-irrigation, this only forms one component of the sediment-water solute exchange. One has to additionally account for the bio-irrigational flux across the sediment-water interface $\bar{J}_{irr}$, which is generated by the flushing of ventilated burrow networks (Aller, 2001; Meile et al., 2001; Wenzhofer and Glud, 2004). To this end, we can calculate the amount of Fe_d removed from each individual burrow (F_{burrow}), expressed as mass per unit of time (*e.g.* mmol Fe d^{-1}). The bio-irrigational flux is then given by the summation over all burrows and normalized per unit of sediment surface area:

$$\bar{J}_{irr} = \left(\sum F_{burrow}\right)/(d_{sed} L_{sed}) \qquad (22)$$

The sediment area normalization is done by the width L_{sed} of the studied sediment domain (width of the 2D-DET gel analysed: 7.7 cm) and the thickness d_{sed} of

the analysed sediment domain (note that d_{sed} drops out further, and that there is no need for knowing the sediment thickness sampled by 2D-DET in front of the gel).

The burrow removal rate (F_{burrow}) can be calculated in two separate ways. In a first procedure, one assumes that F_{burrow} must be equal to the mass of Fe_d that diffuses across the burrow lining into the burrow. The SGF procedure is able to provide the horizontal and vertical fluxes in each point (*i.e.* the two component of the flux vector – see Fig. 42c). So, in theory, F_{burrow} can be calculated as the line integral of the diffusive flux (J_{dif}) over the burrow lining (described by the infinitesimal distance *dl* oriented by its normal vector *n*):

$$F_{burrow} = d_{sed} \int_{burrow\ lining} J_{dif}.n\ dl \qquad (23)$$

Note that the "burrow lining" is not a closed surface area, but the line contour of the burrow in the 2D image of the sediment (see Fig 45c). Because of our planar 2D approach, the line integral is multiplied by the thickness d_{sed} of the analysed sediment domain (note that d_{sed} drops out of the equation when applying Eq. 22 to calculate the bio-irrigation flux).

This procedure hence requires (1) the visual identification of all burrow linings from the sediment photograph. Only burrows that showed clear iron depletion were considered as actively flushed burrows and were taken into account, (2) the superimposition of these burrow linings onto the 2D false coloured image of the reconstructed flux, and (3) the numerical calculation of the line integral. According to the lining shown in black in the Fig. 45c, this procedure generates a bio-irrigation flux of $\bar{J}_{irr}$ = 250 ± 50 µmol $m^{-2}d^{-1}$. The uncertainty corresponds to the general uncertainty (19%) derived above for flux reconstruction by the SGF procedure (Table 5). However, we also found that this procedure was very sensitive to the correct delineation of the burrow linings, and the uncertainty is likely much larger. For example, small spatial offsets can occur between the sediment image and the 2D-DET gel, due to a slight modification of the sediment position during retrieval and transport, or the transformation of the gel geometry during freezing and thawing. For this reason, this first approach for calculating the bio-irrigation flux was not pursued any further.

In a second procedure, we still assume that F_{burrow} represents the mass of Fe_d that diffuses across the burrow lining into the burrow. By means of mass balance, and assuming steady state, the burrow removal rate must be equal to the integral of the production rate over the burrow lumen (Eq. 24), with *dA* the infinitesimal surface of the burrow lumen in contact with the 2D-DET gel.

$$F_{burrow} = -d_{sed} \iint_{burrow\ lumen} R\ dA \qquad (24)$$

Again we made a distinction between actively flushed and non-flushed burrows, but this time, this was done based on the 2D production image (only burrows that showed a clear consumption of dissolved iron were considered as actives). So, based on a combination of the sediment image and consumption areas, we identified actively flushed burrows. This approach avoids any spatial offsets between the sediment image and the 2D-DET gel. Subsequently we delineated the areas of dissolved iron consumption around burrow lumens on the 2D production image. These areas were constrained by the "zero production contour", *i.e.* the line where dissolved iron consumption (negative R) changed into iron production (positive R; boundaries indicated by white lines in Fig. 45c). Application of the above surface integral over these zones provided a value for the bio-irrigational flux of 745 ± 276 µmol m^{-2} d^{-1}. The uncertainty corresponds to the general uncertainty (37%) derived above for production rate reconstruction by the SGF procedure (Table 5). However, this is an overestimate of the true bio-irrigational flux, as the delineated areas of dissolved iron consumption around burrow lumen likely include parts of the burrow walls. As already discussed, there is also consumption within the sediment of the inner burrow wall, which occurs through re-oxidation, and hence, this does not contribute to the bio-irrigational flux. Future studies hence should concentrate on ways to better delineate burrow linings and burrow lumens in 2D-DET images. For now, we compensated for the overestimation of the

bio-irrigational flux in a simplified manner. For three burrow cross-section profiles (Fig. 46), the consumption that occurs inside the burrow lumen represents 55 ± 20% of the total consumption occurring in the burrow surrounding. When rescaling the value obtained above (745 x 0.55), we arrive at a bio-irrigational flux of 410 ± 213 µmol $m^{-2}d^{-1}$. The uncertainty of 52% is obtained by standard error propagation (quadratic sum) of parameters sensitivity (11%), numerical reconstruction (35%) and burrow lumen positioning (37%).

The total flux across the interface (sum of bio-irrigational flux and diffusive flux) is hence 514 ± 233 µmol m^{-2} d^{-1}. Since the 2D-DET procedure provides a measurement of the average pore water concentration on the time scale of a half to a few hours, this value hence represents the average flux over the 5 hour period of measurement. The bio-irrigational flux would account for 80% of the total efflux of dissolved iron, which is in agreement with the 68-99% as estimated by diagenetic model simulation for a "standard" shelf sediment (Raiswell and Canfield, 2012). These values illustrate the importance of bio-irrigation for dissolved iron fluxes in coastal environments. These total iron fluxes are also higher than those based on benthic chamber measurements (Elrod, 2004; Severmann et al., 2010), which report total Fe_d fluxes less than 30 µmol d^{-1} m^{-2} for environments where oxygen levels in the overlying water exceed 100 µmol L^{-1}, while higher values up to 568 µmol d^{-1} m^{-2} are reported for hypoxic environments. Although intertidal, the overlying water during high tide in the estuarine setting studied here is fully oxygenated, and hence, the total Fe_d flux reported here is substantially larger than previously reported values for well oxygenated water columns. First, this can be related to our model approach which assumes a complete transfer to the water column of all removed iron, while in reality, some of this iron may freshly precipitate inside the burrows and stick to the burrow lining (Raiswell, 2011; Homoky et al., 2012). Secondly, an important part of dissolved iron release in benthic chamber is likely to precipitate before being measured (Pakhomova et al., 2007; Severmann et al., 2010). Thirdly, our study site is intertidal and has a high burrow density and active bio-irrigating fauna (*e.g.* Kristensen et al. (2014) for a low salinity environment compared to Wheatcroft (2006) for continental shelf). This likely induces higher bio-irrigational fluxes than the environments where dissolved iron fluxes have been measured by benthic chambers. A forth important factor governing benthic iron recycling is the relative weakness of sulphur cycling (SO_4^{2-}/Na^+ constant within the top 12 cm; unpublished data) compared to the coastal environments where previous flux measurements have been performed (Elrod, 2004; Severmann et al., 2010). Consequently, sulphate reduction is likely substantially lower, and hence less sulphide is produced that would react with iron and immobilize it. Important iron fluxes under oxygenated water column conditions were recently reported by Pakhomova et al. (2007) for a coastal, low salinity environment (Vistula Lagoon; Baltic Sea), reporting Fe_d fluxes between 40 and 270 µmol d^{-1} m^{-2}. Similarly, an Fe(III) flux between 8 and 227 µmol d^{-1} m^{-2} was estimated by Jones et al. (2011) for estuarine sediment at low salinity (Satilla river estuary, Georgia, USA). These studies, in combination with the results obtained here, indicate that coastal sediments can release substantial amounts of dissolved iron under an oxygenated water column.

3.4.3 An iron budget of a coastal sediment

Figure 47 presents the tentative iron budget calculated for one square meter of sediment at the Loire field site. The "apparent recycling rate" (ARR) is defined as the transfer of iron from the dissolved phase back to the solid phase of the sediment, expressed for 1

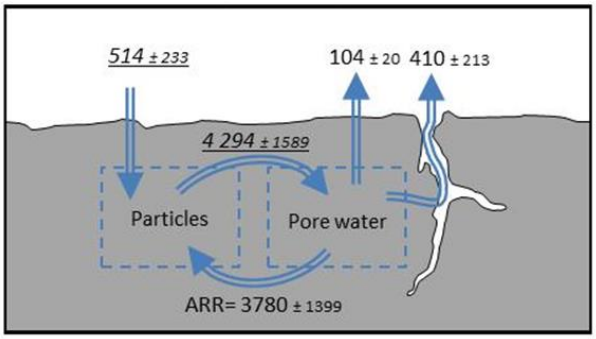

Figure 47 Small scale iron recycling in a suboxic iron-rich sediment in µmol m^{-2} d^{-1}; diffusive flux (104±20) and bio-irrigational flux (410±213) across the water sediment interface are differentiated; values underlined and in italic are calculated assuming steady state.

m^2 of mudflat. The ARR is calculated by (1) integrating the production rate for all pixels that show a negative production rate (i.e. iron consumption) over the whole sediment domain (7.7 cm x 16.2 cm), (2) dividing this quantity by the domain width (L_{sed} = 7.7 cm), and (3) subtracting the bio-irrigational flux (this part of the "consumption" is not truly recycled, but actually leaves the sediment). The word "apparent" is chosen to highlight that the calculation assumes (1) steady state and (2) that within a given pixel only consumption occurs (and no production). This may not always be the case, as within a given localized spot, crypting Fe cycling could occur within the pore water (*i.e.* production and consumption occur at the same time, so the actual consumption is larger). Moreover, it should be noted that if the steady state assumption is not satisfied, the ARR also includes temporal variations (Eq. 1). Applied to the 2D-DET data, we arrive at an ARR of 3780 ± 1399 µmol m^{-2} d^{-1}. An equivalent estimation can be done based on the production rate (*i.e.* only accounting for areas where production is positive) and this provides a value for the "apparent production rate" (APR) of 4240 ± 1569 µmol m^{-2} d^{-1}. Note that in a steady state the APR should match the sum of the ARR (3780 µmol m^{-2} d^{-1}), the diffusive flux across the sediment-water interface (104 µmol m^{-2} d^{-1}) and the bio-irrigational flux (410 µmol m^{-2} d^{-1}). Accordingly, the iron budget estimated here shows only a small deficit of 1.4% (54 µmol m^{-2} d^{-1}), which remains within the uncertainty of the estimated fluxes (Fig. 47). These high ARR values imply that iron recycling is likely more important than previously thought in some coastal sediments. In comparison, the model used by Raiswell and Canfield (2012) for a "typical" shelf sediment calculated an ARR of 574 µmol m^{-2} d^{-1}, which is almost one order of magnitude below our estimate obtained here.

As the "apparent recycling rate" corresponds to the fluxes between the interstitial water and the mineral particles, it characterizes the rejuvenation rate of iron oxide in the sediment and therefore controls the age of iron particles exported to the ocean through resuspension events. The dissolved iron inventory in the pore water of the mudflat (9 680 µmol m^{-2}) can be divided by the total production rate of dissolved Fe (4294 µmol m^{-2} d^{-1}; Fig. 47) to arrive at the mean residence time of iron in the dissolved phase (here ~2.3 days). This residence time characterizes the rate of turnover of the dissolved iron pool. Furthermore, in a steady-state situation, the total efflux of dissolved iron across the sediment-water interface (514 µmol m^{-2} d^{-1}) should be matched by an equal input of iron (hydr)oxides into the sediment (Fig. 47). Each iron atom that enters the sediment goes to a number of cycles in which it is first reductively dissolved and subsequently oxidatively precipitated again. The ratio of the apparent recycling rate over the input of iron (hydr)oxides (or equally the total Fe_d efflux) reveals that each iron atom goes through n = 7.4 redox cycles.

As already noted above, this number does not account for crypting Fe cycling within the pore water. For example, in the water column of seasonal hypoxic systems, it has been shown that suspended Fe(III) (oxy)hydroxides can be reduced by H_2S to Fe(II) at the oxic–anoxic interface, and subsequently, the Fe(II) is re-oxidized to Fe(III) by O_2 above the interface (Ma et al., 2006; Findlay et al., 2014). These transformations form a catalytic redox cycle for iron, which fully occurs in suspension. One could imagine that a similar catalytic redox cycle could occur within the lumen of burrows or within the pore water of burrow linings. The 2D-DET probes employed here do not discriminate between dissolved Fe(II) and Fe(III), and hence, such internal cycling of Fe within the dissolved phase would remain undetected. According the calculated number of n = 7.4 redox cycles should be considered as a conservative estimate.

3.5 Conclusion

The SGF procedure was successfully applied on a two dimensional distribution of total dissolved iron concentrations in an estuarine sediment. The dissolved iron that is produced inside the sediment can follow three ways: (1) diffusion across SWI (2.4%), (2) removal by bio-irrigational flushing in macrofauna burrows (9.6%) and (3) reoxidation and precipitation in the sediment (88.0%). These results hence lead to two main conclusions. Firstly, macrofaunal bio-irrigation substantially increases the efflux, and therefore controls export of dissolved iron from sediments to the coastal ocean. Secondly, our results imply that iron has a high chance of being recycled, and will undergo, on average,

to at least 7.4 cycles of dissolution/precipitation before being released in the water column. This intense recycling is likely to decrease the age of crystalline iron in the sediment and therefore controls the age of particles exported to the ocean through resuspension events. Overall, the 2D SGF procedure developed here has enabled an improved quantitative insight into the geochemical cycling of iron in dynamic benthic environments such as estuarine or coastal mudflats. A better understanding of the spatial dynamics, local geochemical cycling and complex interactions could be potentially achieved by applying the 2D SGF procedure to other chemical compounds.

Acknowledgements

The research leading to these results has received funding from the Région Pays de la Loire (France) through the project RS2E-OSUNA and from the European Research Council under the European Union's Seventh Framework Programme (FP/2007-2013) through ERC Grant 306933 (FJRM).

Partie 2 :

Quantification de la transformation du fer réactif et des éléments associés lors du transfert des particules à travers l'estuaire de la Loire

Partie 2 :

1 Recyclage sédimentaire du manganèse, du fer et du phosphore dans une vasière estuarienne, Loire, France

---

A. Thibault de Chanvalon[1,2], A. Mouret[1], J. Knoery[2], E. Geslin[1], O. Péron[3], E. Metzger[1]

[1] Université d'Angers, LPG-BIAF, UMR CNRS 6112, 49045 Angers Cedex, France
[2] Ifremer, LBCM, Rue de l'Ile d'Yeu, 44300 Nantes, France
[3] Laboratoire Subatech, Groupe Radiochimie, IN2P3/CNRS/EMN/Université de Nantes, 4, rue Alfred Kastler, BP 20722, 44307 Nantes cedex 3, France

D'après l'article soumis dans Journal of Sea Research

Edited by: P. Anschutz

ABSTRACT

The sampling of a mudflat from the Loire estuary during four different seasons brings new information about geochemical cycles in estuarine sediment. Estimation of the reactive stocks of iron and manganese oxides (ascorbate buffered extraction) is interpreted together with pore water concentration. Near the shore, a ^{210}Pb profile reveals important sedimentation during winter campaign due to high flow and heavy wind conditions, that resulted in a 8-cm-deep oxide-rich layer. This initial deposition event fuelled anaerobic respiration that would slowly consume solid oxides maintaining a transitory state along several months. During 3 months, dissolved Mn reaches important concentrations due to Mn-oxide remobilisation which results in a decrease of Mn-stocks (with a rate of 1.4-0.12 mmol m^{-2} d^{-1}). During the same period, Fe-oxide would not be dissolved and thus would prevent (or at least limit) phosphorus release into pore water as shown by decreasing Fe/P ratio of ascorbate extractions. While summer starts, Fe-oxides are reductively dissolved until complete reactive oxide depletion. This second step corresponds also to saturation of Fe-oxides by phosphorus and probably maximum P release to the water column. At the distal sampling station, biogeochemical processes are less intense because flood sedimentation and biomixing of sediment are less important.

RESUME

L'échantillonnage d'une vasière de l'estuaire de la Loire au cours de 4 saisons contrastées apporte de nouvelles informations sur les cycles géochimiques des sédiments estuariens. L'estimation des stocks d'oxydes de fer et de manganèse réactifs (extraits par une solution d'ascorbate tamponné à pH=8) est interprétée en relation avec la composition de l'eau porale. Un profil de ^{210}Pb réalisé proche du rivage et pendant la campagne hivernale indique un important épisode de dépôt de 8cm de haut, probablement lié aux conditions de fort débit et de fort vent et caractérisé par une composition particulièrement riche en oxydes. Ce dépôt est suivi d'une période transitoire de quelques mois, le temps que la respiration anaérobie consomme les stocks d'oxydes déposés. Pendant les 3 premiers mois, les oxydes de manganèse sont remobilisés ce qui diminue leur stock (à la vitesse de 1,4-0,12 mmol m^{-2} d^{-1}) et produit d'importantes concentrations de Mn^{2+} dans l'eau interstitielle. Durant cette période, les oxydes de fer ne sont pas dissous et empêchent probablement (ou limitent) la libération de phosphate dans les eaux porales. Cette évolution se traduit par la diminution progressive du ratio Fe/P mesuré dans les oxydes. Au début de l'été, les oxydes de fer sont dissous jusqu'à leur disparition du sédiment. Pendant cette deuxième période, les oxydes de fer semblent saturés en phosphore ce qui génère un flux maximal de phosphate vers la colonne d'eau. Sur la station éloignée du rivage, les processus biogéochimiques sont moins intenses car tant les dépôts hivernaux, tant le biomixing sont moins importants.

1 Manganese, iron and phosphorus cycling in an estuarine mudflat sediment, Loire, France.

1.1 Introduction

The transport of particles from rivers to coastal environments induces to particles important transformations that would change the fate of reactive Fe and Mn-oxides (Thibault de Chanvalon et al., submitted; Moore et al., 1979; Church, 1986; Raiswell, 2006). Since riverine solid export represents roughly half of the total input flux of reactive iron to the ocean (Raiswell, 2006), estuarine transformations represent an important forcing on the iron cycle. Moreover, at a local scale, particle transformations are likely to strongly control remobilisation of numerous trace metals (*e.g.* As (Dang et al., 2014), Cr and Cu (Turner, 2000)) and of the phosphorus, a key nutrient often limiting in estuarine ecosystems (Rehm, 1985; Meybeck et al., 1988; Sundby et al., 1992; Anschutz et al., 1998).

Particles carried by the river generally stop in the estuary due to the specific hydrodynamics and are stored in sediment, such as mudflat, until the next river flood (Ciffroy et al., 2003b) which would release most of the particles in the coastal environment. During this storage, the important primary production of microphytobenthos benefiting from the sunny mudflat surface fuels intense heterotrophic condition in the sediment. Therefore, few millimetres below the sediment surface, microorganisms' respiration maintains an oxygen-depleted environment that requires the uptake of other oxidants as nitrate, Mn-oxides and Fe-oxides to support anaerobic respiration. Fe and Mn-oxides are thus dissolved and are released in the surrounding water (Froelich et al., 1979). In some cases, reduced Mn and Fe would precipitate in the sediment in a reduced form (*e.g.* $MnCO_3$ and FeS ; *e.g.* Van Cappellen and Wang, 1996); in some other cases, when sediment is mixed with overlying water (due to resuspension events or burrows formation), oxic conditions would favour Fe and Mn oxic precipitation (Aller and Aller, 1986). Finally, sometimes, a part of the dissolved species would not re-precipitate in the sediment and would be exported downstream therefore representing a net loss for the sediment (Watson et al., 1993). The all-over effect of transformation in estuarine sediments leads to an important loss of iron oxides and probably also an important loss of manganese oxides for riverine particles (Thibault de Chanvalon et al., submitted; Moore et al., 1979; Zwolsman and van Eck, 1999; Raiswell, 2006).

The rate of geochemical transformations in intertidal mudflat would theoretically vary according to the sedimentary stock of Mn or Fe-oxides and the intensity of surface primary production. The Mn and Fe-oxides stocks result in turn from a balance between deposition/erosion dynamics and chemical consumption rate. The deposition dynamic on mudflat depends on local context but is generally controlled by wind and flow (Deloffre et al., 2006). In the Loire estuary, the flood pushes stored particles towards the downstream Les Brillantes mudflat (network SYVEL, GIP Loire Estuaire), enriching it in Mn and Fe-oxides. This dynamics would induce large increase of Mn and Fe-oxides stock during winter creating a transitory geochemical state likely to expand over months. The goal of this study is to investigate the dynamics of Mn and Fe-oxides in the sediment along contrasted hydrological seasons and to explore the P enrichment variations of these Fe-oxides. The yearly geochemical cycle of these elements will be described with quantification of their intensities along the year. The importance of both primary producers and bioturbation will be addressed by comparison between two contrasted sites. Therefore, we should be able to identify consequences of the geochemical dynamics on nutrient release and metals fluxes from the sediment to the estuarine environment.

1.2 II Material and methods

1.2.1 Study site

The Loire River drains an 117,045 km^2 basin with a mean flow input of 890 $m^3 s^{-1}$ in its estuary (range from 5200 $m^3 s^{-1}$ and 120 $m^3 s^{-1}$ but once every ten years). Loire estuary is hyper synchronous: it shows an increasing tidal range upstream (Le Floch, 1961)

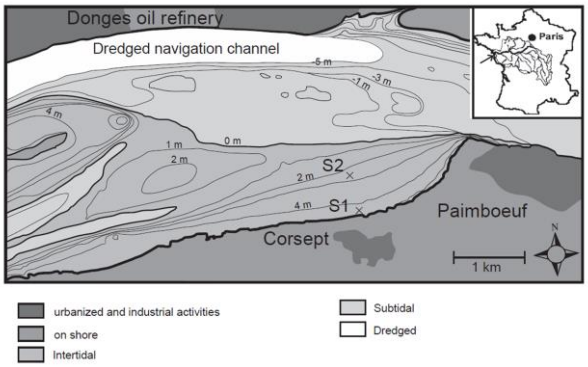

Figure 48 Location of the two sampling sites.

reaching a maximum tidal range of about 7 m. The daily surface salinity change is about 20 (network SYVEL, GIP Loire Estuaire) in the dredged channel, in front of the study sites. Site 1 (47°16'56.00"N; 2°3'47.00"W; Figure 48) is located on the slikke of Les Brillantes mudflat (largest mudflat of the Loire estuary; ~1350 ha), below the Mean High Water Neap Tide level (MHWNT), about 20 m offshore from an active 1m-high eroded cliff. Site 2 (47°17'8.98"N; 42° 3'49.65"W; Figure 48) is located about 500 m offshore. The differences between the two stations rely on the longer emersion time of site 1 that hosts more macrofauna than site 2 (Métais et al., pers. comm.) and is composed to slightly finer sediment (Benyoucef, 2014). Sediment is mainly composed by silt (92%) and clay (6%) with rare horizons more sandy (up to 37% for 63-2000 µm fraction, Benyoucef, 2014). Surface is often covered by a microphytobenthos biofilm with a density varying from Chl a = 20 mg m^{-2} in January to 60 mg m^{-2} in July (Benyoucef et al., 2014).

1.2.2 Sampling strategy

Sampling was performed during four contrasted seasons (Figure 49): in September 2012, flow was low (200 m^3 s^{-1} at Nantes (DREAL-Pays-de-Loire, 2015), water temperature was high (17°C) and sediment salinity high (16); in the beginning of May 2013 at the end of the flood period (flow between 900 and 1800 m^3 s^{-1}), with a water temperature of 13°C and a sediment salinity of 7 and in February 2014 during an important flood (2400 m^3 s^{-1}) with low water temperature (7°C), strong wind (gusts up to 100 km h^{-1}) salinity of 3 and a maximum tidal range. In April 2015, a weekly survey (t_0 - t_1 - t_2 - t_3) was performed on site 1, during one month while flow continuously decreased. When temporally compared to high flood events (Figure 49), the February campaign occurred during a flood event; the April time series was sampled between 1 and 2 months after a flood, the May campaign 75 days after a flood and finally the September campaign were performed 135 days after a high flood event.

1.2.3 Sampling procedures and analyses

For the 3 first campaigns, at each sampled site, three cores (∅=8.2 cm) were taken during low tide and brought back to the lab within the 30 min after the sampling and held at *in situ* temperature for further measurements. The core surface was constantly covered by a very thin (<1 mm) layer of water as observed *in situ*, ensuring water saturation of the sediment. One core was dedicated to microprofiling for dissolved oxygen and pH. After these acquisitions, this core was sub-sampled (∅ = 3cm), sliced, weighted and frozen for solid phase analyses. Within a week, samples were freeze-dried, weighted again to calculate porosity and manually ground using an agate mortar. One aliquot (~2 mg) of this powder was used for organic carbon analysis on a EA1110 CHN/S/O (Thermo Fisher) after 1h-extraction in a HCl saturated atmosphere. Each chromatograph was inspected visually. Accuracy was verified with standards (MS-61 and B2150) and uncertainty, calculated from standard deviation for ten replicates from standard MS-61, was 4.5%. A second aliquot of the powder (~100 mg) was used for extraction of reactive manganese, iron and

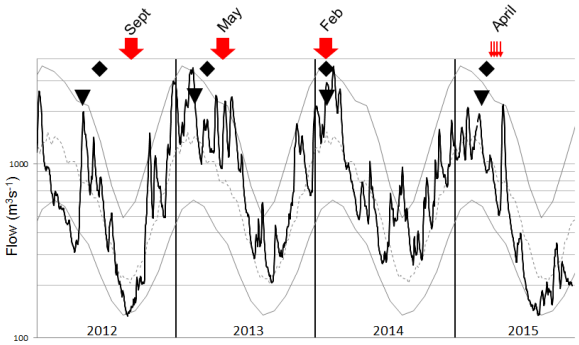

Figure 49 Hydrological context of the 4 campaigns (arrows) with each time the previous flood (triangle) and the previous wind event (diamond) with gusts above 70 km h^{-1}. Black line represents daily flow, dotted and grey lines represent median flow and 20 and 80 percentile of the monthly flow.

associated phosphate. Aliquots were exposed to 10 mL of a solution of ascorbic acid (buffered at pH 8) during 24 hours (Kostka and Luther, 1994; Anschutz et al., 1998; Hyacinthe et al., 2001) which is supposed to extract amorphous Fe(III) that is available for Fe-reducer microorganisms (Hyacinthe et al., 2006) as well as reactive Mn(III) and Mn(IV) oxides (Anschutz et al., 2005).

In each of the two others cores, two 1D DET probes (DET 1D, adapted from Davison and Zhang, 1994; Krom et al., 1994) were deployed during one night. Each DET probe is a perpex support containing 75 drilled cells that correspond to approximately 25 µL allowing a vertical resolution of 2 mm. Each cell was filled with agarose (1.5% w/w) and protected by a PVDF hydrophilic membrane (0.2 µm size pore, Millipore©). Each probe was prepared the week before deployment, conserved in a wet clean plastic bag and 6h-bubbled with N_2 before deployment. During the deployment, the agarose gel equilibrated by diffusion with pore waters. After retrieval, each agarose cell from two probes was eluted in 5mL of HNO_3 (0.01 mol L^{-1}; suprapur© Merck) and further analysed by ICP-AES (Thermo Scientific iCAP 6300 Radial) to measure dissolved iron, manganese and phosphorus. This technique allows sampling dissolved species with a 200 fold dilution according to a vertical resolution of 2 mm over a 2 cm width window. The two others 1D DETs were dedicated to alkalinity measurement following the one-step method of Podda and Michard (1994) adapted by Sarazin et al. (1999) for saline water and by Metzger et al. (2013) for 1D DET. Technically, this method corresponds to an absorbance measurement at 590 nm, 20 minutes after immersion of a 25 µL agarose gel in 1mL of a reagent composed by bromophenol-blue (25 mg L^{-1}), acid formic (4.0 10^{-4} mol L^{-1}) and NaCl (0.4 mol L^{-1}). The agarose gel was removed before measurement. Linearity of absorbance versus alkalinity was verified by calibration (standards prepared with $NaHCO_3$ (from 1 mM to 30 mM); standard deviation of repeated measurements on deionized water represents uncertainty of 0.07 mM.

For the April 2015 survey, one core was sampled each week and sliced under anoxic atmosphere. Pore water was extracted by centrifugation, acidified with HNO_3 and analysed on the ICP-AES as previously described. The sediment was weighted, freeze-dried, ground and analysed as previously described for porosity and solid phase analyses.

During the February campaign a supplementary core was sampled for ^{210}Pb analyses. Core section (2 cm) were stored in double sealed polyethylene bags and were immediately refrigerated until transportation to the laboratory where they were frozen at -28°C. Then, frozen core section were freeze-dried (Heto PowerDry® LL 3000) and subsequently sieved at 2 mm. Freeze dried samples were kept in an auto-desiccator until further use. Sedimentation rate was based on the determination of the excess or unsupported activity ^{210}Pb ($^{210}Pb_{xs}$), which is incorporated rapidly into the sediment from atmospheric fallout and water column scavenging (Appleby and Oldfield, 1992). $^{210}Pb_{xs}$ was calculated as the difference between measured ^{210}Pb (supported + excess) and ^{226}Ra, supported ^{210}Pb and ^{226}Ra being in secular equilibrium. Measurements were performed using a gamma spectrometer Ortec® HPGe GMX30P4-RB coaxial photon detector. Age of each sediment sample was directly estimated from the exponential radioactive decay of ^{210}Pb (λ=0.0311 yr^{-1}; Turner and Delorme, 1996). This approach does not require any hypothesis on sedimentation rate, which would be complicated in such dynamic environment.

1.2.4 Flux and production rate calculations

Flux and production rates have been estimated from pore water profiles using the Savitzky Golay Filter (SGF; (Meysman and Burdorf, in prep.; Savitzky and Golay, 1964). The procedure is based on polynomial interpolation of dataset by SGF resulting in replacement of each data point by a polynomial function of degree three. The polynomial coefficients are calculated to minimize the difference between the value of the polynomial and the value of data points over the length described by the interpolated data point and its *n* neighbours. As *n* increases, the more data points are considered for each polynomials calculation and the smoother the resulting SGF estimation is. Therefore *n* will further be called "filter window". Estimation of the flux is realized using the first spatial derivatives of these polynomials; production is estimated using the second derivatives (Meysman and

Burdorf, in prep.). When data points are too close to the boundary, they have not enough neighbours for running the SGF. These data points require boundary conditions able to described artificial neighbour before running SGF. According to the procedure proposed by (Meysman and Burdorf, in prep.), upper condition was defined such as production at the water sediment interface was zero. Bottom conditions were not necessary since flux and production estimation stops before being too close to the bottom boundary. The smoothing parameter *n* has a large impact on the flux and production estimation (Chapter 1.3). The more *n* increases, the more noise is corrected but the more the risk to neglect some significant signal increases. Thus, the best compromise is evaluated using fractal analysis (Meysman and Burdorf, in prep.).

1.3 Results

Total organic carbon (C_{org}; Figure 50) presents a wide range of content from 1500 µmol g^{-1} (1.8%) up to 3500 µmol g^{-1} (4.2%) with profiles presenting a maximum at the surface and decreasing with depth until roughly 1700 µmol g^{-1}. The decline is mostly located in the first 5 cm depth and is generally sharper for site 2. Moreover, the surface C_{org} content depends on the season with a maximum for the February campaign, intermediate value during May campaign, and no maximum for September campaign. Some profiles of C_{org} are marked by a local minimum in the two first centimetres (site 1 in February and in May and site 2 in May). Porosity profiles (Figure 50) present the expected decline with depth typical to compacting cohesive sediment going from ~0.93 at the surface to ~0.75 for the deepest samples. As for C_{org}, the porosity decrease is smoother in February than in September. The site 2 has systematically a sharper porosity profile than the site 1. The local minima identified for C_{org} profiles are also visible for porosity. In order to simplify representation only one from the 2 duplicates profiles for alkalinity is presented in Figure 50 for each sampling campaign and station. Alkalinity profiles show strong temporal variability for the near shore site

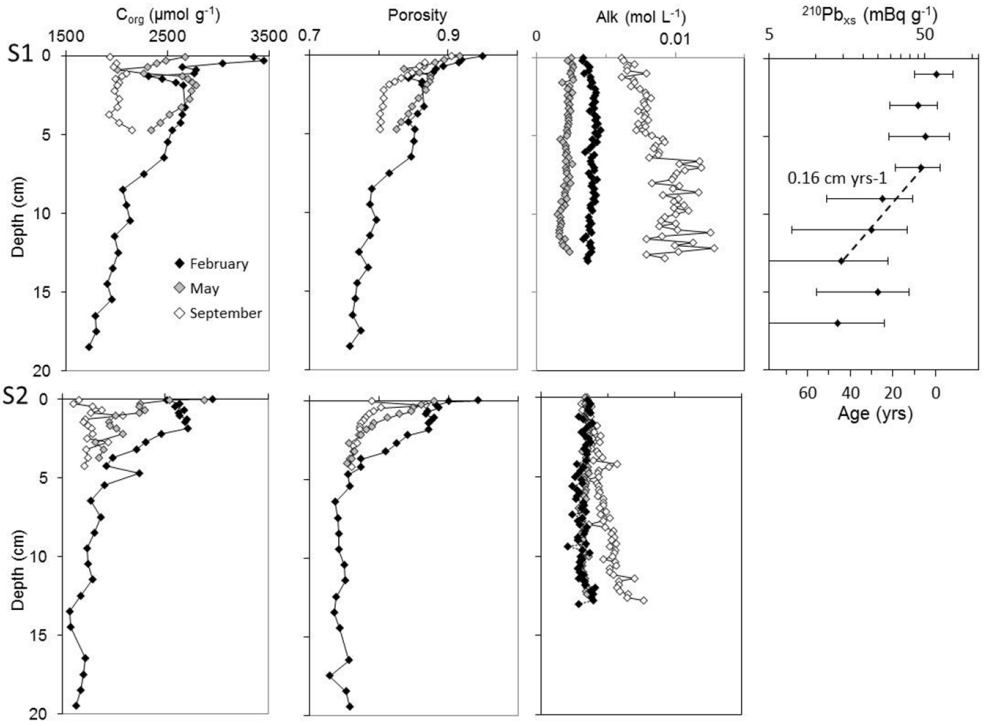

Figure 50 Total organic carbon, porosity and examples of alkalinity profiles for September 2012 (open diamonds), May 2013 (grey diamonds) and February 2014 (black diamonds). Result of ^{210}Pb are only available for Site 1, February 2015. The dotted line represent the maximum row sedimentation rate of 0.16 cm yr^{-1}

1. Surface alkalinity of site 1 ranges from a near oceanic value of 2.5 mmol L^{-1} in May, 3.3 mmol L^{-1} in February, to 6.1 mmol L^{-1} in September, whereas it is constant (3.5 mmol L^{-1}) for the site 2 (500m offshore). Moreover, alkalinity profiles present almost no depth variation, except for September where alkalinity progressively increases up to 10 mmol L^{-1} for site 1 and 5.8 mmol L^{-1} for site 2. $^{210}Pb_{xs}$ profile presents no significant variation on the top 8 cm, below a sharp decrease of activities is visible, down to undetectable levels below 14 cm depth.

Figure 51 presents profiles of dissolved and ascorbate-extracted Fe, Mn and P from September 2012, May 2013, February 2014 and from the last profile (t_3) from the time series of April 2015. Whatever the station or the date, solid reactive manganese oxide ($[Mn]_{asc}$) has a roughly constant concentration of 4.5 ± 1.5 µmol g^{-1} below 10 cm depth which contrasts with very variable $[Mn]_{asc}$ observed above (range from 2.7 to 17.9 µmol g^{-1}). This upper part is generally composed by two zones: (1) an extremely sharp decrease of about 6 ± 3 µmol g^{-1} with in the 0.5 first cm depth (*i. e.* mostly visible on the two first data point of the profiles). And (2), a deeper and smoother $[Mn]_{asc}$ decrease which concerns more atoms and occurs deeper as the delay between the sampling period and the previous flood decreases. Only the sharp surface decrease is visible on profiles of September 2012 to reach the background concentration at 1cm depth. The dissolved Mn-profiles ($[Mn]_d$) have bell-shaped patterns with a maximum that exactly matches with the second gradient depth (*i.e.* about 30 an 50 µmol L^{-1} at 1 cm depth, 170 µmol L^{-1} at 3 cm depth and 100 µmol L^{-1} at 6 cm depth; for May 2013 (site 1 and 2), April 2015 and February 2014 respectively; Figure 51). When no solid second gradient is visible, there is no observed bell shape (September 2012; both sites). As the only exception, February data from site 2 shows no dissolved peak despite a decrease in the extracted manganese between 2 and 6 cm depth.

Solid iron oxide profiles ($[Fe]_{asc}$) have a surface maximum followed by a progressive decrease down to

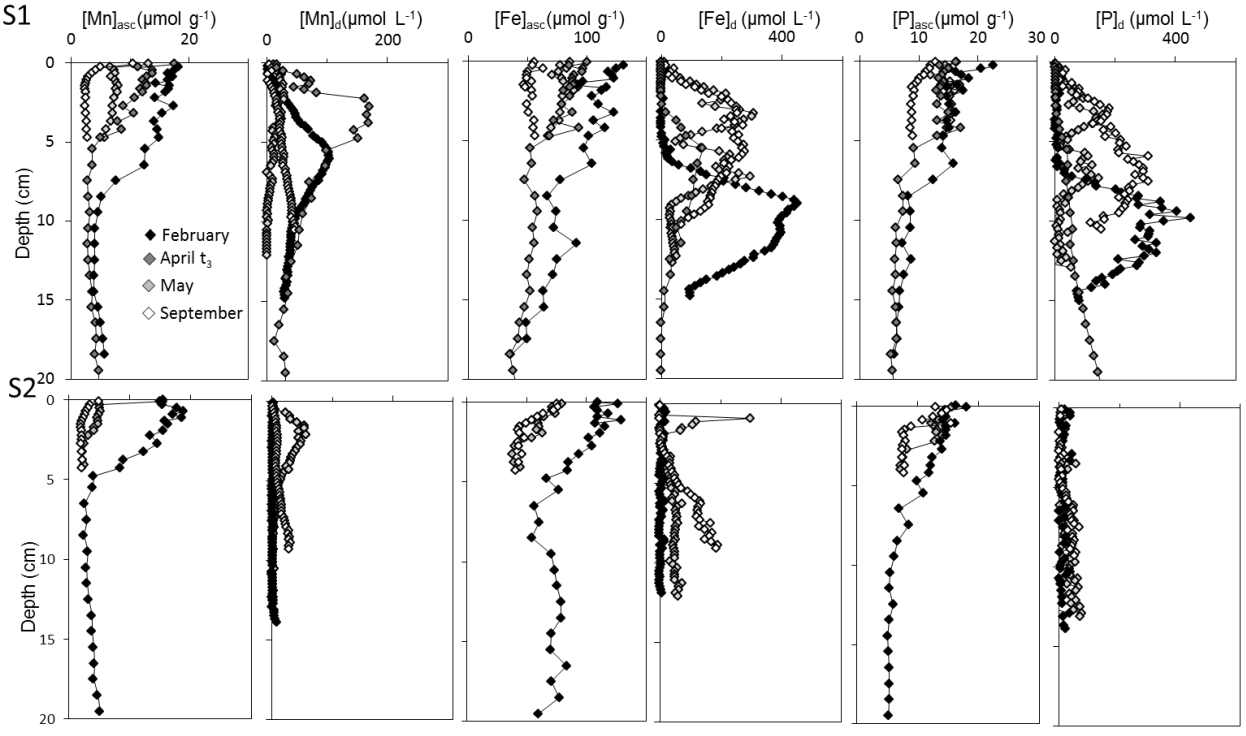

Figure 51 Extracted Mn-oxides, dissolved Mn, extracted Fe-oxides, dissolved Fe, extracted phosphorus and dissolved phosphorus from February 2014 (black diamonds), April 2015 (t_3; dark grey diamonds), May 2013 (clear grey diamonds) and September 2012 (open diamonds). Only one dissolved profile is shown for each situation, the second is similar. There is no data for S2 in April 2015.

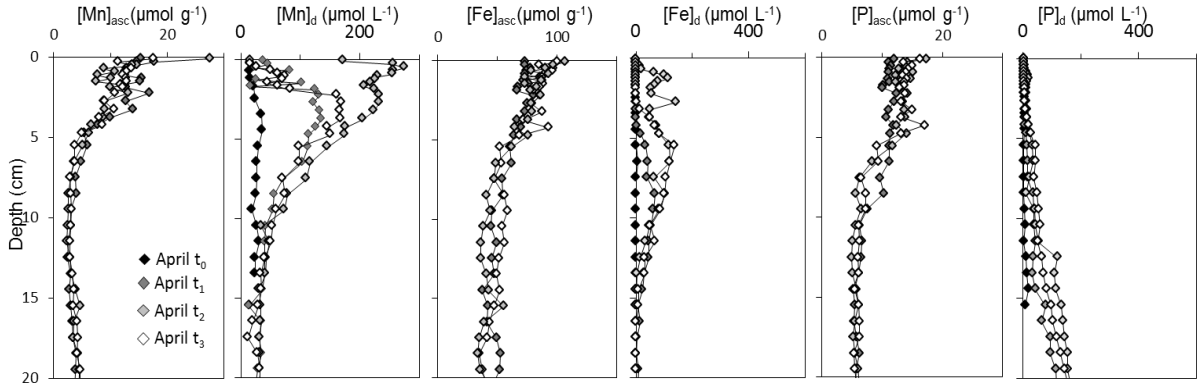

Figure 52 Extracted Mn-oxides, dissolved Mn, extracted Fe-oxides, dissolved iron, extracted phosphorus and dissolved phosphorus from the time serie in Site 1 (S1): t_0 are represented in black (only for profiles of dissolved species), t_1 in dark grey, t_2 in clear grey and t_3 with open symbols.

a constant, background concentration (50 µmol g^{-1} for site 1 and 43 µmol g^{-1} for site 2; Figure 51). At site 1, the gradient is more important as sampling occurs closer to the last flood (Sept<May<April<Feb). Two exceptions are characterized by local and short stronger variations (at 4.5 - 5 cm and 6.5 - 8.5 cm depth for respectively April 2015 and February 2014). There is also a local minimum visible at 0.9 cm depth for May data (as observed for porosity and C_{org}). In the site 2, gradients are restrained to few centimetres and extend deeper as the campaign is closer to the last flood (1.5, 2.75 and between 1.5 and 6.5 cm depth for respectively September, May and February campaign). Site 1 has high dissolved iron concentration ($[Fe]_d$) with one or two well-defined subsurface maxima. For February and April campaigns, $[Fe]_d$ maxima (about 450 and 140 µmol L^{-1} respectively) match to the depth of stronger decreases visible on the solid phase. For May and September, $[Fe]_d$ maxima are located between 2 and 7 cm depth (about 300 µmol L^{-1} for both campaigns). Site 2 has lower $[Fe]_d$ concentration with a smooth increase with depth apart for May when a very narrow a strong pic occurs at 1cm depth (also visible on the replicate).

Extracted solid phosphorus ($[P]_{asc}$) has globally the same pattern than extracted solid iron. $[P]_{asc}$ is maximal on top of sediment and reaches a background value with depth that is about 6 µmol g^{-1} for every sampled core. As described for redox elements, enriched top layers change in content and thickness between sampling periods and sites. In September, $[P]_{asc}$ on top core is about 13 µmol g^{-1} and reaches the background value 2 cm below. For other seasons maximum is above 15 µmol g^{-1} but thickness varies (6.5 and 4.5 respectively for February and May. Dissolved phosphorus shows peaks in February, April and September with maxima located at 10, 7 and 3 cm depth, respectively (with concentrations of 400, 300 and 150 µmol L^{-1}).

All profiles from the April time series obtained by the ascorbate extraction (Figure 52) are very similar to those (t_3) already described in the Figure 51. However, for $[Mn]_{asc}$, slight variation on the upper 5 centimetres are observed. The first profile (t_1) shows no sharp surface gradient but a deeper strong second gradient accounting for 9 µmol g^{-1} between 3.5 cm and 4.75 cm depth, whereas the t_3 profile has a sharp surface gradient and a smooth deeper gradient (loss of 9 µmol g-1 from 1.3 to 4.75 cm depth). The t_2 profile looks like the t_3 profile, but with a low $[Mn]_{asc}$ between 0.7 and 1.1 cm depth of t_2 that coincides to a sudden porosity decrease. Variations between solid profiles cannot only due to spatial heterogeneity since pore water profiles present the highest $[Mn]_d$ values obtained during this study (up to 275 µmol L^{-1}), indicating a high reactivity of manganese likely to explain solid variations. Contrastingly, $[Fe]_d$ and $[P]_d$ profiles from the time series (Figure 52) have the lowest measured concentrations of that study for the site 1. $[P]_d$ presents very smooth increase with depth (below 150 µmol L^{-1} at 20 cm depth).

1.4 Discussion

1.4.1 Sediment diagenesis after flood deposition

The profile of ^{210}Pb of February 2014 (site 1; Figure 50) indicates a homogeneous surface layer down to 8 cm depth followed by a linear decrease corresponding to radioactive decay during a continuous sedimentary deposition. The constant signal of excess ^{210}Pb can be interpreted either as biomixing or as an instantaneous deposit. February corresponds to the lowest densities of macrofauna and with almost no *Nereis* or *Scrobicularia* responsible to most of biomixing at this station (Métais et al, pers. comm.), therefore the second hypothesis is more likely. The important flood and wind observed before and during the February campaign (Figure 49; DREAL-Pays-de-Loire, 2015) are likely responsible of this sedimentation event. Different authors reported frequent events of sedimentation of a 5 - 10 cm thickness on mudflats from the French Atlantic coast (Deloffre et al., 2006 and Goubert et al., 2010). Time series measurement of Loire turbidity (SYVEL network) reports that the stock of sediment usually stored upstream is moved down in front of Les Brillantes mudflat during flood which thus favours sedimentation. $[Mn]_{asc}$, $[Fe]_{asc}$ and $[P]_{asc}$ profiles of February, site 1 (Figure 51) show sharp decreases between (6.5 cm and 8.5 cm) that matches with ^{210}Pb decrease. This correspondence indicates that young sediment is richer in Mn and Fe-oxides. No ^{210}Pb are available for site 2, but ascorbate extraction of February shows a similar pattern up to 4 cm depth probably indicating also a recent, but thinner, layer of freshly deposited sediment. The flood deposit is also characterized by important C_{org} content and porosity (Figure 50).

Since the ascorbate method extracts mostly Fe-oxide available for Fe-reducer microorganisms (Hyacinthe et al., 2006) and reactive Mn oxides (Anschutz et al., 2005), the young enriched layer represents an important stock of reagents for anaerobic respiration. When sampling few hours after the sedimentation event (February; Figure 51); $[Fe]_d$ and $[Mn]_d$ indicate no particular reaction of the new layer but have peaks at the new/old sediment interface probably as relics of the pre-deposition steady state. This delay before oxide consumption corresponds to the time for consumption of oxygen and nitrate available in the pore water of the newly deposited sediment, including the required evolution of microbial community (Aller, 2004). Hence, at the beginning of the time series (t_0; one month after the flood one week after the windy event) still nearly no $[Mn]_d$ and $[Fe]_d$ are observed. However, $[Mn]_d$ increases and reaches a concentration of $[Mn]_d$ (t_1) = 120 µmol L^{-1} after one week, sign of an important Mn-oxide reduction simultaneously to still nearly no Fe-oxide reduction. Oxides reduction after a deposition event are expected to follow this order since Mn-oxide reduction is more energetically efficient than Fe-oxide for anaerobic metabolism (Aller, 2004). Once reductively dissolved, some ions would leave the sediment or re-precipitate in an none-ascorbate extractable form as reduced minerals (*e.g.* $MnCO_3$, FeS) or aged oxides (*e.g.* goethite; Robbins and Callender, 1975; Sundby and Silverberg, 1985; Kendall et al., 2012; Aller, 2014). Consequently, the oxide consumption indicated by the maximum of dissolved concentration in pore waters has to match with a decrease of oxides extracted by ascorbate. In agreement, and according to the spatial variability visible below 10 cm depth, surface stock of $[Fe]_{asc}$ shows no significant variation. Oppositely, $[Mn]_{asc}$ stock calculated on the first ~10 cm (see below) presents a slight decrease from 300 ± 20 mmol m^{-2} to 260 ± 16 mmol m^{-2}. Moreover, $[Mn]_{asc}$ profile evolves from a 2-step pattern with abrupt transition at 3.5 cm depth probably between old and young sediment (Figure 52; t_1) to $[Mn]_{asc}$ profiles characteristic of more aged sediment (t_2 and t_3). Characteristics of "aged" sediment are 1 - the second (deeper) solid gradient of $[Mn]_{asc}$ indicating the ancient sediment-water interface is smoother due to progressive dissolution of Mn-oxides which diffuses upward and re-precipitates in the new oxic layer (Murray and Irvine, 1895; Robbins and Callender, 1975; Aller, 1980; Sundby and Silverberg, 1985) and 2 - the accumulation of authigenic Mn-oxides in this oxic layer which forms a strong surface increase. The superficial authigenic accumulation is also in strong agreement with the other $[Mn]_{asc}$ profiles (Figure 51) apart with profiles from September that have been deposited to recently.

In May, $[Fe]_d$ profiles have high values, indicating that dynamics in site 1 turns to Fe-oxide reduction advantage (Site 1, Figure 51). Moreover, $[Fe]_{asc}$ profiles show no depletion between April and May but a strong decrease between May and September (Site 1, Figure 51). However, the observed $[Fe]_{asc}$ consumption between February and April (site 1, Figure 51) goes against the theoretical order as Mn reduction occurs during this period. This difference between February and April stock could be due to inter-annual variations of the initial stock deposited. Despite low $[Mn]_d$ values, $[Mn]_{asc}$ shows still a decrease between April and September indicating that local and transitory dissolutions can account for a none negligible part of the oxide stock depletion. Finally, the data set from site 1 is in strong agreement with a seasonal geochemical cycle of the mudflat composed by an event of oxide-rich sedimentation during flood (illustrated here by February 2014 data), followed by a progressive consumption of oxides stock (May and April data) towards a steady state (represented here by September samples). Previous studies describing coastal Mn and Fe cycles did not highlight the importance of oxide stocks renewal and mainly explained seasonal variation by water temperature (Thamdrup et al., 1994) or available C_{org} input (Thamdrup et al., 1994; Bianchi et al., 2002, 2007; Dang et al., 2015). In our case, temperature and surface primary production are secondary parameters restrained to the control of the consumption rate of the oxide stock. Despite possible yearly variations, the validity of the relation between ascorbate surface stocks and the delay after the last flood, over four different years, demonstrates the steadiness of this geochemical cycle over time.

1.4.2 **Impact of fauna**

The $[Fe]_{asc}$ profile decreases linearly in the first 1.5 cm of the site 2 of September (Figure 51) whereas it stays constant closer to the shore (site 1). This difference between sites, once steady state is nearly reached, can be explained by different bioturbation intensity. Hence, macrofauna is represented by contrasted communities with a dominance of *Nereis diversicolor* in site 1 (~ 200 ind m^{-2} in September; I. Métais, pers. comm.) compared to a dominance of *Heteromastus filiformis* in site 2 (~ 50 ind m^{-2}; I. Métais, pers. comm.). Therefore and in agreement with the theoretical faster biomixing rate of *N. diversicolor* (Duport et al., 2006; Quintana et al., 2007), the site 1 is likely to be more impacted by bioturbation. At least two processes are likely to increase with bioturbation (Meysman et al., 2006; Kristensen et al., 2012): (1) the biomixing, which would homogenise the solid phase and (2) the bioirrigation, which would increase exchanges between sediment and overlying water by burrows ventilation. In the weakly bioturbated environment (site 2) re-oxidation occurs without major bioturbation interference: dissolved iron diffuses upward and is oxidized by Mn-oxide, nitrate or oxygen on the top ~ 2 cm. The expected resulting profile has a surface maximum in agreement with our dataset ($[Fe]_{asc}$ profile of site 2; September; Figure 51). In a highly bioturbated environment however, diffusive transport became negligible due to the exchanges generated by burrow ventilation events (Thibault de Chanvalon et al., in press; Raiswell, 2011). These exchanges occur along burrow walls which are not permanent and thus do not allow any visible oxide accumulation. Therefore, a high bioturbation short-circuits the preponderant role of the interface in water sediment exchanges resulting to a constant $[Fe]_{asc}$ profile (Figure 51, site 1, September). The Mn oxidation is slower than iron oxidation and not favourable since $[Fe]_d$ is present (*e.g.* Wang and Van Cappellen, 1996; Martin, 2003). Consequently, burrows generate weaker $[Mn]_d$ gradients across lignin. Moreover, the steady state zone of Mn dissolution is closer to the surface and thus more strongly constrained by oxygen diffusion through the surface. These Mn properties can explain that, at the contrary to Fe, Mn-oxide profiles present a well-defined surface accumulation, even with important biomixing (Site 1 and Site 2 September; Figure 51).

A second difference between sites is that sediment closer to the shore (site 1) is globally enriched in C_{org} (Figure 50) probably due to a more intense primary production (Benyoucef et al., 2014; Meleder, pers. com.), which is possible because of the longer emersion time. Alkalinity can be considered as an integrative parameter of anaerobic mineralization intensity (Berner et al., 1970; Sholkovitz, 1973; Soetaert et al., 2007), confirming that intensity of carbon remineralisation is probably more intense at site 1. It is thus expected that

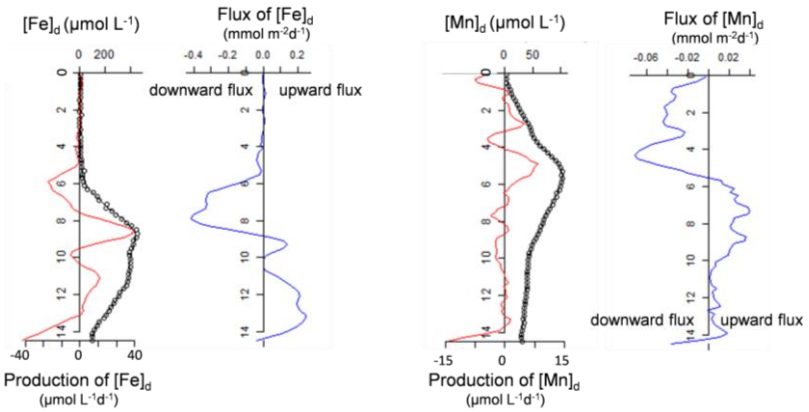

Figure 53 Examples of estimated concentration (black line) superimposed with original data set (open circles), production rate (red line; negative production corresponds to consumption) and upward flux (blue line; negative flux corresponds to downward flux) based on Savitsky-Golay Filter procedure (February. site 1). Upper boundary condition is no production.

site 1 presents a more intense Mn and Fe cycling that site 2. The rate of $[Mn]_{asc}$ and $[Fe]_{asc}$ dissolution was estimated using the SGF procedure performed on the 15 dissolved profiles as illustrated on the Figure 53. Defined as the sum of estimated net production along the entire profile, the apparent production rate (APR) represents the net dissolution rate along the sediment column. As expected, site 1 has a 2-fold to 10-fold more important APR than site 2 (Table 6). Finally, closer to the shore, site 1 benefits to more Mn and Fe oxide deposited during flood (as shown by data of February 2014, Figure 51) and more intense primary production easily buried by a stronger bioturbation.

1.4.3 Yearly budget of reactive Fe, Mn

Tentative of oxide budget is performed by comparing the profiles of ascorbate extraction according to the delay since the last flood on the site 1 (Figure 51). A reactive stock is calculated (ascorbate extracted minus average concentration on the 10 - 20 cm depth) for the upper 41 kg of dry sediment per square meter, which corresponds to the first 10 cm of the February campaign. For September and May campaigns, the profiles are shallower but as they reach the background concentration, one can assume that no more variation will be seen below. As expected, the evolution of stocks content according to time (Figure 54) is an impoverishment of the upper oxide stock. We propose to model the yearly ideal behaviour of the mudflat based on the simplifying assumptions that (1) an oxide stock is deposited during only one event that coincides with the yearly flow maximum, (2) the initial oxide stock is similar for each year and (3) all the consumption is induced by geochemical reaction and (4) no simultaneous consumption of Mn and Fe oxides occurs. In order to respect the fourth assumption and as the important Fe-oxide stock from February is explained by inter-annual variation, the February data were not used for modelling ideal cycle of an ideal

	APR (mmol m^{-2} d^{-1})			
	Site 1		Site 2	
	Fe	Mn	Fe	Mn
Feb	0.58 ± 0.10	0.11 ± 0.01	0.19 ± 0.13	0.01 ± 0.01
April t_1	0.21 ± 0.04	0.75 ± 0.23		
April t_2	1.22 ± 0.53	1.43 ± 0.58		
April t_3	0.41 ± 0.09	1.20 ± 0.36		
May	1.16 ± 0.65	0.22 ± 0.08	0.28 ± 0.09	0.15 ± 0.05
Sept	1.76 ± 1.15	0.18 ± 0.12	0.19 ± 0.06	0.03 ± 0.01

Table 6 Apparent production rate (APR) calculated from the production estimated by Savitzky Golay Filter procedure summed over the whole available profile of $[Mn]_d$ or $[Fe]_d$.

year. Accordingly, stock of reactive Mn starts to decrease few days after the sedimentation event and continues roughly 3 months (dotted line, Figure 54). The decrease of Fe- oxide stock follows and lasts during approximately the same time (black line, Figure 54). The average rates of depletion are about 3 mmol m^{-2} d^{-1} for Mn and 13 mmol m^{-2} d^{-1} for Fe. This rate of Mn depletion is faster than the estimation of 0.6 mmol m^{-2} d^{-1} by Thamdrup et al. (1994) in Aarhus Bay, in agreement with the different methodology used as they define the reactive stock with only the top 2 cm.

In order to join ascorbate extraction profiles with dissolved profiles, APR is represented below the solid budget (Figure 54). Since oxide dissolution represents the main pathway for oxide stock variations induced by geochemical reactions, the APR should be the upper bound of the oxide consumption rate. In agreement, Figure 54 shows that Mn-APR maximum of 1.4 ± 0.5 mmol m^{-2} d^{-1} matches with maximum oxide loss (40 to 60 days after last flood). Fe-APR increases after the deposition event until a maximum of 1.8 ± 1 mmol m^{-2} d^{-1} after 140 days, when an oxide loss is observed. However, APR are always below the rates estimated from reactive stock depletion. For the highest APR values, they reach only 10 % and 50% of the estimated depletion rates for Fe and Mn-oxides respectively. One possible explanation for this gap could be the erosion of surface sediments which is a frequent event occurring on estuarine mudflats (invalid 3rd assumption; Deloffre et al., 2006; Goubert et al., 2010). In this case oxide-rich particles would be removed from the mudflat surface generating an oxide loss independent to oxide dissolution reactions.

To isolate losses due to geochemical reaction budget on solid phase averaged for one year can be performed; assuming steady state, input and output flux can be equalized for both particles and ascorbate reactive iron. Thus :

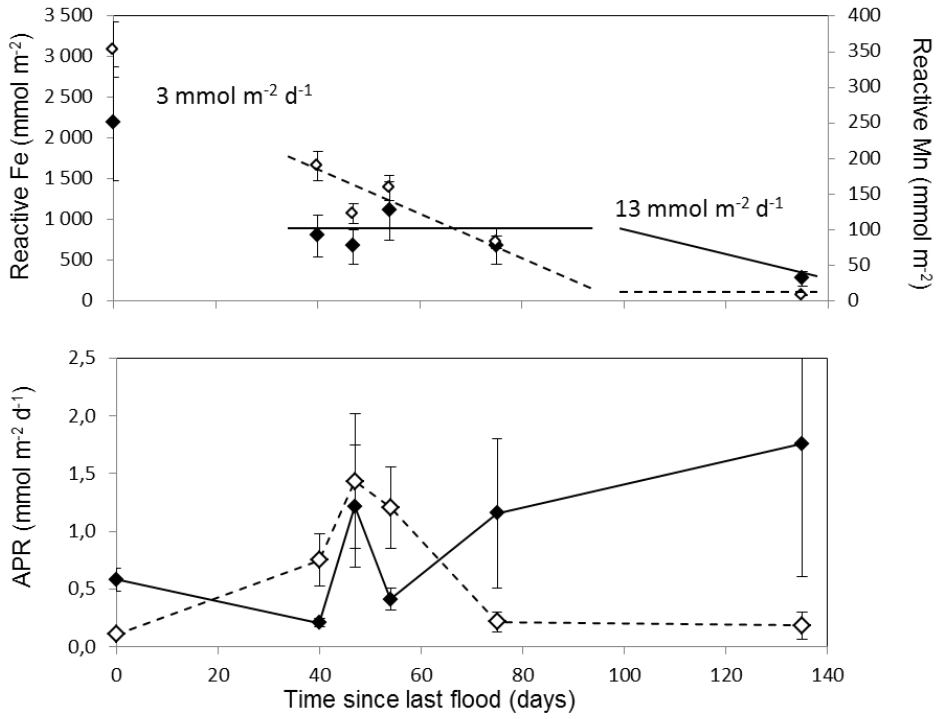

Figure 54 Idealised evolution of Mn (open diamonds) and Fe (black diamonds) on the site 1. Time since the deposition event is calculated from the last flood (Fig. 2). Top: Reactive stocks (ascorbate extracted minus background concentration), error bars represent relative standard deviation of background concentrations, lines represent idealized behaviour with the corresponding rate indicated. Bottom: Apparent production rate estimated from SGF procedure, error bars are standard deviation taking account 2 replicates and ± 1 on the smoothing parameter *n*.

$$J(Fe)_{set} = J(Fe)_b + J(Fe)_e + J(Fe)_g \quad (25)$$

$$J(par)_{set} = J(par)_b + J(par)_e \quad (26)$$

With $J(Fe)_{set}$the flux of ascorbate reactive iron that settle (in mol m^{-2} d^{-1}) and $J(Fe)_b$, $J(Fe)_e$, $J(Fe)_g$ the possible output flux of iron which are respectively being burial, eroded or transformed because geochemical reactions. $J(par)_{set}$,$J(par)_b$,$J(par)_e$ represent similar flux for particles in g m^{-2} d^{-1}. We here assume that the reductively dissolved iron (or any other chemical reaction) represent negligible mass loss for particles. Combination of these equation leads to:

$$\begin{aligned} J(Fe)_{set} &= J(par)_b \frac{J(Fe)_b}{J(par)_b} \\ &+ (J(par)_{set} - J(par)_b) \frac{J(Fe)_e}{J(par)_e} + J(Fe)_g \end{aligned} \quad (27)$$

Then if we assume that $J(Fe)_e / J(par)_e = J(Fe)_{set} / J(par)_{set}$, *i.e.* there is no chemical transformation before any erosion equation can be reorganized such as:

$$J(Fe)_g = J(par)_b \left(\frac{J(Fe)_{set}}{J(par)_{set}} - \frac{J(Fe)_b}{J(par)_b}\right) \quad (28)$$

One can observe that $J(par)_b$ is the burial rate estimated from ^{210}Pb profile (1 010 g $m^{-2}yr^{-1}$) and that the two last ratios correspond to the ascorbate reactive concentration of iron which respectively settles and is buried. Therefore :

$$J(Fe)_g = J(par)_b([Fe]_{asc}(z = 0) - [Fe]_{asc}(z = \infty)) \quad (29)$$

This estimation of geochemical loss is a minimal since it implicitly supposes that the eroded sediment is as oxide-rich as the deposited sediment *i.e.* it neglects geochemical loss of eroded sediment. However the geochemical loss can correspond to two main processes: efflux to the water column but also transformation in iron-sulfur, without possibility to differentiate them. Concentration of settled sediment is estimated from the average concentration of the 7 upper centimeters ($[Fe]_{asc}$ (z = 0) = 103 µmol g^{-1}) and concentration of the burial sediment from the constant bottom concentration observed in September, May and February ($[Fe]_{asc}$ (z = ∞) = 40 µmol g^{-1}). Similar estimation is performed for $[Mn]_{asc}$ and lead to averaged yearly loss of 170 ± 60 µmol m^{-2} d^{-1} and 30 ± 10 µmol m^{-2} d^{-1} for respectively Fe and Mn. These values are in agreement with the upper bound estimated by APR: assuming that these losses occur during the ~3 months of remobilization as proposed in our simple model (Figure 54) they would represent respectively 40% and 10% of the Fe-APR and Mn-APR estimated during the same period. A second explanation could be the sampling resolution. The 2 mm resolution is evidently too large to describe most of the variability of reactions occurring at the microbe scale. Moreover, the centimetre heterogeneity is mostly induced by burrows which generate essentially lateral fluxes. As example, $[Fe]_d$ 2D analysis at sub millimetre resolution estimates a 4 time more intense APR for site 1 in April (Chapter 1.3).

1.4.4 **Phosphorus dynamics**

Despite phosphorus is not a redox element, phosphorus is produced in sediment by organic matter oxidation and by desorption while Fe oxides are reductively dissolved. The latter process controls P fate in surface sediment as shown by the strong similarity of distribution between $[Fe]_d$ and $[P]_d$ (Figure 51 and Figure 52). However, the deepest data show a regular increase typical of $[P]_d$ supplied by deep (> 10 cm) organic matter remineralisation. The strong correlations between $[Fe]_{asc}$ and $[P]_{asc}$ ($r^2 > 0.6$, Figure 56) confirms the strong control imposed by Fe oxides. A seasonal pattern of $[Fe]_{asc}/[P]_{asc}$ going from $[Fe]_{asc}/[P]_{asc}$ ~ 7.2 in February to $[Fe]_{asc}/[P]_{asc}$ ~ 5.2 in September (Figure 56; April samples indicate intermediate values) indicates a more intense consumption of iron oxides than phosphorus probably due to continuous replenishment of P by C_{org} mineralisation. The P enrichment seems to reach a maximum of $[Fe]_{asc}/[P]_{asc}$ =4.3 in May when phosphorus stops to accumulate on iron oxide at this date (similar ratio is found in September; Figure 56). Such saturation ratio is in agreement with the slightly higher value (6-14) reported by (Anschutz et al., 1998) in Eastern Canadian continental margin and in the Portuguese continental slope. Stronger P enrichment (with $[Fe]_{asc}/[P]_{asc}$ mostly between 4 and 1) have been described when authigenic iron phosphate mineral phase was produced (Hyacinthe and Van Cappellen, 2004).

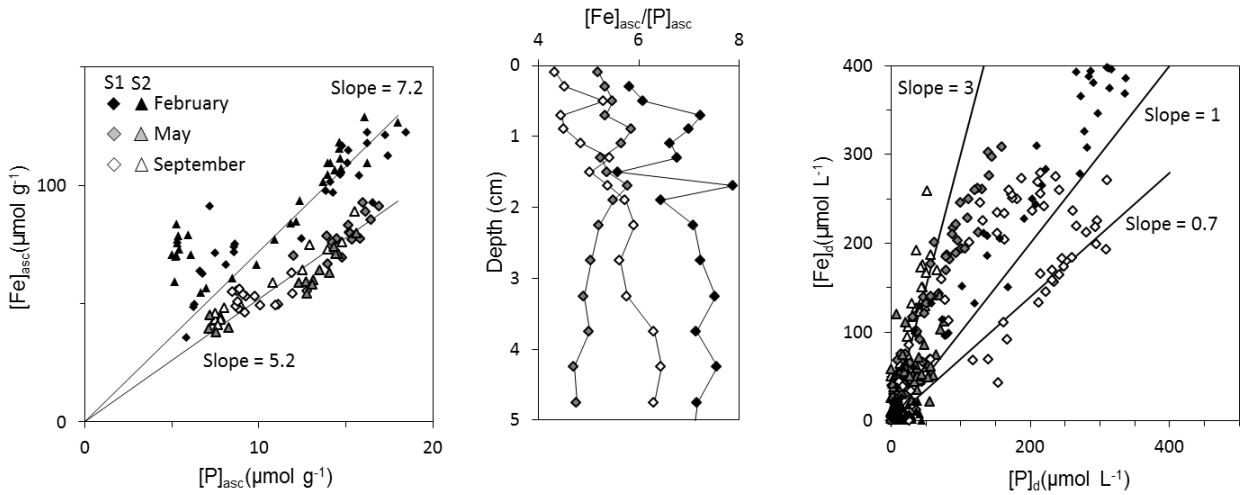

Figure 55 Evolution of Fe and P relation in the ascorbate extraction, according to depth and in the pore water.

The similarity between $[Fe]_d$ and $[P]_d$ profiles (February, May and September; Site 1; Figure 51) also indicates that as soon dissolved iron re-precipitates (when $[Fe]_d$ decreases on top of profiles), as soon $[P]_d$ decreases in a similar way, probably by fast adsorption on freshly precipitated Fe-oxides. The short delay necessary to this fast adsorption could slightly increase residence time of phosphorus in the pore water explaining the lower Fe/P ratio in the dissolved phase compared to solid phase (Figure 56). And second explanation of this low Fe/P ratio in the dissolved phase is the extraction by ascorbate protocol of two solid phases: one with adsoption site for P and one without adsorption site. However the coexistence of $[P]_d$ with not-saturated Fe-oxide has been measured (for example in February), which could indicate a multi-step adsorption process: a first fast step generating the similarity between dissolved profiles and a second slower step allowing freshly dissolved phosphorus to not directly be adsorbed and responsible of the long term $[Fe]_{asc}/[P]_{asc}$ decrease. Such multi-step process has been numerously described for metals adsorption (*e.g.* Moore and Millward, 1988; Ciffroy et al., 2001). Therefore, Fe-oxides buffer slow (over month) processes of phosphorus release (C_{org} remineralisation) by trapping phosphorus (the "iron curtain"; Mortimer, 1971; Charette and Sholkovitz, 2002; Spiteri et al., 2008) until complete oxide saturation (probably at beginning of the summer). This slow adsorption is also visible by the surface $[P]_{asc}$ gradient (without $[Fe]_{asc}$ gradient) where most carbon remineralisation occurs. Dissolved phosphorus analyses present too important uncertainty to describe any buffering effect at $[P]_d$ ~ 5 µmol L^{-1} (Sundby et al., 1992; Anschutz et al., 1998) of this slow adsorption process. On shorter time scale however, reductive dissolution of iron releases phosphorus in pore water that could be rapidly mixed with overlying water by bioirrigation. Increase of phosphorus stock indicates that, on the long term, the slow adsorption is more important than the fast P-release by bioirrigation, but on the short term this last process could represent an important P source for primary producer that account on a yearly average (since Fe/P=5) to ~40 µmol m^{-2} d^{-1}. The phosphate released in estuarine environment from terrigenous sediment was proposed to explain the switch from phosphorus limitation in freshwater to nitrogen limitation in coastal marine water (Jordan et al., 2008).

1.5 Conclusion

Quantification of reactive Fe and Mn oxides with associated P and analyses of pore water composition allows drawing a general pattern of the geochemical yearly cycle in the studied estuarine mudflat. The first control appears to be the seasonal deposition events that bring oxide-rich sediments onto mudflat surface. Then, during roughly 3 months, anaerobic respiration dissolves by reduction Mn oxide. Once dissolved, Mn is likely to re-precipitate (in reduced or oxic forms) or to leave the sediment. Two approaches are proposed in

the present study to quantify the Mn-oxide loss induced by this process. First, a budget based on the oxide stocks indicates a yearly average loss between 0.03 and 3 mmol m^{-2} d^{-1} for Mn-oxides. This large uncertainty is induced by the erosive loss that is weakly constrained. Then a second approach, based on pore water profiles, estimate the upper boundary of geochemical loss by APR and refine the yearly average geochemical loss within the range of 0.03 and 0.35 mmol m^{-2} d^{-1} for Mn-oxides. During the same period of 3 months that follow deposit event, Fe-oxide would be weakly dissolved and would prevent (or at least limit) the phosphorus release by adsorption. After this first period, the reductive dissolution of Fe-oxide becomes more important; increasing the Fe-oxide depletion (estimated between 0.17-1.4 mmol m^{-2} d^{-1} for Fe-oxides) and releasing dissolved iron and associated metals and nutrients to the overlying water. This second period lasts after few months and probably facilitates phosphorus uptake by surface primary producers. This geochemical cycle would be typical of low sulphate and highly bioturbated sediment, undergoing sudden and limited deposition events. A similar approach must be extended to the subtidal estuarine sediment in order to better constrain large scale heterogeneity of benthic fluxes, especially in regards of the impact of dredging in the release of nutrients and therefore in the hypoxic events documented in the Loire estuary.

Acknowledgements

This study is part of the RS2E – OSUNA project funded by the Région Pays de la Loire. Thanks to Cyrille Guindir, Clément Chauvin, Romain Levrard, Livia Defay, Anthony Barbe and Eric Bénéteau for their technical help. A special thanks to the 2015 class of Geology (Licence) of the University of Angers that sampled and analyzed the first pore water profiles of the time series.

Partie 2 :

2 Nouvelles connaissances apportées par l'échantillonnage en deux dimensions sur les relations entre fer et phosphore sédimentaires

ABSTRACT

Input of particles from rivers is considered as the principal source of phosphorus to oceans. Therefore, the PO_4^{3-} released from sediment in coastal and estuarine surface water would strongly influence marine primary production. Here we focus on iron and phosphate dynamics in a intertidal mudflat of the Loire estuary using several diffusive gel probes coupled to colorimetric techniques and hyperspectral imagery (2D-DET-HC probes). These probes allow describing the distribution of dissolved iron (Fe_d) and dissolved reactive phosphorus (DRP) in interstitial water. These results were combined to solid Fe and P extractions with an ascorbate buffered solution (pH=8). We identified 3 main sources of phosphate: (1) an iron bound source, (2) a deep source (below 20 cm depth) generated by upward diffusion of DRP at the sample bottom and (3) patchy sources probably produced by local enrichment of labile organic matter. The iron bound source is investigated comparing the production rates estimated by the Savitsky-Golay-Filter (SGF) procedure (Fe_{prod}/P_{prod} = 4.3±1.6 on the top 4 cm) with the solid stock extracted ($[Fe_{asc}]$= 3.7 $[P_{asc}]$ + 23 µmol g-1 on the top 4 cm). The good agreement between the two independent methods confirms the importance of iron bound phosphate. Vertical profiles of Fe_{prod}/P_{prod} indicate an increase of the saturation state of adsorption sites on iron oxides with depth which highlights the organic initial origin of a part of iron bound phosphate. Finally we estimate the importance of macrofauna in the DRP flux from the sediment towards the water column with SGF procedure applied on one 2D-DET-HC for which burrows were identified in the sediment that faces the gel. Macrofaunal mediated flux was estimated to 85±21 µmol m-2 d-1 which could represent 90±23% of the total DRP flux from the sediment towards the water column

RESUME

Les particules apportées par les fleuves représentent la principale source de phosphore pour les océans. Ainsi, les flux sédimentaires du PO_4^{3-} en milieu côtier ou estuarien influenceraient fortement la production primaire des océans. Nous nous intéressons ici à la dynamique du fer et du phosphore dans une vasière intertidale de l'estuaire de la Loire en utilisant 12 échantillons de type 2D-DET-HC (de l'eau interstitielle prélevée en 2 dimensions par gel DET (*Diffusive Equilibrium in Thin film*) analysés par colorimétrie hyperspectrale) décrivant la distribution du fer dissous (Fe_d) et du phosphore réactif dissous (DRP). Ces images sont complétées par des données de Fe et P solide obtenues par extraction à l'aide d'une solution d'ascorbate tamponnée (pH=8). Nous avons identifié 3 sources principales de phosphate : (1) une source liée au fer, (2) une source en profondeur (en dessous de 20 cm) identifiée par un flux vers le haut estimé en bas des échantillons et (3) une source localisée, probablement produite par des patches enrichis en matière organique labile. La source liée au fer est ensuite étudié par la comparaison des vitesses de production estimé par la procédure SGF (*Savitsky – Golay - Filter*; Fe_{prod}/P_{prod} = 4,3±1,6 sur les 4 1^{ers} centimètres) avec les stocks solide extraits ($[Fe_{asc}]$ = 3,7 $[P_{asc}]$ + 23 µmol.g^{-1} sur les 4 1^{ers} centimètres). La similitude des ratios issues des deux méthodes indépendantes confirme l'importance du phosphate lié au fer. Les profiles verticaux de Fe_{prod}/P_{prod} indiqueraient une augmentation de la saturation des oxydes de fer vis à vis des phosphates ce qui souligne l'origine organique d'une partie des phosphates liés au fer. Enfin, l'importance de la macrofaune dans les flux de DRP a été estimée par la procédure SGF appliquée sur un gel dont le sédiment en vis-à-vis portait des traces évidentes de terriers. Ce flux induit par la macrofaune s'élèverait à 85±21 µmol m^{-2} d^{-1} ce qui représente 90±23% du flux total de DRP du sédiment vers la colonne d'eau.

2 Iron and phosphorus relationship in sediments, new insights from 2D sampling

2.1 Introduction

Phosphorus (P) is an essential macronutrient which limits marine productivity and regulates CO_2 sequestration by the ocean on geological time scales (Broecker and Peng, 1982; Tyrrell, 1999). Rivers are a principal source of oceanic phosphorus, essentially brought in a solid form which sediment in coastal and shelf environment (Meybeck, 1982, 1993; Zhang et al., 2004; Paytan and McLaughlin, 2007). The solid phosphorus of surface sediment is partitioned between lattice-P (Aspila et al., 1976; Williams et al., 1976; Hosomi et al., 1982; Yamada and Kayama, 1987; Ruttenberg, 1992), supposedly apatite (Rootare et al., 1962; Fox et al., 1985; Zhang et al., 2004, 2010); non-lattice or adsorbed P essentially adsorbed onto iron oxyhydroxide minerals (Rehm, 1985; Sundby et al., 1992; Slomp et al., 1996; Anschutz et al., 1998) and carbonate and organic P (Slomp et al., 2004). Since pioneer studies (Jitts, 1959), several authors have highlighted the importance of PO_4^{3-} release from particles for coastal and estuarine surface waters (Callender and Hammond, 1982). Hence, rivers frequently bring large amounts of nitrate (Meybeck, 1982; Turner et al., 2003) compared to the Redfield NO_3^-/PO_4^{3-} ratio of 16 which is usually observed in ocean (Redfield, 1934; Tyrrell and Law, 1997; Tyrrell, 1999). For example, The NO_3^-/PO_4^{3-} ratio of Loire freshwater is always reported above 50 (Meybeck et al., 1988; Gorse et al., 2010; Minaudo et al., 2015). This NO_3^- enrichment indicates that PO_4^{3-} would become the limiting nutrient once the water reaches the ocean. Therefore, P-release during estuarine mixing exerts a strong control on primary production in coastal environments and perhaps generates a switch from P to N limitation. However, since residence time of water in estuaries (roughly 2 weeks in the case of Loire estuary Ciffroy et al., 2003b) is too short to achieve the typical oceanic equilibrium, the high N/P ratio does not systematically indicate that primary production in estuaries is P-limited. It is more likely that most of the time in estuaries, the important turbidity and turbulence limit primary production. Therefore, only phosphate concentration indicates efficiently whether nutrient limits or slows down primary production (Moore et al., 2013).

Four main sources of PO_4^{3-} in the estuarine water column can thus be defined as: (1) Riverine PO_4^{3-} from drainage basin. (2) Exchange between dissolved phase and particles under oxic condition (Ruttenberg, 2003) by adsorption (Fox et al., 1986; Froelich, 1988) or precipitation (essentially as calcium phosphate mineral; Fox et al., 1985). However, the solid-dissolved equilibrium of adsorption is rarely reached in dynamic environments since the frequently assumed 2-steps adsorption kinetics (Fox et al., 1986) requires constant conditions during several weeks (Fox, 1993). (3) Mineralization of organic matter especially at the estuarine entrance where quantity of halophobic species would be degraded (Morris et al., 1978; Meybeck et al., 1988; Gardolinski et al., 2004).(4) upward flux of PO_4^{3-} produced in anoxic sediment during iron (Fe) reduction and remineralization of organic matter (Aller, 1980; Callender and Hammond, 1982; Berner and Rao, 1994; Lillebø et al., 2004; Deborde et al., 2007; Andrieux-Loyer et al., 2008).

Organic matter remineralization and reductive iron dissolution occur in the sediment, mainly below the oxygen penetration depth. Once produced in interstitial water, most PO_4^{3-} would diffuse upward through the oxic layer enriched in iron (oxy)hydroxide. But this superficial layer would drastically decrease the phosphorus efflux, since PO_4^{3-} have strong affinity with iron oxides and would be adsorbed and immobilized (*e.g.* Sundby et al., 1992; Deborde et al., 2008). The flux reduction capacity of the iron oxide rich layer depends on its thickness, on the concentration of adsorption sites and their saturation state. However, some leaks through this iron oxide rich layer can occur. Hence, macrofauna burrows extend to ~20 cm depth and are continuously renewing water therein, which maintains the water infilling burrows in equilibrium with water column. Thus, the inhabited burrows strongly enhance exchanges between interstitial and overlying water (Callender and Hammond, 1982) that

could shortcut the iron-oxide rich layer and directly transfer PO_4^{2-} to the water column. Focusing on a mudflat from the Loire estuary, we aim (1) to describe the Fe and PO_4^{3-} remobilization dynamic in the sediment according to a submillimetre sampling in two dimensions (using 2D-DET techniques) (2) to investigate the relation between PO_4^{3-} production and Fe-oxide and associated P from centimetre scale in 2D (as defined by buffered (pH=8) ascorbate extractions) and (3) to quantify the importance of direct transfer of PO_4^{3-} across burrows (from 2D Savitsky-Golay filter procedure).

2.2 Material and methods

2.2.1 Study site

The Loire estuary drains an 117,045 km^2 basin which represents, at the entrance, a mean flow of 890 m^3 s^{-1}. According to a time-series of freshwater input (Gorse et al., 2010), riverine [PO_4^{3-}] decreases below 0.2 µmol L^{-1} only during phytoplankton bloom (ChlA >10 µg L^{-1}). During these low [PO_4^{3-}] periods, phosphorus probably limits, or at least, slows down sediment surface primary production. However, frequent increase of PO_4^{3-} concentration at the estuary – river interface (Meybeck et al., 1988; Brach-Papa, pers. comm.) followed by important PO_4^{3-} variation with several maxima along the salinity gradient (Meybeck et al., 1988) indicates that other processes than primary production can strongly influence PO_4^{3-} in semi-confined estuarine water. Therefore, sediment (diffusion from pore waters and/or stirring of deposited sediments) has been proposed as a major PO_4^{3-} source in the Loire estuary (Meybeck, 1988).

The studied sediment is located in the largest intertidal mudflat of the estuary ("Les Brillantes", ~1350 ha). Sediment is mainly composed of silt (92%) and clay (6%) with rare sandy horizon (up to 37% for 63-2000 µm fraction; Benyoucef, 2014). The surface of the sediment is often covered by a microphytobenthos biofilm with a density varying from Chl a = 20 mg m^{-2} in January to 60 mg m^{-2} in July (Benyoucef et al., 2014). Sedimentation is controlled by important deposition of iron oxide-rich particles during flood condition followed by progressive depletion during the rest of the year (Chapter 2.1). Site 1 (47°16'56.00"N; 2° 3'47.00"W) is on the slikke, below the Mean High Water Neap Tide level (MHWNT), about 20 m offshore from an one metre high eroded cliff. Site 2 (7°17'8.00"N; 42° 3'49.00"W) is located about 500 m offshore. Site 1 has longer emersion time during each tide cycle, host more macrofauna than site 2 and is composed of slightly finer sediment (Benyoucef, 2014). Moreover, site 1 shows a thicker iron oxides enriched layer than site 2 (about 7 cm and 4 cm in September 2014, about 5 cm and 2 cm in May 2013 respectively, Chapter 2.1). The dataset was sampled during two campaigns, first in September 2012 during low flow conditions (200 m^3 s^{-1} at Nantes; DREAL-Pays-de-Loire, 2015) and warm sediment (17°C) secondly, in May 2013, at the end of the flood period (flow decrease from 1800 to 900 m^3 s^{-1} during the campaign) and with a sediment temperature of 13°C.

2.2.2 Sampling and analyses

The dataset consists of two-dimensional (2D) distributions of total dissolved iron (Fe_d) and dissolved reactive phosphorus (DRP) obtained by insertion of 2D-DET probes (Two-Dimensional Diffusive Equilibrium in Thin film; Harper et al., 1997) into the sediment. The 2D-DET technique quantifies the distribution of a solute in a vertical plane by sampling pore water by diffusive equilibration. Therefore, this sampling technique requires incubating the 2D-DET probe in the sediment during 5 hours. Overall, 13 2D-DET probes were successfully incubated *in situ* and analysed: four gels from site 2 were sampled during theSeptember 2012 campaign; 3 gels from site 2 and 6 gels from site 1 were sampled during May 2013 campaign. Incubations were performed during low tide by deployment of 2D-DET probes in the sediment during the first hour of site emersion and probes were retrieved 4 and 6 hours later for respectively Sept 2012 and May 2013 site 2. For gels from site 1, a time series deployment was performed in order to estimate temporal variation over a half tide cycle (only during mudflat emersion). Three gels were incubated over an entire tidal cycle in order to being retrieved rapidly after emersion time (t_{em}) at t_{em}+1h (n=1) and t_{em}+3h20 (n=2). Three other gels were deployed at t_{em}+1h and retrieval at t_{em}+6h (n=1) and t_{em}+8h (n=2). The gels were analysed for concentration of total dissolved iron

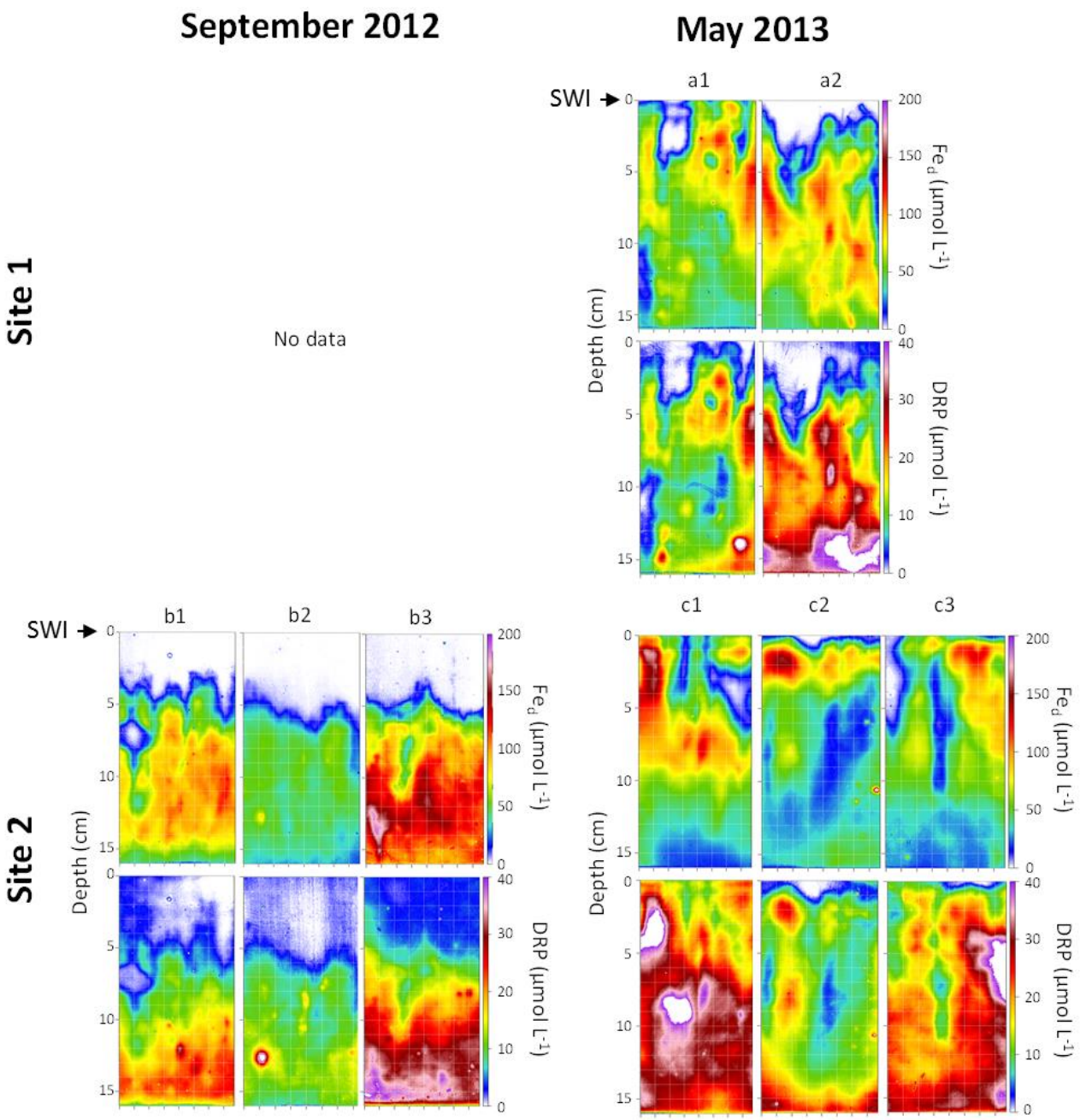

Figure 56 2D distribution of Fe_d and dissolved reactif phosphorus (DRP;resolution of 200 µm x 200 µm) below the water-sediment interface (SWI) sampled during low tide and sediment emersion. Gels with similar letter are distant to less than few decimeters.

(Fe_d) and dissolved reactive phosphorus (DRP) by colorimetry (see details in Chapter 1.1 and 1.3).

During the May 2013 campaign one 2D-DET sampling at each site was complemented by photographs and sampling of the sediment Chapter that faced the 2D-DET probes. Comparison between sedimentary features and particles composition with pore water distribution was possible thanks to these composite 2D samples. The complete treatment and calculation performed on the 2D-DET + photograph + sediment plate for Fe_d from site 1 is described in Chapter 1.1 and Chapter 1.3 with details on these analyses. The sediment plate from site 2 composite

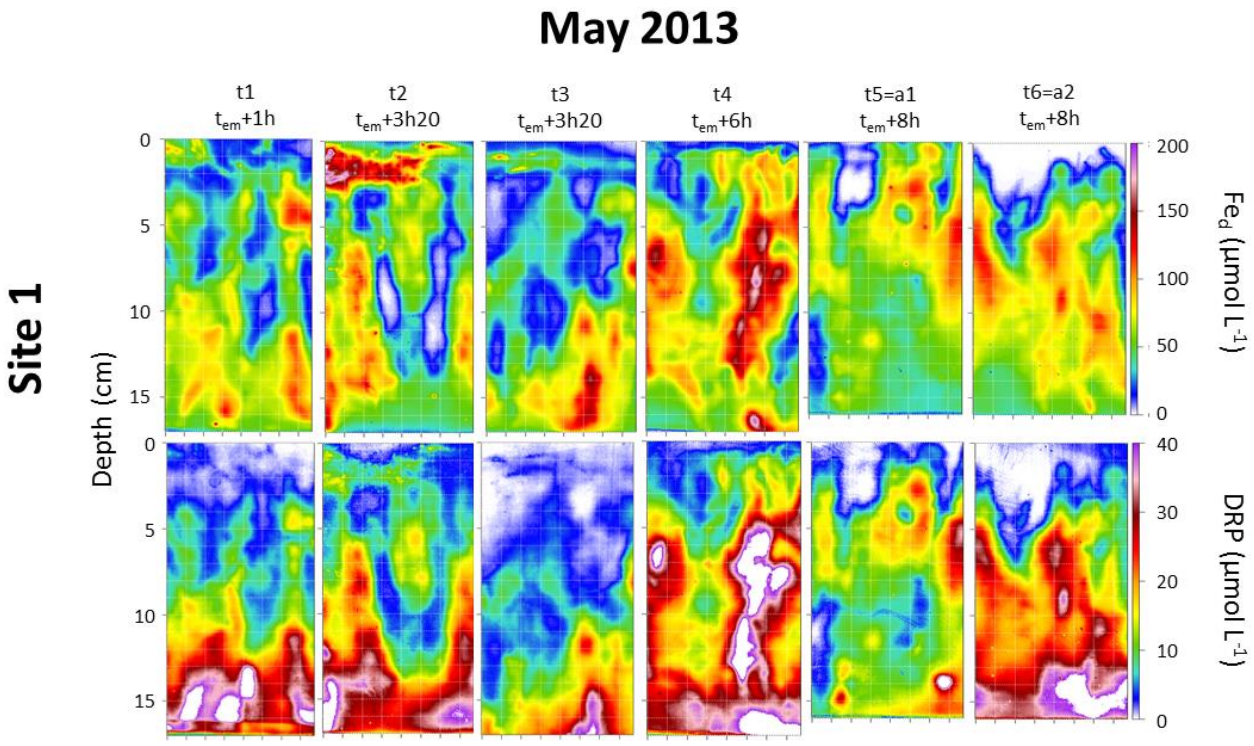

Figure 57 Time series of 2D distribution of Fe_d and DRP (resolution of 200 µm x 200 µm) after emersion. *In situ* incubation of gels t1, t2,t3 have begun before previous emersion.

sample was manually cut within 30 minutes in 1 cm^3 cubes for a surface of 15 cm x 8 cm and sediment cubes were immediately frozen for solid phase analyses. Within a week, samples were freeze-dried and manually ground using an agate mortar. Aliquots of the powder (~100 mg) were digested by 10 mL of a solution of ascorbic acid (buffered at pH 8) during 24 hours (Kostka and Luther, 1994; Anschutz et al., 1998; Hyacinthe et al., 2001, 2006; Hyacinthe and Van Cappellen, 2004) and analysed on ICP-AES (Thermo Scientific iCAP 6300 Radial) for iron and phosphorus content in a random order (overall uncertainty of extraction and analysis <11%). This extraction defined the reactive iron and phosphorus expressed in µmol $g(dry\ sediment)^{-1}$. In sum, the sampling procedure provides five separate images of the site 2 composite sample: a normal bright field image of the face plane of the sampled sediment (1st image), which allows the visual identification of burrows and other sediment structures; afalse-coloured images generated from the 2D-DET gel probe by hyperspectral analysis, which reveal the distribution of Fe_d (2nd image) and DRP (3rd image) in the pore water in two dimensions and at high resolution (pixel size = 200 µm; Harper et al., 1997; Jézéquel et al., 2007; Cesbron et al., 2014) and a false coloured images produced by juxtaposition of concentration of reactive solid iron (4th image) and phosphorus (5th image).

2.2.3 Flux and production rate calculations

Fluxes and production rates have been estimated from 2D pore water Fe_d and DRP distribution using the Savitzky Golay Filter (SGF) procedure developed for 2D-DET data set (Meysman and Burdorf, in prep.; Savitzky and Golay, 1964). 2D datasets were cropped at the left, right and bottom borders to remove boundary effects during the calculation, such as lateral diffusion from the pore water (Harper et al., 1997) or partial desiccation of the gel during experimental handling. The 2D-SGF procedure is based on polynomial interpolation of dataset by SGF resulting in replacement of each data point by a polynomial function of degree three. The polynomial coefficients are calculated to minimize the difference between the

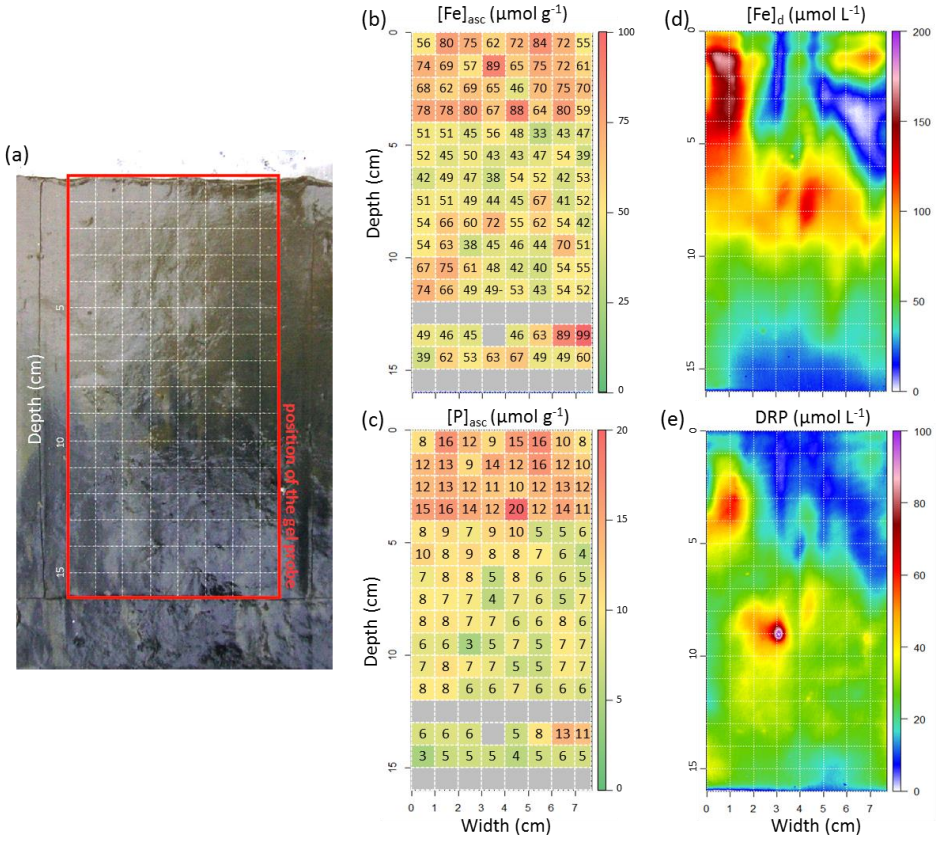

Figure 58 Simultaneous sampling of sediment and pore water in two dimensions; May 2013-site2; gel c1. (a) sediment photograph; (b, c) ascorbate extraction of sediment particles on 1 cm^3 grid; (d, e) 2D DET concentration.

value of the polynomial and the value of data points. Determination of the flux is estimated based on the first spatial derivatives of these polynomials; production is estimated based on the second derivatives (Thibault de Chanvalon et al., in press). Parameters necessary to run the 2D-SGF procedure (Salinity, Temperature and porosity) were estimated for each campaign and each site. Temperature and Salinity were measured by insertion of a WTW Series 3110 conductivity meter in the first centimetre in the sediment and further supposed constant. The vertical distributions of porosity for each sites and campaigns, were estimated from sediment cores sampled simultaneously to the 2D-DET (data are presented in Chapter 2.1) and fitted with an exponential function (such as in Chapter 1.3; Thibault de Chanvalon et al., in press). Lateral variation of porosity was neglected.

2.3 Results

Figure 56 shows the 2D distribution of Fe_d and DRP from 8 DET probes deployed during emersion time for both sites 1 and 2 at two periods. The maximal concentrations for the gels range between 80 and 200 µmol L^{-1} for Fe_d and between 30 and 100 µmol L^{-1} for DRP. The spatial organisation of DRP and Fe_d differs strongly between site/campaign. At site 2, Fe_d and DRP appear above 1cm depth in May 2013 which contrasts to the Fe_d and DRP depletion in the 4 top cm visible in September 2012.

A marked decrease of Fe_d with depth is only observed in May 2013 at site 2 from 10 cm depth whereas in September-site 2 and May-site 1, Fe_d seems to extend at least as deep as the maximum sampling depth. Elongated zones of iron depletion (Fe_d < 20µmol L^{-1}) connected to the surface (or to the iron depleted

layers) are often observed, most of the time with a "finger"-shape (gels b3, c1, c3). One can note for gel b1 the presence of an iron-depleted zone shaped as an onion. Larger iron-depleted zones can be seen on gels a1, a2 and c1. Most of these zones correspond to phosphorus-depleted environments as well. At depth, in May 2013, DRP is enriched while iron is depleted while in September 2012 a better correspondence between both chemicals is observed. Figure 57 shows 2D DET results for a series of deployment along a half-tidal cycle (emersion time) realized in May 2013-site 1. This time series shows no evident tendency of Fe_d distribution according to delay since emersion. However, gels that underwent a period of immersion (gels t1, t2, t3) are characterized by a horizontal layer of high [Fe_d] in the top 3cm. This zone is restrained to the left part of the gel t1 and occurs between 0 and 1.5 cm depth; it reaches Fe_d = 200 µmol L^{-1} between 0 and 2.5 cm depth for the gel t2, and is narrower in the gel t3. Figure 59 focuses on the composite sample from May 2013-site 2 whose gel is numbered c1. The sediment in contact to the gel (a) seems homogeneous, without evident trace of burrows. Sediment colour at the surface is brown, but at 9 cm depth the colour switches to a darker nearly black colour. The corresponding sediment concentration in reactive (ascorbate extractable) iron ($[Fe]_{asc}$; Figure 59b) and phosphorus ($[P]_{asc}$; Figure 59c) ranges respectively from 33 to 100 µmol g^{-1} and 3 to 20 µmol g^{-1}. Most of the variation occurs vertically as shown by the relative standard deviation (rsd) which is more important on columns (mean of 23.9 %, n=8) than on rows (mean of 18.4%, n=18). Hence, $[Fe]_{asc}$ is enriched within the first 4 cm of the sediment (70.2 µmol g^{-1}, σ=10.7, n=36) compared to deeper layers (53.7 µmol g^{-1}, σ =12.3, n=89). However, few zones below 4 cm depth are as rich as the top 4 cm such as a 2 x 2 cm square on the left below 10 cm depth (70.5 µmol g^{-1}) and a 2 x 1 cm zone on the right between 13 and 14 cm depth (94 µmol g^{-1}). $[P]_{asc}$ shows a similar pattern with 12.5 µmol g^{-1} (σ = 2.5) above 4 cm depth and 6.7 µmol g^{-1} (σ = 1.7) below. The vertical variation is slightly more marked than for reactive iron (mean (rsd) is 39.3 % on columns versus 20.5 % on rows) and only one enriched zone is clearly visible (between 13 and 14 cm depth at 12 µmol g^{-1}) at depth. The dissolved species (Figure 59c and Figure 59f) show contrasted distributions. From surface to 8 cm depth, Fe_d presents high lateral variation produced by 2 iron depleted zones. Within a three-cm iron-enriched layer (6 - 9 cm depth), Fe_d distribution is laterally more homogeneous (80 - 120 µmol L^{-1}). Below 10 cm depth, [Fe_d] decreases down to 0 - 20 µmol L^{-1} at 14 cm depth. On the 8 top cm, DRP follows roughly Fe_d distribution but differs by 1) the occurrence of an intense narrow patch (depth = 9 cm; width = 3 cm) not visible on Fed distribution and 2) a globally constant DRP concentration below 9 cm depth which contrast to [Fe_d] important depletion.

Figure 59 shows the 2D distribution of estimated production rates from SGF procedure of gel c1. Productions are very intense within the top 4 mm (~ 200 µmol L^{-1} d^{-1} for Fe_{prod} and ~ 60 µmol L^{-1} d^{-1} for P_{prod}). There is a strong decrease down to roughly -50 and -20 µmol L^{-1} d^{-1} for respectively Fe_{prod} and P_{prod} (thus defining a consumption layer) and then a new increase at 1 cm depth. Below this strong horizontal oscillation, most of the estimated productions vary horizontally according to elongated narrow zone of production that alternate with narrow zones of consumption. The two intense patches of P_{prod} can be observed at 9 cm depth (width = 3 cm and 7 cm) corresponding to [DRP] maxima. 2D production distribution was determined for the entire collection of sampled gels (as shown in Figure 56 and in Figure 57) but are not described in detail here (see Annexe 8).

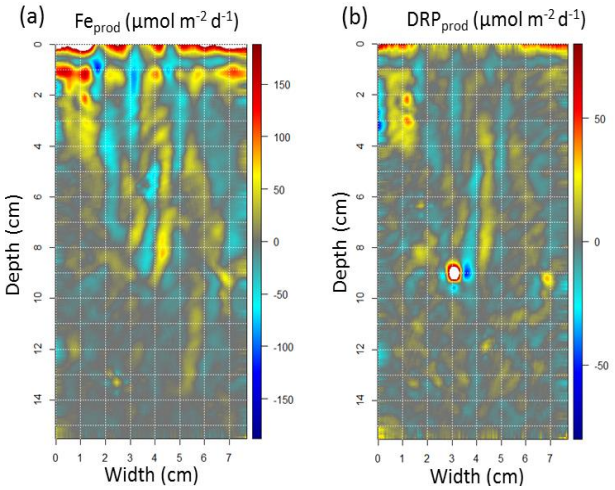

Figure 59 Estimated production rates by the SGF procedure for gel c1 (Figure 58d and Figure 58e)

2.4 Discussion

2.4.1 Iron dynamics – large scale variability: seasonal pattern and site specificity

Les Brillantes mudflat is a low salinity environment characterized by important sediment deposition during winter, followed by compaction and frequent smaller resuspension events eroding progressively unconsolidated sediment (Deloffre et al., 2006). Sediments deposed during winter are rich in reactive iron oxides. In that way, winter sediments fuel a (3-6 months) transitory period until complete iron oxide depletion. Two processes are responsible of the depletion: reductive dissolution of iron in the sedimentary column and erosion of reactive iron oxides-rich sediment (Chapter 2.1). The reductive dissolution intensity can be estimated from Fe_d concentration. The Fe_d distribution from 2D-DET samples (Figure 56) is in strong agreement with 1D-DET profiles (Chapter 2.1). In May 2013, for both sites, high lateral variability at a sub-centimetre scale indicates the strong influence of bioirrigation (as discussed in Chapter 1.1 and 1.3). Despite such lateral variability, Figure 56 shows that iron remobilization occurs at both sites near the SWI indicating probably an important efflux of iron from sediment. These results contrast to results obtained in September that showed for site 2 a remobilization of iron occurring 4 or 5 cm below. Moreover, the important lateral heterogeneity between triplicates shows [Fe_d] maxima ranging from 70 to 200 µmol L^{-1} which indicates a decimetre lateral patchiness in September 2012 - site 2. No 2D dataset is available for September 2012 - site 1 but 1D profiles are similar to May 2013 which suggests similar iron remobilization.

[Fe_d] distribution is the result of a dynamic equilibrium between production and consumption. The 2D dataset and subsequent SGF calculation allow differentiating zones where production is more important than consumption and inversely. The production intensity depends mainly of two variables: organic matter and reactive iron oxide availability. When only weakly reactive iron oxides are available, they become less efficient electron acceptors and are reduced deeper in the sediment. Accordingly, in September 2012, most of the iron oxides stock from winter sediment was consumed and the [Fe_d] increase at depth occurred only below 4cm. However, this deep iron production can also be explained by general weak intensity of organic matter (OM) remineralisation. Oxygen is the ultimate oxidant of most of the organic matter and penetration depth (OPD) can be used as indicator of intensity of OM degradation. The OPD of 4.7 mm in September 2012 - site 2 indicates weak organic matter remineralisation compared to an OPD of 2.0 mm and 1.3 mm for May 2013 site 1 and site 2 respectively ($n > 10$ for each ODP determination, unpublished data). This weak intensity of OM remineralisation can be produced by small input of labile OM from primary production. Therefore, both iron oxide and labile OM availability explain the deep and weak iron production in September. Contrastingly, in May - site 1 and site 2 both labile organic matter and reactive iron oxide would favour more intense and upper Fe_d production.

Iron consumption zones are controlled by either reaction with H_2S from sulfate-reduction which produces the solid FeS or with oxygen which precipitates iron into oxides. The iron depleted zones which are non-evidently connected to the surface (*e.g.* below 10 cm depth in gel c1) are more probably anoxic zones where only reaction with H_2S occurs. The production of FeS generally turns the sediment to black colouration. In May 2013, site 1 shows a black coloration starting from about 17 cm depth (Chapter 1.1), in agreement with no evident iron depleted zone at maximum sampling depth (16 cm depth; Figure 56). In September 2012 - site 2, black coloration appears only below 20 cm depth and no iron depletion zones are visible on gels. In May 2013 however, site 2 shows black coloration that starts at 9 cm depth (Figure 59a) which matches with a general decrease of Fe_d. This decrease extends over the entire width of all gels which indicates important homogeneity of this reaction over several meters (distance between gels). H_2S sensitive sensors (Jézéquel et al., 2007; Cesbron et al., 2014) did not react indicating very low $\sum H_2S$ concentrations in agreement with the smooth gradient of Fe_d observed. The main variables controlling the intensity and the depth at which Fe_d reacts with $\sum H_2S$ are concentrations

of labile OM (that fuels both sulphate-reduction and iron oxide reductive dissolution) and concentration of sulphate. Sulphate concentration depends of salinity resulting, in estuarine environments, from the dynamic between river flood, marine tides and shore freshwater input. Therefore the salinity difference between site 1 (S = 4) and site 2 (S = 7; Chapter 2.1) in May 2013 could induce more sulphate-reduction off shore which explains the shallower decrease of Fe_d at site 2. However, this salinity difference is even stronger for September (S = 16) but without strong apparent sulphate-reduction intensification. The numerous burrows visible on the sediment plate from site 1 (Chapter 1.1) compared to site 2 may explain such apparent paradox as burrows bring oxygen (and other oxidants) in deeper layers in the sediment that oxidizes H_2S preventing sulphides to precipitate with Fe_d. In that way, FeS precipitation and black coloration of the sediment occur deeper in site 1. In September - site 2, the lack of labile organic matter would also explain the apparent weak intensity of sulphate-reduction (see data from Chapter 2.1).

2.4.2 Iron dynamics – small scale variability: role of bioirrigation

The iron depleted zones connected to the surface are probably induced by macrofaunal activities which maintain oxygen in their burrows by renewing frequently the burrow water, filling it with oxygen-rich and iron-poor overlying water. Fe_d reacts with oxygen and precipitates as oxide in few minutes, or alternatively Fe_d is flushed out and replaced by Fe-poor overlying water. Detailed description of Fe_d concentrations and estimated productions related to burrows are provided in Chapter 1.3. However, the relationship between burrows and 2D Fe_d distribution is only possible when a sediment plate is sampled together with a gel probe, which is the case only for gels t4 and c1 (sites 1 and 2 respectively) Moreover, gel c1 has two strongly marked iron depleted zones connected to the surface but the sediment plate (Figure 59a) does not show any evident burrow, which makes a visual description insufficient. Despite these limitations, iron depleted zones are at both stations probably due to flushed burrows, three arguments can be invoked: 1) the depleted zones do not correspond to Fe_{asc} content decreases of the sediment meaning that they must be produced by another process. 2) The candidate process would be able to fuel enough reagents to maintain strong Fe_d gradients (Figure 56). 3) The shapes of the depleted zones are similar to typical burrows shapes built by *Bivalvia*¸ in the case of an onion-shaped feature (gel b1) and build by *Polychaeta*, in the case of finger-shaped features. 4) Burrows are likely to influence the surrounding sediments over few centimetres and therefore, the observed signal could be produced by a burrow in a parallel plan hidden by few millimetres of sediment.

Iron exchange mediated by macrofaunal activities represents a more important flux towards water column than diffusive flux across the water-sediment interface (Chapter 1.3). Similar estimation performed on DRP (gel t4) reveals a diffusive flux across sediment-water interface of 9 ± 3 µmol m^{-2} d^{-1} and flux across burrow lining of 85 ± 21 µmol m^{-2} d^{-1}. These values indicate that macrofaunal-mediated fluxes represent 90 ± 23 % of the DRP flux from sediment towards water column for gel t4 highlighting the importance of *bioirrigation* also for DRP. However, even if one assumes that all iron depleted zones that are connected to the surface are generated by some hypothetical burrow, it is difficult to estimate the length and the shape of the burrow in numerous cases. For example comparing Figure 59d and Figure 59a, the two iron depleted zones near the surface (at width = 3cm and width = 5cm) match perfectly with the zones of iron consumption. However there are numerous consumption zones that are not clearly linked to an iron depleted zone (depth = 2 – 8 cm width = 2 cm and depth = 5 - 10 cm, width = 4 cm) and any choice made to define one zone or another as a burrow would be quite arbitrary. Other chemical species (such as O_2 or NO_3^-) would be necessary to ensure if visible consumptions are linked to active burrows. Consequently, in the present study, samples are characterized with the apparent production rate (APR in µmol m^{-2} d^{-1}), defined as the sum of the positive production estimated by SGF procedure over the whole surface described by each gel. It corresponds for Fe-APR to the rate of iron oxide dissolution that occurs in the sediment making dissolved iron to be available to join water column, to be buried in a FeS form or to precipitate again as an oxide.

The thin shallow layer enriched in Fe_d visible on gels that have undergone immersion (t1, t2, t3) seems produced by constellation of few millimetres patches that look like contamination but are present in the three datasets. More images are necessary to decide the matter and to propose a reasonable explanation. Apart this tricky observation, no influence of the tidal dynamics is observed on Fe_d distribution in agreement with the low permeability expected from muddy sediment. Consequently, sediment seeping and pore water advection produced by tidal pumping (Deborde et al., 2008) is probably negligible at site 1. DRP distribution neither shows influence of tidal pumping.

2.4.3 P behaviour and relation with Fe

The large available dataset of simultaneous Fe_d and DRP concentrations permits to identify 3 sources of phosphorus according to i) DRP distribution and ii) relation with Fe_d distribution. First source: phosphorusadsorbed on iron oxides, produced in the interstitial water simultaneously to Fe_d, i. e. numerous gels present evident similarities between Fe_d and DRP distribution (gels a1, a2, b3 c2 and c3 from Figure 56 and the whole time series from Figure 57). Phosphorus bound to Fe oxides can originate directly from fluviatile particles or can came from previous *in situ* iron oxide enrichment from other DRP sources. Similar sources are frequently reported in the literature (*e.g.* Sundby et al., 1992; Slomp et al., 1996; Anschutz et al., 1998; Hyacinthe and Van Cappellen, 2004).

Second source: the deeper part of the sampled gels which is characterized by a regular increase of DRP concentration with depth despite an often low [Fe_d]. This upward flux is generated by an upward diffusive flux of DRP from the bottom produced by processes which occurs deeper the gels bottom. These processes can be either the nutrient recycling from OM that is oxidized by sulphate-reduction followed by upward diffusion of mineralized nutrients or either the iron oxide reduction by H_2S that releases previously bound DRP.

Third source: frequently, DRP 2D distribution is characterized by intense patches of production of few millimetres width. Figure 59b shows typical examples (at depth = 9 cm; width =3 cm and 7 cm) and Cesbron et al. (2014) report similar features within iron depleted zones of the sediment of Arcachon Bay tidal mudflats. These signals come probably from nutrient release during mineralisation of very labile organic carbon patches. Each 2D distribution of dissolved phosphorus is a composition from these 3 sources, with different relative importance of each source according to the considered location.

To obtain a global overview of DRP sources, the apparent production rates of phosphorus have been calculated. Fe-APR and P-APR are presented in Table 7. September samples have similar P-APR (383 ± 30 µmol m^{-2} d^{-1}, n = 3) but highly variable Fe-APR. These different behaviours between Fe-APR and P-APR are obtained for gel b2 which has a very intense patch of phosphorus (Figure 56). Without this patch both P-APR and Fe-APR would be low for gel b2 in agreement to the low concentrations observed. May 2013 - site 2 has a constant Fe-APR (1920 ± 26 µmol m^{-2} d^{-1}, n = 3) and variable P-APR due to important DRP from patchy labile OM. May 2013-site 1 shows important variation in both Fe-APR and P-APR, the two are correlated (r^2 = 0.48) in agreement with the observation that part of

Sept 2012 – Site 2			May 2013 – Site 2			May 2013 – Site 1		
Gel	Fe-APR	P-APR	Gel	Fe-APR	P-APR	Gel	Fe-APR	P-APR
	µmol m^{-2} d^{-1}			µmol m^{-2} d^{-1}			µmol m^{-2} d^{-1}	
b1	2662	377	c1	1896	649	t1	5461	766
b2	1032	357	c2	1948	390	t2	3201	669
b3	2916	416	c3	1916	448	t3	3240	552
						t4	4240	994
						a1	3097	656
						a2	2104	481

Table 7 Apparent Production Rate (APR) calculated for each 2D-DET, based on SGF procedure estimation.

DRP is from iron bind source. As expected, the important spatial variability produced by burrows (May - site 1) generates an APR for both species of nearly twice the APR of site 2.

The analyses of ascorbate extractions inform about the phosphorus that is bound to iron independently to organic phosphorus. Figure 60a shows that the 8 top centimetres (in red and green) are characterized by a strong correlation (r^2=0.78) with ratios decreasing from $[Fe]_{asc}/[P]_{asc}$ = 5.7 (n = 32; σ = 0.7) in the top 4 cm layer to $[Fe]_{asc}/[P]_{asc}$ = 9 (n = 47; σ = 1.9) below 8 cm depth (Figure 60b). However this ratio evolution is mostly a bias generated by a non-zero intercept of the $[Fe]_{asc}$-$[P]_{asc}$ relationship. If not forcing intercept to zero, the best fit gives an intercept at $[Fe]_{asc}$ = 23 µmol g^{-1} indicating that an important part of iron reactive oxide seems to not have any P bounded, and a slope of 3.7 indicating that $[Fe]_{asc}$ that bears $[P]_{asc}$ is richer in phosphorus than indicated by individual ratio. Below 8 cm depth, $[Fe]_{asc}$ increases in some locations without impacting significantly $[P]_{asc}$. This deep $[Fe]_{asc}$ are probably freshly precipitated FeS or a bias from handling.

The iron bound source of DRP can be identified according to the relation with Fe_d since both species are produced simultaneously in pore water during reductive dissolution of iron oxides. Figure 60c shows the ~300 000 pixels from gel c1 according to the Fe_d and DRP concentrations. Despite superimposition of numerous pixels, several relations between Fe_d and P seem to appear. However, an ideal case of only one patch of simultaneous Fe and DRP production in a non-reactive environment would generate a progressive and conjoint decrease of both concentrations as one move away of

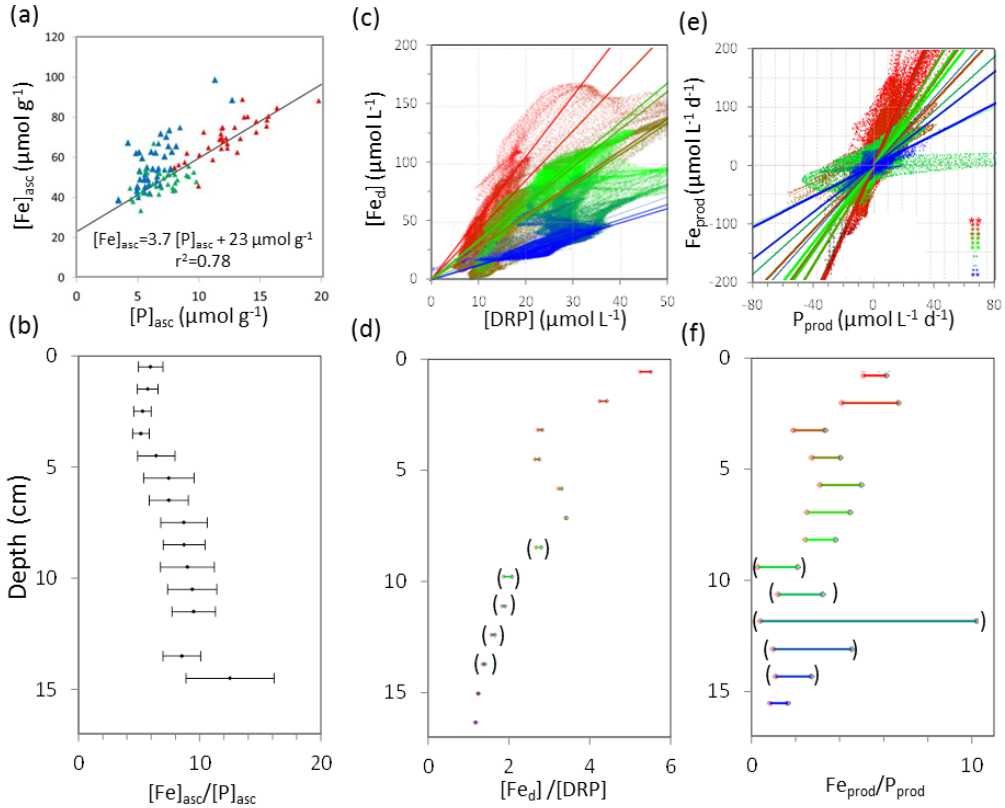

Figure 60 Example of Fe-P relationship for gel c1 (May 2013 - site 2). a) relation between $[Fe]_{asc}$ and $[P]_{asc}$ from Fig. 3b and 3c (red: top 4 cm; green: between 4 and 8 cm; blue: between 8 and 15 cm). Linear regression is calculated on the top 8 cm. b) variation of the mean $[Fe]_{asc}/[P]_{asc}$ ratio according to depth for a layer of 1 cm-thick (error bars correspond to standard error). c) plot of $[Fe_d]$ against [DRP] (extracted from Fig. 3d and 3e; same color code). Lines are best linear regression for each 1.2 cm-thick layer (intercept are forced to zero). d) $[Fe_d]/[DRP]$ as calculated previous slopes (brackets represent $r^2 < 0.5$). e) and f) Similar representation but for Fe_{prod} and P_{prod} estimated by SGF procedure

the source due to diffusion. On a [Fe_d] versus [DRP] plot, this ideal case would produce an entire line from a maximum, which corresponds to the production patch, to zero which would correspond to a sample located at an infinite distance. Theoretically, the ratio would be constant only if ions have same values of diffusive coefficients and as it is not the case for Fe_d and DRP, a slight bombing of the line is expected. In a real environment however, numerous traces from different patches of production would interfere and diffusion prevents precise interpretation of reaction processes. This correction of diffusion corresponds to the estimated production from SGF procedure whose plot is represented in Figure 60e. However, in Figure 60e, data are strongly concentrated around the origin and it is necessary to reduce the dataset by considering together pixels from reduced surfaces in order to interpret that dataset.

We have here chosen to split datasets in 1.2 cm thick layers and to look at the correlation in each layer. In Figure 60c and Figure 60e, colours correspond to layers from red at the surface to blue at the gel bottom. Best linear regressions minimizing errors on [Fe_d] and forcing intercept at zero are also represented with the adequate colour. Slopes of linear models are more robust than individual [Fe_d]/[DRP] ratios performed for each pixel. We will further use the notation [Fe_d]/[DRP] when referring to these slopes. Uncertainty is estimated from the regression coefficient (r^2), and from the difference between calculated slopes as errors are minimized either on [Fe_d] or on [DRP]. Figure 60d and Figure 60f represent slopes obtained from each layer according to their depth for respectively concentration and production datasets. Figure 60d shows and important [Fe_d]/[DRP] decrease with depth, going from [Fe_d]/[DRP] = 5.6 at the surface to [Fe_d]/[DRP] = 2.8 at 3 cm depth followed by a slighter decrease down to [Fe_d]/[DRP] = 1.1 at 16.4 cm depth. Figure 60f shows for Fe_{prod}/P_{prod} about the same pattern. The general regression coefficients are quite high (r^2 > 0.5) above 9 cm depth for both concentration and

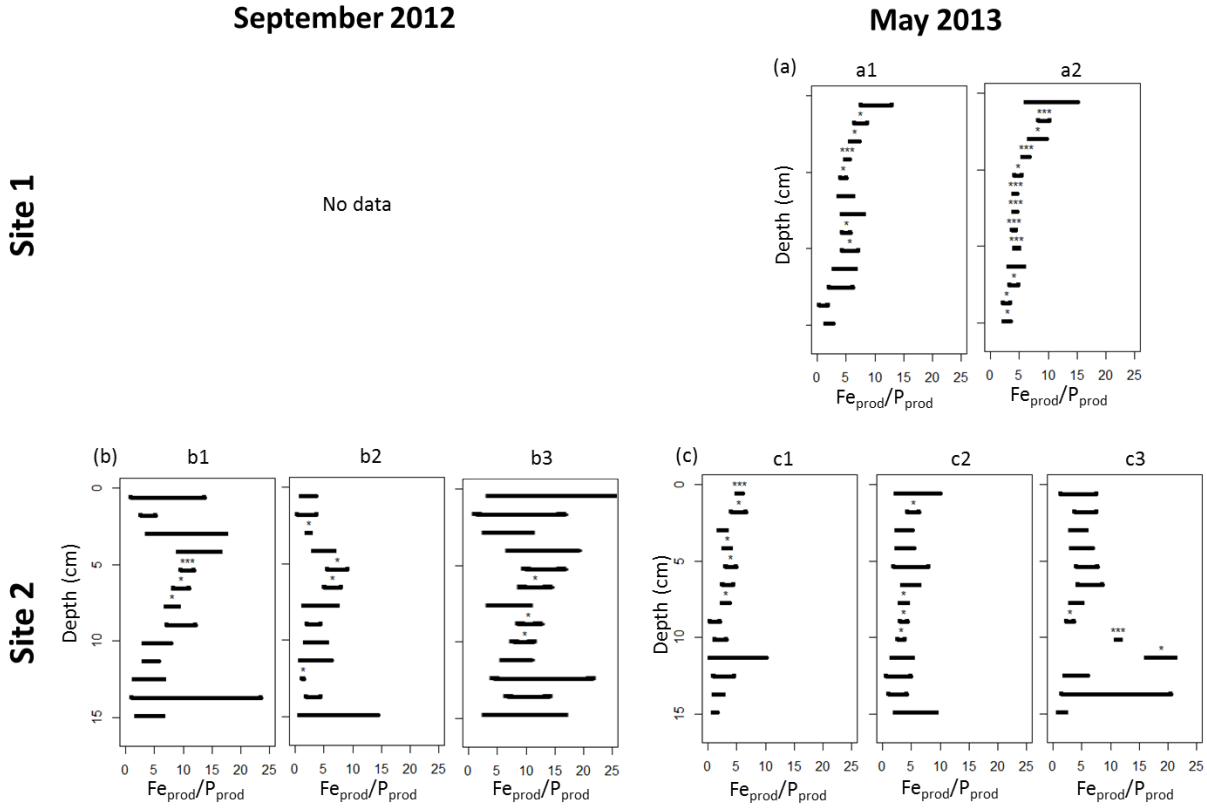

Figure 61 Vertical distribution of the slope of iron and phosphorus productions obtained form different gels. Stars depend on regression coefficient value (* = r^2 > 0,6; *** = r^2 > 0,8)

production correlations. The mean production ratio on the top 4 cm is Fe_{prod}/P_{prod} = 4.3 ± 1.6 which is in agreement with the $[Fe]_{asc} = f([P]_{asc})$ slope of 3.7 and therefore confirms that most of phosphorus released into pore water were adsorbed onto iron oxides within the top 4 centimetres.

Fe_{prod}/P_{prod} profiles are shown for other gels in Figure 61 with regression coefficients represented by numbers of stars (full plot are available in Annexe 8). Layers from September-site 2 have high coefficients of regression ($r^2 > 0.6$) only around 5 cm depth. It corresponds to the appearance of Fe_d and DRP in interstitial water according to a Fe_{prod}/P_{prod} slope which ranges between 7 and 12. These high values indicate a low P content of reactive iron at that depth. The lack of correlation below 10 cm depth is mostly explained by the very weak reactivity of iron during this campaign. The intense patch of DRP from the gel b2 (depth = 14 cm; width = 1 cm) is characterized by a very low slope with Fe_{prod}/P_{prod} = 1.5 ± 0.2 that confirms that most of the produced DRP in these small patches do not originate from iron oxides but from labile OM remineralization. The low Fe_{prod} estimated in the patch indicates that only few iron oxides are dissolved during remineralisation of this labile OM. Further chemical analyses would be necessary to determine the main electron acceptor in this patch. It could also be caused by dissolution of some FeP mineral such as vivianite (Nriagu, 1972; Ruttenberg, 2003; Egger et al., 2015). Gels c2 and c3 have too few significant slopes, moreover the high ratio (with $r^2 > 0.6$) around 10 cm depth of gel c3 is produced by a constellation of few very narrow patches similar to pollution. Gels a1, a2 (times series having similar profiles, available in Annexe 8) and c1 have Fe_{prod}/P_{prod} slopes with generally high r^2 values with the exception of the bottom part (below 11 cm depth) probably due to the more important influence of the upward diffusive DRP source from bottom boundary. The main feature on these gels is a Fe_{prod}/P_{prod} slope decrease on the top 5 cm which indicates an increase of P bound to iron oxide with depth. This variation is probably due to the bottom origin of DRP that diffuses upward and binds mostly to the first (the deeper) available iron oxide met. This progressive enrichment has been proposed on a temporal monthly scale in Chapter 2.1. The decrease goes from Fe_{prod}/P_{prod} = 8 to Fe_{prod}/P_{prod} = 5 at site 1 and from Fe_{prod}/P_{prod} = 5 to Fe_{prod}/P_{prod} = 3 at site 2. The better r^2 values generally observed at site 1 indicates probably a more important Fe bound source of DRP relative to OM sources. Moreover, observations of DRP production and concentration show the more important contribution of DRP from MO-patches at site 2 which explains the lower r^2 value and could be responsible of the lower Fe_{prod}/P_{prod} slope at site 2.

2.5 Conclusion

The simultaneous 2D distribution of Fe_d and DRP obtained with a 2D-DET technique allows discriminating locations of strong Fe_d and DRP consumption due to oxygenated burrows and locations of intense DRP production generated by labile OM degradation. Based on 2D SGF procedure, P release by bioirrigation is estimated to 85 ± 21 µmol m^{-2} d^{-1} (roughly 90% of the total efflux). Moreover, production of Fe_d and DRP can be spatially compared. By isolating zones of iron reductive dissolution with criteria on the correlation coefficient of the best linear fit, the estimated production is likely to inform about the composition of reactive solid phases. By selecting zones as horizontal layers, we show that iron oxides within the top 2 cm are probably unsaturated in P-bound. Thus, in May 2013, superficial iron oxides were likely preventing diffusive P release towards the water column. The coupling of 2D-DET with solid phase analyses brings important information and allow to estimate independently the Fe/P ratio in the solid phase at about Fe/P = 4. However the visual identification realised with the sampling of sediment plates is not enough to well constrain the location of burrows in the sediment. Therefore we recommend identifying burrows influence by the help of geochemical indicators in interstitial water such as O_2 or NO_3^-.

Acknowledgements

This study is part of the RS2E – OSUNA project funded by the Région Pays de la Loire. Thanks to Clement Chauvin, Cyrille Guindir, for their support in the field and laboratory.

Partie 2 :

3 Fer, manganèse et terres rares comme proxies des transformations des particules à travers l'estuaire de la Loire

---

A. Thibault de Chanvalon[1,2], E. Metzger[1], A. Mouret[1], E. Rozuel[2], J. Knoery[2], J-F. Chiffoleau[2], C. Brach-Papa[2]

[1] Université d'Angers, LPG-BIAF, UMR CNRS 6112, 49045 Angers Cedex, France
[2] Ifremer, LBCM, Rue de l'Ile d'Yeu, 44300 Nantes, France

D'après l'article soumis dans Journal of Sea Research

Edited by: P. Anschutz

ABSTRACT

During their transfer across estuaries, particles endure numerous cycles of deposition-resuspension which correspond to as much redox oscillations. These oscillations are likely to modify the particles content of redox sensitive metals such as iron, manganese and two rare earth elements (REE): Ce and Eu. The present paper focuses on the fate of particles from the Loire estuary by comparing chemical transformations during burial of sediment with transformation of suspended particulate matter during transfer across the estuary. The former is estimated from sediment cores sampled in an estuarine intertidal mudflat, the second is evaluated by comparing SPM content from time series of a station upstream the estuary with SPM sampled outside the estuarine embayment at marine salinity. Iron content decreases in the same order of magnitude during each process confirming the important loss of iron (~ 15 % of total iron from riverine SPM) from particles as they reach the ocean through estuaries (Raiswell, 2006). Manganese is probably also lost during the transfer (Trefry and Presley, 1982) but the upstream temporal variability prevents any quantification. Signature of redox sensitive metal is also followed along the salinity gradient taking care of SPM concentration. Particles from a high SPM concentration sample are interpreted as particles that frequently undergo anoxic conditions. The similarity of Ce and Eu signatures between highly concentrated SPM and sedimentary particles suggests that most estuarine transformations are probably induced by early diagenesis during deposition (or anoxic) period.

RESUME

Au cours de leur transfert à travers les estuaires, les particules subissent de nombreux cycles de dépôt-remise en suspension qui correspondent à autant d'oscillations redox. Ces oscillations modifieraient la teneur des particules en certains métaux vulnérables tels que le fer, le manganèse et certaines terres rares (REE) : Ce et Eu. Cette étude se focalise sur l'évolution des particules dans l'estuaire de la Loire en comparant les transformations de particules lors de leur enfouissement sédimentaire avec les transformations des particules lors de leur transfert vers l'océan. La première transformation est estimée par l'échantillonnage de carottes sédimentaires d'une vasière intertidale de l'estuaire, tandis que la seconde est évaluée à l'aune de la différence entre la compositions des particules prélevées en amont de l'estuaire (pendant un suivi temporel) et des particules prélevées en dehors de l'échancrure de l'estuaire, à des salinités marines. La teneur en fer diminue du même ordre de grandeur (~ 15 % du fer initialement présent dans les particules fluviatiles) lors de chacune des transformations, ce qui confirme l'importance de la perte en fer à travers les estuaires (Raiswell, 2006). Le manganèse subit probablement aussi une perte durant son transfert estuarien (Trefry and Presley, 1982) mais la variabilité temporelle des apports fluviaux n'en permet pas la quantification. Les particules issues d'échantillons à forte concentration en MES sont susceptibles de subir plus fréquemment des conditions anoxiques. La similarité des signatures de Ce et Eu entre les échantillons riches en MES et le sédiment met en évidence l'importance des processus diagénétiques lors des dépôts (ou des périodes anoxiques) dans la transformation des particules transférées à travers l'estuaire.

3 Particles transformation through estuaries: Fe, Mn and REE signatures across the Loire Estuary

3.1 Introduction

Estuaries are important reactors for riverine particles by filtering the continental output before release into the ocean. Hence, hydrodynamics of estuaries traps fine particles (Dalrymple et al., 1992) during low-flow periods. During their storage, particles are shuttled between sediment and water column by sedimentation at slack tide, and resuspension during both ebb and flow. This alternation favours the concentration of suspended particulate matter (SPM) which forms a high turbidity zone (HTZ) along the estuary. At the bottom of the water-column, particle concentration in the HTZ can be elevated enough that the settling rate becomes zero and leads to the formation of a fluid mud. When resuspension events are less frequent, the settled particles progressively consolidate into muddy sediment. High density of particles favours heterotrophic conditions by driving up available organic matter and reducing light penetration, and simultaneously reduces convection and oxygen supply. Consequently, the probability for one particle to be in an oxygen depleted environment increases according to particles concentration (HTZ < fluid mud < sediment). Processes controlling the alternation of anoxic and oxic conditions depend of the environment. Resuspension events mix particles from fluid mud and top sediment with particles from HTZ increasing oxygen concentration around the formers and depleting oxygen around the latter (Abril et al., 1999). For particles stored in the muddy sediment, the formations and desertions of burrows by macrofauna generate alternating periods of oxic water supply from surface followed by a return to anoxic conditions (Aller, 1982). These two processes induce redox oscillation with characteristic durations in the range from few hours for the resuspension process to several weeks for burrow formation processes (Meysman et al., 2003a).

The first approaches quantifying the impact of redox oscillations were based on observations of estuarine HTZ and deltaic mobile mud (Aller, 2004; Abril et al., 2010). The different redox-sensitive elements are dissolved according to the order predicted by the sequence of microbial anaerobic respiration processes (Froelich et al., 1979). In a mostly oxic environment affected by short anoxic events, NO_3^- and Mn oxides are the most reactive elements (Abril et al., 1999, 2000; Robert et al., 2004; Audry et al., 2006). At the opposite, in a mostly anoxic environment with short oxic events, stocks of NO_3^- and Mn oxide are rapidly exhausted and Fe oxy(hydr)oxides become the most reactive species (Aller, 1998; Aller and Blair, 2006). The overall impact of these oscillations at the estuary scale has not been properly investigated and only few publications have tried to correlate SPM composition with early diagenetic processes which occur during deposition periods (Trefry and Presley, 1982; Church, 1986; Regnier and Wollast, 1993; Zwolsman and Van Eck, 1993; Zwolsman and van Eck, 1999; Audry et al., 2007; Andrieux-Loyer et al., 2008). In particular, it is not clear whether the repetition of dissolution / precipitation cycles for Fe and Mn oxides would (1) rejuvenate oxides and ultimately increase their bioavailability (Raiswell, 2011); (2) increase iron oxide crystallinity due to the preservation of the most crystalline phases during each dissolution cycle (Thompson et al., 2006); (3) generate a transfer of Fe or Mn oxides from SPM to the sediment (Poulton and Raiswell, 2002; Raiswell, 2006) or (4) result in an oxide loss for SPM (Moore et al., 1979) due to colloidal/nanoparticles shuttle (Lyons and Severmann, 2006; Lam et al., 2012) which favours downstream Fe or Mn export to the open ocean. Improvement of processes knowledge involving Fe and Mn oxides in estuaries would lead to a better understanding of iron supply pathways for oceanic primary production (Martin and Fitzwater, 1988). A better understanding of remobilisation of Fe and Mn-oxides is also critical for the description of long term storage of organic carbon (Lalonde et al., 2012) and for the estimation of trace metal remobilisation in the environment (Négrel, 1997; Turner, 2000).

The present paper focuses on the transformation of particles from the Loire estuary. The Loire river

catchment receives weathered particles from an 117,045 km^2 drainage basin. During high flow, riverine SPM enters into the estuary with maximal concentrations (20 - 200 mg L^{-1}) with high Al-Fe oxy(hydr)oxides (up to 20% w/w for Al_2O_3 and 7% w/w for Fe_2O_3; Grosbois et al., 2001). During summer, a lower concentration, proportional to the flow, is characterised by calcite and organic matter enrichments due to primary production (up to 25 % w/w and 37 % w/w respectively; Manickam et al., 1985; Grosbois et al., 2001; Gorse et al., 2010). Particle residence time in the Loire estuary is on average about 4-10 months (Ciffroy et al., 2003b), *i.e.* until a flood pushes them out the estuary (Gernez et al., 2015). The Fe and Mn oxides transformations affecting estuarine SPM are investigated by an examination of the Fe/Al and Mn/Al ratios from (1) samples from an estuarine intertidal mudflat that describe temporal evolution of the particle stock stored within the estuary for 3 contrasted seasons, and (2) a SPM sampling transect along the salinity gradient describing the progressive transformation of particles for each season. To confirm the occurrence of significant chemical reactions involved in SPM transformations, the variations of (chemically) reactive oxides are evaluated according to differences between total and partial (*i.e.* ascorbate-buffered) solid extractions. Finally, we also use rare earth elements (REE) composition of SPM to trace chemical reactions occurring during anoxic periods as Ce and Eu are the only REE supposedly redox sensitive

3.2 Material and methods

3.2.1 Study site

The Loire river flows at Nantes between 5200 $m^3 s^{-1}$ and 120 $m^3 s^{-1}$ with a mean flow of 890 $m^3 s^{-1}$ (DREAL Pays-de-Loire, 1994). Since riverine SPM has a concentration roughly proportional to the flow with a maximum around 200 mg L^{-1} (SOGREAH, 2010), we define the highly turbid zone (HTZ) for samples with SPM concentrations above 200 mg L^{-1}. Summer concentrations of chlorophyll-a have a median of 14 µg L^{-1} with a yearly maximum above 50 µg L^{-1} (Crouzet, 1983; Meybeck et al., 1988; Minaudo et al., 2015). Dissolved organic matter (DOC) concentration, have been measured between 2.4 and 10 mg L^{-1} by Cauwet

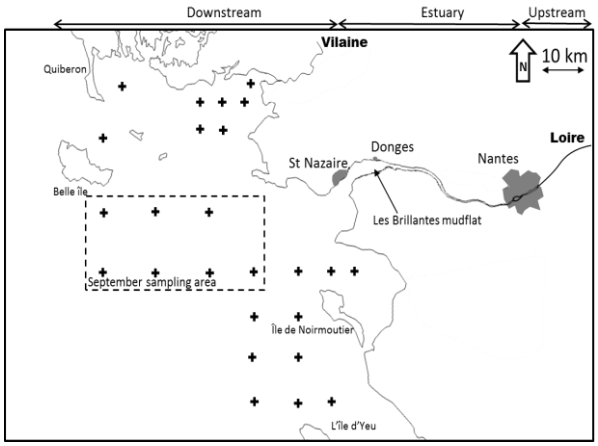

Figure 62 Location of the sampling stations. Black crosses: downstream stations sampled during the May campaign. The dotted rectangle delineates downstream stations sampled during the September campaign.

and Meybeck (1987) and Gorse et al. (2010) with a slight increase during flood. The HTZ dynamics at Donges, 45 km downstream of Nantes (Fig. 1), is described by two re-suspension events of ~ 3 hours characterized by a maximum SPM concentration 1h30 before and 1h30 after the slack of low tide (network SYVEL, GIP Loire Estuaire). The HTZ re-suspended particles are more abundant during spring tides and migrate upstream/downstream according to the river flow. Daily survey of the water column reveals a saline stratification mostly during neap tide and flood, as described in Le Douarec (1978). Nutrients are not conservative along the salinity gradient and are highly variable due to primary production and benthic fluxes (especially for orthophosphate and silicate). Other processes such as hydrolysis of hydroxyapatite, denitrification in the fluid mud and strong nutrient recycling, marked by algal community switches at low salinity (before reaching S = 1 ; Morris et al., 1978; Meybeck et al., 1988), can also be proposed to explain variations of nutrient concentration. Saliot et al. (1988) showed that organic matter in the HTZ is mainly terrigenous (low $\delta^{13}C$ values and high n-alkane CPI values) due to a typical buffering effect of HTZ in which labile organic matter is quickly consumed (Billen et al., 1986; Abril et al., 2002). This buffering effect of the HTZ is further confirmed by the sharp decrease of C_{org} with SPM concentration within the HTZ to a constant value of C_{org}(HTZ) = 3 – 4 % (Billen et al., 1986; Meybeck et al., 1988).

3.2.2 Sampling

Estuarine and downstream SPM were collected during three sampling cruises on "N/O Thalia" along the salinity gradient of the Loire estuary and in the coastal area (Figure 63). Two salinity transects during contrasted tidal amplitudes were conducted during each cruise. Water from roughly 1 m below the surface was continuously pumped using an all-Teflon pumping system made of PFA (Perfluoroalkoxy) tubing connected to a piston pump (ASTI, France) and brought into an on-board, pressurized clean room. Discrete samples (2 L to 5 L) were collected into acid cleaned PFA bottles under a laminar flow. Subsamples were then N_2 overpressure-filtered through pre-weighed acid-cleaned polycarbonate filters (0.4 µm, Nuclepore). After filtration, filters were rinsed with ultrapure water (Milli-Q, Millipore), stored in acid cleaned Petri dishes and frozen. Back to the laboratory, filters were dried to constant weigh in an oven at 50°C.

The second and third cruises were preceded by a weekly to biweekly sampling of "upstream" particles at "Basse-Indre", "Tabarly", "Oudon" and "MontJean" respectively 45, 53, 86, 120 km upstream from St Nazaire. Zero of salinity was verified for each sampling. While the cruises took place, sediment cores were taken at low tide in the mudflat "Les Brillantes", the largest intertidal mudflat of the Loire estuary (1354 ha). The sampling site (47°17'8.00"N; 2°3'49.00"W) is below the mean high water neap tide level (MHWNT), on the slikke, 400 meters offshore from an active cutbank (one meter eroded cliff). There, sediment is mainly composed by silt (92 %) and clay (6 %) with rare sandier horizons (up to 37 % for 63-2000 µm fraction; (Benyoucef, 2014b). Total organic carbon concentrations range from 2 to 3 % w/w and oxygen penetration depth is shallower than 5 mm. Sediment surface is often recovered by a biofilm with a density varying from 20 mg m^{-2} in January to 60 mg m^{-2} in July (Benyoucef et al., 2014). One core (∅ = 8.2 cm) was sampled at each campaign and brought to the field laboratory. Within 6h, the centre of the core was sub-sampled in slices of 2 mm, 5 mm and 1 cm-thick, down to few centimetres. Mud samples were weighed and immediately frozen. During the following week, samples were freeze-dried and ground in an agate mortar.

The first cruise occurred in September 2012 (from 24/09/2012 to 28/09/2012, http://dx.doi.org/10.17600/12070140) during a period of stable, low flow (200 m^3s^{-1} at Nantes (DREAL Pays-de-Loire, 1994, http://dx.doi.org/10.17600/13070070; Fig. 2) and warm water (17 °C). Oxygen depletion usual for this season was measured one week before (network SYVEL, GIP Loire Estuaire) but not during the cruise. Tidal coefficients at St Nazaire (Fig. 1) were of 47 for the downstream transect and 80 for the upstream cruise. During the second campaign (from 19/04/2013 to 26/04/2013, http://dx.doi.org/10.17600/14007900; Fig. 2) Loire flow decreased from 1800 m^3 s^{-1} for neap (tidal coefficient 34) downstream cruise, to 1000 m^3 s^{-1} for upstream and spring tide cruise (tidal coefficient 103). Water temperature was 14 °C. The third campaign (01/02/2014-07/02/2014) was characterized by flood water flow (2400 to 2800 m^3s^{-1}) and a tidal coefficient of 113 for the downstream transect and 50 for the upstream one. Water temperature was around 7 °C; wind and sea-state prevented the collection of samples outside the estuary.

3.2.3 Analyses

Total extractions were processed on entire filters loaded with SPM or on ~ 200 mg aliquots of sediment samples and were digested with a mixture of nitric, hydrochloric and hydrofluoric acids and heated to 130°C in closed Teflon bombs (Rantala and Loring,

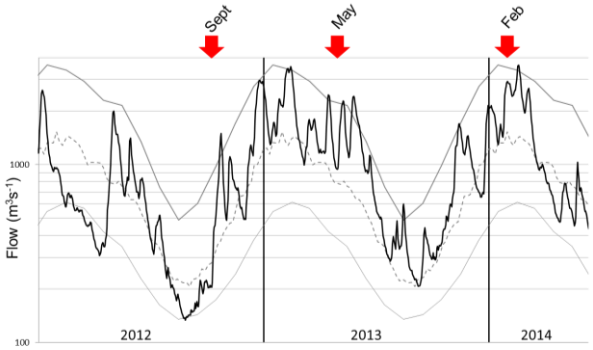

Figure 63 Hydrological context of the 3 campaigns (red arrows). The black line represents daily flow. Dotted and grey lines represent median flow and 20 and 80 percentile of the monthly flow. Data source: DREAL Pays de la Loire.

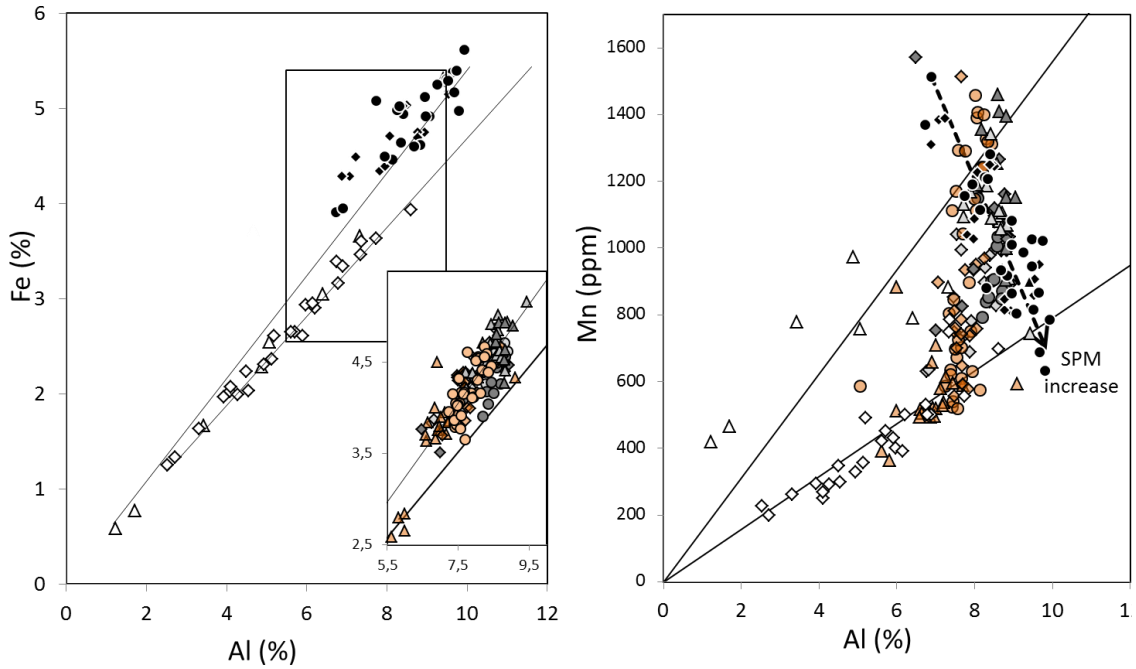

Figure 64 Total Fe (%) vs. Al (%) and Mn (ppm) vs. Al (%) for September 2012 (triangles), May 2013 (diamonds) and February 2014 (circles). The colours correspond to location: white for downstream particles, black for upstream, clear grey for estuary and dark grey for sediment. Solid lines correspond to upstream and oceanic regression trend lines.

1990). Digests were then slowly evaporated to dryness and dry residues were taken up in 50 ml HNO_3 (Suprapur). Analyses of Fe, Al, Mn and REE were performed using an ICP-Q-MS (iCAP Qc, ThermoFisher Scientific) equipped with a Peltier-cooled, quartz cyclonic spray chamber, a 200 µL min^{-1} PFA nebulizer and a Ni sampler and skimmer cones. Elemental concentrations were determined using external calibration (5 to 6 points) in diluted nitric acid (3% v/v, ultrapure). Internal standards of ^{115}In and ^{203}Tl were added to all solutions to correct from instrumental drift. Depending on elements, measurements were performed using standard (STD) or Kinetic Energy Dispersion (KED) modes. For REE analyses, samples were systematically analysed using the KED mode, and special tuning conditions to reduce to a maximum oxide formation within the plasma. Oxide formation rate was evaluated by computing CeO/Ce ratios. During measurements, interferences due to oxide formation with REE elements were checked by injecting a test solution made of Pr, Gd and Ba and measuring resulting signals for PrO, GdO and BaO. Corrections appeared to be necessary only for 151Eu and 157Gd. A reference material (BCR-667) was systematically measured every 10 samples to control ICP-Q-MS response. Our results (n=15) are in good agreement with BCR-667 reference values (Annexe 9). However, the two heaviest (Yb, Lu) and the two lightest (La, Ce) were systematically slightly underestimated resulting in an error of 6 – 8 %.

For ascorbate extractions, samples were incubated in an ascorbate reagent (buffered at pH 8) during 24 hours (Kostka and Luther, 1994). This technique allows to extract most reactive Fe(III) oxyhydroxides (Raiswell et al., 2010) supposedly close to those potentially reduced by microorganisms (Hyacinthe et al., 2006) as well as reactive Mn(III) and Mn(IV) oxides (Anschutz et al., 2005). After extraction, samples were centrifuged (10 min at 3000 rpm) and the supernatant was diluted in HNO_3. Samples were analysed on ICP-AES (Thermo Scientific iCAP 6300 Radial), precision was of 1 and 4% respectively for iron and manganese (twice the relative standard deviation of ICP-AES triplicates). Grain size was analysed for 10 SPM samples (bulk water stored in the black, in a fridge) and for a sediment core from the third campaign, on a Malvern 2000 without preparation treatment (Walling et al., 2000). Analyses were performed less than 4 days after sampling

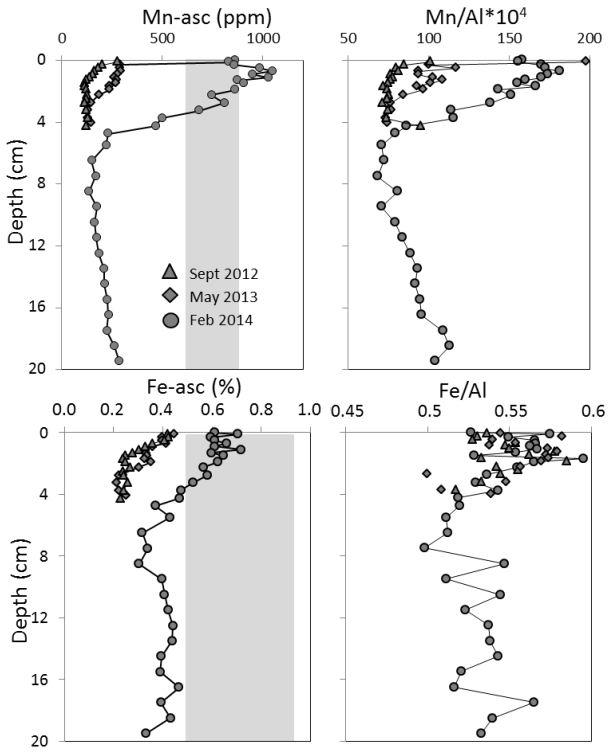

Figure 65 Sediment profiles of iron and manganese concentration extracted by ascorbate and total extraction. The grey zone represents the range of ascorbate extractions for suspended particles in the estuary (February 2014, n = 12).

3.3 Results

Table 8 lists concentrations of Al, Fe, Mn and the sum of all REE concentrations (∑REE) according to the date and location. Upstream and estuarine SPM are characterized by high concentrations of Al, Fe and Mn compared to estuarine sediment and especially to downstream SPM. ΣREE shows a different pattern, as sediment (with ΣREE = 192 ± 20 ppm) has very low variability and is enriched over that of most estuarine, upstream and downstream SPM samples. Only few estuarine samples from the HTZ show more important ΣREE concentration than sediment (up to ~ 700 ppm). Fe and Al are strongly correlated (r^2 > 0.98) with significant differences between upstream and downstream relations (p-value < 10^{-7}; Figure 64). Estuarine samples (both sediment and SPM) are distributed between the upstream and downstream

Location	Type	Date	n	Al (%)	Fe (%)	Mn (ppm)	n	ΣREE (ppm)	n	Fe-asc (%)	Mn-asc (ppm)
Upstream	SPM	Sept 2012	1	9.41	5.34	896					
Upstream	SPM	May 2013	15	8.35 ± 0.88	4.72 ± 0.36	1073 ± 240	4	137 ± 6			
Upstream	SPM	Feb 2014	28	8.78 ± 0.87	4.85 ± 0.55	1040 ± 215					
Estuary	SPM	Sept 2012	24	8.55 ± 0.41	4.67 ± 0.26	1141 ± 169	4	489 ± 180			
Estuary	SPM	May 2013	22	7.97 ± 0.74	4.31 ± 0.34	938 ± 223	22	202 ± 129			
Estuary	SPM	Feb 2014	20	8.52 ± 0.24	4.40 ± 0.22	959 ± 111	18	164 ± 49	12	0.65 ± 0.15	700 ± 73
Ocean	SPM	Sept 2012	7	4.29 ± 2.29	2.08 ± 1.14	722 ± 206					
Ocean	SPM	May 2013	25	5.45 ± 1.58	2.60 ± 0.73	419 ± 159	25	89 ± 43			
Ocean	SPM	Feb 2014									
Estuary	Sediment	Sept 2012	16	7.02 ± 0.30	3.88 ± 0.22	522 ± 64			16	0.29 ± 0.07	145 ± 43
Estuary	Sediment	May 2013	15	7.69 ± 0.19	4.24 ± 0.16	761 ± 232	8	199 ± 7	15	0.32 ± 0.07	267 ± 174
Estuary	Sediment	Feb 2014	32	7.70 ± 0.59	4.16 ± 0.40	926 ± 336	6	195 ± 11	32	0.49 ± 0.12	503 ± 338

Table 8 Summary of dataset. Al and Fe are in % and Mn in ppm of dry sediment (± 1 σ). n is the number of stations sampled for each location and each campaign.

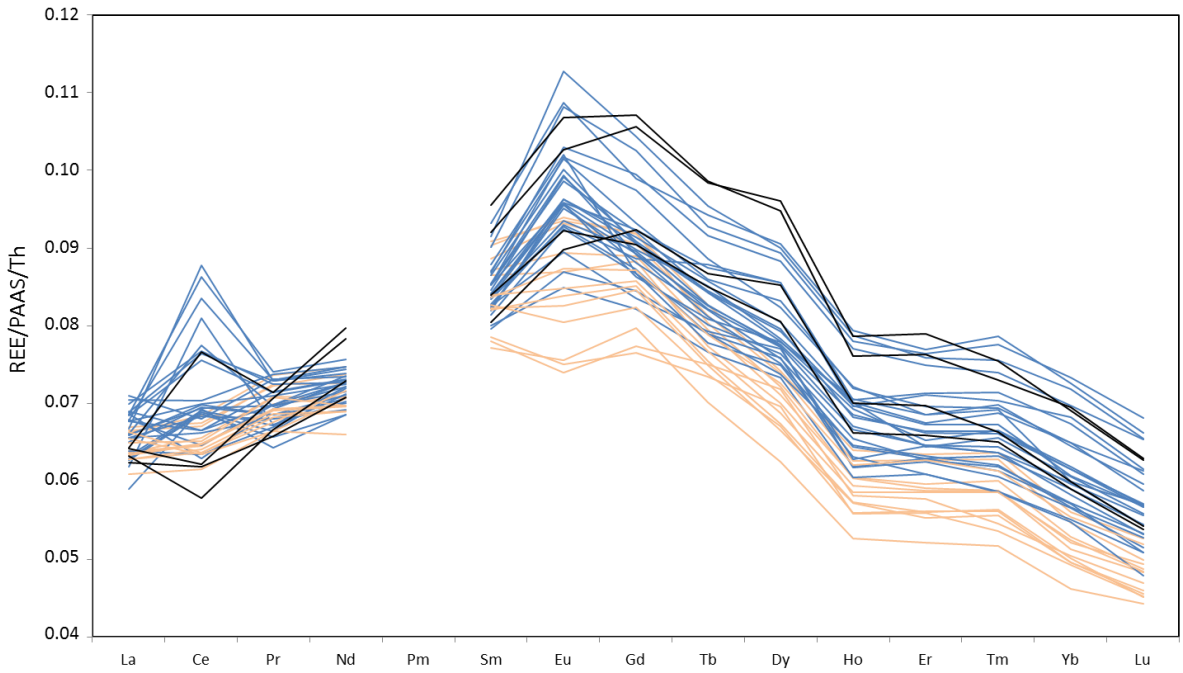

Figure 66 Rare earth spectra normalized on PAAS spectrum and thorium concentration for end-member samples: upstream samples in black; downstream samples in blue (dark grey) and sediment samples in orange (clear grey).

regression trend lines. Mn and Al relationship reveals a clear negative correlation for upstream particles (Figure 64; $r^2 = 0.66$, n = 44, p-value < 10^{-10}), which contrasts with positive and season-dependant correlations for downstream particles ($r^2 = 0.69$ and 0.82, n = 7 and 25, p-value < 10^{-3} and 10^{-15} for respectively September 2012 and May 2013). In the sediment, distribution patterns of both Mn_{asc} (Mn from ascorbate extraction) and Mn/Al profiles (Figure 65) show nearly identical surface enrichments (in the 0 - 4 mm layer for Sept 2012, in the 0 - 20 mm layer for May 2013 and in the 0 - 42 mm layer for February 2014). Although it is less intense, Fe_{asc} shows similar surface enrichment. However, the Fe/Al profile does not show such a clear trend, even if lower values are located at the bottom of the sediment column. The sediment grain size is homogeneous with unimodal silty distribution (D50 = 10.7 ± 1.9 µm, n = 41; data not shown). Some sediment samples present a slight enrichment around 63 µm but all D90 are below 70 µm.

Th-PAAS-normalized concentration of rare earth elements from sediment, upstream and downstream particles are shown in Figure 66. Thorium normalization act as an offset to compare REE-signatures between different samples. The PAAS normalization smoothes the variations between different elementary abundances in order to facilitate the description of the spectrum. After PAAS normalization, expected bell-shaped distributions are observed for nearly all samples. However, numerous intersects between different REE spectra can be seen around local maxima for Ce, Eu and Tm. These slope variations are typically described as "anomalies". Numerous mathematical definitions of "anomalies" occur (*e.g.* Lawrence and Kamber, 2006). In the present study, only elemental ratios are considered for simplicity and because trends are independent of PAAS-normalization (*i.e.* UCC or NASC normalization would lead to the same signature). Therefore, anomaly around the n^{th} REE can be estimated by calculating its ratio vs. its neighbouring REE.

As Ce/La and Ce/Pr are well correlated ($r^2 = 0.96$), they bring the same information and no distinction is made between them. Ce/La is characterized by a constant value in the sediment compared to other SPM samples (Figure 67a). The ratio Eu/Sm (Figure 67b)

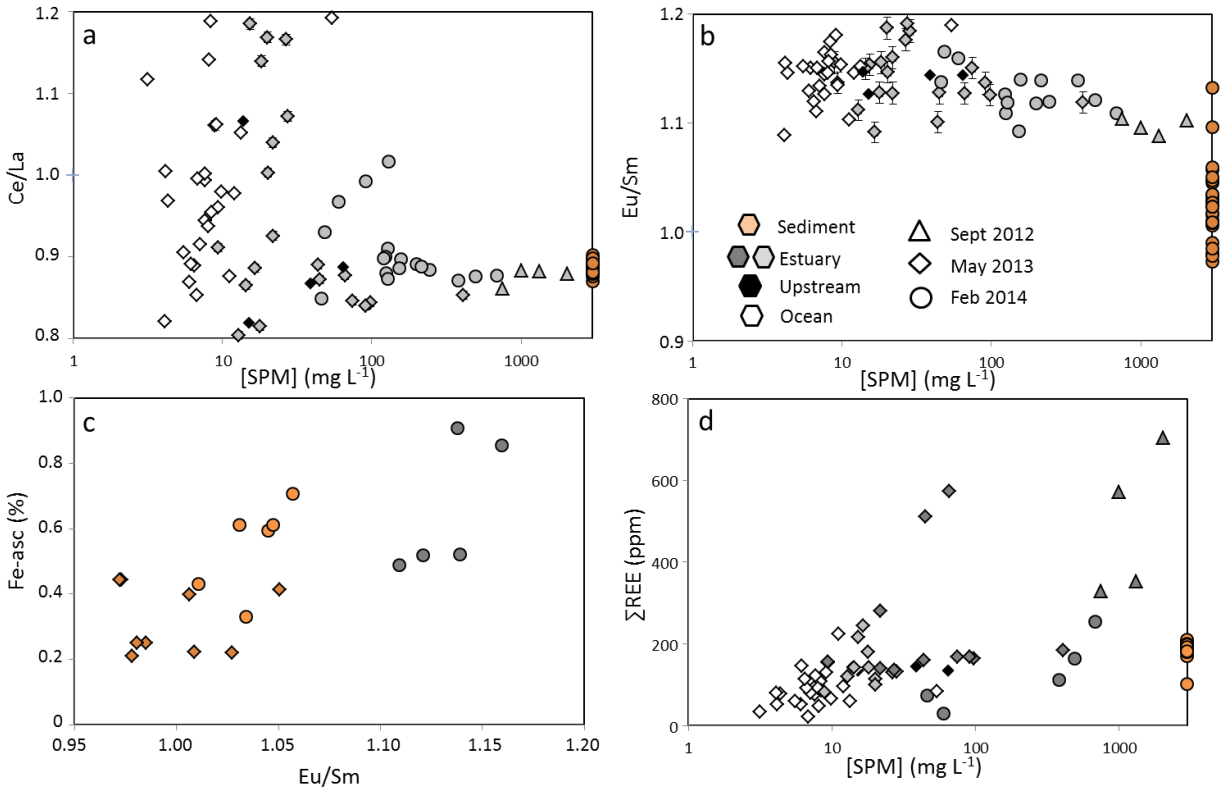

Figure 67 REE signature according to SPM concentration and Fe_{asc} content. Sediment is represented arbitrarily with a particle concentration of 3000 mg L^{-1}.

strongly discriminates sediment samples from SPM (higher Eu/Sm ratio corresponds to surface samples) and is correlated with Fe_{asc} ($r^2 = 0.55$; p-value = 1.3 10^{-6}; Figure 67c). Eu/Gd ratio is weakly correlated to Eu/Sm and is not correlated with any other analysed parameter. Both Tm/Er and Tm/Yb variations were too small compared to analytical uncertainties to bring significant information.

3.4 Discussion

3.4.1 General assumptions

Since mixing from two (or more) SPM sources and *in situ* chemical transformations induce both variations of metal content in sampled SPM, some assumptions are necessary to be made in order to isolate chemical transformations from mixing. First, aluminium will be considered non-mobile and its content exclusively due to terrigenous inputs from the drainage basin. Therefore, normalization of metal content by aluminium would allow discarding the mixing of terrigenous and river born particles.. Secondly, Loire river drainage basin represents the main SPM source in the studied area with SPM discharge range from 0.5 10^6 t yr^{-1} to 2.3 10^6 t yr^{-1} (Figueres et al., 1985; Manickam et al., 1985; Migniot, 1993; Négrel, 1997; Jouanneau et al., 1999; Gorse et al., 2010) versus ~ 0.1 10^6 t yr^{-1} (Jouanneau et al., 1999) for the secondary SPM source (the Vilaine river ; Figure 62). Therefore, variation of metal content due to mixing from other drainage basins would be neglected. Thirdly, as all samples are mainly fine silts, it is unlikely that chemical differences between samples are from some specific sedimentation process that would modify bulk SPM chemical composition. As a consequence of these assumptions, differences between upstream and downstream SPM end-members would be interpreted as chemical particle transformations. Moreover, we further assume that, in average, the particles age increases downstream allowing chemical transformations to progress.

3.4.2 River flux control

Upstream samples (from 4 different locations), show no evident relations between Al, Fe, Mn and distance from Nantes. ANOVA performed on both Fe/Al and Mn/Al with position and date systematically shows a significance of date ($p < 0.01$) and no significance of position. The importance of flow and season on chemical composition of upstream SPM has been described by Grosbois et al. (2001) using a 2-year time series at Brehemont. As we mostly describe upstream inputs during flood ($Q > 1000$ m^3s^{-1} for 2013 and 2014 upstream time series), it is expected that we had sample mostly terrigenous particles (Grosbois et al., 2001). However, the alignment of our samples in the Fe = 0.5575 * Al plot (Figure 64, black symbols) fits extremely well with Grosbois et al. (2001) alignment for low and high flow. Therefore, in first approximation, Fe concentration of upstream particles is efficiently described by a single bearing terrigenous phase mixed with a fraction of river-borne particles that depends on flow and time. However, in more detail, it should be noted that the small deviation around the Fe = f(Al) linear model for upstream particles corresponds to a slight decrease of Fe/Al as the SPM concentration increases (Annexe 10). The upstream behaviour can thus be described by 2 mixing phases: (1) a first phase which is always present and shows constant concentration: SPM_1 and (2) a phase which concentration SPM_2 is variable according to the river flow. This relation corresponds to the equation below (Morris et al., 1987):

$$C = \frac{SPM_1}{SPM}(C_1 - C_2) + C_2 \qquad (30)$$

with C_1 and C_2, the concentrations of phases 1 and 2. Figure 68 shows that this model explains respectively 49 % and 67 % of Al and Mn content variation in the upstream particles (Figure 68) whereas Fe does not significantly vary.

This two-phase mixing model can be used to explain Mn/Al variations and to characterize end-members. Therefore the first phase have a relative content of Al = 6.89 ± 0.85 % and Mn = 1510 ± 220 ppm; and the second phase have Al = 9.84 ± 1.30 % and Mn = 692 ± 103 ppm for high flow. The Mn versus Al plot of these two end-members clearly explains most of the variations of upstream particles (Figure 64). Unfortunately, this upstream Mn/Al signal covers the whole range of Mn/Al ratio described in the downstream end-member and through the estuary, likely hiding signals from estuarine transformation processes.

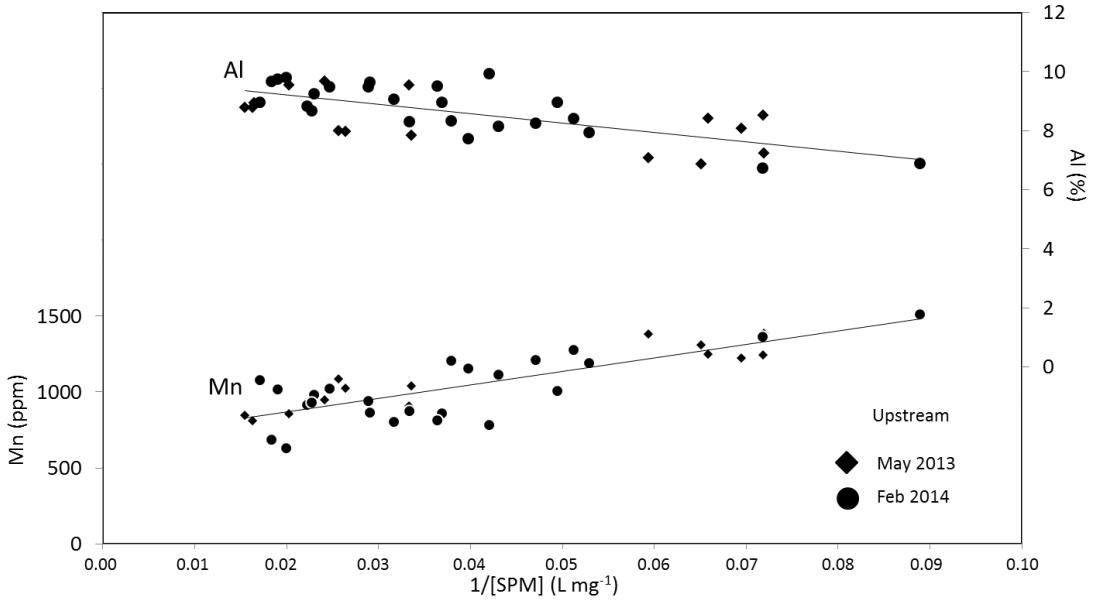

Figure 68 Manganese and aluminum content of upstream SPM according to a mixing between low flow particles and high flow particles (high SPM concentration)

3.4.3 **Signature of benthic transformations**

Residence time of particles in the Loire estuary is less than one month during flood, but up to 10 months during summer (Ciffroy et al., 2003b). This implies a progressive enlargement of particle inventory in the estuary along the year followed by a quasi-complete release during winter floods (mostly in January; Ciffroy et al., 2003b). While particles progressively move downstream, two main environmental parameters vary.

(1) First, daily average salinity presents a progressive increase as the particles move downstream. But as particles move slower than the surrounding water, they suffer also salinity oscillations due to tidal cycles. These salinity variations and their associated ionic strength generate exchanges between dissolved phase (< 0.4 µm) and SPM through processes such as adsorption (Ciffroy et al., 2003a) or colloids flocculation (Sholkovitz, 1978; Escoube et al., 2009). Since dissolved iron (Fe_d) was always measured below 4 % of total iron (dissolved and particulate phases) in the Loire estuary (data not shown), Fe_d cannot explain the changes observed in the particles in the Loire estuary. Furthermore, it shows a conservative behaviour between the upstream (2, 19 and 23 µg L^{-1} for respectively Sept 2012, May 2013 and Feb 2014) and the downstream end members (2 µg L^{-1}; data not shown) indicating no important reactivity.

(2) Secondly, redox conditions can vary. Indeed, particles pass through or settle temporarily in oxygen–depleted zones like the HTZ, the fluid mud or the sediment. In HTZ, fluid mud and top sediment, oscillations of redox conditions are controlled by resuspension and deposition events, mostly driven by tidal cycles (period of oscillation of 6 h) or episodic wind events. Once particles settle and consolidate in a mudflat, redox oscillations become controlled by macrofauna burrowing and the redox oscillation period increases up to few weeks (Wheatcroft et al., 1990; Meysman et al., 2003a, 2008a). Differentiate both processes is beyond the scope of this study but they probably involve different chemical species according to the thermodynamic ladder of early diagenetic primary reactions (Aller, 2004). For short anoxic periods, nitrate and manganese reduction would control redox processes while for longer anoxic periods (few weeks), Fe reduction would be the principal reaction.

Comparison between SPM and bottom sediment Fe_{asc} contents for February 2014 (Figure 65) shows a decreased Mn_{asc} content to 470 - 770 ppm, and a decreased Fe_{asc} content to 0.17 – 55 % w/w. These losses correspond to chemical transformation probably induced by numerous anoxic periods over several years (probably more than 50 years for particles at 15 cm depth, Thibault de Chanvalon et al, this issue). Reductive dissolution of iron oxides followed by a removal to the water column of freshly dissolved atoms or followed by re-precipitation in a non-ascorbate-sensitive solid phase (such as FeS_2) can explain this loss. Figure 69 shows that Mn_{asc}/Al and Mn/Al ratios are strongly correlated in the sediment (with a slope of 1) which clearly demonstrates that the Mn_{asc} loss occurring during anoxic periods corresponds to a net Mn loss. This relationship also indicates that regardless to the season; samples follow the same Mn_{asc}/Al vs. Mn/Al trend line independently to the variation of Mn/Al observed at the upper reaches of the estuary. However, estuarine SPM are not aligned with sediment samples (Figure 69) and present a variable Mn_{asc}/Al enrichment despite a nearly constant Mn/Al content that could be explained by a phase switch from a part of Mn_{asc} to a non-ascorbate-sensitive solid phase occurring when particles settle (or in the very first moment after deposition). Therefore, 2 reactions are necessary to explain the Mn_{asc} during settling (1) a fast transformation from Mn_{asc} to another Mn phase and (2) a loss of Mn_{asc} (generating also a Mn loss) according to the time span in anoxic conditions. The decrease of Fe_{asc} with depth (Figure 65) corresponds to a Fe_{asc} loss during a long anoxic period. As for Mn, the Figure 69 shows that for February 2014, the Fe_{asc} loss corresponds to a net loss of Fe for particles ($r^2 = 0.52$, $p < 10^{-5}$). The relation is less clear for Fe than for Mn probably because numerous ascorbate-extractable iron phases are present (Hyacinthe and Van Cappellen, 2004). Moreover, ascorbate extraction represents only 8 to 20 % of total iron content. In sum, comparison of total and ascorbate Fe and Mn demonstrates that chemical transformations during early diagenesis are likely to strongly modify metals content and Fe/Al and Mn/Al ratios as observed in the SPM.

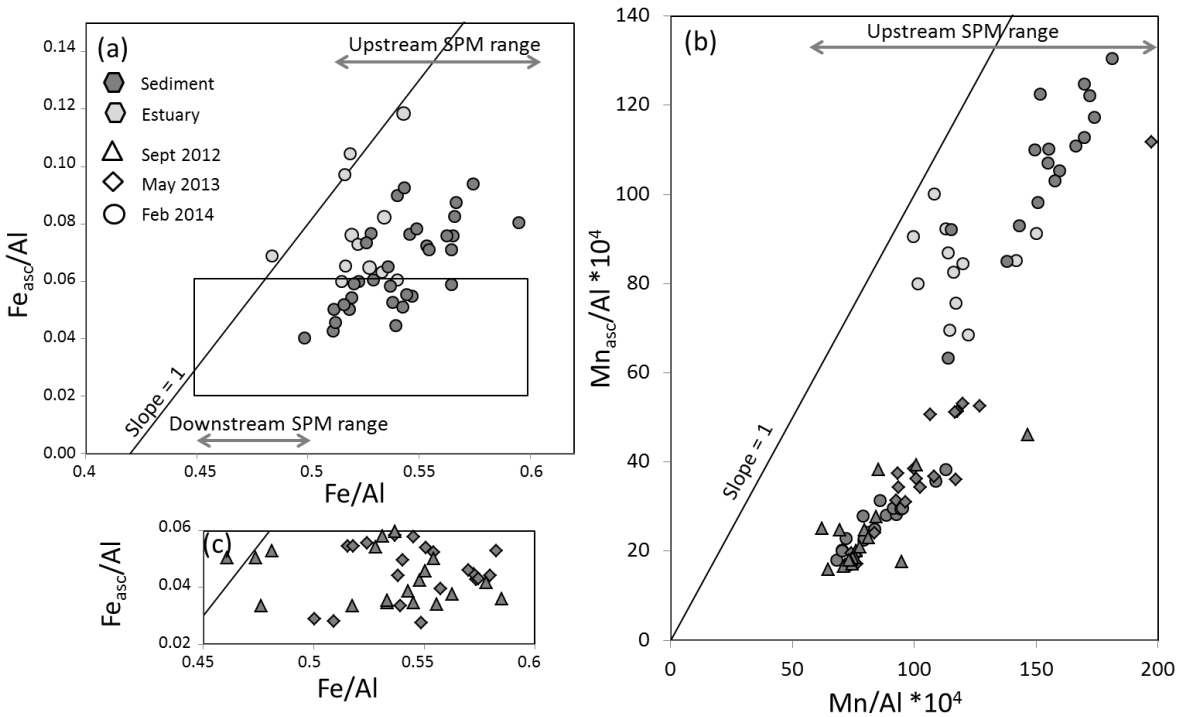

Figure 69 Relation between ascorbate and total extraction in the estuary after normalisation on Al content for (a) Fe and (b) Mn. Panel (c) correspond to a zoom of the rectangle from panel (a).

As for Mn, the Figure 69 shows that for February 2014, the Fe_{asc} loss corresponds to a net loss of Fe for particles ($r^2 = 0.52$, $p < 10^{-5}$). The relation is less clear than for Mn probably because of the fact that ascorbate extraction is less specific for iron. Moreover, ascorbate extraction represents only 8 to 20% of total iron content. In sum, comparison of total and ascorbate Fe and Mn demonstrates that chemical transformations during early diagenesis are likely to strongly modify metals content and Fe/Al and Mn/Al ratios as observed in the SPM.

3.4.4 Long term particles behaviour

The mean time spent by a particle since it entered the estuary increases with the distance from Nantes and can be trace for each cruise by salinity. Figure 70 illustrates the particles ageing through Loire River estuary: as salinity increases, the number of redox oscillations suffered by particles increases too and the Fe content decreases. However, this behaviour is only visible for high flow conditions, probably because it corresponds to downstream sampling compare with low flow conditions which indicates a long term process (more than the average residence time of particles inside the inner estuary *i.e.* several years). The overall transformations due to redox oscillations during estuarine transfer can be estimated by the ratio between the downstream (Fe/Al=0.4780±0.0005) and upstream (Fe/Al = 0.5575 ± 0.0015) end-members (Figure 64) and leads to a loss of 14.3 % ($Fe_{downstream}/Fe_{upstream}$ = 85.7 %) of SPM iron content. Assuming that terrigenous particles have an Al content of 10 % w/w and that reactive iron is in the form $Fe(OH)_3$, estuarine

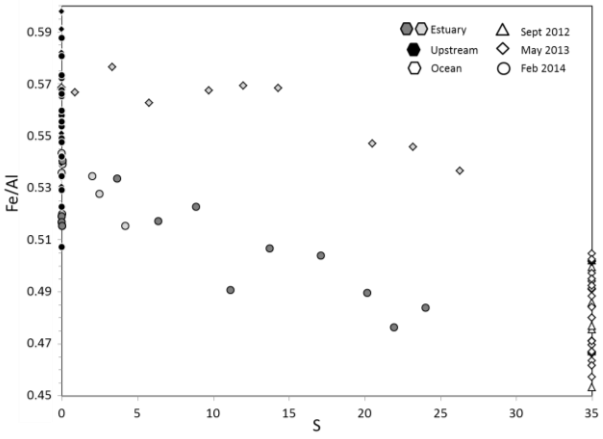

Figure 70 Evolution of Fe/Al ratio according to salinity for high flow campaigns (>1500 $m^3 s^{-1}$)

transfer could represent a loss of 1.52 % of the total mass of terrigenous particles transiting through Loire River estuary. This value, is in very good agreement with the 2 % loss estimated by Raiswell (2006). If this particulate mass loss processes would occur for Mn as well, we cannot observe it, because the signal of Mn/Al variation with salinity during high flow is lost within the wide river end-member variability. However, if Mn/Al ratio was conservative during transfer across the estuary, the downstream Mn/Al ratio should correspond to the mean Mn/Al ratio of the inflowing upstream particles. Yet, the Mn/Al ratios for downstream SPM of May 2013 are lower than most of the upstream ratio (Fig.3). This mismatch is probably induced by a decrease of Mn/Al ratio in particles as they go across the estuary.

Since particles sources can be defined by upstream Fe/Al ratios, the comparison between Fe/Al ratio after redox oscillations during estuarine transfer (Fe/Al = 0.478, iron loss of 14.3 %) and after early diagenesis during burial (Fe/Al = 0.52, iron loss of 6.7 %) shows that estuarine transfer induces more important metal loss than burial. This is a surprising result since SPM are mostly in oxic conditions whereas sediment particles are mostly in anoxic conditions (under which dissolution occurs). Since SPM probably undergoes more redox oscillations, this comparison would show that number of oscillations is more important than time span under anoxic conditions to explain metal loss. However, this interpretation has to be taken with caution since the end-member of early diagenesis is based on a sample from ~ 15 cm depth that could be partially reworked by macrofauna.

3.4.5 **REE behaviour**

The 15 elements (between La and Lu) called rare earth elements, correspond to the progressive filling of the f-electron layer, an inner electron layer that only slightly modifies chemical behaviour of atoms. Therefore it is expected that these atoms present the same behaviour but with a slight fractionation according to their weight. However, two of these elements, Ce and Eu have 2 stable redox states allowing a completely different behaviour in case of redox transformation. The Th-PAAS-normalized REE concentration shows (Figure 66) the expected bell shape spectra for all campaigns and all locations with the most important anomalies around Ce and Eu. The few upstream samples show that ΣREE, Ce and Eu signatures (assessed by Ce/La and Eu/Sm respectively, Figure 67a and Figure 67b) between upstream and downstream particles are not significantly different. By contrast, estuarine SPM shows an important REE enrichment (Table 8), especially during low flow within the HTZ (Figure 67d). These results suggest that REE are strongly reactive inside the estuary in case of high SPM concentration which occurs in the HTZ or in the bottom of the column water. REE content of sediments confirms this reactivity with a specific high and constant signal of ΣREE = 197 ± 9 ppm (n = 14). Similarity of Ce and Eu behaviours between SPM from HTZ and sediments underlines the intimate relation between particle transformation processes within the sediment and the HTZ (Figure 67a and Figure 67b). The Ce and Eu signatures can be explained by dissolution and release during anoxic events (Sholkovitz et al., 1992). However, this loss seems to be followed by complete replenishment in case of long oxic conditions periods as shown by the downstream signature. The correlation between Eu/Sm and Fe_{asc} (Figure 67c), that is not visible between Ce/La and Fe_{asc}, supports the idea that the Eu dynamics is linked to iron recycling by some adsorption processes whereas Ce would have a more autonomous cycle with probably Ce-oxides formation. Overall, the REE analysis strongly highlights the relation between sedimentary processes and the chemical composition of estuarine SPM.

3.5 Conclusion

Sampling particles at different positions in the estuary permitted to describe the effects of estuarine processes on the chemical composition of continental particles entering the Loire estuary. From the Loire River at Nantes to close coastal areas, particles lost 14.3% of Fe content ($Fe_{downstream}/Fe_{upstream}$ = 85.7 %) *i.e.* ~ 1.5 % of the mass of the total riverine discharge. Manganese presents too important upstream variations when normalized by aluminium to allow any quantification, but it appears to be also influenced by estuarine processes. This study brings evidences that this loss can be explained by the redox oscillations

endured by particles during their transport through the estuary, including their temporarily settling on mudflats. We showed first that long mostly anoxic period like in the sediment induces a loss up to 6.7% of iron. Then, the estimation of overall impact of numerous oscillations is based on Fe/Al ratios on SPM, along the salinity gradient during high flow. It reveals a progressive loss occurring outside the embayment, which indicates a long term (several years) process. Finally the relation between sedimentary processes and SPM composition is confirmed by the signature of redox sensitive REE. Sediment and SPM at low concentration have contrasted signatures but since SPM concentration increases, the REE signature becomes a typical sedimentary signature indicating a local source for the HTZ as proposed in the literature.

Acknowledgements

This study is part of the RS2E – OSUNA project funded by the Région Pays de la Loire. Thanks to Cyrille Guindir, Clément Chauvin, Eric Bénéteau, Emmanuelle Rozuel, Dominique Auger, Sylvette Crochet, Bastien Thomas and the N/O Thalia crew for their technical help.

Synthèse et Perspectives

Les estuaires assurent le transfert du produit de l'érosion des continents vers les zones de dépôt sédimentaire. Lors de leur traversée, les particules subissent de nombreuses transformations produisant notamment une modification de leur composition en fer. Cette transformation a été mise en évidence dans l'estuaire de la Loire (Chapitre 2.3) par l'observation d'une modification du rapport Fe/Al dans les particules en suspension. La mise en évidence d'un flux de fer du sédiment vers la colonne d'eau (cf. Chapitres 1.3, 2.1 et 2.3) a montré le rôle important joué par la dissolution réductrice de certains oxydes de fer lors du dépôt des particules. Les mécanismes modulant l'intensité de cette dissolution dépendent principalement de quatre facteurs : 1) la fréquence et la durée des dépôts sédimentaires ; 2) la bioturbation, qui favorise à la fois l'enfouissement des particules vers des zones réactives vis-à-vis des oxydes de fer et les échanges entre les produits de la réaction et la colonne d'eau ; 3) la disponibilité des réactifs entretenant la réaction de dissolution proprement dite, à savoir la teneur en oxydes de fer réactifs du matériel déposé et 4) la disponibilité du 2nd réactif : la matière organique labile. Les modifications de la composition en fer des particules déposées pendant de longues périodes (> 1 mois) ont été quantifiées sur la vasière des Brillantes. En supposant que les phénomènes d'adsorption et de floculation sont négligeables pour expliquer l'évolution de la composition en fer des particules au regard des conditions propres à l'estuaire de la Loire (cf Introduction), l'intensité des modifications réalisées pendant les périodes de dépôt peut être comparée aux observations faites sur les particules en suspension.

1 Fonctionnement de la vasière des Brillantes

1.1 Fonctionnement géochimique de la vasière :

Le modèle du fonctionnement géochimique d'une vasière de l'estuaire de la Loire proposé dans ce travail de doctorat est basé sur l'observation de deux sites de la vasière des Brillantes distants de 500 m selon un tracé perpendiculaire au rivage. Bien que la bioturbation et la quantité de matière organique varient considérablement entre les deux sites, la plus forte variabilité observée s'exerce temporellement, à l'échelle de l'année. En négligeant donc la variabilité interannuelle, il est possible de donner consistance aux observations réalisées lors de périodes contrastées, en les intégrant dans une dynamique commune (Figure 71).

L'importance du dépôt de crue dans la dynamique des processus de recyclage des métaux et du phosphore a pu être mise en évidence malgré l'absence de suivi saisonnier à proprement parler (Chapitre 2.1). Ce dépôt est composé de matière organique (MO) réfractaire (très peu de Chlorophylle a mesurée, Méléder pers. com.) et est riche en oxydes de fer et de manganèse. Les différentes campagnes d'échantillonnage ont permis de caractériser l'évolution des stocks d'oxydes métalliques. Ainsi, quelques temps après dépôt, probablement lorsque l'oxygène et les nitrates ont été consommés, les oxydes métalliques sont dissous. Dans un premier temps (observé en février ; Figure 71), cette dissolution semble produite par la remontée du front de sulfato-réduction, probablement liée à l'éloignement de la source d'oxygène et à la diminution du *biomixing* (qui empêchent ou ralentissent le réapprovisionnement en oxyde de fer des couches anoxiques). Dans un second temps (Figure 71, + 40 jrs), les oxydes de manganèse sont réduits par la respiration anaérobie en absence de nitrate (attestée en avril 2015 par l'application *in situ* du protocole développé dans le Chapitre 1.2). Les flux diffusifs de $Mn(II)_d$ vers la colonne d'eau sont alors très importants et favorisés par une cinétique d'oxydation lente qui lui permet de quitter le sédiment avant de précipiter. Cette période coïncide avec une faible réactivité des oxydes de fer qui s'enrichissent progressivement en phosphore adsorbé (Chapitre 2.1 et 2.2). Dans un troisième temps (~ 75 jours après dépôt), la position de la zone riche en oxygène se rapproche de l'état pré-dépôt de crue à cause de la compaction et de l'érosion (Figure 71; Lesueur and Lesourd, 1999; Deloffre et al., 2006). Simultanément, la macrofaune reconquiert la vasière et favorise ainsi l'approvisionnement en oxydes des couches plus profondes. Ces deux processus permettent d'expliquer un abaissement de la zone de sulfato-réduction. Enfin, après l'épuisement progressif du stock d'oxydes de manganèse, les oxydes de fer sont réduits

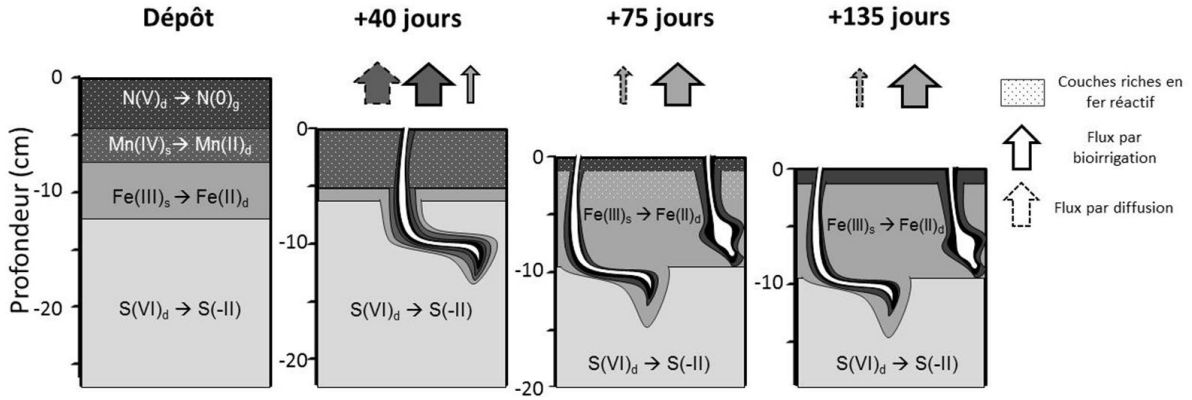

Figure 71 Fonctionnement biogéochimique de la vasière des Brillantes synthétisé à partir d'une schématisation des données obtenues lors des campagnes (de gauche à droite) de février 2015, d'avril 2016 de mai 2014 et de septembre 2013. L'oxygène ne pénètre pas à plus de 5mm et n'est pas représenté. Les fronts redox sont définis, pour Mn(IV) et Fe(III) à partir des zones de production (identifiées visuellement, Figure 51 - site 1) de l'espèce réduite et pour NO_3^- et SO_4^{2-} à partir de la consommation de Fe^{2+} ou Mn^{2+}. Les flèches verticales indiquent un flux vers la colonne d'eau dont l'importance est proportionnelle à la largeur de la flèche. Les flux de phosphate sont du même ordre de grandeur que les flux de fer dissous. De décalage de l'interface correspond à la compaction et à l'érosion progressive du sédiment.

(Figure 71, ~ 135 jours après dépôt), diffusent puis reprécipitent dans le sédiment, ou sont expulsés dans la colonne d'eau avant de former probablement des colloïdes. La *bioirrigation* favorise fortement ce flux vers la colonne d'eau à hauteur d'une contribution représentant 80 % du flux total (Chapitre 1.3). Finalement, plusieurs mois après le dépôt, les stocks initialement déposés d'oxydes métalliques semblent avoir été complètement consommés et ne sont plus visibles dans le sédiment.

La validation de la régularité d'un tel cycle et de son importance première nécessite la réalisation d'un suivi mensuel de la composition de la phase solide pendant au moins 6 mois après un dépôt de crue. Ce suivi s'appuierait sur l'analyse de la teneur en oxydes de fer, de manganèse et en phosphore associé (extrait par une solution d'ascorbate), en FeS et FeS_2 (afin de quantifier la proportion de fer enfoui sous forme réduite) et en plomb 210 (afin d'estimer l'évolution de la profondeur du dépôt de la dernière crue). Un repère vertical gradué pourrait remplacer de manière beaucoup plus simple, une partie des analyses de ^{210}Pb. Le 2nd facteur par ordre d'importance qui contrôle l'évolution de la phase solide dans la vasière semble être l'intensité de la bioturbation. Afin de l'estimer le plus simplement possible, nous recommandons la quantification de la macrofaune simultanément au suivi de la composition de la phase solide. Ainsi, afin d'optimiser les analyses, il ne semble pas primordial d'analyser la phase dissoute (ni en 1D, ni en 2D) dans le cadre de la description du cycle géochimique annuel de la vasière.

Dans le cadre d'une approche centrée sur l'étude du processus de bioturbation les mesures en 2 dimensions ont révélé leur efficacité. En effet, l'important jeu de données obtenu a permis d'identifier 6 mécanismes différents à travers lesquels la bioturbation module l'intensité des processus diagénétiques : 1) l'augmentation, à cause de la *bioirrigation* des flux de Fe_d vers la colonne d'eau (Chapitre 1.3) et du phosphore réactif dissous (DRP, Chapitre 2.2). 2) La dissolution d'une partie des FeS formés lors de l'enfouissement et son export vers la colonne d'eau sous forme de Fe_d (Chapitre 1.3). Ce processus permet notamment l'appauvrissement d'oxydes de fer peu réactifs vis-à-vis de la respiration anaérobie, mais réactifs aux sulfures produits par sulfato-réduction. 3) La *bioirrigation* est aussi responsable de cycles de dissolution-précipitation produits par l'alternance des conditions redox dans le pourtour des terriers (Chapitre 1.3) et capables de modifier la composition chimique et la structure des oxydes présents dans le sédiment. Il n'est pas encore clair dans la littérature si ces oscillations augmentent ou diminuent la réactivité de ces oxydes. 4) L'approvisionnement continu des couches anoxiques en oxydes par le *biomixing* ce qui maintient à plus de 10 cm de profondeur le front de

sulfato-réduction et la production de ΣH_2S (Chapitre 2.2). 5) L'homogénéisation des oxydes par le *biomixing* est probablement responsable de l'absence d'un enrichissement en fer à l'interface eau-sédiment en haut de vasière (Chapitre 2.1) et 6) L'enfouissement de MO labile produisant une forte hétérogénéité particulièrement visible dans la distribution des nutriments par l'existence de tâches (~1cm) d'intense production (Chapitre 1.2 et 2.2). Ces zones très réactives forment probablement des microhabitats dont bénéficie la méiofaune (Chapitre 1.1).

Une connaissance plus précise du comportement des différentes espèces de la macrofaune est nécessaire pour pouvoir en quantifier l'impact. Le suivi proposé ci-dessus devrait apporter des éléments de réponse, mais une connaissance précise du cycle de vie et du comportement des individus des espèces majeures identifiées sur la vasière est nécessaire.

1.2 Fonctionnement et importance des microhabitats benthiques

Le *biomixing* est capable d'enfouir dans des environnements anoxiques de la matière organique (MO) extrêmement labile produite ou déposée à la surface. Les réactions primaires de consommation de la MO s'intensifient à cet endroit et augmentent la concentration des produits de réaction (espèces réduites et nutriments). Ces microenvironnements (d'une taille de l'ordre d'un centimètre) permettent aux espèces présentes de jouir de l'avantage d'un accès à de la MO labile ce qui attire probablement la méiofaune capable de se déplacer dans le sédiment, le cas échéant on appellera ces microenvironnements microhabitats.

Nous avons identifié deux familles de MO à partir de la réactivité du phosphore (production estimé par SGF, Chapitres 1.3 et 2.2) : 1) la MO appelée labile qui est consommée de manière très intense et produit ainsi des halos de forte concentration de DRP et d'éléments réduits (ex : Fe^{2+}) et 2) la MO peu labile qui est consommée de manière plus homogène et qui génère un bruit de fond diffus de nutriment recyclé. Cette seconde famille de MO est mise en évidence par un flux homogène de DRP venant des couches profondes non échantillonnées de la vasière. Toutefois, le DRP peut aussi provenir de sa libération lors de la dissolution des oxydes de fer auxquel il est adsorbé. Il est par contre difficile de mettre en évidence « l'effet tampon » attendu d'un équilibre d'adsorption avec les oxydes de fer (Chapitre 2.1 ; Sundby et al., 1992), tant l'hétérogénéité de la distribution en DRP, produite par leur dissolution, est importante. La quantité de phosphates produits lors de la dissolution des oxydes de fer est très importante dans la vasière des Brillantes (par rapport à Arcachon par exemple ; (Cesbron et al., 2014) ce qui est confirmé par les faibles ratios Fe_{asc}/P_{asc} observés dans le solide (Chapitre 2.1). Cet enrichissement indique que le phosphore n'est probablement pas le nutriment qui limite la production primaire à la surface de la vasière. Par contre, la forte relation entre Fe_d et DRP mise en évidence (Chapitre 2.2) et l'importance de la *bioirrigation* pour les flux de DRP, permet d'approximer le flux de DRP vers la colonne d'eau à celui proposé pour Fe_d. Ainsi, nous avons mis en évidence l'existence d'un flux important de DRP du sédiment vers la colonne d'eau tel que supposé par Meybeck et al. (1988). Ce flux est particulièrement important une fois les oxydes de manganèse épuisés soit approximativement 3 mois après le dernier dépôt de crue (Chapitres 2.1 ; Figure 71). L'impact du flux de phosphore vers la colonne d'eau pourrait ainsi provoquer une augmentation de la production primaire dans l'estuaire.

La description du cycle de l'azote et notamment la description de l'importance des microenvironnements serait largement enrichie par l'application systématique de la méthode développée en Chapitre 1.2 qui permet d'analyser en 2D et simultanément les nitrites et les nitrates. Une description fine de la distribution 2D de l'ammonium serait aussi extrêmement utile, la technique est en cours de développement au laboratoire. Deux processus se déroulant dans la colonne sédimentaire sont susceptibles de consommer les nitrates : la dénitrification (réaction 2 ; Table 2, ou selon la DNRA) et l'oxydation des produits réduits (notamment Fe^{2+} ; réactions 12, Table 2). L'impact de la vasière sur le cycle de l'azote à l'échelle de l'estuaire est la somme de la consommation en nitrate par dénitrification et de la production en ammonium libéré lors de la consommation de la MO.

L'étude de la distribution des foraminifères vivants (Chapitre 1.1) a permis d'identifier l'existence de foraminifères vivant en profondeur, dans des couches caractérisées par une anoxie entrecoupée de courtes périodes d'oxygénation par *bioirrigation*. Les microenvironnements caractérisés par la production conjointe de Fe_d et de DRP (probablement liés à un enrichissement en MO labile) correspondent à des maximums de densité pour *A. tepida*. Cette correspondance pourrait être expliquée par la mobilité des foraminifères et leur capacité à détecter les zones riches en MO labile. Dans la littérature, la mobilité des foraminifères a été attestée par quelques expériences en laboratoire et est nécessaire pour expliquer la distribution verticale de ces derniers. La qualité de l'observation *in situ* pourrait être améliorée en augmentant la résolution d'échantillonnage soit en utilisant une méthode d'enrésinement associée à de la microscopie, soit par une découpe sub-centimétrique du sédiment. L'enrésinement (Bernhard et al., 2003) a l'avantage d'identifier la position de chaque individu mais la méthode est plus longue et donne des résultats statistiquement moins significatifs car ne permet pas d'identifier beaucoup d'individus. De plus, les gradients géochimiques dans le sédiment sont rarement inférieurs à quelques millimètres car sur des distances plus courtes, les flux seraient probablement trop importants pour être maintenus sur une longue période. Un protocole pour étudier la sensibilité des foraminifères est proposé dans la Figure 72. Il s'agit de disposer des foraminifères au milieu d'un couloir caractérisé à l'état initial par un environnement homogène et de suivre leur comportement à l'aide de prise de photographies régulières (un tel système est actuellement développé au laboratoire). Après un temps d'acclimatation, les conditions à l'une des extrémités du couloir sont modifiées et le comportement des foraminifères (leur déplacement préférentiel dans un sens ou dans l'autre) peut être suivi. Des gradients chimiques de matière organique dissoute, d'alcalinité, de pH, de salinité, de nitrate et de phosphate pourraient être testés en condition oxygéné et apporteraient des renseignements cruciaux sur la capacité des foraminifères à détecter et à réagir à de tels gradients chimiques. Les conditions anoxiques permettraient de tester la capacité des foraminifères à détecter O_2, Mn_d, Fe_d et H_2S en plus des précédents gradients.

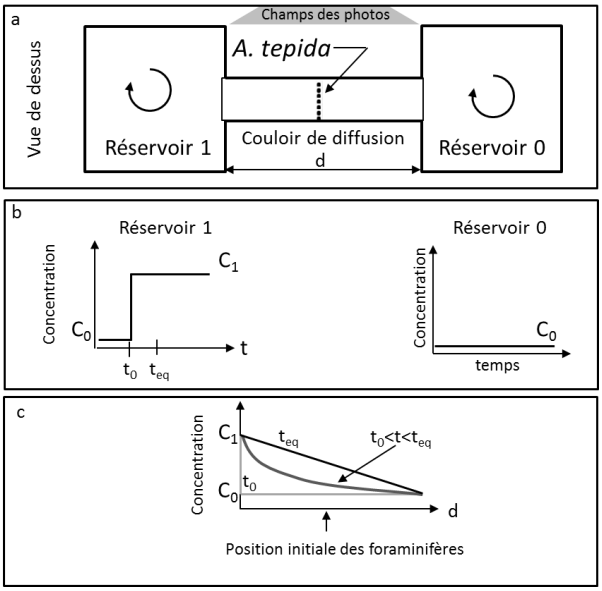

Figure 72 Montage expérimental de mesure de la sensibilité des foraminifères à un gradient chimique. (a) un couloir (de longueur d) rempli d'eau représente l'environnement des foraminifères qui sont positionnées en ligne, au milieu en début d'expérience. Le couloir est connecté à deux réservoirs fixant les conditions aux limites. Un système de photographie automatisé permet de suivre la position des foraminifères au cours du temps. (b) Au temps t_0, la concentration de l'un des réservoirs est modifié de C_0 à C_1, ce qui créé un gradient chimique. (c) un état transitoire permet à la concentration dans le couloir d'augmenter jusqu'à son état d'équilibre à t_{eq}, décrit par une diminution linéaire d'une concentration C_1 au niveau du réservoir 1 jusqu'à une concentration C_0 au niveau du réservoir 0.

2 Importance des estuaires dans le cycle du fer

L'efficacité de la dissolution réductrice des oxydes de fer lors des dépôts à long terme est étudiée en comparaison de la perte du fer subie par les particules à travers l'estuaire de la Loire. Cette comparaison est réalisée à travers le bilan du fer réactif (extractible avec une solution d'ascorbate) à l'échelle de l'estuaire de la Loire (Figure 73). Ce bilan est réalisé en trois étapes :

1) La méthode de calcul *Savitzky Golay Filter procedure* développée dans le Chapitre 1.3 permet de proposer une estimation du flux de fer du sédiment vers la colonne d'eau de 100 µmol.m^{-2}.d^{-1} pour le flux dissous et de 410 µmol.m^{-2}.d^{-1} pour le flux lié à la *bioirrigation* (Figure 73). Ce flux a été estimé sur une seule vasière et sur un site particulier notamment caractérisé par une forte *bioirrigation* et une forte production primaire. La généralisation de données provenant d'un tel site maximiserait donc le flux de Fe_d proposé au bilan.

2) Le fer dissous quittant le sédiment provient de la dissolution de particules dont il est nécessaire de caractériser le devenir : certaines de ces particules vont s'enfouir (*i.e.* rester indéfiniment dans la colonne sédimentaire) et ne compteront plus dans le matériel en suspension, alors qu'une autre fraction des particules sédimentaires va se remettre en suspension. Pour différencier ces particules dans le sédiment nous utiliserons les acronymes PE pour les particules qui vont être enfouies et PRS pour les particules qui vont se remettre en suspension. Ce sont ces dernières qui participent à la perte de fer des particules traversant l'estuaire de la Loire. La masse de particules enfouies peut être estimée à partir des profils de ^{210}Pb (taux de sédimentation net de 1,6 mm.an^{-1}, Chapitre 2.1) et correspond à 2,8 g.m^{-2}.d^{-1}. Lors du dépôt, la concentration observée est de [Fe_{asc}](z = 0) = 103 µmol.g^{-1} contre [Fe_{asc}](z = 15cm) = 41 µmol.g^{-1} au maximum de profondeur observé. Cette diminution de la teneur en oxydes réactifs avec la profondeur correspond à un flux de fer enfoui sous forme d'oxydes réactifs de (41 x 2.8 =) 115 µmol.m^{-2}.d^{-1} (Figure 73) et un flux de fer quittant les PE juste avant l'enfouissement de ([103-41] x 2.8 =) 170 µmol.m^{-2}.d^{-1}. Ce fer quittant les PE peut soit être entrainé vers la colonne d'eau, soit reprécipiter sous forme réduite (par exemple en FeS) avant d'être alors enfoui. Ne pouvant contraindre la répartition entre ces deux puits nous les avons considérés égaux dans ce bilan (85 µmol.m^{-2}.d^{-1}). Ce raisonnement implique que le flux de fer dissous vers la colonne d'eau calculé précédemment (510 µmol.m^{-2}.d^{-1}) provient des PE à hauteur de 85 µmol.m^{-2}.d^{-1}, c'est-à-dire qu'il provient des PRS à hauteur 425 µmol.m^{-2}.d^{-1}. Ainsi, en supposant un flux de fer quittant le sédiment constant dans le temps et homogène sur toute la surface de l'estuaire (5,5 10^{7} m^{2} ; GIP LE, 2004) et qu'à tout moment, suffisamment de PRS soient présentes pour supporter la perte de fer qui leur est liée, il n'est pas besoin de connaitre la répartition exacte de ces PRS dans le temps et dans l'estuaire. Cependant, il est nécessaire de quantifier le flux annuel de particules transitant par l'estuaire ce qui, d'après la littérature citée en introduction, correspondrait à 1,4 10^{9} kg.an^{-1} (Figure 73). Ce flux est représenté par une valeur indicative, uniquement pédagogique, qui correspond au dépôt moyen réalisé par la sédimentation simultanée de l'ensemble des particules transitant par l'estuaire (70 g.m^{-2}.d^{-1}). La perte des PRS en fer rapportée au flux annuel de particules transitant par l'estuaire de la Loire permet d'estimer une perte de 6 µmol.g^{-1} d'oxyde de fer à cause de la dissolution réductrice du fer.

3) La perte de fer total dans les particules en suspension, à travers les estuaires, est estimée dans la littérature à 17,3 % (Poulton and Raiswell, 2002; Haese, 2006). Les données présentées dans le Chapitre 2.3 font état d'une perte de 15 % du fer particulaire par rapport à l'entrée de l'estuaire. Ces valeurs sont extrêmement proches, on utilisera dans le bilan l'estimation réalisée pour la Loire. On suppose, d'après les données du Chapitre 4.3, une teneur en fer des particules de 4,5 %. La moyenne (pondérée du débit) calculée à partir des données de Grosbois et al. (2001) donne une concentration moyenne de fer de 3,4 %. Selon ces 2 estimations la perte en fer des particules traversant l'estuaire est donc de 120 ou 90 µmol.g^{-1} (Figure 73).

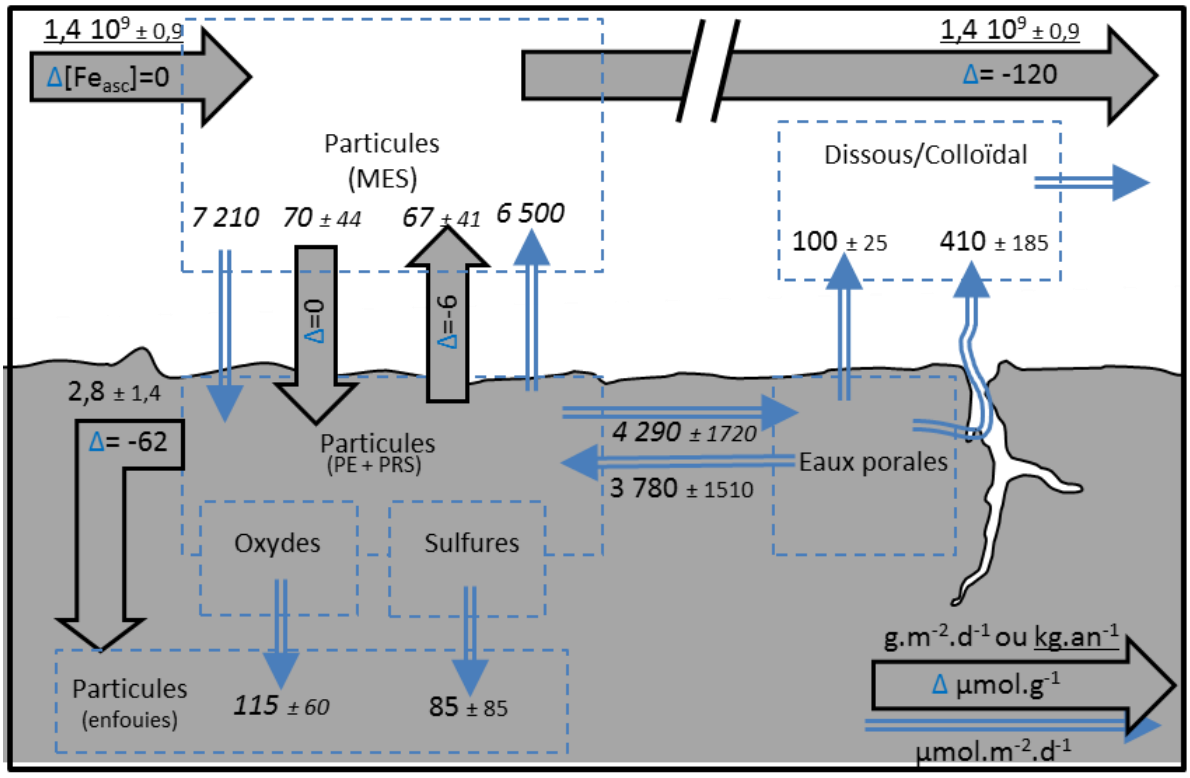

Figure 73 Bilan annuel du cycle du fer à l'échelle de l'estuaire, les large flèches grises indiquent des flux de particules avec l'évolution de leur composition en oxydes de fer depuis leur entrée dans l'estuaire (indiqué par Δ). Les doubles flèches représentent les flux de fer estimés sous forme particulaire ou dissoute. A part le débit moyen annuel en MES (souligné), les données proviennes toutes de cette thèse.

Ce bilan fait apparaitre que la dissolution réductrice subie par les particules lors de la traversée annuelle (on suppose que l'ensemble des particules est rejeté dans l'océan lors d'une seule crue par an) de l'estuaire de la Loire, est responsable de 5 à 8 % de la perte totale en fer subie par les particules. Cependant, la surface de sédiment considérée correspond à la surface de la Loire et de ses vasières intertidales entre Sainte-Luce-sur-Loire (juste à l'amont de Nantes) et St Nazaire en aval. Or, les particules océaniques ayant permis de définir la perte de 15 % ont été prélevées dans la zone couverte par le gradient de salinité (Figure 5), c'est-à-dire jusqu'à 50 km au large de St Nazaire. Ainsi la surface couverte par le gradient de salinité (de l'ordre de 50 x 50 km^2) est supérieure à la surface minimale traversée en une année requise (20 x 20 km^2) pour expliquer la perte observée par les particules en suspension. La dissolution réductrice des oxydes de fer réalisée dans l'estuaire de la Loire est donc un processus suffisamment important pour expliquer la perte en fer des particules lorsque les vasières externes sont prises en compte.

Une suite de ce travail serait de combler les approximations majeures de ce bilan :

-Sur quelle surface s'étend la zone de perte de fer ? Plusieurs sites d'étude contrastés (au moins une vasière externe et une zone subtidale de l'estuaire interne) devraient être échantillonnés par DET-2D pour étudier la variabilité spatiale des processus modulant le flux de fer dissous. Ces approches pourraient être couplées de manière optimale avec des mesures de flux par chambres benthiques afin de vérifier par une seconde méthode les estimations de flux. L'analyse de la composition de sédiment prélevé par carottes le long d'un profil longitudinal partant de Nantes jusqu'à l'ile d'Yeu, pourrait indiquer les zones de plus forte réactivité par la diminution du rapport Fe/Al ou de la teneur en fer réactif.

-Quelle est la variabilité temporelle de ce flux ? Notre proposition de cycle annuel contrainte par un dépôt massif en période de crue doit être validée plus en détail (voir le protocole proposé en §1.1) et sa généralisation à la surface de l'estuaire doit aussi être étudiée. L'impact de la variabilité temporelle des durées de dépôt doit aussi être étudié. En effet, le modèle proposé n'est basé que sur la réactivité des dépôts « sur le long terme » c'est-à-dire des dépôts stables pendant suffisamment longtemps pour que l'équilibre des fronts redox soit établi (Figure 22 ; quelques mois) mais plus court qu'une année puisqu'il faut que les particules traversent l'estuaire pendant ce délai. Or une partie des PRS n'est déposée que pendant quelques heures à quelques jours selon la dynamique du bouchon vaseux, elles subissent donc une dynamique tout à fait particulière.

-Quel est le flux produit par le fer réactif enfoui et n'impactant pas les PRS ? La quantification du FeS formé est assez simple à réaliser par une extraction chimique spécifique et permet de résoudre l'une des inconnues du bilan. Cependant, il est aussi possible qu'une partie du fer réactif se transforme en fer non-réactif par le biais du vieillissement des particules (ce qui n'est pas non plus pris en compte dans le bilan) ou réciproquement, qu'une partie du fer non-réactif à l'ascorbate réagisse avec les sulfures en FeS, puis soit réoxydée par la *bioirrigation* et se transforme en fer réactif. Ces processus et plus généralement l'impact des oscillations redox sur la réactivité des oxydes de fer sont extrêmement mal contraints dans la littérature, et des expériences en réacteurs à partir de particules de la Loire telles que proposées par Abril et al. (2010) pourraient clarifier ces transformations.

-Quel est le devenir de ce flux de fer sortant du sédiment ? Le bilan proposé ici indique pudiquement une phase colloïdale ou dissoute, cependant, les mesures réalisées dans le gradient salin n'ont pas mis en évidence un tel flux. Cela peut être un biais méthodologique lié à la profondeur d'échantillonnage (1 mètre) alors que les eaux de l'estuaire présentent souvent une stratification plus profonde. De plus comme notre étude ne montre pas de stockage dans l'estuaire interne (tel que proposé par Poulton and Raiswell, 2002) il faut nécessairement, pour boucler le bilan, une zone de dépôt de ce fer produit par dissolution réductrice, dépôt qu'il reste à découvrir, quelque part dans l'océan.

Bibliographie

Abril, G., Commarieu, M.-V., Etcheber, H., Deborde, J., Deflandre, B., Živađinović, M. K., Chaillou, G. and Anschutz, P.: In vitro simulation of oxic/suboxic diagenesis in an estuarine fluid mud subjected to redox oscillations, Estuar. Coast. Shelf Sci., 88(2), 279–291, doi:10.1016/j.ecss.2010.04.003, 2010.

Abril, G., Commarieu, M.-V., Maro, D., Fontugne, M., Guérin, F. and Etcheber, H.: A massive dissolved inorganic carbon release at spring tide in a highly turbid estuary: DIC at spring tide in a estuary, Geophys. Res. Lett., 31(9), n/a-n/a, doi:10.1029/2004GL019714, 2004.

Abril, G., Etcheber, H., Le Hir, P., Bassoullet, P., Boutier, B. and Frankignoulle, M.: Oxic/anoxic oscillations and organic carbon mineralization in an estuarine maximum turbidity zone (The Gironde, France), Limnol. Oceanogr., 44(5), 1304–1315, doi:10.4319/lo.1999.44.5.1304, 1999.

Abril, G., Nogueira, M., Etcheber, H., Cabeçadas, G., Lemaire, E. and Brogueira, M. .: Behaviour of Organic Carbon in Nine Contrasting European Estuaries, Estuar. Coast. Shelf Sci., 54(2), 241–262, doi:10.1006/ecss.2001.0844, 2002.

Abril, G., Riou, S. A., Etcheber, H., Frankignoulle, M., de Wit, R. and Middelburg, J. J.: Transient, Tidal Time-scale, Nitrogen Transformations in an Estuarine Turbidity Maximum—Fluid Mud System (The Gironde, South-west France), Estuar. Coast. Shelf Sci., 50(5), 703–715, doi:10.1006/ecss.1999.0598, 2000.

Alldredge, A. L. and Cohen, Y.: Can Microscale Chemical Patches Persist in the Sea? Microelectrode Study of Marine Snow, Fecal Pellets, Science, 235(4789), 689–691, doi:10.1126/science.235.4789.689, 1987.

Allen, G. P.: Etude desprocessus sédimentaires dans l'estuaire de la Gironde, Thèse d'état, Université Bordeaux I., 1972.

Aller, J. Y. and Aller, R. C.: Evidence for localized enhancement of biological associated with tube and burrow structures in deep-sea sediments at the HEEBLE site, western North Atlantic, Deep Sea Res. Part Oceanogr. Res. Pap., 33(6), 755–790, doi:10.1016/0198-0149(86)90088-9, 1986.

Aller, R. C.: Diagenetic Processes Near the Sediment-Water Interface of Long Island Sound. Ii. Fe and Mn, in Adv. Geophys.; (United States), vol. 21:1. [online] Available from: http://www.osti.gov/scitech/biblio/6849382 (Accessed 2 December 2015), 1980.

Aller, R. C.: The Effects of Macrobenthos on Chemical Properties of Marine Sediment and Overlying Water, in Animal-Sediment Relations, edited by P. L. McCall and M. J. S. Tevesz, pp. 53–102, Springer US. [online] Available from: http://link.springer.com/chapter/10.1007/978-1-4757-1317-6_2 (Accessed 22 August 2014), 1982.

Aller, R. C.: Mobile deltaic and continental shelf muds as suboxic, fluidized bed reactors, Mar. Chem., 61(3–4), 143–155, doi:10.1016/S0304-4203(98)00024-3, 1998.

Aller, R. C.: Transport and reactions in the bioirrigated zone, Benthic Bound. Layer, 5, 269–301, 2001.

Aller, R. C.: Conceptual models of early diagenetic processes: The muddy seafloor as an unsteady, batch reactor, J. Mar. Res., 62(6), 815–835, doi:10.1357/0022240042880837, 2004.

Aller, R. C.: 8.11 - Sedimentary Diagenesis, Depositional Environments, and Benthic Fluxes, in Treatise on Geochemistry (Second Edition), edited by H. D. H. K. Turekian, pp. 293–334, Elsevier, Oxford. [online] Available from: http://www.sciencedirect.com/science/article/pii/B9780080959757006112 (Accessed 25 March 2015), 2014.

Aller, R. C. and Aller, J. Y.: The effect of biogenic irrigation intensity and solute exchange on diagenetic reaction rates in marine sediments, J. Mar. Res., 56(4), 905–936, doi:10.1357/002224098321667413, 1998.

Aller, R. C. and Blair, N. E.: Carbon remineralization in the Amazon–Guianas tropical mobile mudbelt: A sedimentary incinerator, Cont. Shelf Res., 26(17–18), 2241–2259, doi:10.1016/j.csr.2006.07.016, 2006.

Alve, E. and Bernhard, J. M.: Vertical migratory response of benthic foraminifera to controlled oxygen concentrations in an experimental mesocosm, Mar Ecol Prog Ser, 116, 137–151, doi:http://dx.doi.org/10.3354/meps116137, 1995.

Alve, E. and Murray, J. W.: Temporal Variability in Vertical Distributions of Live (stained) Intertidal Foraminifera, Southern England, J. Foraminifer. Res., 31(1), 12–24, doi:10.2113/0310012, 2001.

Andrieux-Loyer, F., Philippon, X., Bally, G., Kérouel, R., Youenou, A. and Le Grand, J.: Phosphorus dynamics and bioavailability in sediments of the Penzé Estuary (NW France): in relation to annual P-fluxes and occurrences of Alexandrium Minutum, Biogeochemistry, 88(3), 213–231, doi:10.1007/s10533-008-9199-2, 2008.

Anschutz, P., Dedieu, K., Desmazes, F. and Chaillou, G.: Speciation, oxidation state, and reactivity of particulate manganese in marine sediments, Chem. Geol., 218(3–4), 265–279, doi:10.1016/j.chemgeo.2005.01.008, 2005.

Anschutz, P., Zhong, S., Sundby, B., Mucci, A. and Gobeil, C.: Burial efficiency of phosphorus and the geochemistry of iron in continental margin sediments, Limnol. Oceanogr., 43(1), 53–64, 1998.

Appleby, P. and Oldfield, F.: Applications of lead-210 to sedimentation studies, in Uranium-series disequilibrium: applications to earth, marine, and environmental sciences. 2. ed., 1992.

Arndt, S., Jørgensen, B. B., LaRowe, D. E., Middelburg, J. J., Pancost, R. D. and Regnier, P.: Quantifying the degradation of organic matter in marine sediments: A review and synthesis, Earth-Sci. Rev., 123, 53–86, doi:10.1016/j.earscirev.2013.02.008, 2013.

Aspila, K. I., Agemian, H. and Chau, A. S. Y.: A semi-automated method for the determination of inorganic, organic and total phosphate in sediments, Analyst, 101(1200), 187–197, 1976.

Audry, S., Blanc, G., Schäfer, J., Chaillou, G. and Robert, S.: Early diagenesis of trace metals (Cd, Cu, Co, Ni, U, Mo, and V) in the freshwater reaches of a macrotidal estuary, Geochim. Cosmochim. Acta, 70(9), 2264–2282, doi:10.1016/j.gca.2006.02.001, 2006.

Audry, S., Blanc, G., Schäfer, J. and Robert, S.: Effect of estuarine sediment resuspension on early diagenesis, sulfide oxidation and dissolved molybdenum and uranium distribution in the Gironde estuary, France, Chem. Geol., 238(3–4), 149–167, doi:10.1016/j.chemgeo.2006.11.006, 2007.

Avoine, J., Allen, G. P., Nichols, M., Salomon, J. C. and Larsonneur, C.: Estuary \3- Shelf Interrelationships Suspended-sediment transport in the Seine estuary, France: Effect of man-made modifications on estuary—shelf sedimentology, Mar. Geol., 40(1), 119–137, doi:10.1016/0025-3227(81)90046-3, 1981.

Bacon, J. R. and Davidson, C. M.: Is there a future for sequential chemical extraction?, Analyst, 133(1), 25–46, 2008.

Barbeau, K.: Photochemistry of organic iron (III) complexing ligands in oceanic systems, Photochem. Photobiol., 82(6), 1505–1516, 2006.

Barbeau, K., Rue, E., Bruland, K. and Butler, A.: Photochemical cycling of iron in the surface ocean mediated by microbial iron (III)-binding ligands, Nature, 413(6854), 409–413, 2001.

Barmawidjaja, D. M., Jorissen, F. J., Puskaric, S. and Zwaan, G. J. van der: Microhabitat selection by benthic Foraminifera in the northern Adriatic Sea, J. Foraminifer. Res., 22(4), 297–317, doi:10.2113/gsjfr.22.4.297, 1992.

Bendschneider, K. and R J Robinson: A new spectrophotometric method for determination of nitrite in sea water, J. Mar. Res., 11, 87–96, 1952.

Bennett, W. W., Welsh, D. T., Serriere, A., Panther, J. G. and Teasdale, P. R.: A colorimetric DET technique for the high-resolution measurement of two-dimensional alkalinity distributions in sediment porewaters, Chemosphere, 119, 547–552, doi:10.1016/j.chemosphere.2014.07.042, 2015.

Benyoucef, I.: Télédétection visible proche-infrarouge de la distribution spatio-temporelle du microphytobenthos estuarien, Ph.D. thesis, Université de Nantes, 8 April., 2014a.

Benyoucef, I.: Télédétection visible proche-infrarouge de la distribution spatio-temporelle du microphytobenthos estuarien, Ph.D. thesis, Université de Nantes, 4 August., 2014b.

Benyoucef, I., Blandin, E., Lerouxel, A., Jesus, B., Rosa, P., Méléder, V., Launeau, P. and Barillé, L.: Microphytobenthos interannual variations in a north-European estuary (Loire estuary, France) detected by visible-infrared multispectral remote sensing, Estuar. Coast. Shelf Sci., 136, 43–52, doi:10.1016/j.ecss.2013.11.007, 2014.

Berg, P., Risgaard-Petersen, N. and Rysgaard, S.: Interpretation of measured concentration profiles in sediment pore water, Limnol. Oceanogr., 43(7), 1500–1510, doi:10.4319/lo.1998.43.7.1500, 1998.

Bergquist, B. A., Wu, J. and Boyle, E. A.: Variability in oceanic dissolved iron is dominated by the colloidal fraction, Geochim. Cosmochim. Acta, 71(12), 2960–2974, doi:10.1016/j.gca.2007.03.013, 2007.

Berkeley, A., Perry, C. T., Smithers, S. G., Horton, B. P. and Taylor, K. G.: A review of the ecological and taphonomic controls on foraminiferal assemblage development in intertidal environments, Earth-Sci. Rev., 83(3–4), 205–230, doi:10.1016/j.earscirev.2007.04.003, 2007.

Berner, R. A.: Sedimentary pyrite formation, Am. J. Sci., 268(1), 1–23, doi:10.2475/ajs.268.1.1, 1970.

Berner, R. A.: Early diagenesis : a theoretical approach, Princeton : Princeton University Press., 1980.

Berner, R. A. and Rao, J.-L.: Phosphorus in sediments of the Amazon River and estuary: Implications for the global flux of phosphorus to the sea, Geochim. Cosmochim. Acta, 58(10), 2333–2339, doi:10.1016/0016-7037(94)90014-0, 1994.

Berner, R. A., Scott, M. R. and Thomlinson, C.: Carbonate Alkalinity in the Pore Waters of Anoxic Marine Sediments, Limnol. Oceanogr., 15(4), 544–549, doi:10.4319/lo.1970.15.4.0544, 1970.

Bernhard, J. M. and Alve, E.: Survival, ATP pool, and ultrastructural characterization of benthic foraminifera from Drammensfjord (Norway): response to anoxia, Mar. Micropaleontol., 28(1), 5–17, doi:10.1016/0377-8398(95)00036-4, 1996.

Bernhard, J. M., Buck, K. R., Farmer, M. A. and Bowser, S. S.: The Santa Barbara Basin is a symbiosis oasis, Nature, 403(6765), 77–80, 2000.

Bernhard, J. M., Ostermann, D. R., Williams, D. S. and Blanks, J. K.: Comparison of two methods to identify live benthic foraminifera: A test between Rose Bengal and CellTracker Green with implications for stable isotope paleoreconstructions, Paleoceanography, 21(4), PA4210, doi:10.1029/2006PA001290, 2006.

Bernhard, J. M. and Sen Gupta, B. K. S.: Foraminifera of oxygen-depleted environments, in Modern Foraminifera, pp. 201–216, Barum K. Sen Gupta., 1999.

Bernhard, J. M., Visscher, P. T. and Bowser, S. S.: Submillimeter life positions of bacteria, protists, and metazoans in laminated sediments of the Santa Barbara Basin, Limnol. Oceanogr., 48(2), 813–828, 2003.

Bertier, C.: Dynamique du bouchon vaseux dans l'estuaire de la Loire, 2009.

Bianchi, T. S., Rolff, C., Widbom, B. and Elmgren, R.: Phytoplankton Pigments in Baltic Sea Seston and Sediments: Seasonal Variability, Fluxes, and Transformations, Estuar. Coast. Shelf Sci., 55(3), 369–383, doi:10.1006/ecss.2001.0911, 2002.

Bianchi, T. S., Wysocki, L. A., Stewart, M., Filley, T. R. and McKee, B. A.: Temporal variability in terrestrially-derived sources of particulate organic carbon in the lower Mississippi River and its upper tributaries, Geochim. Cosmochim. Acta, 71(18), 4425–4437, doi:10.1016/j.gca.2007.07.011, 2007.

Billen, G., Cauwet, G., Dessery, S., Meybeck, M. and Somville, M.: Origines et comportement du carbone organique dans l'estuaire de la Loire, Rapp. ProcŠs-Verbaux RèunionsConseil Int. Pour Explot. Mer, 186, 375–391, 1986.

Bivand, R., Pebesma, E. and Gomez-Rubio, V.: Applied Spatial Data Analysis with R, Springer New York, New York, NY. [online] Available from: http://link.springer.com/10.1007/978-0-387-78171-6 (Accessed 16 August 2014), 2008.

Black, A. P. and Riddick, T. M.: Basic mechanisms of coagulation [with discussion], J. Am. Water Works Assoc., 492–504, 1960.

Blanchard, G.: Overlapping microscale dispersion patterns of meiofauna and microphytobenthos, Mar. Ecol. Prog. Ser., 68, 101–111, doi:10.3354/meps068101, 1990.

Bligh, M. W. and Waite, T. D.: Formation, reactivity, and aging of ferric oxide particles formed from Fe(II) and Fe(III) sources: Implications for iron bioavailability in the marine environment, Geochim. Cosmochim. Acta, 75(24), 7741–7758, doi:10.1016/j.gca.2011.10.013, 2011.

Boltovskoy, E.: The foraminifera fauna of the Río de la Plata and its relation to the Caribbean area: Cushman Foundation of Foraminiferal Research, Contribution, 9(1), 17–21, 1958.

Bonaglia, S., Nascimento, F. J. A., Bartoli, M., Klawonn, I. and Brüchert, V.: Meiofauna increases bacterial denitrification in marine sediments, Nat. Commun., 5, 5133, doi:10.1038/ncomms6133, 2014.

Borcard, D., Gillet, F. and Legendre, P.: Numerical Ecology with R, Springer New York, New York, NY. [online] Available from: http://link.springer.com/10.1007/978-1-4419-7976-6 (Accessed 16 August 2014), 2011.

Bottjer, D. J., Hagadorn, J. W. and Dornbos, S. Q.: The Cambrian substrate revolution, GSA Today, 10(9), 1–7, 2000.

Bouchet, V. M. P., Sauriau, P.-G., Debenay, J.-P., Mermillod-Blondin, F., Schmidt, S., Amiard, J.-C. and Dupas, B.: Influence of the mode of macrofauna-mediated bioturbation on the vertical distribution of living benthic foraminifera: First insight from axial tomodensitometry, J. Exp. Mar. Biol. Ecol., 371(1), 20–33, doi:10.1016/j.jembe.2008.12.012, 2009.

Boudreau, B. P.: A method-of-lines code for carbon and nutrient diagenesis in aquatic sediments, Comput. Geosci., 22(5), 479–496, 1996.

Boudreau, B. P.: Diagenetic Models and Their Implementation Modelling Transport and Reactions in Aquatic Sediments, Springer Berlin Heidelberg, Berlin, Heidelberg. [online] Available from: http://catalog.hathitrust.org/api/volumes/oclc/35095947.html (Accessed 9 December 2014), 1997.

Boyd, P. W. and Ellwood, M. J.: The biogeochemical cycle of iron in the ocean, Nat. Geosci., 3(10), 675–682, doi:10.1038/ngeo964, 2010.

Boyle, E., Collier, R., Dengler, A., Edmond, J., Ng, A. and Stallard, R.: On the chemical mass-balance in estuaries, Geochim. Cosmochim. Acta, 38(11), 1719–1728, 1974.

Boyle, R. A., Dahl, T. W., Dale, A. W., Shields-Zhou, G. A., Zhu, M., Brasier, M. D., Canfield, D. E. and Lenton, T. M.: Stabilization of the coupled oxygen and phosphorus cycles by the evolution of bioturbation, Nat. Geosci., 7(9), 671–676, doi:10.1038/ngeo2213, 2014.

Bratton, A. C., Marshall, E. K. and Hendrickson, W. the technical assistance of D. B. and A. R.: A New Coupling Component for Sulfanilamide Determination, J. Biol. Chem., 128(2), 537–550, 1939.

Broecker, W. S. and Peng, T.-H.: Tracers in the Sea, Lamont-Doherty Geological Observatory Columbia University., 1982.

Burdige, D. J.: 5.09 - Estuarine and Coastal Sediments – Coupled Biogeochemical Cycling, in Treatise on Estuarine and Coastal Science, edited by E. Wolanski and D. McLusky, pp. 279–316, Academic Press, Waltham. [online] Available from: http://www.sciencedirect.com/science/article/pii/B9780123747112005118 (Accessed 26 March 2015), 2011.

Burgin, A. J. and Hamilton, S. K.: Have we overemphasized the role of denitrification in aquatic ecosystems? A review of nitrate removal pathways, Front. Ecol. Environ., 5(2), 89–96, doi:10.1890/1540-9295(2007)5[89:HWOTRO]2.0.CO;2, 2007.

Buzas: On the spatial distribution of foraminifera:, Contrib. Cushman Found. Foraminifer. Res., 19, 1–11, 1968.

Buzas, M. A.: Spatial Homogeneity: Statistical Analyses of Unispecies and Multispecies Populations of Foraminifera, Ecology, 51(5), 874–879, doi:10.2307/1933980, 1970.

Buzas, M. A., Hayek, L.-A. C., Jett, J. A. and Reed, S. A.: Pulsating Patches: History and Analyses of Spatial, Seasonal, and Yearly Distribution of Living Benthic Foraminifera, Smithson. Contrib. Paleobiology, (97), 1–91, 2015.

Buzas, M. A., Hayek, L.-A. C., Reed, S. A. and Jett, J. A.: Foraminiferal Densities Over Five Years in the Indian River Lagoon, Florida: A Model of Pulsating Patches, J. Foraminifer. Res., 32(1), 68–92, doi:10.2113/0320068, 2002.

Callender, E. and Hammond, D. E.: Nutrient exchange across the sediment-water interface in the Potomac River estuary, Estuar. Coast. Shelf Sci., 15(4), 395–413, 1982.

Canfield, D. E.: Reactive iron in marine sediments, Geochim. Cosmochim. Acta, 53(3), 619–632, 1989.

Canfield, D. E.: The geochemistry of river particulates from the continental USA: major elements, Geochim. Cosmochim. Acta, 61(16), 3349–3365, 1997.

Canfield, D. E., Raiswell, R. and Bottrell, S. H.: The reactivity of sedimentary iron minerals toward sulfide, Am. J. Sci., 292(9), 659–683, 1992.

Cauwet, G. and Meybeck, M.: Seasonal fluctuations of carbon levels in a temperate river, Loire river (France)., in Transport of Carbon and Minerals in World Major Rivers. Part IV. Mitt. Geol. Paltiont., vol. 64, pp. 359–357, Univ. Hamburg., 1987.

Cesbron, F., Metzger, E., Launeau, P., Deflandre, B., Delgard, M.-L., Thibault de Chanvalon, A., Geslin, E., Anschutz, P. and Jézéquel, D.: Simultaneous 2D Imaging of Dissolved Iron and Reactive Phosphorus in Sediment Porewaters by Thin-Film and Hyperspectral Methods, Environ. Sci. Technol., 48(5), 2816–2826, doi:10.1021/es404724r, 2014.

Charette, M. A. and Sholkovitz, E. R.: Oxidative precipitation of groundwater-derived ferrous iron in the subterranean estuary of a coastal bay, Geophys. Res. Lett., 29(10), 85–1, doi:10.1029/2001GL014512, 2002.

Chernetsky, A.: Trapping of sediment in tidal estuaries, TU Delft, Delft University of Technology., 2012.

Chever, F., Rouxel, O. J., Croot, P. L., Ponzevera, E., Wuttig, K. and Auro, M.: Total dissolvable and dissolved iron isotopes in the water column of the Peru upwelling regime, Geochim. Cosmochim. Acta, 162, 66–82, doi:10.1016/j.gca.2015.04.031, 2015.

Church, T. M.: Biogeochemical factors influencing the residence time of microconstituents in a large tidal estuary, Delaware Bay, Mar. Chem., 18(2–4), 393–406, doi:10.1016/0304-4203(86)90020-4, 1986.

Ciffroy, P., Garnier, J.-M. and Benyahya, L.: Kinetic partitioning of Co, Mn, Cs, Fe, Ag, Zn and Cd in fresh waters (Loire) mixed with brackish waters (Loire estuary): experimental and modelling approaches, Mar. Pollut. Bull., 46(5), 626–641, doi:10.1016/S0025-326X(02)00517-9, 2003a.

Ciffroy, P., Garnier, J.-M. and Khanh Pham, M.: Kinetics of the adsorption and desorption of radionuclides of Co, Mn, Cs, Fe, Ag and Cd in freshwater systems: experimental and modelling approaches, J. Environ. Radioact., 55(1), 71–91, 2001.

Ciffroy, P., Reyss, J.-L. and Siclet, F.: Determination of the residence time of suspended particles in the turbidity maximum of the Loire estuary by 7Be analysis, Estuar. Coast. Shelf Sci., 57(4), 553–568, doi:10.1016/S0272-7714(02)00339-6, 2003b.

Clark, W. C.: Scales of climate impacts, Clim. Change, 7(1), 5–27, 1985.

Conway, T. M. and John, S. G.: Quantification of dissolved iron sources to the North Atlantic Ocean, Nature, 511(7508), 212–215, 2014.

Crouzet, P.: L'eutrophisation de la Loire, Water Supply, (1), 131–144, 1983.

Cushman, J.: Recent foraminifera from off the West Coast of North America: California University, Scripps Institution of Oceanography, Bull. Berkeley Calif. Tech. Ser., 1, 149, 1927.

Dalrymple, R. W., Zaitlin, B. A. and Boyd, R.: Estuarine facies models: conceptual basis and stratigraphic implications: perspective, J. Sediment. Res., 62(6), 1992.

Dang, D. H., Lenoble, V., Durrieu, G., Omanović, D., Mullot, J.-U., Mounier, S. and Garnier, C.: Seasonal variations of coastal sedimentary trace metals cycling: Insight on the effect of manganese and iron (oxy)hydroxides, sulphide and organic matter, Mar. Pollut. Bull., 92(1–2), 113–124, doi:10.1016/j.marpolbul.2014.12.048, 2015.

Dang, D. H., Tessier, E., Lenoble, V., Durrieu, G., Omanović, D., Mullot, J.-U., Pfeifer, H.-R., Mounier, S. and Garnier, C.: Key parameters controlling arsenic dynamics in coastal sediments: An analytical and modeling approach, Mar. Chem., 161, 34–46, doi:10.1016/j.marchem.2014.02.005, 2014.

Darwin, C. R.: The formation of vegetable mould, through the action of worms, with observations on their habits., John Murray, London. [online] Available from: http://darwin-online.org.uk/content/frameset?viewtype=text&itemID=F1357&pageseq=1, 1881.

Davison, W., Grime, G. W., Morgan, J. a. W. and Clarke, K.: Distribution of dissolved iron in sediment pore waters at submillimetre resolution, Nature, 352(6333), 323–325, doi:10.1038/352323a0, 1991.

Davison, W. and Zhang, H.: In situspeciation measurements of trace components in natural waters using thin-film gels, Nature, 367(6463), 546–548, doi:10.1038/367546a0, 1994.

Davison, W., Zhang, H. and Grime, G. W.: Performance Characteristics of Gel Probes Used For Measuring the Chemistry of Pore Waters, Environ. Sci. Technol., 28(9), 1623–1632, doi:10.1021/es00058a015, 1994.

Debenay, J. P., Pages, J. and Diouf, P. S.: Ecological zonation of the hyperhaline estuary of the Casamance River (Senegal): Foraminifera, zooplankton and abiotic variables, Hydrobiologia, 174(2), 161–176, doi:10.1007/BF00014063, 1989.

Debenay, J.-P., Bicchi, E., Goubert, E. and Armynot du Châtelet, E.: Spatio-temporal distribution of benthic foraminifera in relation to estuarine dynamics (Vie estuary, Vendée, W France), Estuar. Coast. Shelf Sci., 67(1–2), 181–197, doi:10.1016/j.ecss.2005.11.014, 2006.

Debenay, J.-P. and Guillou, J.-J.: Ecological transitions indicated by foraminiferal assemblages in paralic environments, Estuaries, 25(6), 1107–1120, doi:10.1007/BF02692208, 2002.

Deborde, J., Anschutz, P., Auby, I., Glé, C., Commarieu, M.-V., Maurer, D., Lecroart, P. and Abril, G.: Role of tidal pumping on nutrient cycling in a temperate lagoon (Arcachon Bay, France), Mar. Chem., 109(1–2), 98–114, doi:10.1016/j.marchem.2007.12.007, 2008.

Deborde, J., Anschutz, P., Chaillou, G., Etcheber, H., Commarieu, M.-V., Lecroart, P. and Abril, G.: The dynamics of phosphorus in turbid estuarine systems: Example of the Gironde estuary (France), Limnol. Oceanogr., 52(2), 862–872, 2007.

Decho, A. W.: Microbial biofilms in intertidal systems: an overview, Cont. Shelf Res., 20(10), 1257–1273, 2000.

Delhez, É. J. M. and Wolk, F.: Diagnosis of the transport of adsorbed material in the Scheldt estuary: A proof of concept, J. Mar. Syst., 128, 17–26, doi:10.1016/j.jmarsys.2012.01.007, 2013.

Deloffre, J.: La sédimentation fine sur les vasières intertidales en estuaires macrotidaux. Processus, quantification et modélisation semi-diurne à l'échelle annuelle, Thèse de doctorat, Rouen, Rouen., 2005.

Deloffre, J., Lafite, R., Lesueur, P., Verney, R., Lesourd, S., Cuvilliez, A. and Taylor, J.: Controlling factors of rhythmic sedimentation processes on an intertidal estuarine mudflat — Role of the turbidity maximum in the macrotidal Seine estuary, France, Mar. Geol., 235(1–4), 151–164, doi:10.1016/j.margeo.2006.10.011, 2006.

Dittmar, T. and Paeng, J.: A heat-induced molecular signature in marine dissolved organic matter, Nat. Geosci., 2(3), 175–179, doi:10.1038/ngeo440, 2009.

Douglas, R. G.: Paleoecology of continental margin basins: a modern case history from the borderland of southern California, Depositional Syst. Act. Cont. Margin Basins SEPM Pac Sect Short Course, 121–156, 1981.

DREAL Pays-de-Loire: hydroweb, [online] Available from: http://www.hydro.eaufrance.fr/presentation/procedure.php (Accessed 30 July 2015), 1994.

DREAL-Pays-de-Loire: DREAL Pays-de-Loire/ Banque HYDRO - MEEDDAT/DGPR/SRNH, [online] Available from: http://www.hydro.eaufrance.fr/i, 2015.

Duport, E., Stora, G., Tremblay, P. and Gilbert, F.: Effects of population density on the sediment mixing induced by the gallery-diffusor Hediste (Nereis) diversicolor O.F. Müller, 1776, J. Exp. Mar. Biol. Ecol., 336(1), 33–41, doi:10.1016/j.jembe.2006.04.005, 2006.

Dupré, B., Viers, J., Dandurand, J.-L., Polve, M., Bénézeth, P., Vervier, P. and Braun, J.-J.: Major and trace elements associated with colloids in organic-rich river waters: ultrafiltration of natural and spiked solutions, Chem. Geol., 160(1–2), 63–80, doi:10.1016/S0009-2541(99)00060-1, 1999.

Eckman, J. E. and Thistle, D.: Small-scale spatial pattern in meiobenthos in the San Diego Trough, Deep Sea Res. Part Oceanogr. Res. Pap., 35(9), 1565–1578, doi:10.1016/0198-0149(88)90103-3, 1988.

Egger, M., Jilbert, T., Behrends, T., Rivard, C. and Slomp, C. P.: Vivianite is a major sink for phosphorus in methanogenic coastal surface sediments, Geochim. Cosmochim. Acta, 169, 217–235, doi:10.1016/j.gca.2015.09.012, 2015.

Eisma, D.: Flocculation and de-flocculation of suspended matter in estuaries, Neth. J. Sea Res., 20(2), 183–199, 1986.

Elrod, V. A.: The flux of iron from continental shelf sediments: A missing source for global budgets, Geophys. Res. Lett., 31(12), doi:10.1029/2004GL020216, 2004.

Enge, A. J., Kucera, M. and Heinz, P.: Diversity and microhabitats of living benthic foraminifera in the abyssal Northeast Pacific, Mar. Micropaleontol., 96–97, 84–104, doi:10.1016/j.marmicro.2012.08.004, 2012.

Ernst, S., Bours, R., Duijnstee, I. and van der Zwaan, B.: Experimental effects of an organic matter pulse and oxygen depletion on a benthic foraminiferal shelf community, J. Foraminifer. Res., 35(3), 177–197, 2005.

Ernst, S. R., Morvan, J., Geslin, E., Le Bihan, A. and Jorissen, F. J.: Benthic foraminiferal response to experimentally induced Erika oil pollution, Mar. Micropaleontol., 61(1–3), 76–93, doi:10.1016/j.marmicro.2006.05.005, 2006.

Escoube, R., Rouxel, O. J., Sholkovitz, E. and Donard, O. F. X.: Iron isotope systematics in estuaries: The case of North River, Massachusetts (USA), Geochim. Cosmochim. Acta, 73(14), 4045–4059, doi:10.1016/j.gca.2009.04.026, 2009.

Fenchel, T.: Worm burrows and oxic microniches in marine sediments. 1. Spatial and temporal scales, Mar. Biol., 127(2), 289–295, doi:10.1007/BF00942114, 1996.

Ferdelman, T. G.: The distribution of sulfur, iron, manganese, copper and uranium in a salt marsh sediment core as determined by a sequential extraction method, Masters thesis, Univ. Delaware., 1988.

Fernandes, S. O., Javanaud, C., Aigle, A., Michotey, V. D., Guasco, S., Deborde, J., Deflandre, B., Anschutz, P. and Bonin, P. C.: Anaerobic nitrification–denitrification mediated by Mn-oxides in meso-tidal sediments: Implications for N2 and N2O production, J. Mar. Syst., 144, 1–8, doi:10.1016/j.jmarsys.2014.11.011, 2015.

Festa, J. F. and Hansen, D. V.: Turbidity maxima in partially mixed estuaries: a two-dimensional numerical model, Estuar. Coast. Mar. Sci., 7(4), 347–359, 1978.

Figuères, G., Martin, J. M. and Meybeck, M.: Iron behaviour in the Zaire estuary, Neth. J. Sea Res., 12(3–4), 329–337, doi:10.1016/0077-7579(78)90035-2, 1978.

Figueres, G., Martin, J., Meybeck, M. and Seyler, P.: A comparative study of mercury contamination in the Tagus Estuary (Portugal) and major French Estuaries (Gironde, Loire, Rhône), Estuar. Coast. Shelf Sci., 20(2), 183–203, 1985.

Filgueiras, A. V., Lavilla, I. and Bendicho, C.: Chemical sequential extraction for metal partitioning in environmental solid samples., J. Environ. Monit., 4(6), 823–857, doi:10.1039/b207574c, 2002.

Finden, D., Tipping, E., Jaworski, G. and Reynolds, C.: Light-induced reduction of natural iron (III) oxide and its relevance to phytoplankton, 1984.

Findlay, A. J., Gartman, A., MacDonald, D. J., Hanson, T. E., Shaw, T. J. and Luther, G. W.: Distribution and size fractionation of elemental sulfur in aqueous environments: The Chesapeake Bay and Mid-Atlantic Ridge, Geochim. Cosmochim. Acta, 142, 334–348, 2014.

Fontanier, C., Jorissen, F. J., Licari, L., Alexandre, A., Anschutz, P. and Carbonel, P.: Live benthic foraminiferal faunas from the Bay of Biscay: faunal density, composition, and microhabitats, Deep Sea Res. Part Oceanogr. Res. Pap., 49(4), 751–785, doi:10.1016/S0967-0637(01)00078-4, 2002.

Fortin, M.-J. and Dale, M. R. T.: Spatial analysis a guide for ecologists, Cambridge University Press, Cambridge, N.Y. [online] Available from: http://public.eblib.com/EBLPublic/PublicView.do?ptiID=228304 (Accessed 16 August 2014), 2005.

Fox, L. E.: The chemistry of aquatic phosphate: inorganic processes in rivers, Hydrobiologia, 253(1–3), 1–16, 1993.

Fox, L. E., Sager, S. L. and Wofsy, S. C.: Factors controlling the concentrations of soluble phosphorus in the Mississippi estuary1, Limnol. Oceanogr., 30(4), 826–832, 1985.

Fox, L. E., Sager, S. L. and Wofsy, S. C.: The chemical control of soluble phosphorus in the Amazon estuary, Geochim. Cosmochim. Acta, 50(5), 783–794, 1986.

François, F., Gerino, M., Stora, G., Durbec, J. and Poggiale, J.: Functional approach to sediment reworking by gallery-forming macrobenthic organisms: modeling and application with the polychaete Nereis diversicolor, Mar. Ecol. Prog. Ser., 229, 127–136, doi:10.3354/meps229127, 2002.

François, F., Poggiale, J.-C., Durbec, J.-P. and Stora, G.: A new approach for the modelling of sediment reworking induced by a macrobenthic community, Acta Biotheor., 45(3–4), 295–319, 1997.

Froelich, P. N.: Kinetic control of dissolved phosphate in natural rivers and estuaries: A primer on the phosphate buffer mechanism1, Limnol. Oceanogr., 33(4), 649–668, 1988.

Froelich, P. N., Klinkhammer, G. P., Bender, M. L., Luedtke, N. A., Heath, G. R., Cullen, D., Dauphin, P., Hammond, D., Hartman, B. and Maynard, V.: Early oxidation of organic matter in pelagic sediments of the eastern equatorial Atlantic: suboxic diagenesis, Geochim. Cosmochim. Acta, 43(7), 1075–1090, doi:10.1016/0016-7037(79)90095-4, 1979.

Gaillardet, J., Viers, J. and Dupré, B.: Trace elements in river waters, in Treatise on geochemistry, vol. 5, pp. 225–272, Elsevier pergamon., 2003.

García-Robledo, E., Corzo, A. and Papaspyrou, S.: A fast and direct spectrophotometric method for the sequential determination of nitrate and nitrite at low concentrations in small volumes, Mar. Chem., 162, 30–36, doi:10.1016/j.marchem.2014.03.002, 2014.

Gardolinski, P. C. F. C., Worsfold, P. J. and McKelvie, I. D.: Seawater induced release and transformation of organic and inorganic phosphorus from river sediments, Water Res., 38(3), 688–692, doi:10.1016/j.watres.2003.10.048, 2004.

Gernez, P., Lafon, V., Lerouxel, A., Curti, C., Lubac, B., Cerisier, S. and Barillé, L.: Toward Sentinel-2 High Resolution Remote Sensing of Suspended Particulate Matter in Very Turbid Waters: SPOT4 (Take5) Experiment in the Loire and Gironde Estuaries, Remote Sens., 7(8), 9507–9528, doi:10.3390/rs70809507, 2015.

Geslin, E., Barras, C., Langlet, D., Nardelli, M. P., Kim, J.-H., Bonnin, J., Metzger, E. and Jorissen, F. J.: Survival, Reproduction and Calcification of Three Benthic Foraminiferal Species in Response to Experimentally Induced Hypoxia, in Approaches to Study Living Foraminifera, edited by H. Kitazato and J. M. Bernhard, pp. 163–193, Springer Japan. [online] Available from: http://link.springer.com/chapter/10.1007/978-4-431-54388-6_10 (Accessed 20 August 2014), 2014.

Geslin, E., Heinz, P., Jorissen, F. and Hemleben, C.: Migratory responses of deep-sea benthic foraminifera to variable oxygen conditions: laboratory investigations, Mar. Micropaleontol., 53(3–4), 227–243, doi:10.1016/j.marmicro.2004.05.010, 2004.

Gilbert, F., Aller, R. C. and Hulth, S.: The influence of macrofaunal burrow spacing and diffusive scaling on sedimentary nitrification and denitrification: An experimental simulation and model approach, J. Mar. Res., 61(1), 101–125, doi:10.1357/002224003321586426, 2003.

GIP LE: Les amplitudes de l'onde de marée. Cahier indicateurs L1.A1, 2002.

GIP LE: Les surfaces marnantes L1.D3, 2004.

GIP LE: Le benthos L2.C1, 2011.

Gledhill, M. and van den Berg, C. M.: Determination of complexation of iron (III) with natural organic complexing ligands in seawater using cathodic stripping voltammetry, Mar. Chem., 47(1), 41–54, 1994.

Gledhill, M. and Buck, K. N.: The Organic Complexation of Iron in the Marine Environment: A Review, Front. Microbiol., 3, doi:10.3389/fmicb.2012.00069, 2012.

Glud, R. N., Forster, S. and Huettel, M.: Influence of radial pressure gradients on solute exchange in stirred benthic chambers, Mar. Ecol. Prog. Ser., 141(1), 303–311, 1996.

Gneiting, T., Ševčíková, H. and Percival, D. B.: Estimators of Fractal Dimension: Assessing the Roughness of Time Series and Spatial Data, Stat. Sci., 27(2), 247–277, doi:10.1214/11-STS370, 2012.

Goldstein, S. T., Watkins, G. T. and Kuhn, R. M.: Microhabitats of salt marsh foraminifera: St. Catherines Island, Georgia, USA, Mar. Micropaleontol., 26(1–4), 17–29, doi:10.1016/0377-8398(95)00006-2, 1995.

Gonzalez, J. L., Dange, C. and Thouvenin, B.: Spéciation des contaminants métalliques en milieu estuarien: Intérêt de la modélisation et application au cadmium, Hydroécologie Appliquée, 13, 37–55, 2001.

Gorry, P. A.: General least-squares smoothing and differentiation by the convolution (Savitzky-Golay) method, Anal. Chem., 62(6), 570–573, doi:10.1021/ac00205a007, 1990.

Gorse, laureline, Coynel, A. and Etcheber, H.: Analyse multi-proxies des eaux du bassin versant de la Loire inférieure et estuarienne, 2010.

Goubert, E., Frenod, E., Peeters, P., Thuillier, P., Vested, H. J. and Bernard, N.: Utilisation de données altimétriques (Altus) dans la caractérisation de climats hydrodynamiques contrôlant le fonctionnement hydrosédimentaire d'une vasière intertidale : cas de l'estuaire de la Vilaine (Bretagne, France), Rev. Paralia, 3, 6.1-6.15, doi:10.5150/revue-paralia.2010.006, 2010.

Goubert, E., Frenod, E., Peeters, P., Thuillier, P., Vested, H. J., Bernard, N., Veron, V. and Allano, L.: Caractérisation du fonctionnement hydrosédimentaire de l'estuaire de la Vilaine à partir d'études bathymétriques et altimétriques (Altus), pp. 81–90, Editions Paralia., 2008.

Grasshoff, K., Kremling, K. and Ehrhardt, M.: Methods of Seawater Analysis, John Wiley & Sons., 2009.

Griess, P.: Bemerkungen zu der Abhandlung der HH. Weselsky und Benedikt „Ueber einige Azoverbindungen" , Berichte Dtsch. Chem. Ges., 12(1), 426–428, doi:10.1002/cber.187901201117, 1879.

Grosbois, C., Négrel, P., Fouillac, C. and Grimaud, D.: Dissolved load of the Loire River: chemical and isotopic characterization, Chem. Geol., 170(1), 179–201, 2000.

Grosbois, C., Négrel, P., Grimaud, D. and Fouillac, C.: An overview of dissolved and suspended matter fluxes in the Loire river basin: natural and anthropogenic inputs, Aquat. Geochem., 7(2), 81–105, 2001.

Gross, O.: Influence of temperature, oxygen and food availability on the migrational activity of bathyal benthic foraminifera: evidence by microcosm experiments, in Life at Interfaces and Under Extreme Conditions, edited by G. Liebezeit, S. Dittmann, and I. Kröncke, pp. 123–137, Springer Netherlands. [online] Available from: http://link.springer.com/chapter/10.1007/978-94-011-4148-2_12 (Accessed 3 October 2014), 2000.

Grzymski, J., Schofield, O. M., Falkowski, P. G. and Bernhard, J. M.: The function of plastids in the deep-sea benthic foraminifer, Nonionella stella, Limnol. Oceanogr., 47(6), 1569–1580, 2002.

Haese, R. R.: The biogeochemistry of iron, in Marine Geochemistry, pp. 241–270, Springer., 2006.

Haese, R. R., Wallmann, K., Dahmke, A., Kretzmann, U., Müller, P. J. and Schulz, H. D.: Iron species determination to investigate early diagenetic reactivity in marine sediments, Geochim. Cosmochim. Acta, 61(1), 63–72, 1997.

Harper, M. P., Davison, W. and Tych, W.: Temporal, spatial, and resolution constraints for in situ sampling devices using diffusional equilibration: Dialysis and DET, Environ. Sci. Technol., 31(11), 3110–3119, 1997.

Heinz, P. and Geslin, E.: Ecological and Biological Response of Benthic Foraminifera Under Oxygen-Depleted Conditions: Evidence from Laboratory Approaches, in Anoxia, edited by A. V. Altenbach, J. M. Bernhard, and J. Seckbach, pp. 287–303, Springer Netherlands. [online] Available from: http://link.springer.com/chapter/10.1007/978-94-007-1896-8_15 (Accessed 7 January 2015), 2012.

Henry, M., Jolivet, J. P. and Livage, J.: Aqueous chemistry of metal cations: hydrolysis, condensation and complexation, in Chemistry, Spectroscopy and Applications of Sol-Gel Glasses, pp. 153–206, Springer. [online] Available from: http://link.springer.com/chapter/10.1007/BFb0036968 (Accessed 30 December 2015), 1992.

Hess, S., Alve, E., Trannum, H. C. and Norling, K.: Benthic foraminiferal responses to water-based drill cuttings and natural sediment burial: Results from a mesocosm experiment, Mar. Micropaleontol., 101, 1–9, doi:10.1016/j.marmicro.2013.03.004, 2013.

Hoffmann, M. R., Yost, E. C., Eisenreich, S. J. and Maier, W. J.: Characterization of soluble and colloidal phase metal complexes in river water by ultrafiltration. A mass-balance approach, Environ. Sci. Technol., 15(6), 655–661, 1981.

Hofmann, A. F., Soetaert, K., Middelburg, J. J. and Meysman, F. J. R.: AquaEnv : An Aqua tic Acid–Base Modelling Env ironment in R, Aquat. Geochem., 16(4), 507–546, doi:10.1007/s10498-009-9084-1, 2010.

Hohenegger, J., Piller, W. and Baal, C.: Reasons for spatial microdistributions of foraminifers in an intertidal pool (northern Adriatic Sea), Mar. Ecol., 10(1), 43–78, 1989.

Hohenegger, J., Piller, W. E. and Baal, C.: Horizontal and vertical spatial microdistribution of foraminifers in the shallow subtidal Gulf of Trieste, northern Adriatic Sea, J. Foraminifer. Res., 23(2), 79–101, doi:10.2113/gsjfr.23.2.79, 1993.

Holmes, D. E., Bond, D. R. and Lovley, D. R.: Electron Transfer by Desulfobulbus propionicus to Fe(III) and Graphite Electrodes, Appl. Environ. Microbiol., 70(2), 1234–1237, doi:10.1128/AEM.70.2.1234-1237.2004, 2004.

Homoky, W. B., Hembury, D. J., Hepburn, L. E., Mills, R. A., Statham, P. J., Fones, G. R. and Palmer, M. R.: Iron and manganese diagenesis in deep sea volcanogenic sediments and the origins of pore water colloids, Geochim. Cosmochim. Acta, 75(17), 5032–5048, doi:10.1016/j.gca.2011.06.019, 2011.

Homoky, W. B., John, S. G., Conway, T. M. and Mills, R. A.: Distinct iron isotopic signatures and supply from marine sediment dissolution, Nat. Commun., 4, doi:10.1038/ncomms3143, 2013.

Homoky, W. B., Severmann, S., McManus, J., Berelson, W. M., Riedel, T. E., Statham, P. J. and Mills, R. A.: Dissolved oxygen and suspended particles regulate the benthic flux of iron from continental margins, Mar. Chem., 134–135, 59–70, doi:10.1016/j.marchem.2012.03.003, 2012.

Hopwood, M. J., Statham, P. J., Skrabal, S. A. and Willey, J. D.: Dissolved iron(II) ligands in river and estuarine water, Mar. Chem., 173, 173–182, doi:10.1016/j.marchem.2014.11.004, 2015.

Hosomi, M., Okada, M. and Sudo, R.: Management of Bottom Sediments Containing Toxic Substances Release of phosphorus from lake sediments, Environ. Int., 7(2), 93–98, doi:10.1016/0160-4120(82)90078-2, 1982.

Huerta-Diaz, M. A., Rivera-Duarte, I., Sañudo-Wilhelmy, S. A. and Flegal, A. R.: Comparative distributions of size fractionated metals in pore waters sampled by in situ dialysis and whole-core sediment squeezing: Implications for diffusive flux calculations, Appl. Geochem., 22(11), 2509–2525, doi:10.1016/j.apgeochem.2007.07.001, 2007.

Huettel, M., Berg, P. and Kostka, J. E.: Benthic Exchange and Biogeochemical Cycling in Permeable Sediments, Annu. Rev. Mar. Sci., 6(1), 23–51, doi:10.1146/annurev-marine-051413-012706, 2014.

Hulth, S., Aller, R. C., Engstrom, P. and Selander, E.: A pH plate fluorosensor (optode) for early diagenetic studies of marine sediments, Limnol. Oceanogr., 47(1), 212–220, 2002.

Hulth, S., Aller, R. C. and Gilbert, F.: Coupled anoxic nitrification/manganese reduction in marine sediments, Geochim. Cosmochim. Acta, 63(1), 49–66, doi:10.1016/S0016-7037(98)00285-3, 1999.

Hunter, K. A. and Boyd, P. W.: Iron-binding ligands and their role in the ocean biogeochemistry of iron, Environ. Chem., 4(4), 221, doi:10.1071/EN07012, 2007.

Hyacinthe, C., Anschutz, P., Carbonel, P., Jouanneau, J.-M. and Jorissen, F. J.: Early diagenetic processes in the muddy sediments of the Bay of Biscay, Mar. Geol., 177(1–2), 111–128, doi:10.1016/S0025-3227(01)00127-X, 2001.

Hyacinthe, C., Bonneville, S. and Van Cappellen, P.: Reactive iron(III) in sediments: Chemical versus microbial extractions, Geochim. Cosmochim. Acta, 70(16), 4166–4180, doi:10.1016/j.gca.2006.05.018, 2006.

Hyacinthe, C. and Van Cappellen, P.: An authigenic iron phosphate phase in estuarine sediments: composition, formation and chemical reactivity, Mar. Chem., 91(1–4), 227–251, doi:10.1016/j.marchem.2004.04.006, 2004.

Ingri, J., Widerlund, A., Land, M., Gustafsson, Ö., Andersson, P. and Öhlander, B.: Temporal variations in the fractionation of the rare earth elements in a boreal river; the role of colloidal particles., Chem. Geol., 166(1), 23–45, 2000.

Jézéquel, D., Brayner, R., Metzger, E., Viollier, E., Prévot, F. and Fiévet, F.: Two-dimensional determination of dissolved iron and sulfur species in marine sediment pore-waters by thin-film based imaging. Thau lagoon (France), Estuar. Coast. Shelf Sci., 72(3), 420–431, doi:10.1016/j.ecss.2006.11.031, 2007.

Jitts, H.: The Absorption of Phosphate by Estuarine Bottom Deposits, Mar. Freshw. Res., 10(1), 7–21, 1959.

Johnson, K. S., Chavez, F. P. and Friederich, G. E.: Continental-shelf sediment as a primary source of iron for coastal phytoplankton, Nature, 398(6729), 697–700, 1999.

Johnson, K. S., Coale, K. H., Elrod, V. A. and Tindale, N. W.: Iron photochemistry in seawater from the equatorial Pacific, Mar. Chem., 46(4), 319–334, 1994.

Johnson, K. S., Gordon, R. M. and Coale, K. H.: What controls dissolved iron concentrations in the world ocean?, Mar. Chem., 57(3), 137–161, 1997.

Jones, C. G., Lawton, J. H. and Shachak, M.: Organisms as ecosystem engineers, in Ecosystem management, pp. 130–147, Springer., 1996.

Jones, M. E., Beckler, J. S. and Taillefert, M.: The flux of soluble organic-iron(III) complexes from sediments represents a source of stable iron(III) to estuarine waters and to the continental shelf, Limnol. Oceanogr., 56(5), 1811–1823, doi:10.4319/lo.2011.56.5.1811, 2011.

Jordan, T. E., Cornwell, J. C., Boynton, W. R. and Anderson, J. T.: Changes in phosphorus biogeochemistry along an estuarine salinity gradient: The iron conveyer belt, Limnol. Oceanogr., 53(1), 172–184, 2008.

Jorissen, F. J.: Benthic foraminifera from the Adriatic Sea: principles of phenotypic variation, Utrecht Micropaleontol. Bull., 37, 1–174, 1988.

Jorissen, F. J.: Benthic foraminiferal microhabitats below the sediment-water interface, in Modern Foraminifera, pp. 161–179, Barum K. Sen Gupta. [online] Available from: http://link.springer.com/chapter/10.1007/0-306-48104-9_10 (Accessed 20 August 2014), 1999.

Jorissen, F. J., Barmawidjaja, D. M., Puskaric, S. and van der Zwaan, G. J.: Vertical distribution of benthic foraminifera in the northern Adriatic Sea: The relation with the organic flux, Mar. Micropaleontol., 19(1–2), 131–146, doi:10.1016/0377-8398(92)90025-F, 1992.

Jorissen, F. J., de Stigter, H. C. and Widmark, J. G. V.: A conceptual model explaining benthic foraminiferal microhabitats, Mar. Micropaleontol., 26(1–4), 3–15, doi:10.1016/0377-8398(95)00047-X, 1995.

Jorissen, F. J., Wittling, I., Peypouquet, J. P., Rabouille, C. and Relexans, J. C.: Live benthic foraminiferal faunas off Cape Blanc, NW-Africa: Community structure and microhabitats, Deep Sea Res. Part Oceanogr. Res. Pap., 45(12), 2157–2188, doi:10.1016/S0967-0637(98)00056-9, 1998.

Jouanneau, J. M., Weber, O., Cremer, M. and Castaing, P.: Fine-grained sediment budget on the continental margin of the Bay of Biscay, Deep Sea Res. Part II Top. Stud. Oceanogr., 46(10), 2205–2220, 1999.

Kendall, B., Anbar, A. D., Kappler, A. and Konhauser, K. O.: The global iron cycle, Fundam. Geobiol., 65–92, 2012.

Kieber, R. J., Skrabal, S. A., Smith, B. J. and Willey, J. D.: Organic Complexation of Fe(II) and Its Impact on the Redox Cycling of Iron in Rain, Environ. Sci. Technol., 39(6), 1576–1583, doi:10.1021/es040439h, 2005.

Koller, H., Dworschak, P. C. and Abed-Navandi, D.: Burrows of Pestarella tyrrhena (Decapoda: Thalassinidea): hot spots for Nematoda, Foraminifera and bacterial densities, J. Mar. Biol. Assoc. U. K., 86(5), 1113–1122, 2006.

Koschorreck, M., Brookland, I. and Matthias, A.: Biogeochemistry of the sediment–water interface in the littoral of an acidic mining lake studied with microsensors and gel-probes, J. Exp. Mar. Biol. Ecol., 285–286, 71–84, doi:10.1016/S0022-0981(02)00520-8, 2003.

Kostka, J. E. and Luther, G. W.: Partitioning and speciation of solid phase iron in saltmarsh sediments, Geochim. Cosmochim. Acta, 58(7), 1701–1710, doi:10.1016/0016-7037(94)90531-2, 1994.

Kostka, J. E. and Luther, G. W.: Seasonal cycling of Fe in saltmarsh sediments, Biogeochemistry, 29(2), 159–181, 1995.

Krause, S., Tecklenburg, C., Munz, M. and Naden, E.: Streambed nitrogen cycling beyond the hyporheic zone: Flow controls on horizontal patterns and depth distribution of nitrate and dissolved oxygen in the upwelling groundwater of a lowland river, J. Geophys. Res. Biogeosciences, 118(1), 54–67, doi:10.1029/2012JG002122, 2013.

Kristensen, E.: Direct measurement of ventilation and oxygen uptake in three species of tubicolous polychaetes (Nereis spp.), J. Comp. Physiol., 145(1), 45–50, 1981.

Kristensen, E.: Oxygen and carbon dioxide exchange in the polychaete Nereis virens: influence of ventilation activity and starvation, Mar. Biol., 101(3), 381–388, 1989.

Kristensen, E.: Impact of polychaetes (Nereis spp. and Arenicola marina) on carbon biogeochemistry in coastal marine sedimentsPresented during the ACS Division of Geochemistry symposium ?Biogeochemical Consequences of Dynamic Interactions Between Benthic Fauna, Microbes and Aquatic Sediments?, San Diego, April 2001., Geochem. Trans., 2(12), 92, doi:10.1039/b108114d, 2001.

Kristensen, E., Delefosse, M., Quintana, C. O., Flindt, M. R. and Valdemarsen, T.: Influence of benthic macrofauna community shifts on ecosystem functioning in shallow estuaries, Mar. Ecosyst. Ecol., 1, 41, doi:10.3389/fmars.2014.00041, 2014.

Kristensen, E., PenhaLopes, G., Delefosse, M., Valdemarsen, T., Quintana, C. O. and Banta, G. T.: REVIEW What is bioturbation? The need for a precise definition for fauna in aquatic sciences, Mar. Ecol. Prog. Ser., 446, 285–302, doi:10.3354/meps09506, 2012.

Krom, M. D., Davison, P., Zhang, H. and Davison, W.: High-resolution pore-water sampling with a gel sampler, Limnol. Oceanogr., 39(8), 1967–1972, 1994.

Kuma, K., Nakabayashi, S., Suzuki, Y. and Matsunaga, K.: Dissolution rate and solubility of colloidal hydrous ferric oxide in seawater, Mar. Chem., 38(1–2), 133–143, doi:10.1016/0304-4203(92)90072-I, 1992.

Kuma, K., Nishioka, J. and Matsunaga, K.: Controls on iron (III) hydroxide solubility in seawater: the influence of pH and natural organic chelators, Limnol. Oceanogr., 41(3), 396–407, 1996.

Lalonde, K., Mucci, A., Ouellet, A. and Gélinas, Y.: Preservation of organic matter in sediments promoted by iron, Nature, 483(7388), 198–200, doi:10.1038/nature10855, 2012.

Lam, P. J., Ohnemus, D. C. and Marcus, M. A.: The speciation of marine particulate iron adjacent to active and passive continental margins, Geochim. Cosmochim. Acta, 80, 108–124, doi:10.1016/j.gca.2011.11.044, 2012.

Langezaal, A. M., Ernst, S. R., Haese, R. R., van Bergen, P. F. and van der Zwaan, G. J.: Disturbance of intertidal sediments: the response of bacteria and foraminifera, Estuar. Coast. Shelf Sci., 58(2), 249–264, doi:10.1016/S0272-7714(03)00078-7, 2003.

Langezaal, A. M., Jorissen, F. J., Braun, B., Chaillou, G., Fontanier, C., Anschutz, P. and van der Zwaan, G. J.: The influence of seasonal processes on geochemical profiles and foraminiferal assemblages on the outer shelf of the Bay of Biscay, Cont. Shelf Res., 26(15), 1730–1755, doi:10.1016/j.csr.2006.05.005, 2006.

Langlet, D., Geslin, E., Baal, C., Metzger, E., Lejzerowicz, F., Riedel, B., Zuschin, M., Pawlowski, J., Stachowitsch, M. and Jorissen, F. J.: Foraminiferal survival after long-term in situ experimentally induced anoxia, Biogeosciences, 10(11), 7463–7480, doi:10.5194/bg-10-7463-2013, 2013.

Larner, B. L., Seen, A. J. and Townsend, A. T.: Comparative study of optimised BCR sequential extraction scheme and acid leaching of elements in the certified reference material NIST 2711, Anal. Chim. Acta, 556(2), 444–449, doi:10.1016/j.aca.2005.09.058, 2006.

Larsen, L. H., Damgaard, L. R., Kjær, T., Stenstrøm, T., Lynggaard-Jensen, A. and Revsbech, N. P.: Fast responding biosensor for on-line determination of nitrate/nitrite in activated sludge, Water Res., 34(9), 2463–2468, doi:10.1016/S0043-1354(99)00423-6, 2000.

Lawrence, M. G. and Kamber, B. S.: The behaviour of the rare earth elements during estuarine mixing—revisited, Mar. Chem., 100(1–2), 147–161, doi:10.1016/j.marchem.2005.11.007, 2006.

Le Douarec, P.: L'intrusion saline dans l'estuaire de la Loire., Université de Nantes., 1978.

Le Floch, J.-F.: Propagation de la marée dynamique dans l'estuaire de la Seine et en Seine maritime., Thèse d'Etat, Paris., 1961.

Lee, J., McEnery, M., Kahn, E. and Schuster, F.: Symbiosis and the evolution of larger foraminifera, Micropaleontology, 118–140, 1979.

Legendre, P. and Fortin, M.-J.: Spatial pattern and ecological analysis, Vegetation, 80, 107–138, 1989.

Legendre, P. and Fortin, M.-J.: Comparison of the Mantel test and alternative approaches for detecting complex multivariate relationships in the spatial analysis of genetic data, Mol. Ecol. Resour., 10(5), 831–844, doi:10.1111/j.1755-0998.2010.02866.x, 2010.

Lesueur, P. and Lesourd, S.: Sables, chenaux, vasières..., Ifremer ed., 1999.

Leutenegger, S. and Hansen, H. J.: Ultrastructural and radiotracer studies of pore function in foraminifera, Mar. Biol., 54(1), 11–16, doi:10.1007/BF00387046, 1979.

Liang, L. and Morgan, J. J.: Chemical aspects of iron oxide coagulation in water: Laboratory studies and implications for natural systems, Aquat. Sci., 52(1), 32–55, 1990.

Lillebø, A. I., Neto, J. M., Flindt, M. R., Marques, J. C. and Pardal, M. A.: Phosphorous dynamics in a temperate intertidal estuary, Estuar. Coast. Shelf Sci., 61(1), 101–109, doi:10.1016/j.ecss.2004.04.007, 2004.

Liu, X. and Millero, F. J.: The solubility of iron in seawater, Mar. Chem., 77(1), 43–54, 2002.

Loeblich, A. and Tappan, H.: Present status of foraminiferal classification, Stud. Benthic Foraminifera, 93–102, 1992.

Loubere, P., Jacobsen, B., Klitgaard Kristensen, D., Husum, K., Jernas, P. and Richaud, M.: The structure of benthic environments and the paleochemical record of foraminifera, Deep Sea Res. Part Oceanogr. Res. Pap., 58(5), 535–545, doi:10.1016/j.dsr.2011.02.011, 2011.

Lovley, D. R.: Dissimilatory Fe(III) and Mn(IV) reduction., Microbiol. Rev., 55(2), 259–287, 1991.

Lovley, D. R., Holmes, D. E. and Nevin, K. P.: Dissimilatory Fe(III) and Mn(IV) Reduction, in Advances in Microbial Physiology, vol. 49, pp. 219–286, Elsevier. [online] Available from: http://linkinghub.elsevier.com/retrieve/pii/S0065291104490055 (Accessed 22 April 2014), 2004.

Lovley, D. R., Ueki, T., Zhang, T., Malvankar, N. S., Shrestha, P. M., Flanagan, K. A., Aklujkar, M., Butler, J. E., Giloteaux, L., Rotaru, A.-E., Holmes, D. E., Franks, A. E., Orellana, R., Risso, C. and Nevin, K. P.: Geobacter, in Advances in Microbial Physiology, vol. 59, pp. 1–100, Elsevier. [online] Available from: http://linkinghub.elsevier.com/retrieve/pii/B9780123876614000045 (Accessed 7 July 2015), 2011.

Lynts, G. W.: Relationship of Sediment-size Distribution to Ecologic Factors in Buttonwood Sound, Florida Bay, J. Sediment. Res., 36(1), 66–74, 1966.

Lyons, T. W. and Severmann, S.: A critical look at iron paleoredox proxies: New insights from modern euxinic marine basins, Geochim. Cosmochim. Acta, 70(23), 5698–5722, doi:10.1016/j.gca.2006.08.021, 2006.

Ma, S., Noble, A., Butcher, D., Trouwborst, R. E. and Luther, G. W.: Removal of H2S via an iron catalytic cycle and iron sulfide precipitation in the water column of dead end tributaries, Estuar. Coast. Shelf Sci., 70(3), 461–472, doi:10.1016/j.ecss.2006.06.033, 2006.

MacIntyre, H. L., Geider, R. J. and Miller, D. C.: Microphytobenthos: The ecological role of the "secret garden" of unvegetated, shallow-water marine habitats. I. Distribution, abundance and primary production, Estuaries, 19(2), 186–201, doi:10.2307/1352224, 1996.

Magnuson, M. L., Lytle, D. A., Frietch, C. M. and Kelty, C. A.: Characterization of Submicrometer Aqueous Iron(III) Colloids Formed in the Presence of Phosphate by Sedimentation Field Flow Fractionation with Multiangle Laser Light Scattering Detection, Anal. Chem., 73(20), 4815–4820, doi:10.1021/ac010702m, 2001.

Maldonado, M. T. and Price, N. M.: Reduction and transport of organically bound iron by Thalassiosira oceanic (Bacillariophyceae), J. Phycol., 37(2), 298–310, doi:10.1046/j.1529-8817.2001.037002298.x, 2001.

Manickam, S., Barbaroux, L. and Ottmann, F.: Composition and mineralogy of suspended sediment in the fluvio-estuarine zone of the Loire River, France, Sedimentology, 32(5), 721–741, doi:10.1111/j.1365-3091.1985.tb00484.x, 1985.

Martin, J. H. and Fitzwater, S. E.: Iron deficiency limits phytoplankton growth in the north-east Pacific subarctic, Nature, 331(6154), 341–343, doi:10.1038/331341a0, 1988.

Martin, J.-M. and Meybeck, M.: Elemental mass-balance of material carried by major world rivers, Mar. Chem., 7(3), 173–206, doi:10.1016/0304-4203(79)90039-2, 1979.

Martin, S. T.: Precipitation and dissolution of iron and manganese oxides, in Environmental Catalysis, Vicki H. Grassian., 2003.

Martiny, J. B. H., Bohannan, B. J. M., Brown, J. H., Colwell, R. K., Fuhrman, J. A., Green, J. L., Horner-Devine, M. C., Kane, M., Krumins, J. A., Kuske, C. R., Morin, P. J., Naeem, S., Øvreås, L., Reysenbach, A.-L., Smith, V. H. and Staley, J. T.: Microbial biogeography: putting microorganisms on the map, Nat. Rev. Microbiol., 4(2), 102–112, doi:10.1038/nrmicro1341, 2006.

Maurice, L.: Biodégradabilité de la matière organique dans le bouchon vaseux et la crème de vase de l'estuaire de la Loire, Oceanol. Acta, 17(5), 501–516, 1994.

McManus, J., Berelson, W. M., Coale, K. H., Johnson, K. S. and Kilgore, T. E.: Phosphorus regeneration in continental margin sediments, Geochim. Cosmochim. Acta, 61(14), 2891–2907, doi:10.1016/S0016-7037(97)00138-5, 1997.

Mehra, O. P. and Jackson, M. L.: Iron oxide removal from soils and clays by a dithionite-citrate system buffered with sodium bicarbonate, in National conference on clays and clays minerals, vol. 7, pp. 317–327., 1958.

Meile, C., Koretsky, C. M. and Cappellen, P. V.: Quantifying bioirrigation in aquatic sediments: an inverse modeling approach, Limnol. Oceanogr., 46(1), 164–177, 2001.

Metzger, E., Langlet, D., Viollier, E., Koron, N., Riedel, B., Stachowitsch, M., Faganeli, J., Tharaud, M., Geslin, E. and Jorissen, F.: Artificially induced migration of redox layers in a coastal sediment from the Northern Adriatic, Biogeosciences, 11(8), 2211–2224, doi:10.5194/bg-11-2211-2014, 2014.

Metzger, E., Simonucci, C., Viollier, E., Sarazin, G., Prévot, F. and Jézéquel, D.: Benthic response to shellfish farming in Thau lagoon: Pore water signature, Estuar. Coast. Shelf Sci., 72(3), 406–419, doi:10.1016/j.ecss.2006.11.011, 2007.

Metzger, E., Viollier, E., Simonucci, C., Prévot, F., Langlet, D. and Jézéquel, D.: Millimeter-scale alkalinity measurement in marine sediment using DET probes and colorimetric determination, Water Res., 47(15), 5575–5583, 2013.

Meybeck, M.: Carbon, nitrogen, and phosphorus transport by world rivers, Am J Sci, 282(4), 401–450, 1982.

Meybeck, M.: C, N, P and S in rivers: from sources to global inputs, in Interactions of C, N, P and S Biogeochemical cycles and global change, pp. 163–193, Springer., 1993.

Meybeck, M., Cauwet, G., Dessery, S., Somville, M., Gouleau, D. and Billen, G.: Nutrients (organic C, P, N, Si) in the eutrophic River Loire (France) and its estuary, Estuar. Coast. Shelf Sci., 27(6), 595–624, doi:10.1016/0272-7714(88)90071-6, 1988.

Meyers, M. B., Fossing, H. and Powell, E. N.: Microdistribution of interstitial meiofauna, oxygen and sulfide gradients, and the tubes of macro-infauna, Mar. Ecol.-Prog. Ser., 35, 223–241, doi:10.3354/meps035223, 1987.

Meysman, F. J. . and Burdorf, L.: The estimation of geochemical rates and fluxes in aquatic sediments, in prep.

Meysman, F. J., Boudreau, B. P. and Middelburg, J. J.: When and why does bioturbation lead to diffusive mixing?, J. Mar. Res., 68(6), 881–920, 2010a.

Meysman, F. J. R., Boudreau, B. P. and Middelburg, J. J.: Relations between local, nonlocal, discrete and continuous models of bioturbation, J. Mar. Res., 61(3), 391–410, doi:10.1357/002224003322201241, 2003a.

Meysman, F. J. R., Boudreau, B. P. and Middelburg, J. J.: Modeling reactive transport in sediments subject to bioturbation and compaction, Geochim. Cosmochim. Acta, 69(14), 3601–3617, doi:10.1016/j.gca.2005.01.004, 2005a.

Meysman, F. J. R., Galaktionov, O. S., Glud, R. N. and Middelburg, J. J.: Oxygen penetration around burrows and roots in aquatic sediments, J. Mar. Res., 68(2), 309–336, doi:10.1357/002224010793721406, 2010b.

Meysman, F. J. R., Galaktionov, O. S., Madani, S. and Middelburg, J. J.: Modelling Biological Interactions in Aquatic Sediments as Coupled Reactive Transport, in Interactions Between Macro- and Microorganisms in Marine Sediments, edited by E. Kristensen, R. R. Haese, and J. E. Kostka, pp. 359–388, American Geophysical Union. [online] Available from: http://onlinelibrary.wiley.com/doi/10.1029/CE060p0359/summary (Accessed 21 August 2014b), 2005.

Meysman, F. J. R., Malyuga, V. S., Boudreau, B. P. and Middelburg, J. J.: A generalized stochastic approach to particle dispersal in soils and sediments, Geochim. Cosmochim. Acta, 72(14), 3460–3478, doi:10.1016/j.gca.2008.04.023, 2008a.

Meysman, F. J. R., Middelburg, J. J. and Heip, C. H. R.: Bioturbation: a fresh look at Darwin's last idea, Trends Ecol. Evol., 21(12), 688–695, doi:10.1016/j.tree.2006.08.002, 2006.

Meysman, F. J. R., Middelburg, J. J., Herman, P. M. J. and Heip, C. H. R.: Reactive transport in surface sediments. II. Media: an object-oriented problem-solving environment for early diagenesis, Comput. Geosci., 29(3), 301–318, doi:10.1016/S0098-3004(03)00007-4, 2003b.

Meysman, F., Malyuga, V., Boudreau, B. and Middelburg, J.: Quantifying particle dispersal in aquatic sediments at short time scales: model selection, Aquat. Biol., 2(3), 239–254, doi:10.3354/ab00054, 2008b.

Migniot, C.: Etude des propriétés physiques de différents sédiments très fins et de leur comportement sous des actions hydrodynamiques, Houille Blanche, (7), 591–620, 1968.

Migniot, C.: Bilan de l'hydrologie et de l'hydrosédimentaire de l'estuaire de la Loire au cours des deux dernières décennies, Association pour la protection de l'environnement de l'estuaire de la Loire et Port autonome de Nantes-Saint Nazaire. [online] Available from: http://oaidoc.eau-loire-bretagne.fr/exl-doc/doc00004390.pdf, 1993.

Millero, F. J.: The thermodynamics of the carbonate system in seawater, Geochim. Cosmochim. Acta, 43(10), 1651–1661, doi:10.1016/0016-7037(79)90184-4, 1979.

Millero, F. J.: Thermodynamics of the carbon dioxide system in the oceans, Geochim. Cosmochim. Acta, 59(4), 661–677, doi:10.1016/0016-7037(94)00354-O, 1995.

Millero, F. J., Sotolongo, S. and Izaguirre, M.: The oxidation kinetics of Fe(II) in seawater, Geochim. Cosmochim. Acta, 51(4), 793–801, doi:10.1016/0016-7037(87)90093-7, 1987.

Millero, F. J., Yao, W. and Aicher, J.: The speciation of Fe (II) and Fe (III) in natural waters, Mar. Chem., 50(1), 21–39, 1995.

Minaudo, C., Meybeck, M., Moatar, F., Gassama, N. and Curie, F.: Eutrophication mitigation in rivers: 30 years of trends in spatial and seasonal patterns of biogeochemistry of the Loire River (1980–2012), Biogeosciences, 12(8), 2549–2563, doi:10.5194/bg-12-2549-2015, 2015.

Moatar, F. and Meybeck, M.: Compared performances of different algorithms for estimating annual nutrient loads discharged by the eutrophic River Loire, Hydrol. Process., 19(2), 429–444, doi:10.1002/hyp.5541, 2005.

Molina-Cruz, A. and Ayala-López, A.: Influence of the hydrothermal vents on the distribution of benthic foraminifera from the Guaymas Basin, Mexico, Geo-Mar. Lett., 8(1), 49–56, 1988.

Monbet, P., McKelvie, I. D. and Worsfold, P. J.: Combined Gel Probes for the In Situ Determination of Dissolved Reactive Phosphorus in Porewaters and Characterization of Sediment Reactivity, Environ. Sci. Technol., 42(14), 5112–5117, doi:10.1021/es8001663, 2008.

Moodley, L.: Southern North Sea seafloor and subsurface distribution of living benthic foraminifera, Neth. J. Sea Res., 27(1), 57–71, doi:10.1016/0077-7579(90)90034-E, 1990.

Moodley, L. and Hess, C.: Tolerance of Infaunal Benthic Foraminifera for Low and High Oxygen Concentrations, Biol. Bull., 183(1), 94–98, 1992.

Moodley, L., van der Zwaan, G. J., Rutten, G. M. W., Boom, R. C. E. and Kempers, A. J.: Subsurface activity of benthic foraminifera in relation to porewater oxygen content: laboratory experiments, Mar. Micropaleontol., 34(1–2), 91–106, doi:10.1016/S0377-8398(97)00044-3, 1998.

Moore, C. M., Mills, M. M., Arrigo, K. R., Berman-Frank, I., Bopp, L., Boyd, P. W., Galbraith, E. D., Geider, R. J., Guieu, C., Jaccard, S. L., Jickells, T. D., La Roche, J., Lenton, T. M., Mahowald, N. M., Marañón, E., Marinov, I.,

Moore, J. K., Nakatsuka, T., Oschlies, A., Saito, M. A., Thingstad, T. F., Tsuda, A. and Ulloa, O.: Processes and patterns of oceanic nutrient limitation, Nat. Geosci., 6(9), 701–710, doi:10.1038/ngeo1765, 2013.

Moore, J. K., Doney, S. C., Glover, D. M. and Fung, I. Y.: Iron cycling and nutrient-limitation patterns in surface waters of the World Ocean, Deep Sea Res. Part II Top. Stud. Oceanogr., 49(1), 463–507, 2001.

Moore, R., Burton, J., Williams, P. L. and Young, M.: The behaviour of dissolved organic material, iron and manganese in estuarine mixing, Geochim. Cosmochim. Acta, 43(6), 919–926, 1979.

Moore, R. M. and Millward, G. E.: The kinetics of reversible Th reactions with marine particles, Geochim. Cosmochim. Acta, 52(1), 113–118, doi:10.1016/0016-7037(88)90060-9, 1988.

Morris, A., Mantoura, R., Bale, A. and Howland, R.: Very low salinity regions of estuaries: important sites for chemical and biological reactions, 1978.

Morris, A. W., Bale, A. J., Howland, R. J. M., Loring, D. H. and Rantala, R. T. T.: Controls of the chemical composition of particle populations in a macrotidal estuary (Tamar Estuary, U.K.), Cont. Shelf Res., 7(11–12), 1351–1355, doi:10.1016/0278-4343(87)90039-2, 1987.

Morse, J. W., DiMarco, S. F., Hebert, A. B. and Sell, K. S.: A scaling approach to spatial variability in early diagenetic processes, in The Interactions between Sediments and Water, pp. 25–29, Springer. [online] Available from: http://link.springer.com/chapter/10.1007/978-94-017-3366-3_5 (Accessed 30 June 2014), 2003.

Mortimer, C. H.: Chemical exchanges between sediments and water in the Great Lakes-speculations on probable regulatory mechanisms, Limnol Ocean., 16(2), 387–404, 1971.

Mortimer, R. J. G., Krom, M. D., Harris, S. J., Hayes, P. J., Davies, I. M., Davison, W. and Zhang, H.: Evidence for suboxic nitrification in recent marine sediments., Mar. Ecol. Prog. Ser., 236(1), 31–35, 2002.

Morvan, J., Debenay, J.-P., Jorissen, F., Redois, F., Bénéteau, E., Delplancke, M. and Amato, A.-S.: Patchiness and life cycle of intertidal foraminifera: Implication for environmental and paleoenvironmental interpretation, Mar. Micropaleontol., 61(1–3), 131–154, doi:10.1016/j.marmicro.2006.05.009, 2006.

Mucci, A.: The solubility of calcite and aragonite in seawater at various salinities, temperatures, and one atmosphere total pressure, Am. J. Sci., 283(7), 780–799, doi:10.2475/ajs.283.7.780, 1983.

Mucci, A., Sundby, B., Gehlen, M., Arakaki, T., Zhong, S. and Silverberg, N.: The fate of carbon in continental shelf sediments of eastern Canada: a case study, Deep Sea Res. Part II Top. Stud. Oceanogr., 47(3–4), 733–760, doi:10.1016/S0967-0645(99)00124-1, 2000.

Murray, J. and Irvine, R.: XXXII.—On the Manganese Oxides and Manganese Nodules in Marine Deposits, Earth Environ. Sci. Trans. R. Soc. Edinb., 37(4), 721–742, doi:10.1017/S0080456800032816, 1895.

Murray, J. M. H., Meadows, A. and Meadows, P. S.: Biogeomorphological implications of microscale interactions between sediment geotechnics and marine benthos: a review, Geomorphology, 47(1), 15–30, doi:10.1016/S0169-555X(02)00138-1, 2002.

Nardelli, M. P., Barras, C., Metzger, E., Mouret, A., Filipsson, H. L., Jorissen, F. and Geslin, E.: Experimental evidence for foraminiferal calcification under anoxia, Biogeosciences, 11(14), 4029–4038, doi:10.5194/bg-11-4029-2014, 2014.

Négrel, P.: Multi-element Chemistry of Loire Estuary Sediments: Anthropogenic vs. Natural Sources, Estuar. Coast. Shelf Sci., 44(4), 395–410, 1997.

Négrel, P. and Grosbois, C.: Changes in chemical and 87Sr/86Sr signature distribution patterns of suspended matter and bed sediments in the upper Loire river basin (France), Chem. Geol., 156(1–4), 231–249, doi:10.1016/S0009-2541(98)00182-X, 1999.

Négrel, P., Grosbois, C. and Kloppmann, W.: The labile fraction of suspended matter in the Loire River (France): multi-element chemistry and isotopic (Rb–Sr and C–O) systematics, Chem. Geol., 166(3), 271–285, 2000.

Noffke, A., Hensen, C., Sommer, S., Scholz, F., Bohlen, L., Mosch, T., Graco, M. and Wallmann, K.: Benthic iron and phosphorus fluxes across the Peruvian oxygen minimum zone, Limnol. Oceanogr., 57(3), 851–867, doi:10.4319/lo.2012.57.3.0851, 2012.

Nomaki, H., Chikaraishi, Y., Tsuchiya, M., Toyofuku, T., Ohkouchi, N., Uematsu, K., Tame, A. and Kitazato, H.: Nitrate uptake by foraminifera and use in conjunction with endobionts under anoxic conditions, Limnol. Oceanogr., 59(6), 1879–1888, doi:10.4319/lo.2014.59.6.1879, 2014.

NRC: Basic research opportunities in earth science, National Research Council (U.S.) and Committee on Basic Research Opportunities in the Earth Sciences;National Academy Press, Washington, D.C. [online] Available from: http://site.ebrary.com/id/10071366 (Accessed 17 December 2015), 2001.

Nriagu, J. O.: Stability of vivianite and ion-pair formation in the system Fe3(PO4)2 - H3PO4 - H2O, Geochim. Cosmochim. Acta, 36(4), 459–470, 1972.

Pagès, A., Teasdale, P. R., Robertson, D., Bennett, W. W., Schäfer, J. and Welsh, D. T.: Representative measurement of two-dimensional reactive phosphate distributions and co-distributed iron(II) and sulfide in seagrass sediment porewaters, Chemosphere, 85(8), 1256–1261, doi:10.1016/j.chemosphere.2011.07.020, 2011.

Pakhomova, S. V., Hall, P. O. J., Kononets, M. Y., Rozanov, A. G., Tengberg, A. and Vershinin, A. V.: Fluxes of iron and manganese across the sediment–water interface under various redox conditions, Mar. Chem., 107(3), 319–331, doi:10.1016/j.marchem.2007.06.001, 2007.

Panieri, G., Gamberi, F., Marani, M. and Barbieri, R.: Benthic foraminifera from a recent, shallow-water hydrothermal environment in the Aeolian Arc (Tyrrhenian Sea), Mar. Geol., 218(1–4), 207–229, doi:10.1016/j.margeo.2005.04.002, 2005.

Paterson, D. M.: Short-term changes in the erodibility of intertidal cohesive sediments related to the migratory behavior of epipelic diatoms, Limnol. Oceanogr., 34(1), 223–234, 1989.

Pawlowski, J., Bolivar, I., FAHRNI, J. F., VARGAS, C. D. and Bowser, S. S.: Molecular evidence that Reticulomyxa filosa is a freshwater naked foraminifer, J. Eukaryot. Microbiol., 46(6), 612–617, 1999.

Paytan, A. and McLaughlin, K.: The Oceanic Phosphorus Cycle, Chem. Rev., 107(2), 563–576, doi:10.1021/cr0503613, 2007.

Pfeifer, K., Hensen, C., Adler, M., Wenzhfer, F., Weber, B. and Schulz, H. D.: Modeling of subsurface calcite dissolution, including the respiration and reoxidation processes of marine sediments in the region of equatorial upwelling off Gabon, Geochim. Cosmochim. Acta, 66(24), 4247–4259, 2002.

Phipps, M., Daniel: Benthic foraminifera of the Portuguese margin: Impact of organic supplies on the density, biodiversity and composition of the faunas, Université d'Angers. [online] Available from: https://tel.archives-ouvertes.fr/tel-00993121/ (Accessed 28 April 2015), 2012.

Pina-Ochoa, E., Hogslund, S., Geslin, E., Cedhagen, T., Revsbech, N. P., Nielsen, L. P., Schweizer, M., Jorissen, F., Rysgaard, S. and Risgaard-Petersen, N.: Widespread occurrence of nitrate storage and denitrification among Foraminifera and Gromiida, Proc. Natl. Acad. Sci., 107(3), 1148–1153, doi:10.1073/pnas.0908440107, 2010.

Pischedda, L., Cuny, P., Esteves, J. L., Poggiale, J.-C. and Gilbert, F.: Spatial oxygen heterogeneity in a Hediste diversicolor irrigated burrow, Hydrobiologia, 680(1), 109–124, doi:10.1007/s10750-011-0907-x, 2012.

Podda, F. and Michard, G.: Mesure colorimétrique de l'alcalinité, Comptes Rendus Académie Sci. Sér. 2 Sci. Terre Planètes, 319(6), 651–657, 1994.

Pokrovsky, O. S. and Schott, J.: Iron colloids/organic matter associated transport of major and trace elements in small boreal rivers and their estuaries (NW Russia), Chem. Geol., 190(1), 141–179, 2002.

Postma, D. and Jakobsen, R.: Redox zonation: Equilibrium constraints on the Fe (III)/SO4-reduction interface, Geochim. Cosmochim. Acta, 60(17), 3169–3175, 1996.

Poulton, S. W. and Canfield, D. E.: Development of a sequential extraction procedure for iron: implications for iron partitioning in continentally derived particulates, Chem. Geol., 214(3–4), 209–221, doi:10.1016/j.chemgeo.2004.09.003, 2005.

Poulton, S. W., Krom, M. D. and Raiswell, R.: A revised scheme for the reactivity of iron (oxyhydr)oxide minerals towards dissolved sulfide, Geochim. Cosmochim. Acta, 68(18), 3703–3715, doi:10.1016/j.gca.2004.03.012, 2004.

Poulton, S. W. and Raiswell, R.: The low-temperature geochemical cycle of iron: from continental fluxes to marine sediment deposition, Am. J. Sci., 302(9), 774–805, 2002.

Press, W. H., Flannery, B. P., Teukolsky, S. A. and Vetterling, W. T.: Numeric recipes in C: the art of scientific computing, Camb. Univ. Press Camb., 1992.

Pritchard, D.: Estuarine circulation patterns, Proceeding ASCE, 81, 1–11, 1955.

Pucci, F., Geslin, E., Barras, C., Morigi, C., Sabbatini, A., Negri, A. and Jorissen, F. J.: Survival of benthic foraminifera under hypoxic conditions: Results of an experimental study using the CellTracker Green method, Mar. Pollut. Bull., 59(8–12), 336–351, doi:10.1016/j.marpolbul.2009.08.015, 2009.

Quintana, C. O., Tang, M. and Kristensen, E.: Simultaneous study of particle reworking, irrigation transport and reaction rates in sediment bioturbated by the polychaetes Heteromastus and Marenzelleria, J. Exp. Mar. Biol. Ecol., 352(2), 392–406, doi:10.1016/j.jembe.2007.08.015, 2007.

Raiswell, R.: Towards a global highly reactive iron cycle, J. Geochem. Explor., 88(1–3), 436–439, doi:10.1016/j.gexplo.2005.08.098, 2006.

Raiswell, R.: Iron Transport from the Continents to the Open Ocean: The Aging-Rejuvenation Cycle, Elements, 7(2), 101–106, doi:10.2113/gselements.7.2.101, 2011.

Raiswell, R., Benning, L. G., Tranter, M. and Tulaczyk, S.: Bioavailable iron in the Southern Ocean: the significance of the iceberg conveyor belt, Geochem. Trans., 9(1), 7, doi:10.1186/1467-4866-9-7, 2008.

Raiswell, R. and Canfield, D. E.: The Iron Biogeochemical Cycle Past and Present, Geochem. Perspect., 1(1), 1–222, 2012.

Raiswell, R., Vu, H. P., Brinza, L. and Benning, L. G.: The determination of labile Fe in ferrihydrite by ascorbic acid extraction: methodology, dissolution kinetics and loss of solubility with age and de-watering, Chem. Geol., 278(1), 70–79, 2010.

Rantala, R. T. T. and Loring, D. H.: Determination of Lithium in the NRCC Marine Sediments: MESS-1, BCSS-1, PACS-1 and the NIST River Sediment: SRM 2704, Geostand. Newsl., 14(3), 475–476, 1990.

Rauret, G., Lopez-Sanchez, J. F., Sahuquillo, A., Rubio, R., Davidson, C., Ure, A. and Quevauviller, P.: Improvement of the BCR three step sequential extraction procedure prior to the certification of new sediment and soil reference materials, J. Environ. Monit., 1(1), 57–61, 1999.

Redfield, A. C.: On the proportions of organic derivatives in sea water and their relation to the composition of plankton, University Press of Liverpool, Liverpool, UK., 1934.

Regnier, P. and Wollast, R.: Distribution of trace metals in suspended matter of the Scheldt estuary, Mar. Chem., 43(1–4), 3–19, doi:10.1016/0304-4203(93)90212-7, 1993.

Rehm, E.: The distribution of phosphorus in the Weser river estuary, Environ. Technol., 6(1–11), 53–64, 1985.

Revsbech, N. P. and Glud, R. N.: Biosensor for laboratory and lander-based analysis of benthic nitrate plus nitrite distribution in marine environments, Limnol. Oceanogr. Methods, 7(11), 761–770, doi:10.4319/lom.2009.7.761, 2009.

Revsbech, N. P., SøRensen, J., Blackburn, T. H. and Lomholt, J. P.: Distribution of oxygen in marine sediments measured with microelectrodes, Limnol. Oceanogr., 25(3), 403–411, doi:10.4319/lo.1980.25.3.0403, 1980.

Richter, G.: Beobachtungen zur O¨ kologie einiger Foraminiferen des Jade Gebietes, Nat. Volk, 91, 163–170, 1961.

Rickard, D.: The solubility of FeS, Geochim. Cosmochim. Acta, 70(23), 5779–5789, doi:10.1016/j.gca.2006.02.029, 2006.

Riisgård, H. U. and Larsen, P. S.: Water pumping and analysis of flow in burrowing zoobenthos: an overview, Aquat. Ecol., 39(2), 237–258, doi:10.1007/s10452-004-1916-x, 2005.

Rijkenberg, M. J. A., Gerringa, L. J. A., Timmermans, K. R., Fischer, A. C., Kroon, K. J., Buma, A. G. J., Wolterbeek, B. T. and de Baar, H. J. W.: Enhancement of the reactive iron pool by marine diatoms, Mar. Chem., 109(1–2), 29–44, doi:10.1016/j.marchem.2007.12.001, 2008.

Risgaard-Petersen, N., Langezaal, A. M., Ingvardsen, S., Schmid, M. C., Jetten, M. S. M., Op den Camp, H. J. M., Derksen, J. W. M., Piña-Ochoa, E., Eriksson, S. P., Peter Nielsen, L., Peter Revsbech, N., Cedhagen, T. and van der Zwaan, G. J.: Evidence for complete denitrification in a benthic foraminifer, Nature, 443(7107), 93–96, doi:10.1038/nature05070, 2006.

Robbins, J. A. and Callender, E.: Diagenesis of manganese in Lake Michigan sediments, Am. J. Sci., 275(5), 512–533, doi:10.2475/ajs.275.5.512, 1975.

Robert, S., Blanc, G., Schäfer, J., Lavaux, G. and Abril, G.: Metal mobilization in the Gironde Estuary (France): the role of the soft mud layer in the maximum turbidity zone, Mar. Chem., 87(1–2), 1–13, doi:10.1016/S0304-4203(03)00088-4, 2004.

Robertson, D., Teasdale, P. R. and Welsh, D. T.: A novel gel-based technique for the high resolution, two-dimensional determination of iron (II) and sulfide in sediment, Limnol. Oceanogr. Methods, 6(10), 502–512, doi:10.4319/lom.2008.6.502, 2008.

Robertson, D., Welsh, D. T. and Teasdale, P. R.: Investigating biogenic heterogeneity in coastal sediments with two-dimensional measurements of iron(II) and sulfide, Environ. Chem., 6(1), 60–69, 2009.

Rootare, H. M., Deitz, V. R. and Carpenter, F. G.: Solubility product phenomena in hydroxyapatite-water systems, J. Colloid Sci., 17(3), 179–206, 1962.

Rose, A. L. and David Waite, T.: Reconciling kinetic and equilibrium observations of iron(III) solubility in aqueous solutions with a polymer-based model, Geochim. Cosmochim. Acta, 71(23), 5605–5619, doi:10.1016/j.gca.2007.02.024, 2007.

Round, F.: The ecology of benthic algae, in Algae and man, pp. 138–184, Springer., 1964.

Røy, H., Huettel, M. and Jørgensen, B. B.: The influence of topography on the functional exchange surface of marine soft sediments, assessed from sediment topography measured in situ, Limnol. Oceanogr., 50(1), 106–112, 2005.

Rueler, J. G. and Ades, D. R.: The role of iron nutrition in photosynthesis and nitrogen assimilation in Scenedesmus quadricauda(Chlorophyceae), J. Phycol., 23(3), 452–457, 1987.

Ruttenberg, K. C.: Development of a sequential extraction method for different forms of phosphorus in marine sediments, Limnol. Oceanogr., 37(7), 1460–1482, 1992.

Ruttenberg, K. C.: 8.13 - The Global Phosphorus Cycle, in Treatise on Geochemistry, edited by H. D. H. K. Turekian, pp. 585–643, Pergamon, Oxford. [online] Available from: http://www.sciencedirect.com/science/article/pii/B0080437516081536 (Accessed 11 December 2015), 2003.

Ryther, J. H. and Dunstan, W. M.: Nitrogen, phosphorus, and eutrophication in the coastal marine environment, Science, 171(3975), 1008–1013, 1971.

Saffert, H. and Thomas, E.: Living foraminifera and total populations in salt marsh peat cores: Kelsey Marsh (Clinton, CT) and the Great Marshes (Barnstable, MA), Mar. Micropaleontol., 33(3–4), 175–202, doi:10.1016/S0377-8398(97)00035-2, 1998.

Saliot, A., Tronczynski, J., Scribe, P. and Letolle, R.: The application of isotopic and biogeochemical markers to the study of the biochemistry of organic matter in a macrotidal estuary, the Loire, France, Estuar. Coast. Shelf Sci., 27(6), 645–669, doi:10.1016/0272-7714(88)90073-X, 1988.

Santner, J., Larsen, M., Kreuzeder, A. and Glud, R. N.: Two decades of chemical imaging of solutes in sediments and soils – a review, Anal. Chim. Acta, doi:10.1016/j.aca.2015.02.006, 2015.

Santschi, P. H., Anderson, R. F., Fleisher, M. Q. and Bowles, W.: Measurements of diffusive sublayer thicknesses in the ocean by alabaster dissolution, and their implications for the measurements of benthic fluxes, J. Geophys. Res., 96(C6), 10641, doi:10.1029/91JC00488, 1991.

Sarazin, G., Michard, G. and Prevot, F.: A rapid and accurate spectroscopic method for alkalinity measurements in sea water samples, Water Res., 33(1), 290–294, doi:10.1016/S0043-1354(98)00168-7, 1999.

Savitzky, A. and Golay, M. J. E.: Smoothing and Differentiation of Data by Simplified Least Squares Procedures., Anal. Chem., 36(8), 1627–1639, doi:10.1021/ac60214a047, 1964.

Schnetger, B. and Lehners, C.: Determination of nitrate plus nitrite in small volume marine water samples using vanadium(III)chloride as a reduction agent, Mar. Chem., 160, 91–98, doi:10.1016/j.marchem.2014.01.010, 2014.

Schubel, J. and Kennedy, V.: Estuary as a Filter: An Introduction, Estuary Filter Acad. Press Orlando FL 1984 P 1-11 10 Ref, 1984.

Sen Gupta, B. K.: Modern foraminifera, Kluwer Academic Publishers, Dordrecht; Boston. [online] Available from: http://public.eblib.com/EBLPublic/PublicView.do?ptiID=197729 (Accessed 22 April 2014), 1999.

Senn, A.-C., Kaegi, R., Hug, S. J., Hering, J. G., Mangold, S. and Voegelin, A.: Composition and structure of Fe(III)-precipitates formed by Fe(II) oxidation in water at near-neutral pH: Interdependent effects of phosphate, silicate and Ca, Geochim. Cosmochim. Acta, 162, 220–246, doi:10.1016/j.gca.2015.04.032, 2015.

Severmann, S., McManus, J., Berelson, W. M. and Hammond, D. E.: The continental shelf benthic iron flux and its isotope composition, Geochim. Cosmochim. Acta, 74(14), 3984–4004, doi:10.1016/j.gca.2010.04.022, 2010.

Sholkovitz, E.: Interstitial water chemistry of the Santa Barbara Basin sediments, Geochim. Cosmochim. Acta, 37(9), 2043–2073, doi:10.1016/0016-7037(73)90008-2, 1973.

Sholkovitz, E. R.: Flocculation of dissolved organic and inorganic matter during the mixing of river water and seawater, Geochim. Cosmochim. Acta, 40(7), 831–845, doi:10.1016/0016-7037(76)90035-1, 1976.

Sholkovitz, E. R.: The flocculation of dissolved Fe, Mn, Al, Cu, Ni, Co and Cd during estuarine mixing, Earth Planet. Sci. Lett., 41(1), 77–86, doi:10.1016/0012-821X(78)90043-2, 1978.

Sholkovitz, E. R., Shaw, T. J. and Schneider, D. L.: The geochemistry of rare earth elements in the seasonally anoxic water column and porewaters of Chesapeake Bay, Geochim. Cosmochim. Acta, 56(9), 3389–3402, 1992.

Shuttleworth, S. M., Davison, W. and Hamilton-Taylor, J.: Two-Dimensional and Fine Structure in the Concentrations of Iron and Manganese in Sediment Pore-Waters, Environ. Sci. Technol., 33(23), 4169–4175, doi:10.1021/es990184l, 1999.

Simmons, H. B.: Some effect of uplet discharge on estuarine hydraulics, Proceeding Soc CIv Engin, 81, 1–20, 1955.

Slomp, C. P., Epping, E. H., Helder, W. and Raaphorst, W. V.: A key role for iron-bound phosphorus in authigenic apatite formation in North Atlantic continental platform sediments, J. Mar. Res., 54(6), 1179–1205, 1996.

Slomp, C. P., Thomson, J. and de Lange, G. J.: Controls on phosphorus regeneration and burial during formation of eastern Mediterranean sapropels, Mar. Geol., 203(1–2), 141–159, doi:10.1016/S0025-3227(03)00335-9, 2004.

Snider, L. J., Burnett, B. R. and Hessler, R. R.: The composition and distribution of meiofauna and nanobiota in a central North Pacific deep-sea area, Deep Sea Res. Part Oceanogr. Res. Pap., 31(10), 1225–1249, doi:10.1016/0198-0149(84)90059-1, 1984.

Soetaert, K. E. R., Petzoldt, T. and Setzer, R. W.: Solving differential equations in R: package deSolve, J. Stat. Softw., 33 [online] Available from: http://depot.knaw.nl/6480/ (Accessed 15 June 2015), 2010.

Soetaert, K., Hofmann, A. F., Middelburg, J. J., Meysman, F. J. R. and Greenwood, J.: The effect of biogeochemical processes on pH, Mar. Chem., 105(1–2), 30–51, doi:10.1016/j.marchem.2006.12.012, 2007.

Soetaert, K. and Meysman, F.: Reactive transport in aquatic ecosystems: Rapid model prototyping in the open source software R, Environ. Model. Softw., 32, 49–60, doi:10.1016/j.envsoft.2011.08.011, 2012.

SOGREAH: développement et éxploitation d'un modèle hydrosédimentaire en trois dimensions sur l'estuaire de la Loire, SOGREAH consultants. [online] Available from: http://www.loire-estuaire.org/upload/espace/1/outils/modeles_hydro_sedimentaires/rapport_sogreah_R10.pdf (Accessed 30 July 2015), 2010.

Sørensen, J., Jørgensen, B. B. and Revsbech, N. P.: A comparison of oxygen, nitrate, and sulfate respiration in coastal marine sediments, Microb. Ecol., 5(2), 105–115, doi:10.1007/BF02010501, 1979.

Spiteri, C., Cappellen, P. V. and Regnier, P.: Surface complexation effects on phosphate adsorption to ferric iron oxyhydroxides along pH and salinity gradients in estuaries and coastal aquifers, Geochim. Cosmochim. Acta, 72(14), 3431–3445, doi:10.1016/j.gca.2008.05.003, 2008.

Steefel, C. I. and Van Cappellen, P.: A new kinetic approach to modeling water-rock interaction: The role of nucleation, precursors, and Ostwald ripening, Geochim. Cosmochim. Acta, 54(10), 2657–2677, doi:10.1016/0016-7037(90)90003-4, 1990.

Stief, P.: Stimulation of microbial nitrogen cycling in aquatic ecosystems by benthic macrofauna: mechanisms and environmental implications, Biogeosciences, 10(12), 7829–7846, doi:10.5194/bg-10-7829-2013, 2013.

de Stigter, H. C., van der Zwaan, G. J. and Langone, L.: Differential rates of benthic foraminiferal test production in surface and subsurface sediment habitats in the southern Adriatic Sea, Palaeogeogr. Palaeoclimatol. Palaeoecol., 149(1–4), 67–88, doi:10.1016/S0031-0182(98)00193-X, 1999.

Stockdale, A., Davison, W. and Zhang, H.: Micro-scale biogeochemical heterogeneity in sediments: A review of available technology and observed evidence, Earth-Sci. Rev., 92(1–2), 81–97, doi:10.1016/j.earscirev.2008.11.003, 2009.

Stockdale, A., Davison, W. and Zhang, H.: Formation of iron sulfide at faecal pellets and other microniches within suboxic surface sediment, Geochim. Cosmochim. Acta, 74(9), 2665–2676, doi:10.1016/j.gca.2010.02.005, 2010.

Strickland, J. D. H. and Parsons, T. R.: A practical handbook of seawater analysis, Fisheries Research Board of Canada., 1972.

Stumm, W.: Chemistry of the solid-water interface: processes at the mineral-water and particle-water interface in natural systems, 1992.

Stumm, W., Morgan, J. J. and Black, A.: Chemical aspects of coagulation [with discussion], J. Am. Water Works Assoc., 971–994, 1962.

Sundby, B., Anderson, L. G., Hall, P. O., Iverfeldt, Â. and Westerlund, S. F.: The effect of oxygen on release and uptake of cobalt, manganese, iron and phosphate at the sediment-water interface, Geochim. Cosmochim. Acta, 50(6), 1281–1288, 1986.

Sundby, B., Gobeil, C., Silverberg, N. and Mucci, A.: The phosphorus cycle in coastal marine sediments, Limnol Ocean., 37(6) [online] Available from: http://avto.aslo.info/lo/toc/vol_37/issue_6/1129.pdf (Accessed 2 October 2014), 1992.

Sundby, B. and Silverberg, N.: Manganese fluxes in the benthic boundary layer, Limnol. Oceanogr., 30(2), 372–381, doi:10.4319/lo.1985.30.2.0372, 1985.

Taillefert, M., Bono, A. B. and Luther, G. W.: Reactivity of Freshly Formed Fe(III) in Synthetic Solutions and (Pore)Waters: Voltammetric Evidence of an Aging Process, Environ. Sci. Technol., 34(11), 2169–2177, doi:10.1021/es990120a, 2000.

Tebo, B. M. and Obraztsova, A. Y.: Sulfate-reducing bacterium grows with Cr (VI), U (VI), Mn (IV), and Fe (III) as electron acceptors, FEMS Microbiol. Lett., 162(1), 193–199, 1998.

Tessier, A., Campbell, P. G. and Bisson, M.: Sequential extraction procedure for the speciation of particulate trace metals, Anal. Chem., 51(7), 844–851, 1979.

Thamdrup, B., Fossing, H. and Jørgensen, B. B.: Manganese, iron and sulfur cycling in a coastal marine sediment, Aarhus bay, Denmark, Geochim. Cosmochim. Acta, 58(23), 5115–5129, doi:10.1016/0016-7037(94)90298-4, 1994.

Theberge, S. M. and Luther, G. W.: Determination of the electrochemical properties of a soluble aqueous FeS species present in sulfidic solutions, Aquat. Geochem., 3(3), 191–211, 1997.

Thibault de Chanvalon, A., Metzger, E., Mouret, A., Cesbron, F., Knoery, J., Rozuel, E., Launeau, P., Nardelli, M. P., Jorissen, F. J. and Geslin, E.: Two-dimensional distribution of living benthic foraminifera in anoxic sediment layers of an estuarine mudflat (Loire estuary, France), Biogeosciences, 12(20), 6219–6234, doi:10.5194/bg-12-6219-2015, 2015a.

Thibault de Chanvalon, A., Metzger, E., Mouret, A., Cesbron, F., Knoery, J., Rozuel, E., Launeau, P., Nardelli, M. P., Jorissen, F. J. and Geslin, E.: Two-dimensional distribution of living benthic foraminifera in anoxic sediment layers of an estuarine mudflat (Loire estuary, France), Biogeosciences, 12(20), 6219–6234, doi:10.5194/bg-12-6219-2015, 2015b.

Thibault de Chanvalon, A., Metzger, E., Mouret, A., Geslin, E., Knoery, J. and Meysman, F. J. R.: Two dimensional mapping of iron release in marine sediments at submillimetre scale., Mar. Chem., doi:10.1016/j.marchem.2016.04.003, in press.

Thibault de Chanvalon, A., Metzger, E., Mouret, A., Rozuel, E., Geslin, E., Chiffoleau, J.-F., Knoery, J. and Brach-Papa, C.: Particles transformation through estuaries: Loire estuary, J. Sea Res., submitted.

Thibault de Chanvalon, A., Mouret, A., Geslin, E., Knoery, J., Péron, O. and Metzger, E.: Manganese, iron and phosphorus cycling in an estuarine mudflat sediment, Loire, France., J. Sea Res., submitted.

Thompson, A., Chadwick, O. A., Rancourt, D. G. and Chorover, J.: Iron-oxide crystallinity increases during soil redox oscillations, Geochim. Cosmochim. Acta, 70(7), 1710–1727, doi:10.1016/j.gca.2005.12.005, 2006.

Thomsen, L. and Altenbach, A. V.: Vertical and areal distribution of foraminiferal abundance and biomass in microhabitats around inhabited tubes of marine echiurids, Mar. Micropaleontol., 20(3–4), 303–309, doi:10.1016/0377-8398(93)90039-Z, 1993.

Thouvenin, B., Gonzalez, J. L., Chiffoleau, J. F., Boutier, B. and Le Hir, P.: Modelling Pb and Cd dynamics in the Seine estuary, Hydrobiologia, 588(1), 109–124, doi:10.1007/s10750-007-0656-z, 2007.

Thouvenin, B., Le Hir, P. and Romana, L. A.: Dissolved oxygen model in the Loire Estuary, in Changes in Fluxes in Estuaries: Implications from Science to Management, pp. 169–178, Keith R. Dyer, Robert Joseph Orth, Fredensburg, Denmark., 1994.

Travis, J. L. and Bowser, S. S.: The motility of Foraminifera, in Biology of the Foraminifera, pp. 91–155, J.J. Lee O.R. Anderson, London., 1991.

Trefry, J. H. and Presley, B. J.: Manganese fluxes from Mississippi Delta sediments, Geochim. Cosmochim. Acta, 46(10), 1715–1726, doi:10.1016/0016-7037(82)90112-0, 1982.

Turbé, A., De Toni, A., Benito, P., Lavelle, P., Lavelle, P., Camacho, N. R., Van Der Putten, W. H., Labouze, E. and Mudgal, S.: Soil biodiversity: functions, threats and tools for policy makers, [online] Available from: http://hal.ird.fr/bioemco-00560420/ (Accessed 23 December 2015), 2010.

Turner, A.: Trace-metal partitioning in estuaries: importance of salinity and particle concentration, Mar. Chem., 54(1), 27–39, 1996.

Turner, A.: Trace Metal Contamination in Sediments from U.K. Estuaries: An Empirical Evaluation of the Role of Hydrous Iron and Manganese Oxides, Estuar. Coast. Shelf Sci., 50(3), 355–371, doi:10.1006/ecss.1999.0573, 2000.

Turner, A. and Millward, G. E.: Suspended Particles: Their Role in Estuarine Biogeochemical Cycles, Estuar. Coast. Shelf Sci., 55(6), 857–883, doi:10.1006/ecss.2002.1033, 2002.

Turner, L. J. and Delorme, L. D.: Assessment of 210Pb data from Canadian lakes using the CIC and CRS models, Environ. Geol., 28(2), 78–87, 1996.

Turner, R. E., Rabalais, N. N., Justic, D. and Dortch, Q.: Global patterns of dissolved N, P and Si in large rivers, Biogeochemistry, 64(3), 297–317, 2003.

Tyrrell, T.: The relative influences of nitrogen and phosphorus on oceanic primary production, Nature, 400(6744), 525–531, doi:10.1038/22941, 1999.

Tyrrell, T. and Law, C. S.: Low nitrate:phosphate ratios in the global ocean, Nature, 387(6635), 793–796, doi:10.1038/42915, 1997.

Vader, W. J. M.: A preliminary investigation into the reactions of the infauna of the tidal flats to tidal fluctuations in water level, Neth. J. Sea Res., 2(2), 189–222, doi:10.1016/0077-7579(64)90009-2, 1964.

Van Cappellen, P. and Wang, Y.: Cycling of iron and manganese in surface sediments; a general theory for the coupled transport and reaction of carbon, oxygen, nitrogen, sulfur, iron, and manganese, Am. J. Sci., 296(3), 197–243, 1996.

Van der Zee, C., Roberts, D. R., Rancourt, D. G. and Slomp, C. P.: Nanogoethite is the dominant reactive oxyhydroxide phase in lake and marine sediments, Geology, 31(11), 993–996, doi:10.1130/G19924.1, 2003.

Van der Zwaan, G. J., Duijnstee, I. A. P., den Dulk, M., Ernst, S. R., Jannink, N. T. and Kouwenhoven, T. J.: Benthic foraminifers: proxies or problems?: A review of paleocological concepts, Earth-Sci. Rev., 46(1–4), 213–236, doi:10.1016/S0012-8252(99)00011-2, 1999.

Van der Zwaan, G. J. V. D. and Jorissen, F. J.: Biofacial patterns in river-induced shelf anoxia, Geol. Soc. Lond. Spec. Publ., 58(1), 65–82, doi:10.1144/GSL.SP.1991.058.01.05, 1991.

Van Leussen, W.: Aggregation of particles, settling velocity of mud flocs a review, in Physical processes in estuaries, pp. 347–403, Springer., 1988.

Viers, J., Dupré, B., Braun, J.-J., Deberdt, S., Angeletti, B., Ngoupayou, J. N. and Michard, A.: Major and trace element abundances, and strontium isotopes in the Nyong basin rivers (Cameroon): constraints on chemical weathering processes and elements transport mechanisms in humid tropical environments, Chem. Geol., 169(1), 211–241, 2000.

Viers, J., Dupré, B. and Gaillardet, J.: Chemical composition of suspended sediments in World Rivers: New insights from a new database, Sci. Total Environ., 407(2), 853–868, doi:10.1016/j.scitotenv.2008.09.053, 2009.

Volkenborn, N., Meile, C., Polerecky, L., Pilditch, C. A., Norkko, A., Norkko, J., Hewitt, J. E., Thrush, S. F., Wethey, D. S. and Woodin, S. A.: Intermittent bioirrigation and oxygen dynamics in permeable sediments: An experimental and modeling study of three tellinid bivalves, J. Mar. Res., 70(6), 794–823, 2012.

Volkenborn, N., Polerecky, L., Wethey, D. S. and Woodin, S. A.: Oscillatory porewater bioadvection in marine sediments induced by hydraulic activities of *Arenicola marina*, Limnol. Oceanogr., 55(3), 1231–1247, doi:10.4319/lo.2010.55.3.1231, 2010.

Von Gunten, U. and Schneider, W.: Primary products of the oxygenation of iron (II) at an oxic—anoxic boundary: Nucleation, aggregation, and aging, J. Colloid Interface Sci., 145(1), 127–139, 1991.

Waeles, M., Riso, R. D., Cabon, J.-Y., Maguer, J.-F. and L'Helguen, S.: Speciation of dissolved copper and cadmium in the Loire estuary and over the North Biscay continental shelf in spring, Estuar. Coast. Shelf Sci., 84(1), 139–146, doi:10.1016/j.ecss.2009.06.011, 2009.

Waeles, M., Riso, R. D., Maguer, J.-F. and Le Corre, P.: Distribution and chemical speciation of dissolved cadmium and copper in the Loire estuary and North Biscay continental shelf, France, Estuar. Coast. Shelf Sci., 59(1), 49–57, doi:10.1016/j.ecss.2003.07.009, 2004.

Waite, T. D. and Morel, F. M.: Photoreductive dissolution of colloidal iron oxides in natural waters, Environ. Sci. Technol., 18(11), 860–868, 1984.

Walling, D. E., Owens, P. N., Waterfall, B. D., Leeks, G. J. L. and Wass, P. D.: The particle size characteristics of fluvial suspended sediment in the Humber and Tweed catchments, UK, Sci. Total Environ., 251–252, 205–222, doi:10.1016/S0048-9697(00)00384-3, 2000.

Wang, F., Tessier, A. and Hare, L.: Oxygen measurements in the burrows of freshwater insects, Freshw. Biol., 46(3), 317–327, 2001.

Wang, Y. and Van Cappellen, P.: A multicomponent reactive transport model of early diagenesis: Application to redox cycling in coastal marine sediments, Geochim. Cosmochim. Acta, 60(16), 2993–3014, 1996.

Watson, P. G., Frickers, P. E. and Howland, R. J. M.: Benthic fluxes of nutrients and some trace metals in the Tamar Estuary, SW England, Netherland J. Aquat. Ecol., 27(2–4), 135–146, 1993.

Wells, M. L. and Goldberg, E. D.: The distribution of colloids in the North Atlantic and Southern Oceans, Limnol. Oceanogr., 39(2), 286–302, 1994.

Wenzhofer, F. and Glud, R. N.: Small-scale spatial and temporal variability in coastal benthic O2 dynamics: Effects of fauna activity, Limnol. Oceanogr., 49, 1471–1481, 2004.

Wheatcroft, R. A.: Time-series measurements of macrobenthos abundance and sediment bioturbation intensity on a flood-dominated shelf, Prog. Oceanogr., 71(1), 88–122, doi:10.1016/j.pocean.2006.06.002, 2006.

Wheatcroft, R. A., Jumars, P. A., Smith, C. R. and Nowell, A. R. M.: A mechanistic view of the particulate biodiffusion coefficient: step lengths, rest periods and transport directions, J. Mar. Res., 48(1), 177–207, 1990.

Widdows, J. and Brinsley, M.: Impact of biotic and abiotic processes on sediment dynamics and the consequences to the structure and functioning of the intertidal zone, J. Sea Res., 48(2), 143–156, 2002.

Williams, J., Jaquet, J. and Thomas, R.: Forms of phosphorus in the surficial sediments of Lake Erie, J. Fish. Board Can., 33(3), 413–429, 1976.

Wolanski, E.: Estuarine ecohydrology, Elsevier., 2007.

Wood, E. D., Armstrong, F. a. J. and Richards, F. A.: Determination of nitrate in sea water by cadmium-copper reduction to nitrite, J. Mar. Biol. Assoc. U. K., 47(1), 23–31, doi:10.1017/S002531540003352X, 1967.

Wood, P. A.: Controls of variation in suspended sediment concentration in the River Rother, West Sussex, England, Sedimentology, 24(3), 437–445, 1977.

Wu, J., Boyle, E., Sunda, W. and Wen, L.-S.: Soluble and colloidal iron in the oligotrophic North Atlantic and North Pacific, Science, 293(5531), 847–849, 2001.

Wu, J., Jelinski, D. E., Luck, M. and Tueller, P. T.: Multiscale Analysis of Landscape Heterogeneity: Scale Variance and Pattern Metrics, Geogr. Inf. Sci., 6(1), 6–19, doi:10.1080/10824000009480529, 2000.

Wu, J. and Li, H.: Concepts of scale and scaling, in Scaling and uncertainty analysis in ecology, pp. 3–15, Springer. [online] Available from: http://link.springer.com/content/pdf/10.1007/1-4020-4663-4_1.pdf (Accessed 22 September 2015), 2006.

Wu, J. and Luther, G. W.: Size-fractionated iron concentrations in the water column of the western North Atlantic Ocean, Limnol. Oceanogr., 39(5), 1119–1129, 1994.

Yamada, H. and Kayama, M.: Distribution and dissolution of several forms of phosphorus in coastal marine-sediments, Oceanol. Acta, 10(3), 311–321, 1987.

Yoshida, M., Kuma, K., Iwade, S., Isoda, Y., Takata, H. and Yamada, M.: Effect of aging time on the availability of freshly precipitated ferric hydroxide to coastal marine diatoms, Mar. Biol., 149(2), 379–392, doi:10.1007/s00227-005-0187-y, 2006.

Zhang, H. and Davison, W.: Diffusional characteristics of hydrogels used in DGT and DET techniques, Anal. Chim. Acta, 398(2), 329–340, 1999.

Zhang, J.-Z., Fischer, C. J. and Ortner, P. B.: Potential availability of sedimentary phosphorus to sediment resuspension in Florida Bay., Glob. Biogeochem. Cycles, 18(4), n/a-n/a, doi:10.1029/2004GB002255, 2004.

Zhang, J.-Z., Guo, L. and Fischer, C. J.: Abundance and Chemical Speciation of Phosphorus in Sediments of the Mackenzie River Delta, the Chukchi Sea and the Bering Sea: Importance of Detrital Apatite, Aquat. Geochem., 16(3), 353–371, doi:10.1007/s10498-009-9081-4, 2010.

Zhu, Q. and Aller, R. C.: A rapid response, planar fluorosensor for measuring two-dimensional pCO2 distributions and dynamics in marine sediments, Limnol. Oceanogr. Methods, 8, 326–336, doi:10.4319/lom.2010.8.326, 2010.

Zhu, Q. and Aller, R. C.: Two-dimensional dissolved ferrous iron distributions in marine sediments as revealed by a novel planar optical sensor, Mar. Chem., 136–137, 14–23, doi:10.1016/j.marchem.2012.04.002, 2012.

Zhu, Q., Aller, R. C. and Fan, Y.: Two-dimensional pH distributions and dynamics in bioturbated marine sediments, Geochim. Cosmochim. Acta, 70(19), 4933–4949, doi:10.1016/j.gca.2006.07.033, 2006.

Zorn, M. E., Lalonde, S. V., Gingras, M. K., Pemberton, S. G. and Konhauser, K. O.: Microscale oxygen distribution in various invertebrate burrow walls, Geobiology, 4(2), 137–145, doi:10.1111/j.1472-4669.2006.00074.x, 2006.

Zwolsman, J. J. G. and van Eck, G. T. M.: Geochemistry of major elements and trace metals in suspended matter of the Scheldt estuary, southwest Netherlands, Mar. Chem., 66(1–2), 91–111, doi:10.1016/S0304-4203(99)00026-2, 1999.

Zwolsman, J. J. G. and Van Eck, G. T. M.: Dissolved and particulate trace metal geochemistry in the Scheldt estuary, SW Netherlands (water column and sediments), Netherland J. Aquat. Ecol., 27(2–4), 287–300, 1993.

Tables

Table 1 Spéciation moyenne du fer solide dans les matière en suspension des rivière (n = 34), en océan côtier (profondeur < 1000 m; n = 46) et en océan profond (profondeur > 1000 m; n = 56) ; Poulton et Raiswell 2002. 19

Table 2 Réactions biochimiques et physiques principales se déroulant dans les 20 premiers centimètres de la colonne sédimentaire. Ces équations sont issues des travaux de Froelich et al. (1979) et Lovley (1991) et ont été modifiées par Mucci et al. (2000) et Soetaert et al. (2007) ; elles supposent une oxydation complète de la matière organique (production de CO_2), elles ne prennent pas en compte la nitrification de l'ammoniac produit (représenté ici par l'acide associé, majoritaire en milieu océanique, l'ammonium), supposent une dissolution totale du CO_2 (pas de formation de bulles par exemple) et représentent la somme des espèce de carbone inorganique dissous par HCO_3^- (dont l'équilibre instantané avec $CO_{2(d)}$, CO_3^{2-} et H_2CO_3 est fonction de la salinité, de la température et du pH). Les variations de pH (dpH) sont calculées pour les conditions suivantes: pH=8,2, T=25°C, S=35, p= 1atm, γ^N = 0,156 et γ^P = 0,0094 (stœchiométrie de Redfield). ΔTA indique la variation d'alcalinité total. Soetaert et al., 2007. 20

Table 3 Estimation of uncertainties from numerical reconstruction by the Mean Reconstruction Bias (MRB; Eq. 9) for the misfit between the "true" concentration, diffusive flux and production rate values and the "reconstructed" concentration, flux and rate values. Maximum values for diffusive flux and production rate (in bold) defined the uncertainty due to numerical reconstruction (Table 5). 74

Table 4 Estimation of uncertainties from parameters sensitivity. Parameter uncertainties (1st column) are represented by the vertical branch of red crosses from Fig.44. The uncertainties induced on the characteristic flux and on the characteristic production rate correspond to the vertical branch of the Fig.44 and are indicated in the 2nd and 3rd column. The overall uncertainties from parameters sensitivity are calculated by quadratic sum and are reported in the Table 5. 79

Table 5 Overall estimation of the SGF procedure uncertainties. Uncertainty from numerical reconstruction and parameter sensitivity are from Table 3 and Table 4 respectively. Uncertainty for surface topography is from Røy et al. (2005) and uncertainty for surface positioning corresponds to the relative standard deviation of the 3 transects used to calculate the diffusive flux across the SWI. The overall uncertainties are calculated by quadratic sum. 80

Table 6 Apparent production rate (APR) calculated from the production estimated by Savitzky Golay Filter procedure summed over the whole available profile of $[Mn]_d$ or $[Fe]_d$. 101

Table 7 Apparent Production Rate (APR) calculated for each 2D-DET, based on SGF procedure estimation. 117

Table 8 Summary of dataset. Al and Fe are in % and Mn in ppm of dry sediment (± 1 σ). n is the number of stations sampled for each location and each campaign. 129

Figures

Figure 1 (a) Localisation du bassin versant de la Loire (b) Carte géologique simplifié du bassin versant de la Loire, d'après Dhivert (2014). Le rectangle rouge indique la localisation de la Figure 5. 3

Figure 2 Exemple d'une année hydrologique illustrée par le débit (en bleu) et la concentration en matière en suspension ([MES] ; en noir) à Montjean-sur-Loire (entre Nantes et Angers; Gorse 2010 et DREAL Pays-de-Loire, 2015) 4

Figure 3 Evolution spatiale et annuelle des médianes mensuelles (calculées sur la période 2002-2012) de concentration de Chlorophylle a, phosphate et nitrate (Minaudo et al., 2015) 4

Figure 4 Suivi annuel de la composition des particules en suspension et du débit pour les années 1996-1997 (Grosbois et al., 2001) 5

Figure 5 Carte de l'estuaire de la Loire (géoportail, SHOM, IGN). En rouge, isocontours de salinité journalière de surface à S=30 le 20 février 2014 (trait plein) et le 7 août 2015 (pointillés) estimés par le modèle mars3D (d'après previmer.org). Le débit de la Loire à ces date est respectivement de 3000 m^3s^{-1} et de 130 m^3s^{-1} (DREAL Pays de la Loire). 6

Figure 6 Dynamique temporelle et verticale de l'influence des crues et des marées illustrées à partir : en haut, du coefficient de marée (pointillés) et des estimations de salinité (calculé à partir de la conductivité, en noir pour la « surface » et en gris en « profondeur ») et en bas, du débit (pointillés) et de la turbidité (en noir pour la « surface » et en gris en « profondeur »). Les deux capteurs sont situé à Donges et distants verticalement de 4 m (réseau SYVEL - GIP LE; DREAL Pays de la Loire). 7

Figure 7 Champs des vitesses moyennées sur un cycle de marée (dites résiduelles) caractéristiques d'un estuaire. D'après Allen et al., 1972 cité par Deloffre 2006 7

Figure 8 Enveloppe des marées (maximum et minimum de hauteur d'eau) pour: (1) en gris, faible coefficient de marée (47) fort débit (1500 $m^3.s^{-1}$) ; (2) en noir, fort coefficient (90) faible débit (240 $m^3.s^{-1}$). Sources: GPMNSN, DREAL Pays de la Loire, DDT49, DTM44, d'après le GIP Loire Estuaire (Cahier indicateur L1.A1) 8

Figure 9 (a) Représentation simplifiée de profils de concentrations le long du gradient de salinité de l'estuaire permettant d'identifier la réactivité d'un élément dissous (b) Exemple d'estimation des flux par la méthode géométrique (voir texte) à partir d'un des profils précédent. Les échelles verticales sont arbitraires. 9

Figure 10 Distribution de la MES estimée à partir d'images satellites (SPOT 4; Gernez et al., 2015) les 21 février 2013 (faible coefficient de marée, fort vent, débit maximum des 15 derniers jours: 3560 $m^3.s^{-1}$) et 28 mars 2013 (fort coefficient de marée, vent faible, débit maximum des 15 derniers jours: 1800 $m^3.s^{-1}$). Les croix indiquent la position du chenal de navigation. 10

Figure 11 Schéma conceptuel du cycle annuel d'engraissement d'une vasière, réalisé à partir du suivi d'une vasière subtidale de l'estuaire de la Seine (Lesueur et Lesourd, 1999) 11

Figure 12 Exemple de répartition estivale du microphytobenthos estival sur la vasière des Brillantes, au cours d'une vingtaine d'année. L'indicateur utilisé est le NDVI (Normalized Difference Vegetation Index) calculé à partir d'une image multispectrale du satellite SPOT (Benyoucef, 2014). Les mesures *in situ* réalisées entre 2013 et 2015, font état d'une concentration en Chl a de l'ordre de 40 à 200 $mg.m^{-2}$ sur les deux premiers millimètres de sédiment (Méléder, pers. com.).....13

Figure 13 Diagramme de l'impact du biomixing sur l'hétérogénéité, modifié d'après Meysman et al., 2008. [a] d'après Fenchel, (1996); Wenzhofer and Glud (2004), [b] d'après Alldredge and Cohen (1987); Zhu et al. (2006) [c] d'après Heinz and Geslin (2012); Nardelli et al. (2014) [d] d'après Meysman et al. (2003).....14

Figure 14 Un foraminifère benthique (*Ammonia tepida*) avec son réseau de pseudopodes (Debenay et al., 1998) 15

Figure 15 (a) Diagramme Eh-pH pour le système Fe-O-H à 25°C, 10^5 Pa et une concentration de fer dissous de 10^{-10} $mol.kg^{-1}$ d'après la base de donnée LLNL (Lawrence Livermore National Lab.) cité par Takeno (2005). (b,c) Modèle de spéciation de Fe(III) et Fe(II) dissous à S=35, en ne prenant en compte que les complexes inorganiques (Millero et al., 1995).....16

Figure 16 (a) Evolution de la teneur en fer et en carbone organique dissous (COD) lors de filtration successive d'un échantillon venant de la rivière Awout (Cameroun). Cette rivière draine un bassin versant de foret tropicale et présente un pH=4,74 et [DOC]~40$mg.L^{-1}$; Dupré et al., 1999). Les concentrations des filtrats à 0,2 µm proviennent de deux techniques de filtrations différentes. (b) Concentration de fer en fonction de la concentration en COD (Viers et al., 2000). 1200 µg L^{-1}~ 20 µmol L^{-1}.....17

Figure 17 Cycle du fer réactif d'après Raiswell (2006) en $Tg.y^{-1}$ (1 Tg = 10^{12} g). La largeur des flèches est proportionnelle au flux de fer représenté. Haese (2006) propose un flux entre l'estuaire et l'océan côtier sensiblement différent à 163-251 $Tg.y^{-1}$ (*i.e.* une perte en estuaire de 108 à 167 $Tg.y^{-1}$).....18

Figure 18 Spéciation du fer solide dans les particules en suspension de l'estuaire de Beaulieu, le fer extrait à l'hydroxylamine est en blanc, le fer total (extrait avec HF-$HClO_4$-HNO_3) est en noir, Moore et al., 1979. 19

Figure 19 (a) profile des concentration de fer dissous (<0,4 µm) dans différents océans, l'enrichissement en surface dans l'océan Atlantique est probablement lié à un apport de poussière du Sahara (Bergquist et al., 2007; Kirayama et al., 2009), (b) spéciation du fer (Wu et al., 2001; Boyle et al., 2005); cité par Boyd and Ellwood, 2010 19

Figure 20 Démonstration de l'importance de la coagulation en estuaire (Sholkovitz 1976). (a) concentration en matière humique (classe de matière organique) ayant coagulée après 30 minutes de mélange entre de l'eau de 4 rivières d'Écosse et de l'eau de mer filtrée (la portion de chacune est indiquée par la salinité), (b) idem pour le fer, les concentrations sont exprimées en µg.L (d'eau de rivière) $^{-1}$. Les concentrations en *acide humique* et en fer en amont des estuaires sont indiquées. Les concentrations de fer mesurées en amont de l'estuaire de la Loire sont généralement comprises entre 10 et 30 $\mu g.L^{-1}$ (Brach-Papa, pers. com.).....22

Figure 21 Exemple de profiles de fer dissous selon la salinité. (a) Estuaire du Connecticut (E-U) à deux périodes différentes après filtration à 0,7 µm, le caractère non conservatif n'est visible qu'en cas de très forte concentration (1 $\mu mol.L^{-1}$ ~ 56 $\mu g.L^{-1}$; Boyle 1977), la flèche rouge correspond aux concentrations mesurées en amont de l'estuaire de la Loire (Brach-Papa pers. com.) (b) Estuaire du Congo (Zaïre), chaque trait correspond à une concentration après filtration à respectivement (de haut en bas) 1,2; 0,45 ; 0,22 ; 0,05 et 0,025 µm (Figuères et al., 1978). 22

Figure 22 Profondeur de consommation des principaux oxydants dans la colonne sédimentaire après évènement de remise en suspension. Le temps nécessaire pour atteindre l'état stationnaire des réactions du fer est estimé plus long car les oxydes de fer (solide) représentent un stock plus important que les autres oxydants. Aller (2004) 23

Figure 23 (a) Modélisations de profiles typiquement observés dans la colonne sédimentaire. (b) vitesse des réactions primaires et secondaires en fonction de la profondeur. Pfeifer (2002) 24

Figure 24 Processus diagénétiques idéalisés affectant la composition en fer des particules (a) dans la condition de référence (état stationnaire, pas de perte par diffusion dans la colonne d'eau, symétrie des processus de précipitation sous forme oxidée et réduite), (b) dans une condition d'intensification de la consommation du carbone organique, (c) en cas de biodiffusion. Modifié d'après Aller (1982) 25

Figure 25 Schematic view of the "jaw device" for simultaneous sampling of sediment and pore water. 38

Figure 26 Sediment sampling methodology for living foraminiferal analyses. (a) Usual 1D hand coring and layer slicing. (b) Sediment sampling with the second jaw of the "jaw device" (Fig. 25) and representation of the sediment cubic slicing. 39

Figure 27 1D geochemical features. (a) Vertical profile of total solid organic carbon (filled circles, uncertainty smaller than symbol size) and profiles of salinity (white and grey diamonds). (b) Typical profiles of dissolved oxygen; the profile with dark-grey diamonds is considered bioturbated. (c, d, e) Vertical profiles of manganese (c), iron (d) and phosphorus (e) in dissolved (white and grey diamonds for DET replicates) and reactive solid phase (ascorbate-leached) from the core (black circles)..... 40

Figure 28 (a) Picture of the sediment plate before cube slicing for foraminiferal analysis (sediment–water interface at the top). (b) Picture of the analysed gel after colorimetric reactions: dissolved iron shown in dark pink and dissolved phosphorus in turquoise (burrows superimposed). The black rectangle corresponds to the gel limit, the blue rectangle to the limit of available data set of dissolved iron and phosphorus and the red rectangle to the limit of the available data set of foraminiferal distribution. 41

Figure 29 (a, b) Two-dimensional concentrations after numerical analysis of dissolved reactive phosphorus (DRP) and dissolved iron. The distribution of burrows is shown on the DRP plot. Red lines represent the boundary of foraminiferal analysis. (c-d) 2-D distribution of *A. tepida* densities and dissolved iron from the sediment plate with burrow distribution. 41

Figure 30 Vertical comparison of *A. tepida* densities from the two cores (filled and open triangles) and the "jaw device" sampling (each box plot represents the distribution of one layer; bars are first and third quartiles for the boxes length and whiskers are below 1.5 interquartiles; open circles are outliers). 43

Figure 31 Moran's index correlograms for 3 to 8 cm depth. (a) Moran's index correlogram for *A. tepida* with a 1 cm resolution. (b) Moran's index correlogram for [Fe]dissolved with a 1 cm resolution. An asterisk indicates significant differences from zero; error bars are twice the standard deviation. The numbers are the number of pairs for each order of neighbours. 45

Figure 32 Putative mechanisms explaining the *A. tepida* density profile (OPD: oxygen penetration depth). 47

Figure 33 Kinetics of nitrite colorimetric reaction on a gel. A: color evolution of the standard curve over time. B: extracted reflectance (green channel) from images. C: overtime profile evolution across the edge of a well (black line on the images A; 19.5 µmol L-1 NO2-) 57

Figure 34 2D nitrite concentration distribution and examples of selected profiles for a sieved and homogenized sediment of the Brillantes mudflat Loire estuary, artificially bioturbated by a 3 cm-diameter tube. Dots are data and lines are smoothed profiles. 59

Figure 35 2D nitrite (left), nitrite + reduced nitrate (middle), calculated nitrate (right) for an incubated sediment from the Brillantes mudflat, Loire estuary 60

Figure 36 2D nitrite distribution (left) and examples of selected profiles for an incubated sediment of the Brillantes mudflat, Loire estuary. Dots are data and lines smoothed profiles. 61

Figure 37 2D nitrate distribution (left) and examples of selected profiles for an incubated sediment of the Brillantes mudflat, Loire estuary. Dots are data and lines smoothed profiles. 61

Figure 38 (a) schematic view of the "jaw device" for simultaneous sampling sediment and pore water, (b) photograph of the sediment after retrieval, (c) photograph of the DET-2D gel after colorimetric reactions: dissolved iron appears in dark pink and dissolved phosphorus in turquoise, (d) concentration of dissolved iron in false colour. The analysis of the correspondences between iron and sediment is performed in Fig.45. 68

Figure 39 Savitsky-Golay filter (SGF) procedure applied on 2D synthetic datasets (a) idealized concentration distribution $C_{idealx,y}$ (white crosses on dataset 3 indicate the position of most important production patches), (b) "estimated" concentration $C_{estimatedx,y}$, (c) error on the concentration estimation $\Delta C_{x,y}$ and (d) vertical profile extracted from the middle section of C_{ideal} (red) and $C_{estimated}$ (black). 74

Figure 40 SGF procedure applied on 2D synthetic datasets: (a) idealized flux distribution $J_{xidealx,y}$, (b) "estimated" flux $J_{xestimatedx,y}$. In red: positive downward fluxes. In blue: upward fluxes, (c) error on the

downward flux estimation $\Delta Jxx,y$ and (d) vertical profile extracted from the middle section of $Jxidealx,y$ (red) and $Jxestimatedx,y$ (black).....75

Figure 41 SGF procedure applied on 2D synthetic datasets: (a) idealized reaction rate distribution $Ridealx,y$, (b) "estimated" reaction rate $Restimatedx,y$, (c) error on the reaction rate estimation $\Delta Rx,y$ and (d) vertical profile extracted from the middle section of $Ridealx,y$ (red) and $Restimatedx,y$ (black). 76

Figure 42 Two dimensional Savitzky-Golay procedure applied on experimental dataset: (a) porosity profile (triangle) and modelled exponential functions of porosity (plain line); the uncertainty on the porosity used to estimate parameter sensitivity is represented by the dotted lines, (b) experimental dataset of dissolved iron concentration in false colour, (c) estimated downward flux from SGF (downward flux in red and upward flux in blue) and (d) estimated reaction rate from SGF. 77

Figure 43 Sediment-water interface estimated flux: (a) 1D iron profile averaged over 0.5 cm thick layers extracted from the 2D iron distribution, grey area represent ±1 standard deviation; the arrow indicates the chemical gradient extracted and the corresponding flux, (b) position of the sediment water interface (SWI) in red, and the uncertainty of ±1 mm on its position (in black and blue); the corresponding averaged dissolved iron upward fluxes estimated from the 2D SGF procedure are indicated in µmol m^{-2} d^{-1} and (c) lateral variability of benthic fluxes according to the SWI position. 78

Figure 44 Sensitivity of the model to parameters uncertainty: (a-b-c) standard deviation of the production rate distribution, (d-e-f) Flux across water-sediment interface (black line) with uncertainty due to interface positioning (± 1 mm; grey area); red crosses indicate experimental parameters uncertainties (horizontal branch) and corresponding impact on modelling uncertainty (vertical branch). 79

Figure 45 (a) Photograph of the sediment plate with a centimetre grid (white dashed lines); continuous lines within pink rectangles correspond to the 3 examples of cross-sections studied (Fig. 46), (b) dissolved iron concentration in false colour with schematic representation of burrows and (c) Fe_d production rate estimated by SGF, with delimitations of active burrows' surfaces; in black, direct identification by superimposition on the sediment photograph and in white, delimitation according to the interpretation of consumption. 80

Figure 46 (a) Zoom of the photograph on the three red rectangles from the Fig. 8a: in white, the selected transect across burrow with vertical white bars identifying burrow linings, (b) Fe_d concentration (dotted line) and production rate (black line) along the selected transects with grey areas identifying burrow lumen; percentages of iron consumption inside the burrow bore relatively to the total consumption estimated on the transect are indicated.....82

Figure 47 Small scale iron recycling in a suboxic iron-rich sediment in µmol m^{-2} d^{-1}; diffusive flux (104±20) and bio-irrigational flux (410±213) across the water sediment interface are differentiated; values underlined and in italic are calculated assuming steady state. 84

Figure 48 Location of the two sampling sites. 94

Figure 49 Hydrological context of the 4 campaigns (arrows) with each time the previous flood (triangle) and the previous wind event (diamond) with gusts above 70 km h^{-1}. Black line represents daily flow, dotted and grey lines represent median flow and 20 and 80 percentile of the monthly flow. 94

Figure 50 Total organic carbon, porosity and examples of alkalinity profiles for September 2012 (open diamonds), May 2013 (grey diamonds) and February 2014 (black diamonds). Result of ^{210}Pb are only available for Site 1, February 2015. The dotted line represent the maximum row sedimentation rate of 0.16 cm yr^{-1} 96

Figure 51 Extracted Mn-oxides, dissolved Mn, extracted Fe-oxides, dissolved Fe, extracted phosphorus and dissolved phosphorus from February 2014 (black diamonds), April 2015 (t_3; dark grey diamonds), May 2013 (clear grey diamonds) and September 2012 (open diamonds). Only one dissolved profile is shown for each situation, the second is similar. There is no data for S2 in April 2015. 97

Figure 52 Extracted Mn-oxides, dissolved Mn, extracted Fe-oxides, dissolved iron, extracted phosphorus and dissolved phosphorus from the time serie in Site 1 (S1): t_0 are represented in black (only for profiles of dissolved species), t_1 in dark grey, t_2 in clear grey and t_3 with open symbols. 98

Figure 53 Examples of estimated concentration (black line) superimposed with original data set (open circles), production rate (red line; negative production corresponds to consumption) and upward flux (blue line; negative flux corresponds to downward flux) based on Savitsky-Golay Filter procedure (February. site 1). Upper boundary condition is no production. 101

Figure 54 Idealised evolution of Mn (open diamonds) and Fe (black diamonds) on the site 1. Time since the deposition event is calculated from the last flood (Fig. 2). Top: Reactive stocks (ascorbate extracted minus background concentration), error bars represent relative standard deviation of background concentrations, lines represent idealized behaviour with the corresponding rate indicated. Bottom: Apparent production rate estimated from SGF procedure, error bars are standard deviation taking account 2 replicates and ± 1 on the smoothing parameter *n*. 102

Figure 55 Evolution of Fe and P relation in the ascorbate extraction, according to depth and in the pore water. 104

Figure 56 2D distribution of Fe_d and dissolved reactif phosphorus (DRP;resolution of 200 µm x 200 µm) below the water-sediment interface (SWI) sampled during low tide and sediment emersion. Gels with similar letter are distant to less than few decimeters. 111

Figure 57 Time series of 2D distribution of Fe_d and DRP (resolution of 200 µm x 200 µm) after emersion. *In situ* incubation of gels t1, t2,t3 have begun before previous emersion. 112

Figure 58 Simultaneous sampling of sediment and pore water in two dimensions; May 2013-site2; gel c1. (a) sediment photograph; (b, c) ascorbate extraction of sediment particles on 1 cm^3 grid; (d, e) 2D DET concentration. 113

Figure 59 Estimated production rates by the SGF procedure for gel c1 (Figure 58d and Figure 58e) 114

Figure 60 Example of Fe-P relationship for gel c1 (May 2013 - site 2). a) relation between $[Fe]_{asc}$ and $[P]_{asc}$ from Fig. 3b and 3c (red: top 4 cm; green: between 4 and 8 cm; blue: between 8 and 15 cm). Linear regression is calculated on the top 8 cm. b) variation of the mean $[Fe]_{asc}/[P]_{asc}$ ratio according to depth for a layer of 1 cm-thick (error bars correspond to standard error). c) plot of $[Fe_d]$ against [DRP] (extracted from Fig. 3d and 3e; same color code). Lines are best linear regression for each 1.2 cm-thick layer (intercept are forced to zero). d) $[Fe_d]/[DRP]$ as calculated previous slopes (brackets represent $r^2 < 0.5$). e) and f) Similar representation but for Fe_{prod} and P_{prod} estimated by SGF procedure 118

Figure 61 Vertical distribution of the slope of iron and phosphorus productions obtained form different gels. Stars depend on regression coefficient value (* = $r^2 > 0,6$; *** = $r^2 > 0,8$) 119

Figure 62 Location of the sampling stations. Black crosses: downstream stations sampled during the May campaign. The dotted rectangle delineates downstream stations sampled during the September campaign. 126

Figure 63 Hydrological context of the 3 campaigns (red arrows). The black line represents daily flow. Dotted and grey lines represent median flow and 20 and 80 percentile of the monthly flow. Data source: DREAL Pays de la Loire. 127

Figure 64 Total Fe (%) vs. Al (%) and Mn (ppm) vs. Al (%) for September 2012 (triangles), May 2013 (diamonds) and February 2014 (circles). The colours correspond to location: white for downstream particles, black for upstream, clear grey for estuary and dark grey for sediment. Solid lines correspond to upstream and oceanic regression trend lines. 128

Figure 65 Sediment profiles of iron and manganese concentration extracted by ascorbate and total extraction. The grey zone represents the range of ascorbate extractions for suspended particles in the estuary (February 2014, n = 12). 129

Figure 66 Rare earth spectra normalized on PAAS spectrum and thorium concentration for end-member samples: upstream samples in black; downstream samples in blue (dark grey) and sediment samples in orange (clear grey). 130

Figure 67 REE signature according to SPM concentration and Fe_{asc} content. Sediment is represented arbitrarily with a particle concentration of 3000 mg L^{-1}. 131

Figure 68 Manganese and aluminum content of upstream SPM according to a mixing between low flow particles and high flow particles (high SPM concentration) 132

Figure 69 Relation between ascorbate and total extraction in the estuary after normalisation on Al content for (a) Fe and (b) Mn. Panel (c) correspond to a zoom of the rectangle from panel (a). 134

Figure 70 Evolution of Fe/Al ratio according to salinity for high flow campaigns (>1500 $m^3 s^{-1}$) 134

Figure 71 Fonctionnement biogéochimique de la vasière des Brillantes synthétisé à partir d'une schématisation des données obtenues lors des campagnes (de gauche à droite) de février 2015, d'avril 2016 de mai 2014 et de septembre 2013. L'oxygène ne pénètre pas à plus de 5mm et n'est pas représenté. Les fronts redox sont définis, pour Mn(IV) et Fe(III) à partir des zones de production (identifiées visuellement, Figure 51 - site 1) de l'espèce réduite et pour NO_3^- et SO_4^{2-} à partir de la consommation de Fe^{2+} ou Mn^{2+}. Les flèches verticales indiquent un flux vers la colonne d'eau dont l'importance est proportionnelle à la largeur de la flèche. Les flux de phosphate sont du même ordre de grandeur que les flux de fer dissous. De décalage de l'interface correspond à la compaction et à l'érosion progressive du sédiment.....141

Figure 72 Montage expérimental de mesure de la sensibilité des foraminifères à un gradient chimique. a – un couloir (de longueur d) rempli d'eau représente l'environnement des foraminifères qui sont positionnées en ligne, au milieu en début d'expérience. Le couloir est connecté à deux réservoirs fixant les conditions aux limites. Un système de photographie automatisé permet de suivre la position des foraminifères au cours du temps. b - Au temps t_0, la concentration de l'un des réservoirs est modifié de C_0 à C_1, ce qui créé un gradient chimique. c – un état transitoire permet à la concentration dans le couloir d'augmenter jusqu'à son état d'équilibre à $t_{eq,}$ décrit par une diminution linéaire d'une concentration C_1 au niveau du réservoir 1 jusqu'à une concentration C_0 au niveau du réservoir 0. 143

Figure 73 Bilan annuel du cycle du fer à l'échelle de l'estuaire, les large flèches grises indiquent des flux de particules avec l'évolution de leur composition en oxydes de fer depuis leur entrée dans l'estuaire (indiqué par Δ). Les doubles flèches représentent les flux de fer estimés sous forme particulaire ou dissoute. A part le débit moyen annuel en MES (souligné), les données proviennes toutes de cette thèse. 145

Annexes

Annexe 1

Solid geochemistry

The two cores were used to constrain geochemistry. They were stored at *in situ* temperature until processing, and were processed in a field laboratory. The first core was dedicated to solid phase geochemistry and microelectrode profiling (see section 2.2.3). The solid phase was characterized by total organic carbon, reactive iron, manganese and phosphorus. After profiling, the core was sub-sampled using a tube of 3 cm diameter and sliced every 2 mm until 2 cm and every 5 mm until 5 cm depth (Fig 2 A). After slicing, samples were immediately frozen with dry ice. Within a week, sampled were freeze-dried, the weight difference before and after freeze-drying served to calculate porosity. Next, samples were manually ground using an agate mortar and separated into two aliquots for chemical analyses.

The first aliquot of freeze-dried sediment (between 50 and 150 mg) was incubated in 10 mL of a solution of ascorbic acid (buffered at pH 8) during 24 hours to extract the reactive solid phase. This technique is commonly used (Kostka and Luther, 1995; Anschutz et al., 1998; Hyacinthe et al., 2001; Hyacinthe and Van Cappellen, 2004) and allows to extract both amorphous Fe(III) oxyhydroxides (Kostka and Luther, 1994) supposedly close to those reduced by microorganisms (Hyacinthe et al., 2006) as well as Mn(III) and Mn(IV) oxides (Anschutz et al., 2005). After extraction, samples were centrifuged (15 mn at 3000 rpm) and the supernatant was diluted in Ultrapure© HCl (1% weight). Next, samples were analyzed on ICP-AES (Thermo Scientific iCAP 6300 Radial), uncertainty is 1, 8 and 4% for respectively iron, phosphorus and manganese (twice the relative standard deviation of ICP-AES triplicates). The second aliquot, between 1.5 and 3 mg, was used for organic carbon analysis. It was performed on EA1110 CHN/S/O (Thermo Fisher) after 1h-extraction in a HCl saturated atmosphere. Each chromatograph was inspected visually. Accuracy was verified with standards (MS-61 and B2150) and incertitude, calculated from standard deviation for ten replicates from standard MS-61, was 4.5%.

Annexe 2

1D Pore water analysis

Oxygen, dissolved iron, manganese and phosphorus were analyzed. The core dedicated to oxygen profiling and solid phase remained emerged in the *in situ* temperature tank. The sediment water interface was roughly visually estimated during profiling. During data treatment, the interface was repositioned according to the break visible in the O_2 profile after the start of the concentration decrease. 18 oxygen profiles (each time two profiles were measured simultaneously) were realized using Clark's type electrodes (50µm tip diameter) mounted on an automated micromanipulator (Unisense©, Denmark) within the first 5 mm at a 100 µm vertical resolution. Profiling was done within 1 hour after sampling.

Diffusive Equilibrium in Thin film in one dimension probes (DET 1D, adapted from Davison and Zhang, 1994; Krom et al., 1994) were used for dissolved iron, manganese and phosphorus. Two probes were prepared from DGT-Research© supports, less than one week before deployment. Each support corresponds to 75 cells of 22 µL and has a vertical resolution of 2 mm. They were cleaned during 1 week using 10 % Suprapur Merck nitric acid and rinsed three time with milli-Q water (Millipore©). A solution (1.5% w/w) of agarose in Milli-Q water was poured into the probe, the excess gel was removed with a Teflon-coated razor blade and then covered with a PVDF hydrophilic membrane (0.2 µm size pore, Millipore©) (Metzger et al., 2007, 2014). Each probe was conserved in a wet clean plastic bag and finally bubbled with N_2 during 6h before deployment in the third core. After one night incubation in the core at *in situ* temperature, probes were retrieved and DET gel pieces were sampled using a small plastic tip and eluted in 5mL of a 0.01 mol L^{-1} suprapur© Merck nitric acid solution (dilution factor of the pore water of about 200). Iron, manganese and phosphorus were then analyzed by ICP-AES (Thermo Scientific iCAP 6300 Radial). Sodium was supposed constant through the sediment column, and used as internal standard. Incertitude is less than 10% for dissolved iron and manganese and 30% for phosphorus.

Annexe 3

2D pore water analysis

The DET 2D probe was analyzed in order to obtain the concentrations of dissolved iron, dissolved reactive phosphate (DRP) and the qualitative distribution of H_2S (Cesbron et al., 2014). The 2D DET probe was unfrozen during 10 minutes at ambient temperature; next, the plastic-coated aluminum plate was taken out and the polyacrylamide thin-film was taken off. The PVC adhesive film was scanned with a common commercial flatbed scanner (Canon Canoscan LiDE 600F) and analyzed in blue intensity (from RGB decomposition) with ImageJ© software. The unfrozen gel is laid on a white board and recovered by a reactive gel. The reactive gel was a 0.46mm thick polyacrylamide gel incubated during 1 hour in a reactive solution containing ascorbic acid 3 10^{-2}M, sulfuric acid 5.58 10^{-1}M, potassium antimony(III) tartrate hydrate 3.2 10^{-4}M, ammonium molybdate tetrahydrate 1.86 10^{-2}M and ferrozine 1.22 10^{-2}M, final concentrations. This is an improvement compared to Cesbron (2014) as only one reactive gel is made, instead of two, reducing handling time considerably.

Twenty five minutes after contact, a picture (reflectance analysis) of superposed gels was taken with a hyperspectral camera (HySpex VNIR 1600) and analyzed with the software ENVI (Environment for Visualizing Image, RSI) to obtain DRP and dissolved iron concentrations. The resolution (length of pixels) was 211*216µm^2. The HySpex VNIR 1600 camera is sensitive to 160 channels (spectral resolution of 4.5 nm), which is much more precise than the three channels of 100 nm resolution from standard RGB (Red, Green, Blue) images. Standards, made following (Cesbron et al., 2014) gave one end-member spectrum for each measured species (mean of 2470±5 pixels) and a third end-member spectrum for the background (Fig 4). Next, after logarithmic transformation of reflectance, linear combination between these three end-members applied on each pixel (of both standard and probe gels), gave the proportion of each one expressed on that pixel. For the two chemical species, this proportion was multiplied by the respective known concentration of end-members (here 18.58 µM for DRP and 253.56 µM for dissolved iron). Next, a calibration with the standard is made (six points for each species: from 3.52 to 59.31 µM for DRP and from 16.46 to 253.56 µM for iron). The exactness of the method is verified by 1) comparison between measured+calculated and real concentrations of standards (mean difference of 4,4% for iron and 7,3% for DRP), 2) the expression of background end-members from linear combination (here 0.95±0.06 compared to the theoretical value of 1.00) and 3) the error from linear combination, here of 3.4±0.5%. The estimated complete incertitude is then 9,8% for iron and 11,2% for DRP.

To compare the geochemical species distribution (at submillimeter resolution) with foraminiferal density (at centimeter resolution), a handmade R code was written allowing the decrease of chemical resolution from 0.2 mm down to 1 cm. As 1 centimeter is equal to 46.3*47.4 pixels, the code takes for each centimeter the average concentration of 46*47=2162 pixels. Thus 0.3*0.4 pixels are lost for each centimeter square which correspond to 1.27% of the surface *i.e.* 2.3 cm^2 for the entire gel. This loss is attributed to each side, and then neglected.

Annexe 4

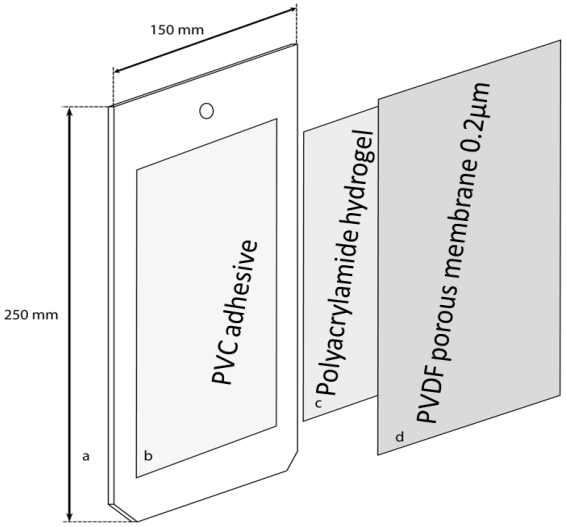

Legend: : 2D-DET gel probe: a) 3mm-thick acrylic support, b) commercial PVC tape, c) 1mm-thick polyacrylamide hydrogel, d) PVDF hydrophilic membrane

Annexe 5

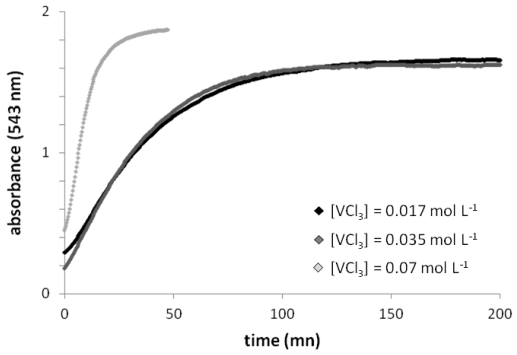

Legend: Nitrate reduction kinetics for different concentrations of vanadium chloride at 30°C. Black curve: $[VCl_3]$ = 0.017 mol L^{-1} (Schnetger and Lehners, 2014). Dark gray curve: $[VCl_3]$ = 0.035 mol L^{-1}. Light gray curve: $[VCl_3]$ = 0.07 mol L^{-1}. Nitrate concentration: 40 µmol L^{-1}. Note the increase of the initial absorbance for strong VCl_3 concentrations showing the interference of the reducing agent at 543 nm..

Annexe 6

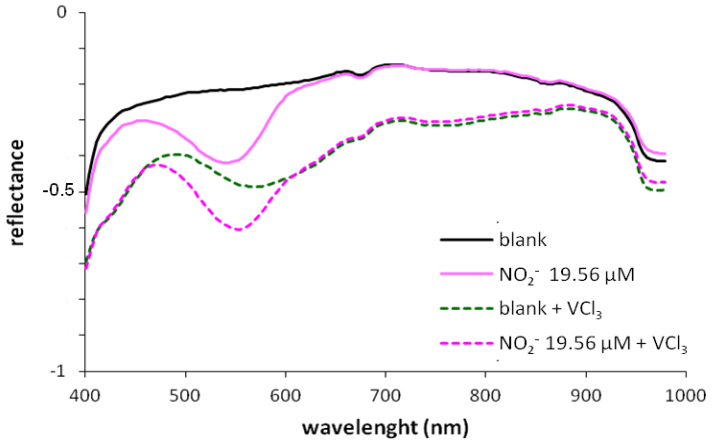

Legend: Spectra of gels before (standard + Griess reagent gels, continuous lines) and after addition of a VCl_3 gel layer (dashed lines) for the blank and a nitrite standard (19.56 µmol L^{-1}). One can see the overlap the Azo dye and vanadium chloride spectra.

Annexe 7

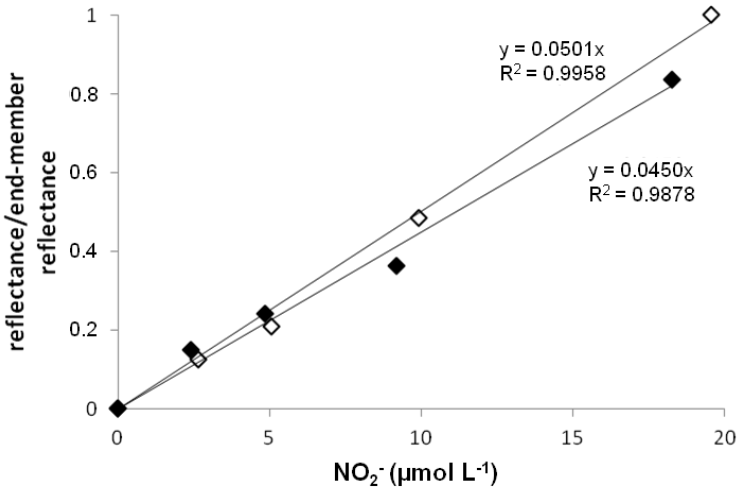

Legend: Standard curves for nitrite (white diamonds) and nitrate (black diamonds) for a three layers gel (Griess reagent+standards+VCl_3 gels). Incubation time for nitrate reduction was about 20 minutes at 50 °C. Standard error on reflectance is smaller than diamonds size.

Annexe 8

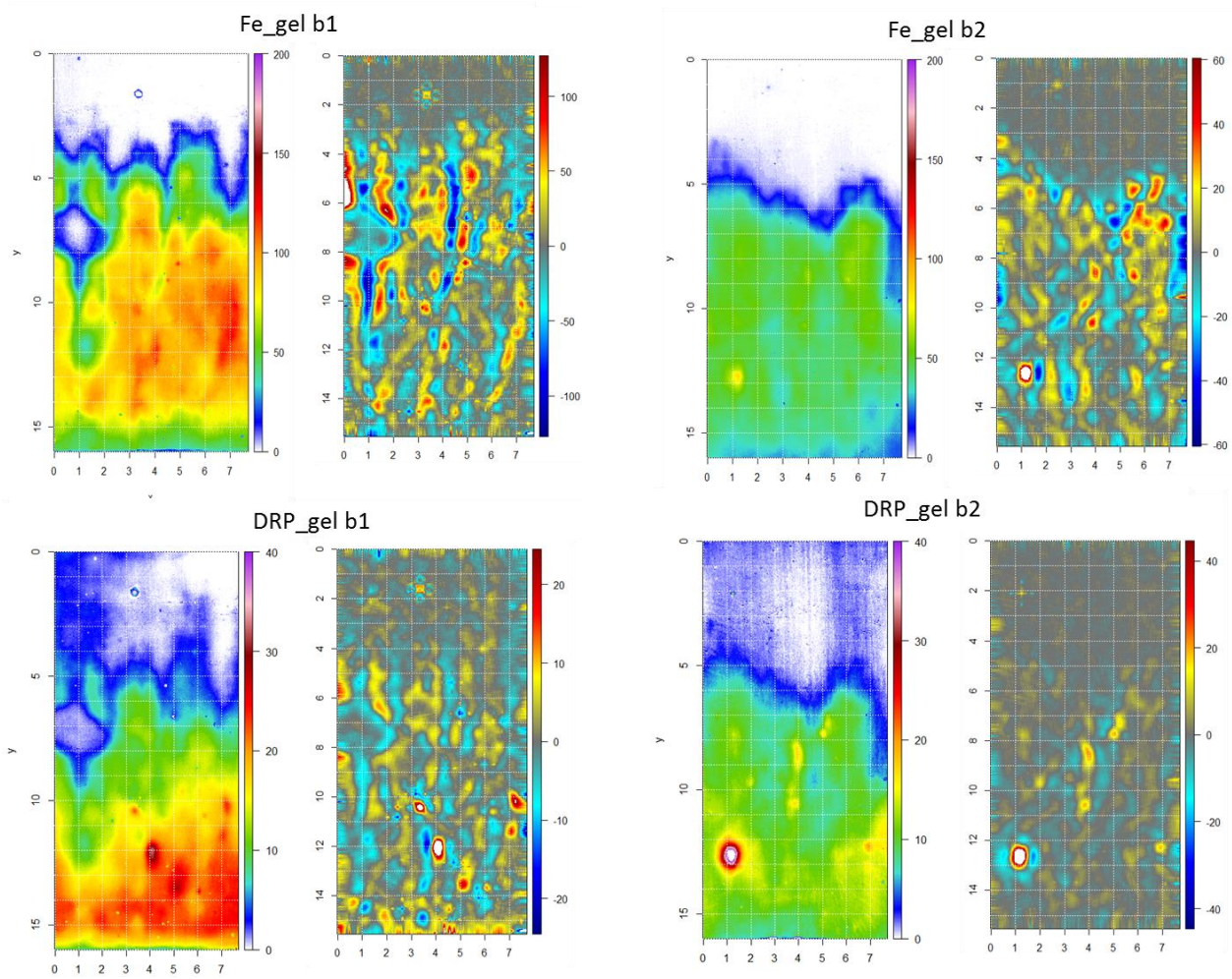

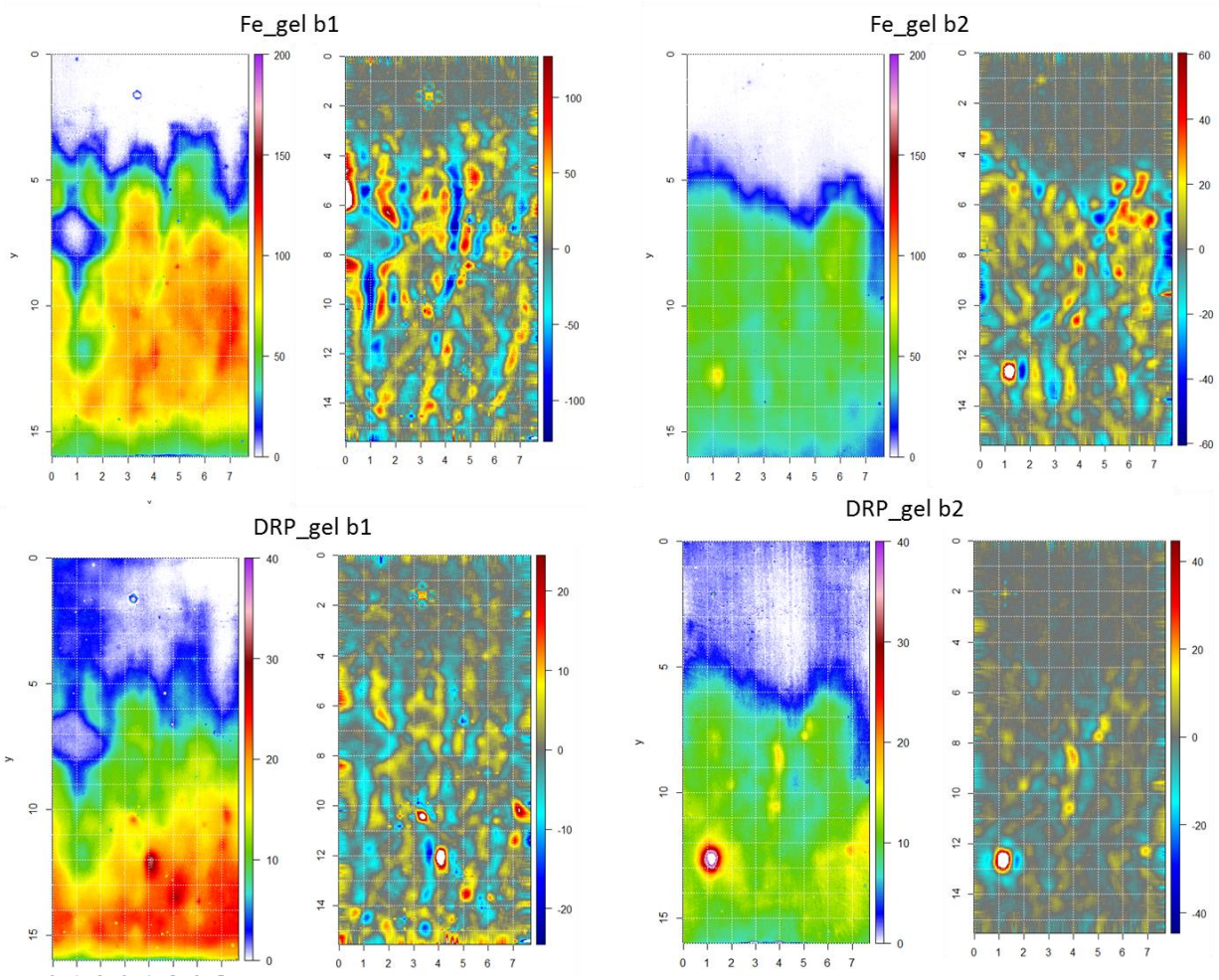

Annexe 6 suite

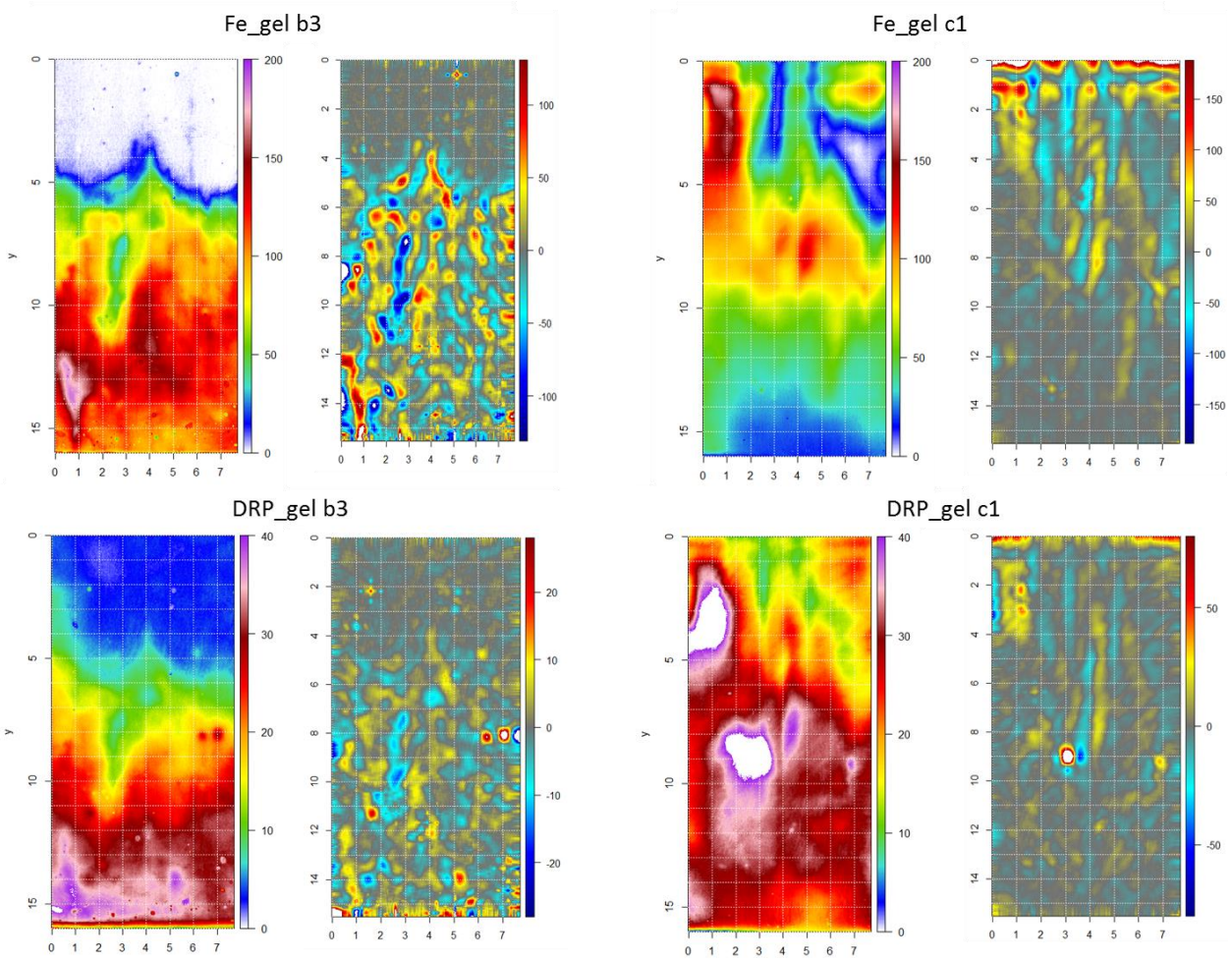

Annexe 6 suite

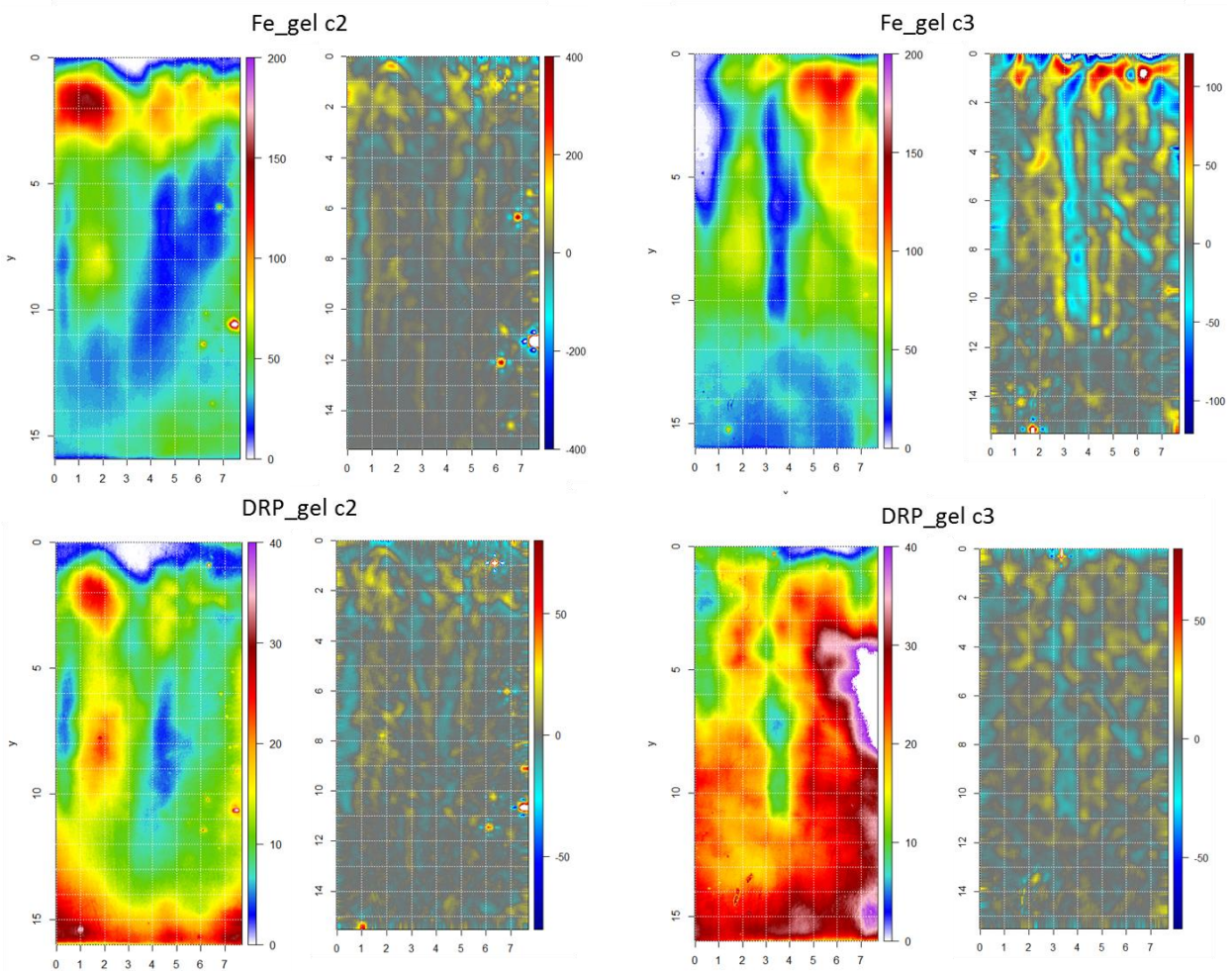

Annexe 6 suite

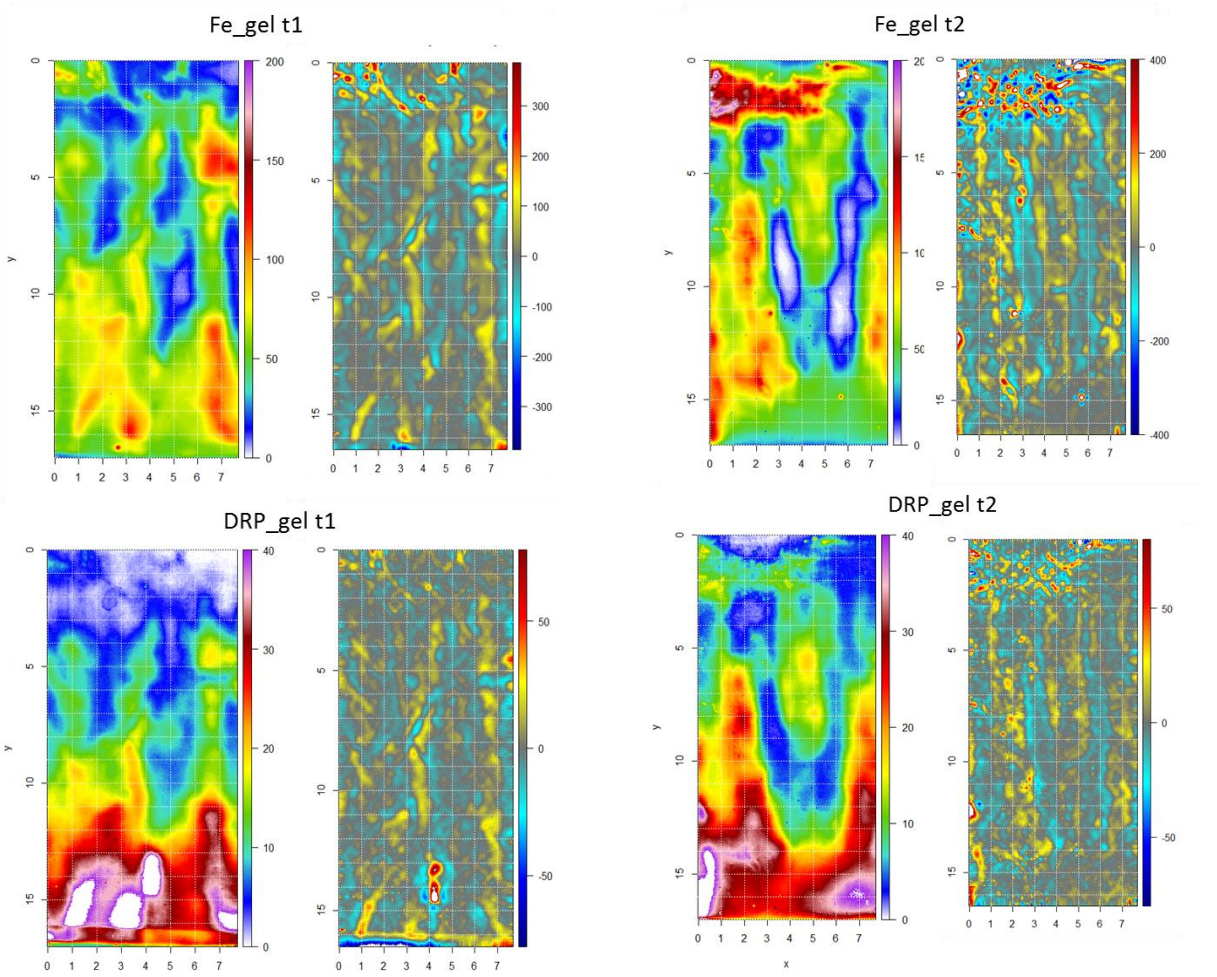

Annexe 6 suite

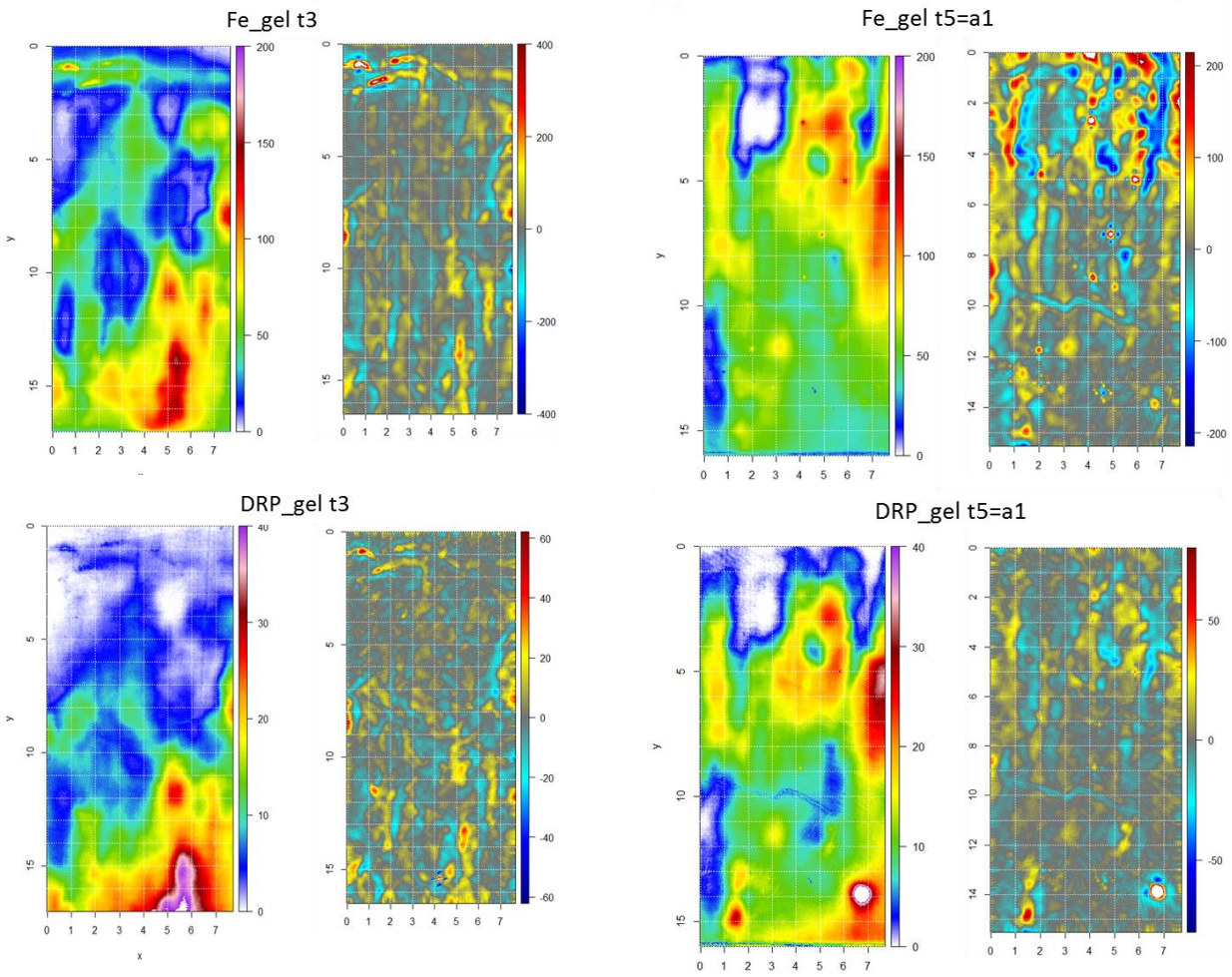

Annexe 6 suite

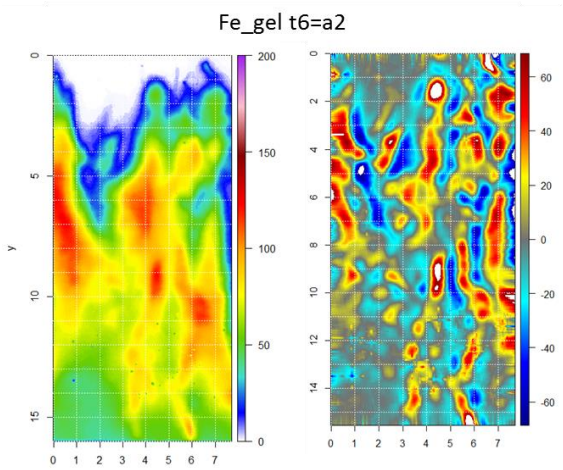

Annexe 6 : A gauche, concentration en Fe et DRP (en µmol L^{-1}) ; a droite, vitesse de production estimé par SGF pour Fe et DRP (en µmol L^{-1} d^{-1}). Les profondeur sont indiqué a partir de l'interface eau-sediment.

Annexe 9

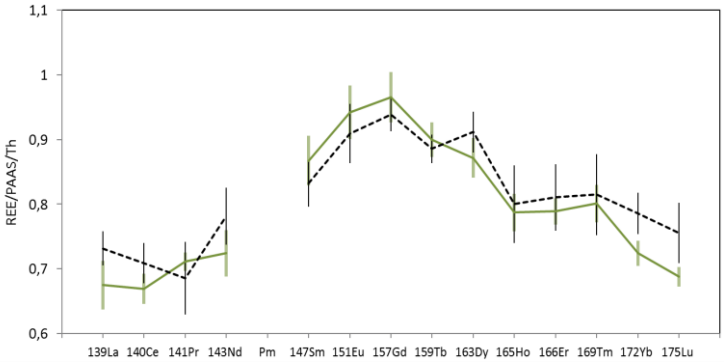

Legend: Certified material with solid line for the average of 15 analyses (error bars represent twice the standard deviation) and dotted line for BCR-667 proposed values. Represented values are normalized on PAAS (Post Archean Australian Shale; Taylor and McLennan. 1985)

Annexe 10

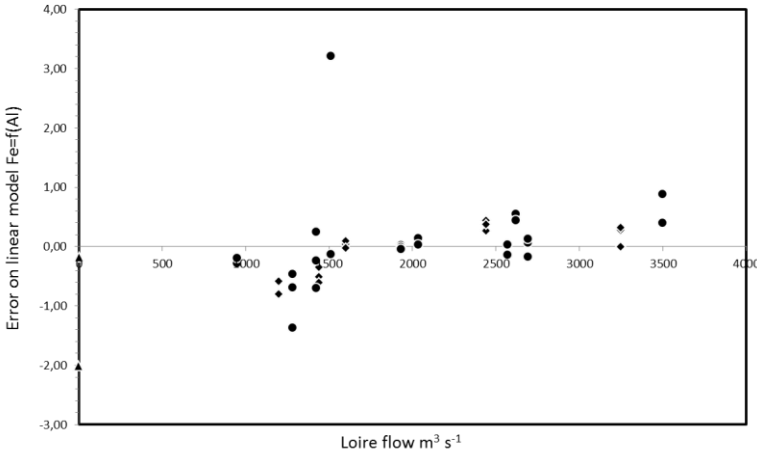

Legend: Data spread around the Fe/Al model for upstream particules represented as a function of the river flow.

UNIVERSITE BRETAGNE LOIRE

UNIVERSITÉ DE NANTES

Thèse de Doctorat

Aubin THIBAULT DE CHANVALON

Transformations de la phase solide à travers l'estuaire de la Loire en relation avec son environnement chimique et biologique.

Solid phase transformations through Loire Estuary in relations to chemical and biological environment

1.2 Résumé

Avant d'atteindre l'océan, les particules drainées par la Loire subissent d'importantes transformations chimiques dans l'estuaire. L'objectif de cette étude est d'identifier et de caractériser les processus majeurs de transformation impliquant le fer (et dans une moindre mesure Al, Mn, PO_4^{3-} et les terres rares).

L'analyse de particules en suspension a montré une diminution de 15% du fer contenu dans les particules traversant l'estuaire. La dissolution réductive des oxydes de fer durant leurs périodes de dépôt apparait comme l'une des voies réactionnelles principales. Cependant les dépôts sont caractérisés par une forte hétérogénéité spatiale due aux activités de la macrofaune benthique. Pour surmonter cette difficulté, de nouvelles méthodes de calcul, d'analyses à haute résolution et en deux dimensions de la composition de l'eau interstitielle, des particules déposées et de la méiofaune benthique ont été développées. Ainsi, nous montrons que l'activité de la macrofaune semble responsable de 80% du flux de fer dissous du sédiment vers la colonne d'eau, estimé à 0,5 mmol.m^{-2}.d^{-1}. Ces vitesses de réaction requièrent un temps de résidence dans le sédiment d'une dizaine d'années pour expliquer la perte visible de fer dans les particules en suspension, temps largement supérieur au temps de résidence moyen dans l'estuaire. Il apparait donc nécessaire de prendre en compte la réactivité des dépôts dans une plus large zone qui s'étendrait jusqu'aux vasières externes pour rendre compte des transformations du fer solide à travers l'estuaire.

Mots clés
Estuaire, Fer, Phosphore, Nitrate, Foraminifère benthique, Diagenèse précoce, Loire, Bioturbation

1.1 Abstract

Before reaching the ocean, riverine particles from the Loire watershed undergo important chemical transformations in the estuary. This study aims to identify and characterize main processes involving iron (and to a lesser extent Al, Mn, PO_4^{3-} and rare earths elements).

Suspended particulate matter data show that 15% of their iron is lost through the estuary. Reductive iron dissolution during deposition periods is likely to explain most of this loss. However, estuarine sediments are characterized by high spatial heterogeneity due to macrofaunal activities. To overcome this difficulty, new methodologies of high resolution and two-dimensional analyses and calculation of pore water, sediment and benthic meiofauna were developed. These developments enable to estimate the impact of macrofaunal activity to 80% of dissolved iron export from sediment towards water column, and a total flux of 0.5 mmol m^{-2} d^{-1}. Such kinetics requires a 10-year of residence time of particles within the sediment in order to match to observed iron loss on suspended particles. This time is much longer than the mean particle residence time in the estuary. Therefore, sediment reactivity over a larger surface that stretches to the external mudflats has to be taken into account to explain transformation of solid iron through the estuary.

Key Words
Estuary, Iron, Phosphorus, Nitrate, Benthic foraminifera, Precocious diagenesis, Loire, Bioturbation

L'Université Bretagne Loire